



City Research Online

City, University of London Institutional Repository

Citation: Thomaidis, I. M. (2020). Analytical and numerical investigation of the seismic behaviour of bridges with rocking piers. (Unpublished Doctoral thesis, City, University of London)

This is the accepted version of the paper.

This version of the publication may differ from the final published version.

Permanent repository link: <https://openaccess.city.ac.uk/id/eprint/25234/>

Link to published version:

Copyright: City Research Online aims to make research outputs of City, University of London available to a wider audience. Copyright and Moral Rights remain with the author(s) and/or copyright holders. URLs from City Research Online may be freely distributed and linked to.

Reuse: Copies of full items can be used for personal research or study, educational, or not-for-profit purposes without prior permission or charge. Provided that the authors, title and full bibliographic details are credited, a hyperlink and/or URL is given for the original metadata page and the content is not changed in any way.

City Research Online:

<http://openaccess.city.ac.uk/>

publications@city.ac.uk

*Analytical and Numerical Investigation of the Seismic
Behaviour of Bridges with Rocking Piers*

Ioannis M. Thomaidis

*A thesis submitted in partial fulfilment for the degree of
Doctor of Philosophy*



City, University of London

School of Mathematics, Computer Science & Engineering

Civil Engineering Department

Research Centre for Civil Engineering Structures

London, October 2020



City, University of London

School of Mathematics, Computer Science & Engineering
Civil Engineering Department

Research Centre for Civil Engineering Structures

Doctoral Dissertation:

***Analytical and Numerical Investigation of the Seismic Behaviour of
Bridges with Rocking Piers***

Doctoral Candidate:

Ioannis M. Thomaidis, DiplEng., MSc

(ioannis.thomaidis@city.ac.uk)

1st supervisor:

Professor Andreas J. Kappos

(andreas.kappos.1@city.ac.uk)

2nd supervisor:

Dr. Alfredo Camara

(alfredo.camara@city.ac.uk)

Examiners:

Dr. Agathoklis Giaralis, City, University of London

Professor Matthew DeJong, UC Berkeley

London, October 2020

To Kyriaki, Michalis and Giorgos (the twin brothers)

Contents

Contents	vii
List of Figures	xiii
List of Tables	xxiii
Acknowledgements	xxv
Declaration	xxvi
Abstract	xxvii
List of Symbols	xxix
List of Abbreviations	xxxiii

Chapter 1 Introduction

1.1 Problem Statement	1
1.2 Scope and Research Objectives	4
1.3 Layout of the Dissertation.....	5

Chapter 2 Review of the State-of-the-Art

2.1 Introduction.....	7
2.2 Principles of Rocking Pier Isolation in Bridges and Differences from Conventional Methods	10
2.3 Analytical Modelling of the Rocking Response	13
2.3.1 Rocking Columns.....	14
2.3.1.1 Dynamics of Free-standing Rocking Columns	14
2.3.1.2 Modelling of Impact in Free-standing Rocking Columns	17
2.3.1.3 Key Findings about Free-standing Rocking Columns	21

2.3.1.4	Effect of Vertical Component of Ground Motion on Free-standing Rocking Columns.....	24
2.3.1.5	Alternative Configurations for Rocking Columns.....	25
2.3.2	Frames with Rocking Columns	26
2.3.2.1	Dynamics and Modelling of Impact in Frames with Free-standing Rocking Columns.....	26
2.3.2.2	Key Findings about Frames with Free-standing Rocking Columns.....	28
2.3.2.3	Alternative Configurations for Frames with Rocking Columns.....	30
2.4	Inherent Disadvantages in Free-standing Rocking Piers and Enhanced Rocking Pier Configurations	31
2.4.1	Inherent Disadvantages in Free-standing Rocking Piers	31
2.4.1.1	Effect of Recentring Capacity	31
2.4.1.2	Effect of Energy Dissipation	31
2.4.1.3	Effect of Rocking Interface Behaviour.....	34
2.4.2	Enhanced Rocking Pier Configurations	35
2.5	Studies Specific to Bridges with Rocking Pier Isolation.....	38
2.6	Identified Gaps	40

Chapter 3 Analytical Modelling of Symmetric Bridges with Rocking Piers

3.1	Introduction	41
3.2	Analytical Model of the Rocking Response	42
3.2.1	Kinematics.....	44
3.2.2	Initiation of Rocking Motion.....	45
3.2.3	Equation of Motion during Rocking.....	46
3.2.4	Impact on the Abutment Backwall	50
3.2.5	Impact at the Rocking Interfaces	52
3.3	Analysis Framework.....	57
3.3.1	Description of the Studies Bridges	57
3.3.2	Representation of Seismic Action	58
3.3.2.1	Single-frequency Pulse-type Ground Motions	58
3.3.2.2	Multi-frequency Synthetic Ground Motions	59
3.3.3	Failure Criteria	60

3.3.4	Analysis Parameters.....	61
3.3.4.1	Modelling of the Abutment-Backfill System – Stiffness.....	61
3.3.4.2	Modelling of the Abutment-Backfill System – Damping.....	64
3.3.4.3	Effect of Gap Size.....	65
3.3.4.4	Effect of Pounding.....	66
3.3.5	Effect of the Abutment-Backfill System on Bridges with Rocking Piers.....	67
3.3.5.1	Rocking Response under Single-frequency Pulse-type Ground Motions.....	67
3.3.5.2	Rocking Response under Multi-frequency Synthetic Ground Motions.....	70
3.4	Closing Remarks.....	72
Chapter 4	Analytical Modelling of Asymmetric Bridges with Rocking Piers	
4.1	Introduction.....	75
4.2	Analytical Model of the Rocking Response	75
4.2.1	Kinematics	77
4.2.2	Initiation of Rocking Motion	79
4.2.3	Equation of Motion during Rocking	81
4.2.4	Impact on the Abutment Backwall.....	85
4.2.5	Impact at the Rocking Interfaces	86
4.3	Analysis Framework	91
4.3.1	Description of the Studies Bridges.....	92
4.3.2	Representation of Seismic Action.....	93
4.3.3	Failure Criteria.....	93
4.3.4	Simplification of Analysis Procedure	94
4.3.5	Effect of the Degree of Asymmetry on Bridges with Rocking Piers.....	99
4.4	Closing Remarks.....	103
Chapter 5	Non-conventional Pier Configurations in Bridges with Rocking Piers	
5.1	Introduction.....	107
5.2	Analytical Model of the Rocking Response	108
5.2.1	Kinematics	109

5.2.2	Equation of Motion during Rocking.....	112
5.2.3	Impact at the Rocking Interfaces	114
5.3	Analysis Framework.....	116
5.3.1	Description of the Studies Bridges	117
5.3.2	Representation of Seismic Action	119
5.3.2.1	Single-frequency Pulse-type Ground Motions	119
5.3.2.2	Multi-frequency Synthetic Ground Motions	119
5.3.3	Failure Criteria	119
5.3.4	Effect of the Non-conventional Pier Configurations on Bridges with Rocking Piers	120
5.3.4.1	Rocking Response under Single-frequency Pulse-type Ground Motions	120
5.3.4.2	Rocking Response under Multi-frequency Synthetic Ground Motions	121
5.4	Closing Remarks	124

Chapter 6 Comparative Assessment of Conventional Seismic and Rocking Pier Isolation

6.1	Introduction	127
6.2	Description of the Bridge Model and Analysis Outline	128
6.2.1	Original Bridge Overpass	128
6.2.2	Finite Element Modelling.....	129
6.2.2.1	Bridge with Conventional Seismic Isolation.....	129
6.2.2.1.1	Bridge with Short Piers.....	132
6.2.2.1.2	Bridge with Tall Piers.....	134
6.2.2.2	Bridge with Rocking Pier Isolation	135
6.2.3	Representation of Seismic Action	137
6.2.4	Analysis Process.....	139
6.3	Analysis Parameters for the Bridges with Rocking Pier Isolation	140
6.3.1	Mesh Scheme for the Rocking Piers	140
6.3.2	Coefficient of Friction at the Rocking Interfaces	141
6.4	Seismic Response of Bridges with Conventional Seismic and Rocking Pier Isolation..	142
6.4.1	Bridge with Short Piers	143

6.4.1.1 Superstructure Displacements.....	143
6.4.1.2 Superstructure Bending Moments.....	145
6.4.1.3 Pier Drifts.....	147
6.4.1.4 Pier Bending Moments	149
6.4.1.5 Pier Recentring Capacity	153
6.4.2 Bridge with Tall Piers	154
6.4.2.1 Superstructure Displacements.....	155
6.4.2.2 Superstructure Bending Moments.....	156
6.4.2.3 Pier Drifts.....	158
6.4.2.4 Pier Bending Moments	159
6.4.2.5 Pier Recentring Capacity	161
6.5 Closing Remarks.....	162

Chapter 7 Conclusions and Recommendations for Future Research

7.1 Conclusions.....	167
7.1.1 Analytical Modelling of Bridges with Rocking Piers.....	168
7.1.2 Proposal of Non-Conventional Pier Configurations for Bridges with Rocking Piers	171
7.1.3 Comparative Assessment of Conventional Seismic Isolation and Rocking Pier Isolation in Bridges	172
7.2 Recommendations for Future Research	174
7.2.1 Analytical Modelling of Bridges with Rocking Piers.....	175
7.2.2 Proposal of Non-Conventional Pier Configurations for Bridges with Rocking Piers	178
7.2.3 Comparative Assessment of Conventional Seismic Isolation and Rocking Pier Isolation in Bridges	179

Appendix A Supplement to Chapter 3

A.1 Analytical Model of the Rocking Response [§3.2].....	181
A.1.1 Impact at the Rocking Interfaces [§3.2.5].....	181
A.2 Analysis Framework [§3.3]	184

Appendix B Supplement to Chapter 4

B.1 Analytical Model of the Rocking Response [§4.2] 185
B.1.1 Impact at the Rocking Interfaces [§4.2.5]..... 185

Appendix C Supplement to Chapter 6

C.1 Description of the Bridge Model and Analysis Outline [§6.2]..... 189
C.1.1 Original Bridge Overpass [§6.2.1]..... 189

Appendix D References

..... 193

Appendix E Relevant Publications

..... 211

List of Figures

Fig. 1-1	View of the colonnade of the Temple of Athena at Aegina, Greece constructed around 480BC. (<i>figure taken from Drosos & Anastasopoulos 2015</i>).....	2
Fig. 1-2	Schematic of the deformed shape of the (A) contemporary moment-resisting frame and (B) frame with rocking columns under horizontal seismic loads, and the corresponding force-displacement ($F-u$) behaviour. (<i>figure taken from Makris 2014</i>).....	3
Fig. 2-1	(A) View of the South Rangitikei Rail Bridge, New Zealand, and (B) the rocking surface at the pier base. (<i>figure taken from Ma & Khan 2008</i>).....	8
Fig. 2-2	View of the low-damage connection installed at the (A) bottom and (B) top surfaces of the rocking piers in the Wigram-Magdala Link Bridge, New Zealand. (<i>figure taken from Routledge et al. 2016</i>).....	8
Fig. 2-3	(A) Schematic of a free-standing rocking column during rocking motion, and (B) the effect of size (R) on the seismic rocking response of the member. (<i>figure taken from Makris 2014</i>)	11
Fig. 2-4	Strength or acceleration amplitude to initiate rocking motion ($g \cdot \tan \alpha$) in a free-standing rocking column, accounting for the influence of its slenderness (α).....	11
Fig. 2-5	Idealised moment-rotation ($M-\theta$) behaviour of a free-standing rocking column, representing the ‘recentering moment’ of the member. (<i>figure taken from Makris 2014</i>)	12
Fig. 2-6	Free-body diagram for a free-standing rocking column at the onset of rocking motion. (<i>figure taken from Makris 2014</i>)	14
Fig. 2-7	Schematic of a free-standing rocking column tilting (A) about the CR O, and (B) about a migrating kinematic CR. (<i>figure taken from Kalliontzis et al. 2016</i>).....	18
Fig. 2-8	Ratios of the experimental values of the CoR at the rocking interfaces ($\eta_{exp.}$) to those obtained from the analytical approaches ($\eta_{anal.}$) of Housner (1963) and Kalliontzis <i>et al.</i> (2016). Results obtained for rectangular free-standing rocking columns with different aspect ratio (h/b) and interface materials	20
Fig. 2-9	Dimensionless intensity regions in terms of ω_p/p and $a_p/g \cdot \tan \alpha$ highlighting where analysis with pulse-type motions is more reliable and where it is more sensitive, when rocking structures are examined. (<i>figure taken from Acikgoz & DeJong 2014</i>).....	22
Fig. 2-10	OMAS for a free-standing rocking column with slenderness $\alpha = 14^\circ$ when subject to acceleration pulses of (A) sine, (B) symmetric and (C) antisymmetric Ricker type. Blue shapes refer always to Mode 0, while red shapes to Mode 1 and 2. (<i>figure taken from Makris & Vassiliou 2012</i>).....	23
Fig. 2-11	Rocking spectrum in terms of (A) relative rotation (θ) and (B) angular velocity ($\dot{\theta}$) for free-standing rocking columns with different slenderness (α), when subject to	

	the Pacoima Dam motion recorded during the 1971 San Fernando earthquake. (figure taken from Makris & Konstantinidis 2003).....	24
Fig. 2-12	Effect of horizontal ($\ddot{u}_{g,x}$) and vertical components of ground motion ($\ddot{u}_{g,z}$) expressed through the trigonometric functions of cosine and sine type, respectively, accounting for the influence of the slenderness (α). Results obtained when $\theta = 0$	25
Fig. 2-13	Schematic of a frame with free-standing rocking columns of equal height (symmetric) during rocking motion. (figure taken from Makris & Vassiliou 2013)	26
Fig. 2-14	Schematic of a frame with free-standing rocking columns of unequal height (asymmetric) (A) when sustaining counter-clockwise rotation of the columns, (B) at the at-rest position, and (C) when sustaining clockwise rotation of the columns. (figure taken from Dimitrakopoulos & Giouvanidis 2015)	28
Fig. 2-15	(A) Ratio \widehat{R}/R as described by Eq. (2-18) and (B) CoR at the rocking interfaces (η) for free-standing rocking columns (Housner 1963) and for relevant symmetric frames (Makris & Vassiliou 2013), accounting for the influence of the superstructure mass effect (γ). Results obtained when $\alpha = 0.1$ rad.....	29
Fig. 2-16	OMAS for a symmetric frame with free-standing rocking columns and for the corresponding asymmetric configuration. Results obtained when subject to positive and negative acceleration pulses of (A) symmetric and (B) antisymmetric Ricker type. (figure taken from Dimitrakopoulos & Giouvanidis 2015).....	29
Fig. 2-17	Experimental setup of a frame-type system with rocking piers having steel-to-steel and plastic-to-steel interface materials. (figure taken from Cheng 2008)	34
Fig. 2-18	Force-drift ($F-d$) behaviour of a free-standing rocking pier. Results obtained for a quasi-static cyclic test with (A) lower and (B) higher external axial loads. (figure taken from Roh & Reinhorn 2010b)	35
Fig. 2-19	Rocking pier with FSHB, including the moment-rotation ($M-\theta$) behaviour that is offered by (A) the unbonded tendon and (B) the dissipating devices, as well as (C) the resulting hysteresis behaviour. (figure taken from Palermo & Pampanin 2008)	36
Fig. 2-20	Rocking pier with HSRB, including (A) the pre-decompression and (B) post-decompression stages. (figure taken from Ou et al. 2007)	37
Fig. 2-21	Schematic of a bridge with (A) conventional seismic isolation through elastomeric bearings and (B) rocking pier isolation. (figure taken from Agalianos et al. 2017)	39
Fig. 3-1	Schematic of a symmetric bridge supported on N rectangular-in-elevation free-standing rocking piers, and on frictionless sliding bearings at the abutment seats. The bridge is at the at-rest position	43
Fig. 3-2	Schematic of a symmetric bridge with rocking piers during rocking motion, and the positive sign convention	45
Fig. 3-3	Longitudinal influence of the abutment-backfill system (q) in symmetric bridges with rocking piers, accounting for the influence of (A) the size of the piers (R), (B)	

	the superstructure mass effect (γ) and the number of piers (N). Results obtained when the spring stiffness (k) and the dashpot coefficient (c) are constant.....	50
Fig. 3-4	Schematic of the pounding problem considered in the rocking motion of a symmetric bridge with rocking piers, including (A) the pre-pounding state with a longitudinal velocity of the superstructure $\dot{u}_{deck,I}^{CG}$ and (B) the post-pounding state with an associated deck velocity $\dot{u}_{deck,II}^{CG}$	51
Fig. 3-5	Schematic of the impact problem considered in the rocking motion of a symmetric bridge with rocking piers that (A) undergoes counter-clockwise (negative) rotation with an angular velocity of the piers $\dot{\theta}_I$, (B) impacts at the corresponding pivot points, and then reverses to (C) clockwise (positive) rotation with an angular velocity of the piers $\dot{\theta}_{II}$	53
Fig. 3-6	CoR at the rocking interfaces (η) for symmetric bridges with rocking piers and for equivalent frames (Makris & Vassiliou 2013), accounting for the influence of the superstructure mass effect (γ). Results obtained when $\bar{L} = 1$	56
Fig. 3-7	CoR at the rocking interfaces (η) for symmetric bridges with rocking piers, accounting for the influence of (A) the length of the end spans (L_1), (B) the length of the intermediate spans (L_2), and (C) the number of piers (N). Results obtained when the deck mass is constant	56
Fig. 3-8	Response acceleration spectra of the set of ARs, and matching to EC8 target spectrum with PGA = 0.36 g and site conditions C	59
Fig. 3-9	Force-displacement ($F-u$) behaviour of the abutment-backfill system in the longitudinal direction (Kappos <i>et al.</i> 2007)	61
Fig. 3-10	Histories of the longitudinal displacement of the superstructure (u_{deck}^{CG}) for the symmetric bridge with $N = 3$ rocking piers, considering three alternatives for the abutment-backfill stiffness. Results obtained when subject to (A) AR2 and (B) AR4.....	63
Fig. 3-11	Histories of the longitudinal displacement of the superstructure (u_{deck}^{CG}) for the symmetric bridge with $N = 7$ rocking piers, considering three alternatives for the abutment-backfill stiffness. Results obtained when subject to (A) AR5 and (B) AR8.....	64
Fig. 3-12	Histories of the longitudinal displacement of the superstructure (u_{deck}^{CG}) for the symmetric bridge with $N = 7$ rocking piers, considering three alternatives for the gap size. Results obtained when subject to (A) AR1 and (B) AR6	65
Fig. 3-13	Histories of the longitudinal displacement of the superstructure (u_{deck}^{CG}) for the symmetric bridge with $N = 7$ rocking piers, considering three alternatives for the CoR value to describe pounding. Results obtained when subject to (A) AR3 and (B) AR9.....	66
Fig. 3-14	FMAS for the symmetric bridges and for the equivalent frames with $N = 3$ and $N = 7$ rocking piers. Results obtained when subject to acceleration pulses of (A) sine, (B) symmetric and (C) antisymmetric Ricker type	68
Fig. 3-15	Peak responses of the longitudinal displacement of the superstructure (u_{deck}^{CG}) for the symmetric bridges and for the equivalent frames with (A) $N = 3$ and (B) $N = 7$ rocking piers. Results obtained when subject to ARi	70

Fig. 3-16	Histories of the longitudinal displacement of the superstructure (u_{deck}^{CG}) for the symmetric bridges with rocking piers and for the equivalent frames. Results obtained for (A) the structure with $N = 3$ piers when subject to AR3 and for (B) the structure with $N = 7$ piers when subject to AR6	71
Fig. 4-1	Schematic of an asymmetric bridge supported on two rectangular-in-elevation free-standing rocking piers, and on frictionless sliding bearings at the abutment seats. The bridge is at the at-rest position.....	76
Fig. 4-2	Schematic of an asymmetric bridge with rocking piers during rocking motion. The structure sustains (A) counter-clockwise (positive) rotation of the piers, and (B) clockwise (negative) rotation of the piers.....	77
Fig. 4-3	Longitudinal influence of the abutment-backfill system (q) in bridges with rocking piers of different degree of asymmetry, accounting for the influence of the mass of the short pier ($m_{pier,2}$). Results obtained when the tall pier section and the deck mass are constant.....	84
Fig. 4-4	Schematic of the pounding problem considered in the rocking motion of an asymmetric bridge with rocking piers, including (A) the pre-pounding state with a longitudinal velocity of the superstructure $\dot{u}_{deck,I}^{CG}$, and (B) the post-pounding state with an associated deck velocity $\dot{u}_{deck,II}^{CG}$	85
Fig. 4-5	Schematic of the impact problem considered in the rocking motion of an asymmetric bridge with rocking piers that (A) undergoes counter-clockwise (positive) rotation with an angular velocity of the tall pier $\dot{\varphi}_I$, (B) impacts at the corresponding pivot points, and then reverses to (C) clockwise (negative) rotation with an angular velocity of the tall pier $\dot{\varphi}_{II}$	86
Fig. 4-6	CoR at the rocking interfaces (η) for bridges with rocking piers of different degree of asymmetry and for equivalent frames (Dimitrakopoulos & Giouvanidis 2015), accounting for the influence of the short pier height (H_2). Results obtained when the tall pier section and the deck mass are constant	90
Fig. 4-7	CoR at the rocking interfaces (η) for asymmetric bridges with rocking piers, accounting for the influence of (A) the length of the end spans (L_1) and (B) the length of the intermediate spans (L_2). Results obtained when the deck mass is constant.....	91
Fig. 4-8	Response acceleration spectra of the set of ARs, and matching to EC8 target spectrum with PGA = 0.6 g and site conditions C.....	94
Fig. 4-9	Comparison of the rigorous and simplified models for the range of the dependent variables (A) $\partial\varphi_{CD}/\partial\varphi$, (B) $\partial^2\varphi_{CD}/\partial\varphi^2$, (C) $\partial\theta_{deck}/\partial\varphi$ and (D) $\partial^2\theta_{deck}/\partial\varphi^2$ with respect to the DoF φ . Results obtained for the moderately asymmetric bridge with rocking piers of $\bar{h} = 1.25$ and $\alpha_1 = 0.1$ rad	96
Fig. 4-10	Comparison of the rigorous and simplified models for the range of the dependent variables (A) $\partial\varphi_{CD}/\partial\varphi$, (B) $\partial^2\varphi_{CD}/\partial\varphi^2$, (C) $\partial\theta_{deck}/\partial\varphi$ and (D) $\partial^2\theta_{deck}/\partial\varphi^2$ with respect to the DoF φ . Results obtained for the highly asymmetric bridge with rocking piers of $\bar{h} = 2$ and $\alpha_1 = 0.1$ rad	97
Fig. 4-11	Histories of the longitudinal (u_{deck}^{CG}) and vertical displacements of the superstructure (v_{deck}^{CG}) as well as superstructure rotation (θ_{deck}) for the moderately	

	asymmetric bridge with rocking piers of $\bar{h} = 1.25$, considering the rigorous and simplified models for $\partial\varphi_{CD}/\partial\varphi$, $\partial^2\varphi_{CD}/\partial\varphi^2$, $\partial\theta_{deck}/\partial\varphi$ and $\partial^2\theta_{deck}/\partial\varphi^2$. Results obtained when subject to (A) AR8 and (B) AR1098
Fig. 4-12	Histories of the longitudinal (u_{deck}^{CG}) and vertical displacements of the superstructure (v_{deck}^{CG}) as well as superstructure rotation (θ_{deck}) for the highly asymmetric bridge with rocking piers of $\bar{h} = 2$, considering the rigorous and simplified models for $\partial\varphi_{CD}/\partial\varphi$, $\partial^2\varphi_{CD}/\partial\varphi^2$, $\partial\theta_{deck}/\partial\varphi$ and $\partial^2\theta_{deck}/\partial\varphi^2$. Results obtained when subject to (A) AR2 and (B) AR399
Fig. 4-13	Peak responses of the (A) longitudinal (u_{deck}^{CG}) and (B) vertical displacements of the superstructure (v_{deck}^{CG}) as well as (C) superstructure rotation (θ_{deck}), (D) relative rotation of the left rocking pier (θ_1) and (E) relative rotation of the right rocking pier (θ_2) for the bridges with rocking piers of different degree of asymmetry. Results obtained when subject to ARi101
Fig. 4-14	Histories of the (A) longitudinal (u_{deck}^{CG}) and (B) vertical displacements of the superstructure (v_{deck}^{CG}) as well as (C) superstructure rotation (θ_{deck}), (D) relative rotation of the left rocking pier (θ_1) and (E) relative rotation of the right rocking pier (θ_2) for the bridges with rocking piers of different degrees of asymmetry. Results obtained when subject to AR7102
Fig. 5-1	Schematic of rocking piers with (A) rectangular section (or R), (B) I-shaped cross-section (or IC) and (C) I-shaped longitudinal section (or IL). The piers are at the at-rest position.....108
Fig. 5-2	Schematic of rocking piers with (A) R, (B) IC and (C) IL configurations during rocking motion.....109
Fig. 5-3	Total mass (m_{tot}) of bridges with rocking piers of different configuration, accounting for the influence of number of piers (N). Results obtained when the pier dimensions and the deck section are constant110
Fig. 5-4	Mass moment of inertia of a rocking pier with respect to its CG (I_{pier}^{CG}) for different pier configurations, accounting for the influence of pier height (H). Results obtained when the pier width is constant111
Fig. 5-5	Superstructure mass effect (γ) for bridges with rocking piers of different configuration, accounting for the influence of pier height (H). Results obtained when the pier width and the deck mass are constant112
Fig. 5-6	Shape factor $p_{sec,1}$ for rocking piers of different configuration, accounting for the influence of pier height (H). Results obtained when the pier width is constant113
Fig. 5-7	Longitudinal influence of the abutment-backfill system (q) for bridges with rocking piers of different configuration, accounting for the influence of pier height (H). Results obtained when the pier width and the deck mass are constant114
Fig. 5-8	Shape factors (A) $p_{sec,2}$ and (B) $p_{sec,3}$ for rocking piers of different configuration, accounting for the influence of pier height (H). Results obtained when the pier width is constant116

Fig. 5-9	CoR at the rocking interfaces (η) for bridges with rocking piers of different configuration, accounting for the influence of pier height (H). Results obtained when the pier width and the deck mass are constant.....	116
Fig. 5-10	Response acceleration spectra of the set of ARs, and matching to EC8 target spectrum with PGA = 0.72 g and site conditions C.....	119
Fig. 5-11	FMAS for the bridges with rocking piers of different configuration. Results obtained when subject to acceleration pulses of (A) sine, (B) symmetric and (C) antisymmetric Ricker type.....	120
Fig. 5-12	Peak responses of the longitudinal displacement of the superstructure (u_{deck}^{CG}) for the bridges with rocking piers of different configuration. Results obtained when subject to ARi applying to the design earthquake conditions (PGA = 0.36 g)	122
Fig. 5-13	Histories of the longitudinal displacement of the superstructure (u_{deck}^{CG}) for the bridges with rocking piers of different configuration. Results obtained when subject to (A) AR3 and (B) AR9 applying to the design earthquake conditions (PGA = 0.36 g)	123
Fig. 5-14	Peak responses of the longitudinal displacement of the superstructure (u_{deck}^{CG}) for the bridges with rocking piers of different configuration. Results obtained when subject to ARi applying to the ‘extreme’ earthquake conditions (PGA = 0.72 g)	124
Fig. 6-1	Bridge with CSI that is supported on short and tall piers: (A) layout in the longitudinal direction, (B) different cross-sections of the superstructure, (C) generated mesh in the foundation-pier-cap beam, (D) beam element embedded in the piers, and (E) layout of the abutment-backfill system as well as mesh generation in the abutment seat	130
Fig. 6-2	Bridge with CSI that is supported on short piers: (A) modelling of the LRBs, and (B) bilinear force-displacement behaviour of the LRBs located at the piers and at the abutments.....	132
Fig. 6-3	Bilinear force-displacement behaviour of the LRBs located (A) at the piers and (B) at the abutments for the bridge with CSI that is supported on tall piers	135
Fig. 6-4	Bridge with RPI that is supported on short and tall piers: (A) layout in the longitudinal direction, (B) mesh for the whole bridge, (C) generated mesh in the superstructure at the contact regions, (D) generated mesh in the foundation-rocking pier, (E) beam element embedded in the piers, and (F) contact interactions at the rocking interfaces.....	136
Fig. 6-5	Time-history of the individual scaled records Ri, and matching of their response acceleration spectra to the EC8 target spectrum with PGA = 0.24 g and site conditions B.....	139
Fig. 6-6	Histories of the total longitudinal drifts of (A) pier P1 ($d_{P1,x}$) and (B) pier P2 ($d_{P2,x}$) for the RPI bridge with short piers. Results obtained when subject to the scaled R1, considering three alternatives for the mesh scheme of the rocking piers ...	140
Fig. 6-7	(A) Layout of the corner joints at the bottom surface of the rocking piers, and histories of the total horizontal displacements of pier P1 ($u_{P1,xy}$) subject to the	

	scaled (B) R5 and (C) R11, and of pier P2 ($u_{P2,xy}$) subject to (D) R3 and (E) R6 for the RPI bridge with short piers. Results obtained considering two alternatives for the static CoF value to describe sliding at the rocking interfaces 142
Fig. 6-8	Peak superstructure relative displacements of segment (P1-P2) in the (A) longitudinal ($u_{deck,x}$) and (B) transverse directions ($u_{deck,y}$) for the CSI and RPI bridges with short piers. Results obtained when subject to the scaled Ri..... 143
Fig. 6-9	Peak permanent superstructure displacements of segment (P1-P2) in the (A) longitudinal ($u_{deck,x-(per.)}$) and (B) transverse directions ($u_{deck,y-(per.)}$) for the CSI and RPI bridges with short piers. Results obtained when subject to the scaled Ri 145
Fig. 6-10	Peak total BMs in the longitudinal direction at (A) the side span (A1-P1) ($M_{deck,y-(A1-P1)}$) and (B) the side span (P2-A2) ($M_{deck,y-(P2-A2)}$) as well as (C) the intermediate span (P1-P2) ($M_{deck,y-(P1-P2)}$) for the CSI and RPI bridges with short piers. Results obtained when subject to the scaled Ri..... 146
Fig. 6-11	FE model of the RPI bridge with short piers during rocking motion in the longitudinal direction, and differential uplifts of the superstructure at the different supports..... 146
Fig. 6-12	Peak total drifts of pier P1 in the (A) longitudinal ($d_{P1,x}$) and (B) transverse directions ($d_{P1,y}$) and of pier P2 in the (A) longitudinal ($d_{P2,x}$) and (B) transverse directions ($d_{P2,y}$) for the CSI and RPI bridges with short piers. Results obtained when subject to the scaled Ri..... 148
Fig. 6-13	Peak drift components separated into rigid body and bending drifts of pier P1 in the (A) longitudinal ($d_{P1,x}$) and (B) transverse directions ($d_{P1,y}$) and of pier P2 in the (A) longitudinal ($d_{P2,x}$) and (B) transverse directions ($d_{P2,y}$) for the RPI bridge with short piers. Results obtained when subject to the scaled Ri..... 149
Fig. 6-14	(A) Position of the examined pier sections in the beam elements, as well as peak BMs in the longitudinal direction of pier P1 at (B) section 1 ($M_{P1,y-(1)}$), (C) section 2 ($M_{P1,y-(2)}$) and (D) section 3 ($M_{P1,y-(3)}$) for the CSI and RPI bridges with short piers. Results obtained when subject to the scaled Ri..... 150
Fig. 6-15	Typical BM diagram of pier P1 in the (A) CSI and (B) RPI bridges with short piers, accounting for the mean BM values when subject to the scaled Ri 151
Fig. 6-16	Peak BMs in the longitudinal direction of pier P2 at (A) section 1 ($M_{P2,y-(1)}$), (B) section 2 ($M_{P2,y-(2)}$) and (C) section 3 ($M_{P2,y-(3)}$) for the CSI and RPI bridges with short piers. Results obtained when subject to the scaled Ri..... 152
Fig. 6-17	Typical BM diagram of pier P2 in the (A) CSI and (B) RPI bridges with short piers, accounting for the mean BM values when subject to the scaled Ri 153
Fig. 6-18	(A) Layout of the corner joints at the bottom surface of the rocking piers, and histories of the total horizontal displacements of pier P1 ($u_{P1,xy}$) subject to the scaled (B) R1 and (C) R2 and of pier P2 ($u_{P2,xy}$) subject to (D) R5 and (E) R7 for the RPI bridge with short piers 154
Fig. 6-19	Peak superstructure relative displacements of segment (P1-P2) in the (A) longitudinal ($u_{deck,x}$) and (B) transverse directions ($u_{deck,y}$) for the CSI and RPI bridges with tall piers. Results obtained when subject to the scaled Ri..... 155
Fig. 6-20	Peak permanent superstructure displacements of segment (P1-P2) in the (A) longitudinal ($u_{deck,x-(per.)}$) and (B) transverse directions ($u_{deck,y-(per.)}$) for the CSI

and RPI bridges with tall piers. Results obtained when subject to the scaled Ri 156

Fig. 6-21 Peak total BMs in the longitudinal direction at (A) the side span (A1-P1) ($M_{deck,y-(A1-P1)}$) and (B) the side span (P2-A2) ($M_{deck,y-(P2-A2)}$) as well as (C) the intermediate span (P1-P2) ($M_{deck,y-(P1-P2)}$) for the CSI and RPI bridges with tall piers. Results obtained when subject to the scaled Ri 157

Fig. 6-22 Peak total drifts of pier P1 in the (A) longitudinal ($d_{P1,x}$) and (B) transverse directions ($d_{P1,y}$) and of pier P2 in the (A) longitudinal ($d_{P2,x}$) and (B) transverse directions ($d_{P2,y}$) for the CSI and RPI bridges with tall piers. Results obtained when subject to the scaled Ri 159

Fig. 6-23 (A) Position of the examined pier sections in the beam elements, as well as peak BMs in the longitudinal direction of pier P2 at (B) section 1 ($M_{P2,y-(1)}$), (C) section 2 ($M_{P2,y-(2)}$) and (D) section 3 ($M_{P2,y-(3)}$) for the CSI and RPI bridges with tall piers. Results obtained when subject to the scaled Ri 160

Fig. 6-24 Typical BM diagram of pier P2 in the (A) CSI and (B) RPI bridges with tall piers, accounting for the mean BM values when subject to the scaled Ri 161

Fig. 6-25 (A) Layout of the corner joints at the bottom surface of the rocking piers, and histories of the total horizontal displacements of pier P1 ($u_{P1,xy}$) subject to the scaled (B) R1 and (C) R2 and of pier P2 ($u_{P2,xy}$) subject to (D) R5 and (E) R7 for the RPI bridge with tall piers 162

Fig. 7-1 Schematic of a rectangular pier with rocking surfaces and end grooves formed with (A) sharp edges, and (B) rounded edges (highlighted in red) 177

Fig. A-1 Schematic of the impact problem considered in the rocking motion of a symmetric bridge that (A) undergoes clockwise (positive) rotation with an angular velocity of the piers $\dot{\theta}_I$, (B) impacts at the corresponding pivot points and then reverses to (C) counter-clockwise (negative) rotation with an angular velocity of the piers $\dot{\theta}_{II}$ 182

Fig. A-2 Flowchart of the MATLAB code to formulate the rocking motion of a symmetric bridge with rocking piers..... 184

Fig. B-1 Schematic of the impact problem considered in the rocking motion of an asymmetric bridge that (A) undergoes clockwise (negative) rotation with an angular velocity of the tall pier $\dot{\phi}_I$, (B) impacts at the corresponding pivot points and then reverses to (C) counter-clockwise (positive) rotation with an angular velocity of the tall pier $\dot{\phi}_{II}$ 186

Fig. C-1 Overpass T7, Egnatia Motorway, N. Greece: (A) captured in Google Earth (2011) view (Gkatzogias 2017) and (B) schematic in the longitudinal direction (Egnatia Motorway 2002, Gkatzogias 2017) 189

Fig. C-2	Schematic of the box girder section of Overpass T7 (Egnatia Motorway 2002, Paraskeva 2013) at the positions of (A) abutments, (B) piers and (C) spans.....	190
Fig. C-3	Schematic of lateral cross-section of Overpass T7 (Egnatia Motorway 2002, Gkatzogias 2017) in the locations of (A) Pier 1 and (B) Abutment 1.....	191
Fig. C-4	Schematic in the longitudinal direction of Abutment 2 of Overpass T7 (Egnatia Motorway 2002, Paraskeva 2013)	192

List of Tables

Table 2-1	Principles of different construction methods for earthquake-resistant bridges, when employing (i) a ‘traditional’ moment resisting frame, (ii) a conventional seismic isolation technique and (iii) ‘bare’ rocking pier isolation. (<i>table adapted from Makris 2014</i>)10
Table 2-2	Experimental studies determining the CoR values at the rocking interfaces ($\eta_{exp.}$) for rectangular free-standing rocking columns with different aspect ratio (h/b), slenderness (α) and interface materials. The values of η are calculated according to the analytical approaches of Housner (1963) ($\eta_{Hous.}$) and Kalliontzis <i>et al.</i> (2016) ($\eta_{Kall.}$). The effect of the CR in Eq. (2-15) is equal to $k = 0.72$19
Table 2-3	Rocking columns supplemented with additional devices to improve the seismic performance of the free-standing configuration. Principles and main findings...25
Table 2-4	Frames with rocking columns supplemented with additional devices to improve the seismic performance of the free-standing configuration. Principles and main findings30
Table 2-5	Equivalent viscous damping ratio (ζ) for different models presented in the literature, accounting for experimental CoR values at the rocking interfaces ($\eta_{exp.}$) for rectangular free-standing rocking columns with different slenderness (α). Value of ζ_{in} is assumed equal to 3%33
Table 2-6	Rocking piers with enhanced configurations. Principles and main findings37
Table 3-1	Information for the generated ARs, including the Peak Ground Acceleration (PGA), the Peak Ground Velocity (PGV), the Peak Ground Displacement (PGD), and the Arias Intensity (I_A)59
Table 3-2	Spring stiffness values of the abutment-backfill system (k), considering three alternatives. Results obtained for the bridge configuration with $N = 3$ piers62
Table 3-3	Spring stiffness values of the abutment-backfill system (k), considering three alternatives. Results obtained for the bridge configuration with $N = 7$ piers63
Table 4-1	Information for the bridges with rocking piers of different degree of asymmetry, including the deck mass (m_{deck}), the pier masses ($m_{pier,1}$ and $m_{pier,2}$), and the total mass (m_{tot}) as well as the stabilising factors of the superstructure mass effect (γ) and the longitudinal influence of the abutment-backfill system (q)93
Table 5-1	Formulae for the shape factor $p_{sec,1}$ for piers of different configuration113

Table 5-2	Formulae for the shape factors $p_{sec,2}$ and $p_{sec,3}$ for piers of different configuration 115
Table 5-3	Information for the bridges with rocking piers of different configuration, including the deck mass (m_{deck}), the pier mass (m_{pier}) and the total mass (m_{tot}) as well as the critical section of the pier (A_c) and the induced normalised axial load (v_{Ed})..... 118
Table 5-4	Stabilising factors for the bridges with rocking piers of different configuration, including the superstructure mass effect (γ) and the longitudinal influence of the abutment-backfill system (q)..... 118
Table 6-1	Information for the Ri ground motions selected for the dynamic analyses, including the Record Sequence Number (RSN) (PEER NGA-West 2 database, Ancheta <i>et al.</i> 2013), the scale factors selected, the earthquake event, the moment magnitude (M_w), the mechanism of the seismic event, the closest distance from the recording site to the ruptured area (R_{rup}), and the average shear wave velocity to a depth of 30 m ($V_{s,30}$)..... 138

Acknowledgements

small note, hopefully expressing though, my deep gratitude to those who contributed to this work:

My first supervisor *Prof. Andreas Kappos*; I am thoroughly blessed to have him as my advisor and mentor. My gratitude to him is not limited to his huge contribution to this thesis, but also to my personal life, giving me the opportunity to move abroad and start this research journey back in 2016. His enthusiasm, professionalism, extensive knowledge, creative ideas and constant support throughout my research studies were valuable to my professional development, and I am more than grateful for all the lessons learnt;

My second supervisor *Dr. Alfredo Camara*; a very promising researcher with strong background in earthquake-resistant bridges, who has been there every step of the way as a supervisor and friend, supporting, helping and sharing his valuable pieces of advice more than any PhD student could hope from a second supervisor, and for those I am sincerely grateful;

City, University of London, the School of Mathematics Computer Science & Engineering, and the Research Centre for Civil Engineering Structures, for funding my research efforts through a 4-year Doctoral Studentship along with travel and conference attendance funds;

Prof. Matthew DeJong, and *Dr. Agathoklis Giaralis*, for providing constructive feedback and valuable comments on my doctoral dissertation and transfer report;

Dr. Kostas Gkatzogias; a true friend and a young researcher with strong background in the field of earthquake-resistant bridges, who helped me with several aspects of this thesis and supported me throughout this research journey. *Prof. Nicos Makris* (Southern Methodist University); the external advisor for this thesis who encouraged me to deal with the fascinating topic of rocking. *Prof. Elias Dimitrakopoulos* (The Hong Kong University of Science and Technology); an old friend, who gave me the opportunity to hold very valuable discussions on several aspects of rocking;

I am very grateful to all my fellow *PhD candidates* and *friends* outside of the university for their love and support and for making these years an unforgettable experience.

Last and most importantly, to my *family* to whom this work is dedicated; they are always by my side supporting me psychologically and emotionally, wherever my journey takes me.

Ioannis Thomaidis
London, November 2020

Declaration

I grant powers of discretion to the University Librarian to allow this dissertation to be copied in whole or in part without further reference to me (the Author). This permission covers only single copies made for study purposes, subject to normal conditions of acknowledgement.

Abstract

Conventional seismic design of bridges aims to provide to the structure the necessary strength and ductility to withstand seismic forces. However, significant level of damage is expected in these structures, as clearly demonstrated after recent strong earthquakes; this damage is deemed as acceptable by current code provisions. In recent years, the need for alternative design methodologies that can limit structural damage and guarantee post-earthquake serviceability was highlighted. An alternative seismic isolation technique that can combine these concepts is based on the rocking behaviour. The rocking movement is expected to relieve the structure from deformation, stresses and ultimately damage due to the lack of monolithic joints.

The research community has explored the feasibility of rocking isolation in structures that included columns, then frames, and finally bridges. The relatively few real-life applications of rocking isolation in bridge piers and the several simplifications that were adopted to study this behaviour in previous works, motivated the present study to examine this isolation technique in realistic bridge configurations and determine its effectiveness in earthquake-resistant bridges. Therefore, in view of the identified gaps in the literature on bridges with rocking pier isolation, the present study presents (i) simplified analytical tools to predict the longitudinal rocking response of bridges with rocking piers, (ii) proposals of rocking piers with non-conventional shapes in cross-section and in elevation accounting for the concept of accelerated bridge construction, and (iii) a comparative numerical assessment of conventional seismic isolation and rocking pier isolation in bridges, accounting also for the effect of the pier height/slenderness.

In this context, simplified models for predicting the longitudinal response of regular and irregular bridges with rocking piers are presented to expand the initial studies on the corresponding frame models without end supports presented in previous studies. This is done by accounting for all the salient features of a bridge structure in a performance assessment context, and by integrating the dynamic interaction between the structural members. It is shown that the simple frame model without end supports is not capable of predicting the behaviour of a realistic bridge configuration. Additionally, the effect of asymmetry in the height of the piers seems to be negligible in a seismic performance context, although the response parameters vary considerably.

Rocking piers with non-conventional shapes are proposed to enhance the seismic performance of the ‘traditional’ configurations that are usually employed in earthquake-resistant bridges. These proposals build on the inherent advantages that rocking mechanism and accelerated bridge construction offer, thus leading to lighter sections compared to the ‘traditional’ configurations, but leaving open the question of seismic performance due to the fact that the inherent restoring mechanisms are also reduced. The results from several analyses using both single- and multi-frequency ground motions show that rocking piers with relatively light section reduce the rocking amplitudes and protect to higher extent the integrity of the abutment-backfill system than the relatively heavy section that is the one usually adopted in earthquake-resistant bridges.

The comparative numerical assessment of the ‘conventional’ seismic isolation technique and the ‘unconventional’ one based on the rocking mechanism considers a bridge configuration that is expected to be unfavourable for the latter, while several simplifications that were found in previous studies with regard to the analysis of bridges with rocking pier isolation are addressed. It is shown that the rocking alternative improves some aspects of the conventional design, especially in terms of the recentring capability of the entire system. However, considerable flexural strains are found in the rocking piers and this should be considered in the design, while the vertical movement of the rocking piers is detrimental to the flexural response of the superstructure. These effects seem to be less severe in bridges with tall/slender piers compared to those on short/squat members.

Finally, proposals for future research are made with a view to (i) progressively improving and validating the analytical tools presented herein, and (ii) further examining the seismic performance of bridges with rocking pier isolation as well as enhancing the seismic performance of the ‘bare’ configurations that were addressed herein.

List of Symbols

Upper Case Latin

A	area
B	half-width / width
BC	length from pivot point B (or B') to C (or C')
D	diameter
E	modulus of elasticity
F	lateral force
G	shear modulus
H	half-height
I	mass moment of inertia (rotational mass) / moment of inertia
I _A	Arias intensity
K	static stiffness
L	length
M	bending moment
M _w	earthquake moment magnitude
N	number of piers / axial force
O, O', A, A', B, B', C, C', D, D', E, E'	pivot points
Q	effect of non-conservative forces
R	semi-diagonal or size / distance
S	spectral / shape factor
T	period / kinetic energy / temperature
V	lateral force / potential energy / shear velocity
W	work
X	longitudinal direction
Y	transverse direction
Z	vertical direction

Lower Case Latin

b	half-width / width
c	dashpot coefficient
d	drift
e	coefficient of restitution

f	reaction force / stress
h	half-height / height
k	effect of extended contact surface / spring stiffness / dynamic stiffness coefficient
m	mass
p	frequency parameter of a column or pier / shape factor
q	contribution of the abutment-backfill system / behaviour factor
r	distance
sgn	sign function
t	time / thickness
u	horizontal relative displacement
v	vertical relative displacement

Indices

0	initial value
AB	related to pivot points A and B
AC	related to pivot points A and C
ab	abutment
ad	abutment dashpot
as	abutment spring
abut.	abutment
anal.	analytical
α	acceleration
BC	related to pivot points B and C
BD	related to pivot points B and D
b	superstructure / bulk modulus
bw	backwall
bot	bottom
CD	related to pivot points C and D
CG	centre of gravity
cd	design compressive strength
ck	characteristic compressive strength
cr.	critical
Ed	design action
e	elastic
exp.	experimental
f	flange / factor
g	inertia
Hous.	Housner

I	before impact / importance class
IC	I-shaped cross-section
II	after impact
IL	I-shaped longitudinal or ‘barbell’
i	single elastomer
in	intrinsic / inertia
im	impact
init.	initial
jo	joint
Kall.	Kalliontzis <i>et al.</i>
L	lead core
LRB(ab)	LRB located at the abutment seats
LRB(pi)	LRB located at the top of the piers
m	mean
max	maximum
min	minimum
N, eq.	temperature increment
N, con.	thermal contraction
N, exp.	thermal expansion
n	negative
nc	non-conservative forces
O, A, A', B, B', C, C', D, D', E, E'	pivot points
ov	overturning
P	pier
p	pulse-type motion / positive / post-elastic
per.	permanent
R	rectangular / elastomer
r	inertor / rotational
rup	ruptured area
s	soil
sec	section
sim.	simplified
top	top
tot	total
v	axial
w	wall / web
X, x	longitudinal direction
Y	transverse direction
y	transverse direction / yield
z	vertical direction

Greek

α	slenderness / acceleration amplitude / dimensionless factor
β	factor / linear hysteretic damping factor
γ	superstructure mass effect / safety factor
η	coefficient of restitution
θ	relative rotation
Λ	impulse
λ	dimensionless factor of asymmetry / impact force
μ	ductility factor
μ_s	static coefficient of friction
ν	Poisson's ratio / normalised axial force
ξ	viscous damping ratio
ρ	material mass density
ϕ	angle defined by the horizontal axis / friction angle
ψ	angle defined by the horizontal axis
ω	circular frequency

Operations, Other

\dot{x}	first time-derivative of x
\ddot{x}	second time-derivative of x
\bar{x}	smaller length of contact surface / dynamic / normalised x
\hat{x}	equivalent to x

List of Abbreviations

2D	Two-dimensional
3D	Three-dimensional
AR	Artificial Record
ABC	Accelerated Bridge Construction
ASCE	American Society of Civil Engineers
AASHTO	American Association of State Highway and Transportation Officials
BM	Bending Moment
B31	beam elements with linear interpolation of the curvature
CG	Centre of Gravity
CR	Centre of Rotation
CS	Contact Surface
CEN	Comité Européen de Normalisation
CoF	Coefficient of Friction
CoR	Coefficient of Restitution
CoV	Coefficient of Variation
CSI	Conventional Seismic Isolation
C3D8	linear brick first-order element with full integration
C3D8R	linear brick first-order element with reduced integration
Caltrans	California Department of Transportation
DoF	Degree of Freedom
EC8	Eurocode 8
EoM	Equation of Motion
FE	Finite Element
FHD	Frictional Hinge Damper
FRP	Fibre-Reinforced Polymer
FEMA	Federal Emergency Management Agency
FMAS	Failure Minimum Acceleration Spectrum
FRP1	Single-segment Pier with Fibre-Reinforced Polymer
FRP4	Four-segment Pier with Fibre-Reinforced Polymer
FSHB	Flag-Shaped Hysteretic Behaviour
FRP4-R	Four-segment Pier with Fibre-Reinforced Polymer and Rubbers
FRP4-S	Four-segment Pier with Fibre-Reinforced and Steel Angles
GM	Geometric Mean
HHT	Hilber-Hughes-Taylor
HSRB	Hybrid Sliding-Rocking Behaviour
IC	I-shaped Cross-section

IL	I-shaped Longitudinal or ‘barbell’
LB	Lower Bound
LRB	Lead Rubber Bearing
OMAS	Overtuning Minimum Acceleration Spectrum
PGA	Peak Ground Acceleration
PGD	Peak Ground Displacement
PGV	Peak Ground Velocity
PEER	Pacific Earthquake Engineering Research Center
R	Rectangular
RC	Reinforced Concrete
RPI	Rocking Pier Isolation
RSN	Record Sequence Number
SRSS	Square Root of the Sum of Square
T3D2	truss element
UB	Upper Bound

Chapter 1

Introduction

1.1 Problem Statement

The importance of bridges in transport networks has long been highlighted, considering that their potential failure may cause casualties and other losses, both economic and societal. In a seismic design context, current reinforced concrete bridge typologies fall within two main categories: a system with firm connection (monolithic or through fixed bearings) between the deck and the piers, referred to as ‘*ductile pier*’ bridges, and a system where the deck is supported on the piers through non-fixed bearings (usually elastomeric, but other options do exist); in the absence of any firm connection, the latter system is referred to as ‘*seismic isolation*’, and in this thesis it will subsequently be referred to as a bridge with ‘*conventional seismic isolation*’ to distinguish it from ‘*unconventional*’ isolation techniques such as ‘*rocking pier isolation*’ (stated in some cases as ‘*structural rocking isolation*’ to distinguish it from the ‘*geotechnical*’ perspective, see §2.1 for these definitions) that will be discussed later. The ultimate aim of these conventional systems is to ensure the continuity between the different parts of the structure, while providing to the gravitational forces a clear path to the ground. In seismic regions, conventional bridges should have the ability to withstand moderate earthquakes without damage, while under ‘extreme’ earthquakes the conventional seismic design (i.a., CEN 2005a) ensures that collapse does not occur by allowing piers to develop substantial inelastic deformations and permanent lateral displacements for the entire system (i.e., including piers and isolation devices).

The effects of the recent earthquakes in 2010 in Maule, Chile ($M_w = 8.8$) (i.a., Kawashima *et al.* 2011), in 2011 in Tohoku, Japan ($M_w = 9$) (i.a., Kajitani *et al.* 2013), as well as those in 2016 in Central Italy ($M_w = 6.2$) (i.a., Fiorentino *et al.* 2017) and in Kaikoura, New Zealand ($M_w = 7.8$) (i.a., Palermo *et al.* 2017) clearly confirmed that the performance of conventional bridge typologies may satisfy life safety requirements, but the high level of damage tolerated by current codes requires either extensive repairs or replacement following the earthquake, thus disrupting the traffic conditions and leading to environmental impacts (Wacker *et al.* 2005). Therefore, the need to redefine the limit states adopted so far in earthquake-resistant bridges by means of reducing the damage that would normally be concentrated in their critical zones is underlined, with a view to accounting for both direct (e.g., restoration) and indirect (e.g., loss of functionality) economic losses from earthquake events. A seismic isolation technique that can result in earthquake-resistant bridges with such seismic performance is based on the rocking behaviour of the vertical members, and this is the focus of this thesis. The design paradigm of rocking isolation is described by objects that simply rest on the rocking surfaces (i.e., bottom and, if needed, top dependent on the structure examined), and rocking movement is characterised as a sequence of rigid body rotations of these

objects that are disrupted by impacts each time they return to their original position of equilibrium, and it continues until the total energy is dissipated through these impacts. Despite the familiar, intuitive nature of rocking motion, it is in fact a nonlinear process that is highly complex and sensitive to initial conditions.

The motivation of utilising rocking behaviour as an isolation technique to enhance the seismic performance of bridges originates from a construction method that was used for the first time thousands of years ago by ancient builders, probably due to the lack of methods for creating integral systems. Indeed, several ancient temples with rocking columns can be found in the Mediterranean, like the colonnade (peristylon) of the Temple of Athena at Aegina in Greece shown in Fig. 1-1, which stands there for millennia showing the satisfactory performance of these ‘unconventional’ structures (Drosos & Anastasopoulos 2015). Several researchers (i.a., Psycharis *et al.* 2000, Drosos & Anastasopoulos 2014) concluded that the resilience of this ancient configuration with rocking columns is due to the following structural advantages of the rocking principle;



Fig. 1-1 View of the colonnade of the Temple of Athena at Aegina, Greece constructed around 480BC. (*figure taken from Drosos & Anastasopoulos 2015*)

- These configurations result in structural systems with negative stiffness as opposed to the more contemporary moment-resisting frames that have positive stiffness in order to endure horizontal loads, as shown in Fig. 1-2. In this regard, resonance is practically unfeasible to occur in structures with rocking columns, considering that the excitation should have a very specific frequency range (DeJong 2012).
- The restoring mechanisms of a structure with rocking columns derive from the physical properties of translational and rotational masses, hence in most cases recentring is achieved physically.

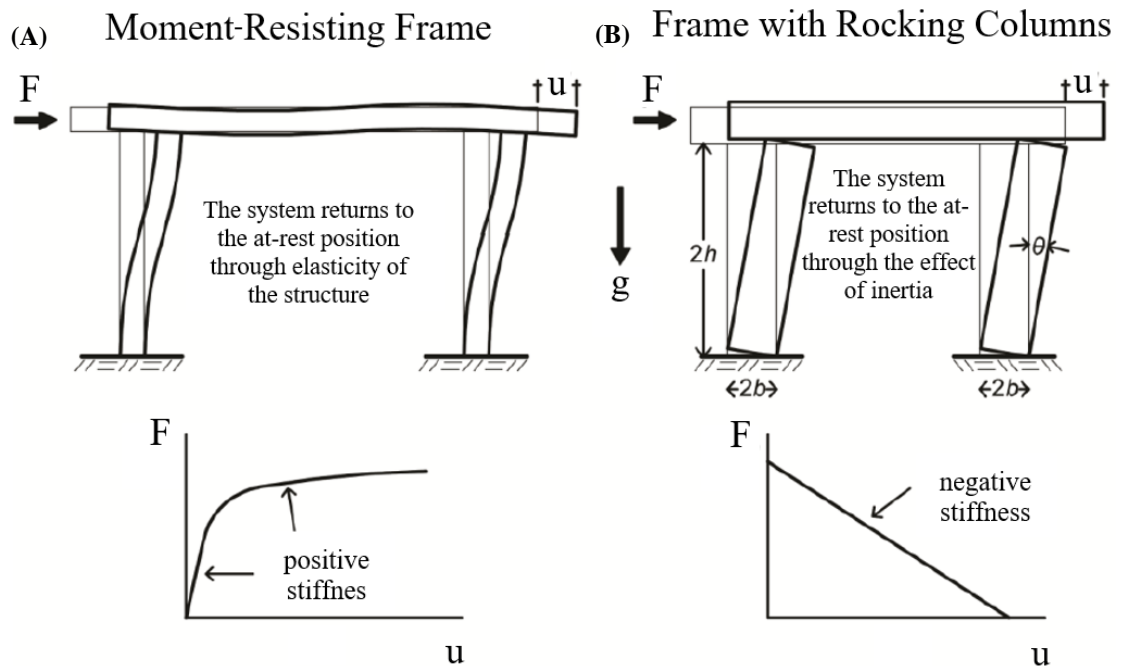


Fig. 1-2 Schematic of the deformed shape of the (A) contemporary moment-resisting frame and (B) frame with rocking columns under horizontal seismic loads, and the corresponding force-displacement (F - u) behaviour. (figure taken from Makris 2014)

Extending this ‘unconventional’ isolation technique in bridges, rocking pier isolation is well aligned with accelerated bridge construction due to the simple connections that are required between the rocking piers and the adjacent structural members (i.e., foundation and superstructure). It is noted that accelerated bridge construction has been proposed as a construction technique that can minimize disturbance (i.e., closures and/or traffic lane or speed restrictions) and guarantee post-earthquake serviceability. This is mainly achieved via (i) prefabrication, which decreases the on-site construction time and has the additional benefits of higher construction quality and greater work-zone safety (Doolen *et al.* 2011), and (ii) simple on-site installation of the structural elements (i.a., Mantawy *et al.* 2016), thus allowing fast replacement and restoration of the members after a severe earthquake event compared to the cast-in-situ structures in which the integral joints hinder the restoration procedure.

Overall, the research community has conducted a progressive implementation of structural rocking isolation in structures that goes from columns to frames and finally to bridges. Despite the fact that the extensive research that has been conducted for ‘bare’ (or free-standing) and ‘hybrid’ (i.e., supplemented with additional devices to enhance the seismic performance of the free-standing configuration) rocking columns and relevant frames proved that this isolation technique can enhance the lateral stability of these structures compared to the corresponding ‘traditional’ systems with integral joints, the proposals regarding bridges with rocking piers have entailed several simplifications, ignoring all the salient features of a realistic bridge configuration and, in this regard, the civil engineering community is reluctant to implement such ‘unconventional’ systems in real engineering bridge projects (i.a., Beck & Skinner 1974, Routledge *et al.* 2016). Therefore, there is an increasing need to examine in-depth the rocking behaviour of realistic bridge

configurations to identify the inherent advantages and obstacles that stem from rocking piers in order for this technology to mature and be implemented in future engineering bridge design applications.

1.2 Scope and Research Objectives

In the light of the previous considerations (§1.1), the key aims of the present research study are to (i) *explore the implementation of rocking pier isolation in realistic bridge configurations accounting for the main features of a bridge structure, taking also into account the advantages of using accelerated bridge construction*, and (ii) *establish whether rocking pier isolation can be considered as an isolation technique for the next generation of earthquake-resistant bridges*. In order to achieve these aims, the following specific research objectives were identified;

(i) Identify Gaps in the State-of-the-Art

Carry out a thorough review of the available literature in an effort to identify research gaps to be addressed in this thesis. The first research topic is related to the analytical dynamics governing the complex behaviour of rocking objects, considering that these studies form the basis of the analytical solutions to be developed in this thesis. This review is extended to the inherent disadvantages that govern the seismic response of free-standing rocking piers, and it includes proposals on pier configurations that aim at improving the seismic performance of the ‘bare’ rocking isolation technique. Finally, studies related to the consideration of rocking pier isolation as part of a realistic bridge structure are presented.

(ii) Analytical Modelling of Bridges with Rocking Piers

Development of a simplified model for predicting the longitudinal response of regular bridges with rocking piers (or symmetric with respect to the height of the supporting piers) as well as irregular/asymmetric bridges with rocking piers, accounting for all the relevant features of a bridge structure, including the end supports.

(iii) Proposal of Non-conventional Pier Configurations for Bridges with Rocking Piers

Exploration of non-conventional pier configurations that improve the ‘traditional’ rocking piers with rectangular section, both from the economic and seismic performance points of view. This is carried out accounting for the inherent advantages that rocking pier isolation in combination with accelerated bridge construction offer in bridges with respect to the ‘traditional’ construction methods.

(iv) Comparative Assessment of Conventional Seismic Isolation and Rocking Pier Isolation in Bridges

Carry out a comparative numerical study of conventional seismic isolation and rocking pier isolation in bridges, to identify advantages and disadvantages of each approach. This objective also encompasses delineation of the range of pier height/slenderness in which rocking pier isolation is more efficient.

1.3 Layout of the Dissertation

The present thesis is divided in seven chapters and four appendixes, and it is structured in line with the research objectives outlined in §1.2. Following the introductory considerations of the present chapter on the problem statement and the objectives of the study, a review of the current state-of-the-art related to research objective (i) is presented in Chapter 2, while research objective (ii) is addressed in Chapters 3 (for symmetric bridges) and 4 (for asymmetric bridges). The research objectives (iii) and (iv) are addressed in Chapters 5 and 6, respectively, while overall conclusions and future steps to further develop rocking pier isolation in bridges are discussed in Chapter 7. Supplementary information related to the analytical developments in Chapters 3 and 4 are presented in Appendixes A and B, while Appendix C presents details of the original overpass bridge adopted for the comparative assessment in Chapter 6. A list of references follows in Appendix D, and Appendix E includes a record of articles published so far in peer-reviewed journals and conference proceedings. A more detailed description of the core chapters of the dissertation is provided in the following.

Chapter 3 provides a simplified energy-based analytical model for predicting the longitudinal response of a symmetric bridge with an arbitrary number of free-standing rocking piers. This formulation is based on some assumptions that facilitate the analytical development, and, in that sense, they have been found essential for analytical approaches of this type. The proposed model constitutes an extension of the corresponding frame model with free-standing rocking columns presented in previous studies by integrating in the response the effect of the abutment and the backfill behind it, as well as the interaction between the structural members. The parameters that govern the behaviour of the abutment-backfill system are explored in parametric analyses to establish their effect on rocking response, and the overturning spectra that are usually adopted in these studies are extended to a new spectrum to account for all possible failure modes. The newly developed model is compared in a design and in a seismic performance context with the model adopted so far for bridges using both single-frequency and multi-frequency ground motions, to establish the necessity for considering the influence of the abutment-backfill system on the response of bridges with rocking pier isolation.

In the same context, Chapter 4 provides an analytical model accounting for the effect of two free-standing rocking piers of same section but different height, thus generalising/extending the analytical model presented in Chapter 3. In this regard, the newly developed model extends the corresponding asymmetric frame model with free-standing rocking columns presented in previous

studies. Considering the significant complexity in the formulation of the equations of motion of this system, a procedure to simplify them and to reduce the associated high computational cost is presented. This model is used to study the seismic performance of asymmetric bridges with free-standing rocking piers under ‘extreme’ earthquake conditions with a view to establishing the effect of the level of asymmetry in the height of the piers.

Novel improved pier configurations for a bridge with rocking piers are presented in Chapter 5, studied using the analytical model developed in Chapter 3. The proposed pier configurations exploit the merits of accelerated bridge construction through prefabrication and on-site installation in the context of rocking pier isolation. The analytical derivations that are required for predicting the response of a bridge structure with free-standing rocking piers are presented in Chapter 5 accounting for the variations in pier shape. The efficiency of the proposed pier configurations in a bridge with rocking pier isolation is examined using both design and ‘extreme’ earthquake conditions.

Chapter 6 compares through numerical analyses the seismic performance of bridges supported on free-standing rocking piers with those with conventional base isolation using rigorous three-dimensional finite element models with material nonlinearities and contact at the rocking interfaces. Two bridge configurations are considered for the comparison, based on an existing overpass bridge with unequal pier heights, which is also modified by increasing the original pier height to address the effect of pier height/slenderness. The developed numerical models account for all the simplifications adopted in the analytical procedures presented in Chapters 3, 4, 5, and at the same time extend the numerical analyses presented in previous studies. The comparison focuses on detecting the differences in terms of the stability of the structure (i.e., considering response parameters such as displacements, drifts and bending moments), rather than focusing on the safety of each design alternative against the corresponding failure mode that has been examined in several studies in the past.

Finally, Chapter 7 summarises the main conclusions from the present thesis and makes specific recommendations for future research required for further establishing the concept of rocking pier isolation in bridges.

Chapter 2

Review of the State-of-the-Art

2.1 Introduction

The concept of seismic isolation in structures has been widely adopted after World War II in order to resist strong earthquakes (Makris 2018). In bridges, this is usually achieved by introducing a continuous isolation interface between the deck and the substructure (piers, abutments) with low shear stiffness resulting in the elongation of the fundamental period of the bridge, while energy dissipation devices are optionally employed to control the subsequent increase in relative displacements at the isolation interface. Indeed, numerous devices have been successfully deployed in the last four decades to isolate structures subject to ground motions, and these can be classified according to their operational mechanisms (Housner *et al.* 1997, Symans & Constantinou 1999). The fundamental principles for the design of structural devices, explicitly stated in modern bridge and building design codes (e.g., CEN 2005a, AASHTO 2010, ASCE 2016), may be summarised as follows; (i) support the superstructure and relevant vertical actions and provide lateral flexibility while being able to sustain non-seismic actions (e.g., brake, wind actions), (ii) whenever needed, provide energy dissipation to control relative displacements, and (iii) provide sufficient recentring capability to prevent substantial residual displacements.

The performance of bridges with conventional seismic isolation during recent strong earthquakes, mentioned in §1.1, highlighted the high level of damage that is allowed by the current codes and pointed to the need of redefining the limit states in earthquake-resistant bridges. Hence, it is anticipated that isolation technology for mitigating seismic risk to bridges will continue attracting the interest of the engineering community in the years to come, potentially resorting to ‘unconventional’ systems that provide reliability and robustness. This is the case with rocking mechanism. In principle, rocking action offers a favourable seismic isolation effect that relieves the structure from deformation and damage during strong earthquakes as well as reduces the need for post-earthquake interventions in the structure (Giouvanidis & Dong 2020). Therefore, the main design objective in bridges with rocking pier isolation is to reduce or eliminate damage in the structure (typically the bridge piers) but in a ‘more natural’ way, without the need of special (and expensive) hardware, as required in conventional seismic isolation. Rocking isolation is not a new technique. Extensive research that was conducted on the seismic response of ancient monuments proved that their survival over millennia in earthquake-prone regions is mainly due to their rocking behaviour (i.a., Psycharis *et al.* 2000, Papantonopoulos *et al.* 2002). Despite its benefits, though, the implementation of rocking isolation in modern engineering projects has been scarce.

So far, rocking isolation has been investigated by employing two different techniques dependent on the location of the rocking surface. This is related to structural rocking isolation (or

pier rocking) and geotechnical rocking isolation (foundation rocking). These techniques are conceptually similar, but quite different with regard to the rocking behaviour and the resulting effects of rocking movement;

- Structural Rocking Isolation

In this case the rocking surface is defined between the piers and their foundations, while the pier-to-deck connection can take various forms, including (i) an integral joint, (ii) separated through isolation bearings or (iii) a direct support. Several researchers have studied this configuration analytically (i.a., Makris & Vassiliou 2014a, Giouvanidis & Dimitrakopoulos 2017a), numerically (i.a., ElGawady & Dawood 2012, Sideris 2015), and experimentally (i.a., Marriott *et al.* 2009, ElGawady & Sha'Ian 2011) by focusing on (i) the recentring capability of the rocking piers, (ii) the use of damping devices to increase energy dissipation in the rocking elements, and (iii) the behaviour of the rocking surfaces as well as the potential use of different materials to improve its performance. Structural rocking isolation in bridges has been first implemented in the South Rangitikei Rail Bridge in New Zealand shown in Fig. 2-1A (Beck & Skinner 1974, Ma & Khan 2008, Frost & Tilby 2014), where the piers are allowed to rock without sliding on a surface carefully designed and constructed at the base of the rocking piers, as shown in Fig. 2-1B; this configuration has shown remarkable seismic performance after several ground motions (Chouw 2017, Makris & Aghagholizadeh 2019).

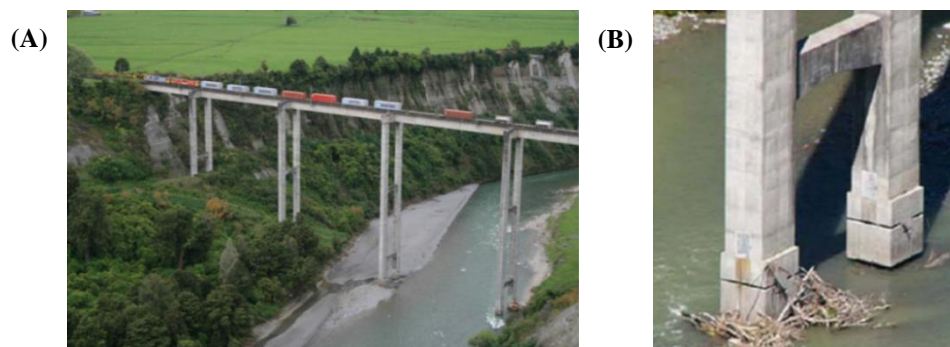


Fig. 2-1 (A) View of the South Rangitikei Rail Bridge, New Zealand, and (B) the rocking surface at the pier base. (figure taken from Ma & Khan 2008)



Fig. 2-2 View of the low-damage connection installed at the (A) bottom and (B) top surfaces of the rocking piers in the Wigram-Magdala Link Bridge, New Zealand. (figure taken from Routledge *et al.* 2016)

The most recent implementation of pier rocking in bridges is the Wigram-Magdala Link Bridge in New Zealand (Routledge *et al.* 2016), where steel piers filled with unreinforced concrete and supplemented with post-tensioned tendons are allowed to rock at both ends. The rocking surface is constructed with steel plates on which low-damage connections are anchored at both bottom and top joints as shown in Fig. 2-2A, B, respectively.

- Geotechnical Rocking Isolation

In this approach, the piers are monolithically connected to a shallow foundation, and the rocking interface is between the foundation and the ground below. This rocking approach has been adopted by recent provisions (AASHTO 2011). Several researchers have studied this configuration analytically (i.a., Psycharis & Jennings 1983), numerically (i.a., Anastasopoulos *et al.* 2010, Xie *et al.* 2019), and experimentally (i.a., Hung *et al.* 2011, Anastasopoulos *et al.* 2012). The main research topics in this approach are (i) the interaction between the rocking members and underlying soil, particularly the consequences of the impact of the foundation-pier system on the behaviour of the soil, and (ii) the recentring capability of the system.

Recently, a rigorous 3D Finite Element (FE) analysis using ABAQUS was conducted by Agalianos *et al.* (2017) to compare the seismic performance of a 5-span bridge with rocking piers and rocking foundations. It was shown that in most of the examined cases both bridges with different rocking approaches resisted strong seismic actions, and they were ready to be used after the event. However, although the geotechnical approach showed slightly better seismic performance against overturning compared to the ‘bare’ structural perspective, the underlying soil showed significant residual settlements and rotations, revealing that this is the price to be paid for its superior stability. The substantial settlements of the underlying soil due to the severe impacts of the pier foundation was also seen in the centrifuge tests by Pelekis *et al.* (2019), showing that this effect can be more significant in soft soils than stiff ones. On the contrary, the rocking pier solution is insensitive to the type of foundation soil in that respect. Taking the above into consideration, structural and geotechnical rocking isolation are two distinct mechanisms with common goals of mitigating the seismic effects at the piers and increasing their recentring capacity, but they are based on different approaches. The present thesis focuses on bridges with structural rocking isolation, referred in the following as bridges with ‘*rocking pier isolation*’ or ‘*rocking piers*’.

In this respect, the principles of rocking pier isolation in bridges and the fundamental differences with the conventional construction methods are described in §2.2. The three following sections are related to the research objectives outlined in §1.2. Specifically, §2.3 starts with the analytical modelling of a rocking column (§2.3.1), and it is followed by the frame with rocking columns that approximates the corresponding bridge configuration (§2.3.2). This chapter continues with §2.4 that discusses the inherent disadvantages of the ‘bare’ rocking isolation technique along with the current proposals on pier configurations that aim at mitigating them, while §2.5 presents studies related to rocking pier isolation as part of the entire bridge structure. Finally, §2.6 identifies research gaps that are later addressed in this thesis.

2.2 Principles of Rocking Pier Isolation in Bridges and Differences from Conventional Methods

Structures that are isolated through rocking isolation show a fundamentally different seismic behaviour compared to structures adopting ‘traditional’ construction methods, referring either to integral or seismically isolated systems. The principles in a bridge that utilises (i) the ‘traditional’ moment resisting frame, (ii) a conventional seismic isolation technique, and (iii) ‘bare’ rocking pier isolation were introduced by Makris & Konstantinidis (2003); Table 2-1 summarises the basic design concepts along with the main response-controlling quantities for bridges with the different design philosophy. As can be seen, the ‘bare’ rocking isolation technique is completely different from the ‘traditional’ methods in terms of the parameters that dominate the seismic response as well as the design philosophy.

Table 2-1 Principles of different construction methods for earthquake-resistant bridges, when employing (i) a ‘traditional’ moment resisting frame, (ii) a conventional seismic isolation technique and (iii) ‘bare’ rocking pier isolation. (table adapted from Makris 2014)

	(i) ‘Traditional’ Moment Resisting Frame	(ii) Conventional Seismic Isolation	(iii) ‘Bare’ Rocking Pier Isolation
Strength	Moderate to appreciable $\ddot{u}_g = 0.1 \text{ g} - 0.25 \text{ g}$	Low $\ddot{u}_g = 0.03 \text{ g} - 0.09 \text{ g}$	Moderate to high $\ddot{u}_g = g \cdot \tan \alpha$
Stiffness	Positive (variable due to yielding)	Positive (low and constant)	Negative (constant)
Ductility	Appreciable $\mu = 3-6$	Very large $\mu = 10-30$	Zero
Damping	Moderate	Moderate to high	Low
Seismic Resistance	Appreciable strength and ductility	Low strength and stiffness. Accommodates large displacements	Appreciable rotational inertia
Design Philosophy	Equivalent static	Equivalent static	Dynamic

To discuss in more detail the principles of ‘bare’ rocking pier isolation, consider Fig. 2-3A that shows a rocking column with height $2h$ and width $2b$ rotating around the pivot point or Centre of Rotation (CR) O with a relative rotation θ when subjected to a horizontal ground acceleration \ddot{u}_g ; it is noted that the ensuing discussion describes also an equivalent frame with larger size, as will be explained in §2.3.2.1. The size of this column is defined as the distance from the Centre of Gravity (CG) of the member to the CR O and is equal to $R = \sqrt{h^2 + b^2}$, while the slenderness is described as $\alpha = \tan^{-1}(b/h)$.

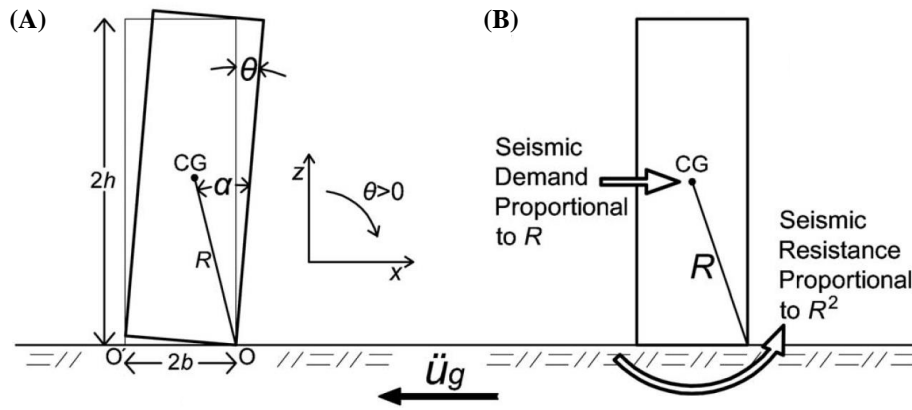


Fig. 2-3 (A) Schematic of a free-standing rocking column during rocking motion, and (B) the effect of size (R) on the seismic rocking response of the member. (figure taken from Makris 2014)

Initiation of rocking motion in a free-standing column occurs when the member uplifts, and this is described in the literature as ‘strength’. This condition is satisfied when the ‘overturning moment’ with respect to the imminent CR O equals the ‘recentering moment’, thus returning the expression for rocking initiation that was presented for the first time by Milne (1885)

$$\begin{array}{ccccccc} \text{Overturning} & \text{Recentering} & \text{Seismic} & & \text{Seismic} & & \\ \text{Moment} & \text{Moment} & \text{Demand} & & \text{Resistance} & & \\ m\ddot{u}_g h & = & mgb & \Leftrightarrow & \ddot{u}_g & = & g \frac{b}{h} = g \frac{R \sin a}{R \cos a} = \overbrace{g \tan a}^{\text{Seismic Resistance}}, \end{array} \quad (2-1)$$

in which m is the mass of the column, and g is the gravitational acceleration. Eq. (2-1) shows that the strength of a rocking column depends solely on the variations in the value of slenderness of the member, and Fig. 2-4 presents this effect. It is observed that non-slender members show very high strength (up to 1 g), contrary to the slender members that show only moderate values of strength.

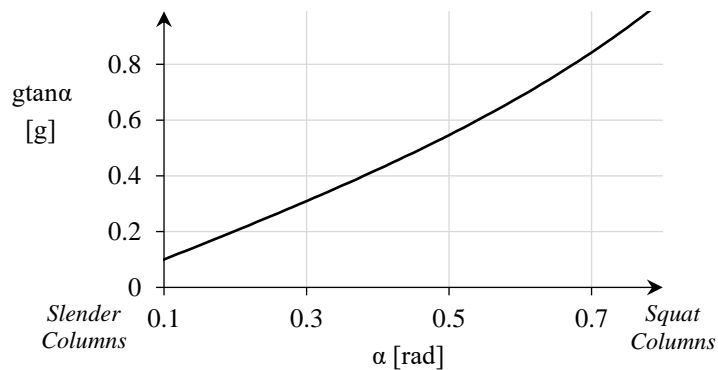


Fig. 2-4 Strength or acceleration amplitude to initiate rocking motion ($g \tan \alpha$) in a free-standing rocking column, accounting for the influence of its slenderness (α).

The most attractive concept of rocking isolation in earthquake engineering compared to the ‘traditional’ ways of construction is probably the inherent negative stiffness in rocking motion. This concept can reduce dramatically the seismic forces in the structure by reducing the spectral

acceleration (Makris & Konstantinidis 2003). Fig. 2-5 shows an idealised moment-rotation ($M-\theta$) relationship during the rocking motion of a free-standing rocking column, which was first introduced by Muto *et al.* (1960). The model assumes infinite stiffness before rocking starts (not totally valid for rocking piers as shown by Roh & Reinhorn 2009, see §2.4.1.3 and Fig. 2-18), until the magnitude of the applied moment reaches the value $m \cdot g \cdot R \cdot \sin\alpha$ (i.e., ‘recentering moment’ in Eq. (2-1)). From this point onwards, the restoring capability of the rocking column decreases linearly until it reaches zero for $\theta = \alpha$, at which point the member overturns.

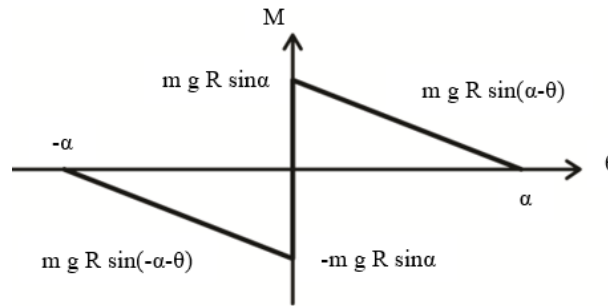


Fig. 2-5 Idealised moment-rotation ($M-\theta$) behaviour of a free-standing rocking column, representing the ‘recentering moment’ of the member. (figure taken from Makris 2014)

As can be seen in Table 2-1, rocking pier isolation in its ‘bare’ form has no ductility and minimal damping. Albeit the former can be considered partially as an advantage due to the fact that residual displacements are not possible in the context adopted so far for earthquake-resistant bridges, the latter reveals the inherent weakness of rocking pier isolation that is the low energy dissipation compared to the ‘traditional’ ways of construction. This is attributed to the fact that, in theory (see Kalliontzis & Sritharan 2018), no energy is dissipated during rocking motion as can be seen in Fig. 2-5, while attenuation of rocking motion is only achieved during impacts at the rocking surfaces (see §2.4.1.2 and Table 2-5).

Consider again the free-standing rocking column presented in Fig. 2-3A. As soon as the excitation is capable of inducing uplift according to Eq. (2-1), the rocking motion starts and the dynamic moment equilibrium about the CR O gives

$$\underbrace{m\ddot{u}_g R \cos(\alpha - \theta)}_{\text{Seismic Demand}} = \underbrace{I_O \ddot{\theta} + \underbrace{mgR \sin(\alpha - \theta)}_{\text{Recentering Moment}}}_{\text{Dynamic Seismic Resistance}}, \quad (2-2)$$

where $I_O = \int r^2 dm$ is the mass moment of inertia (or rotational mass) of the element with respect to O, r represents the size (or distance) of a differential mass element dm from the pivot O, and $\ddot{\theta}$ is the angular acceleration of the column. In this regard, the ‘dynamic seismic resistance’ increases quadratically with the increment of the size of the column, whereas the ‘seismic demand’ increases only linearly (Fig. 2-3B) (Kirkpatrick 1927, Ikegami & Kishinouye 1947 and 1950). Hence, the second power of size on the right-hand-side of Eq. (2-2) can always ensure stability regardless of

the level of intensity of the ground shaking (\ddot{u}_g). This observation led Makris & Kampas (2016a) to propose the leverage of supplemental rotational inertia on rocking columns for enhanced stability.

Eq. (2-2) reveals why the design philosophy of an equivalent static analysis is not applicable to rocking. To elaborate further, suppose that an equivalent static approach is adopted for the rocking analysis. The rocking member experiences nearly zero angular acceleration ($\ddot{\theta} = 0$) and, therefore, the equivalent static moment equilibrium about CR O gives

$$\underbrace{m\ddot{u}_g R \cos(a - \theta)}_{\text{Seismic Demand}} = \underbrace{mgR \sin(a - \theta)}_{\text{Recentering Moment}} \Leftrightarrow \ddot{u}_g = g \tan(a - \theta). \quad (2-3)$$

Note that Eq. (2-3) is identical to Eq. (2-2) after excluding the effect of I_O . It is observed that under quasi-static lateral loading, the overturning stability of a free-standing rocking column depends only on the variations in its slenderness (a) and the ground motion (\ddot{u}_g), being independent of the size of the column (R). In this regard, Eq. (2-3) shows that the value of the acceleration amplitude that can induce overturning reduces compared to that describing the strength of the member (Eq. (2-1)) and, therefore, as soon as the column enters rocking motion, it will most probably overturn. The equivalent static procedure has been followed by more than a century for calculating the acceleration amplitude of seismic events through the overturning of tombstones with specific dimensions. However, Eq. (2-2) shows that an earthquake motion capable of inducing uplift needs a higher acceleration amplitude to overturn the rocking column, thus the acceleration amplitude is underestimated substantially when Eq. (2-3) is utilised.

2.3 Analytical Modelling of the Rocking Response

While Kirkpatrick (1927) was the first who addressed the complex dynamics in the seismic response of rocking columns, it was Housner (1963) who made it better known to the civil engineering community, proving that the rocking motion of a free-standing column is independent of the mass of the member and, therefore, the rocking structure was named as an ‘inverted pendulum’. The analytical model proposed by Housner has been proven sufficient to predict the rocking behaviour of free-standing columns, not to a single event where the response may show high variability due to the imperfections of the specimen and the variations in the initial conditions, but to ensembles of ground motions where the seismic response, in a statistical sense, is predictable with sufficient accuracy for seismic design and evaluation (Bachmann *et al.* 2018). Concerns have been raised, though, related to the consideration of a 3D model for the prediction of seismic response in cylindrical rocking columns, stating that the 2D model presented by Housner may be unconservative (see i.a. Chatzis & Smyth 2012, Di Egidio *et al.* 2014, Vassiliou *et al.* 2017,

Vassiliou 2017). In any case, the work of Housner set the basis for the ensuing analytical research on rocking columns and relevant frames that are presented in §2.3.1 and §2.3.2, respectively.

2.3.1 Rocking Columns

2.3.1.1 Dynamics of Free-standing Rocking Columns

Following Housner's work, a number of studies have addressed the complex dynamic response of one of the simplest man-made structures, the free-standing column. For this configuration to start rocking motion under horizontal ($\ddot{u}_{g,x}$) and vertical earthquake excitations ($\ddot{u}_{g,z}$), and to avoid other possible movements such as sliding and upthrow (i.e., contact is lost with the foundation, stated in some cases as 'jumping'), a number of conditions must be fulfilled. Fig. 2-6 shows the free-body diagram for a single column with dimensions $2h$ and $2b$ just before entering rocking motion ($\theta = 0$) about the CR O' . The dynamic equilibrium at this instant gives

$$\sum F_x = 0 \Leftrightarrow f_x = m[\ddot{u}_{g,x} + \ddot{x}], \quad (2-4)$$

$$\sum F_z = 0 \Leftrightarrow f_z = m[g + \ddot{u}_{g,z} + \ddot{z}], \quad (2-5)$$

$$\sum M_{CG} = 0 \Leftrightarrow I_{CG} \ddot{\theta} = -f_x h + f_z b, \quad (2-6)$$

where f_x and f_z are the horizontal and the vertical reaction forces at the CR O' at the moment of initiation, respectively, $\ddot{x} = h \cdot \ddot{\theta}$, $\ddot{z} = -b \cdot \ddot{\theta}$, $\ddot{\theta}$ is the angular acceleration of the member at the moment of initiation and is derived from Eqs. (2-4) to (2-6), while I_{CG} is the mass moment of inertia of the column with respect to its CG; for rectangular columns $I_{CG} = m \cdot R^2/3$.

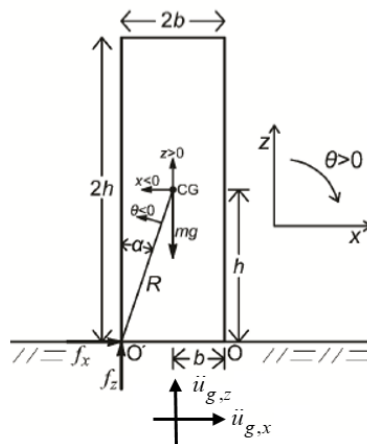


Fig. 2-6 Free-body diagram for a free-standing rocking column at the onset of rocking motion. (figure taken from Makris 2014)

The first condition that needs to apply in order for a free-standing column to enter rocking motion is that the horizontal ground acceleration should have a minimum amplitude to make the ‘overturning moment’ about O’ exceed the ‘restoring moment’ due to the weight of the column and the vertical inertia force (Yim *et al.* 1980)

$$\overbrace{m\ddot{u}_{g,x}h}^{\text{Overturning Moment}} > \overbrace{m[g+\ddot{u}_{g,z}]b}^{\text{Restoring Moment}} \Leftrightarrow \ddot{u}_{g,x} > [g+\ddot{u}_{g,z}]\tan a. \quad (2-7)$$

The second condition is that the column does not lose completely contact with the base due to the vertical component of the ground shaking. This is avoided if the value of f_z is larger than zero at any instant (Ishiyama 1982, Sinopoli 1989).

The third, and last, condition for rocking initiation is that the column does not slide with respect to the horizontal base, which is the case if

$$\mu_s \geq \frac{f_x}{f_z}, \quad (2-8)$$

where μ_s is the static Coefficient of Friction (CoF) of the column-base surface. Substituting Eqs. (2-4) and (2-5) into Eq. (2-8) gives the condition for a free-standing column to enter rocking motion without sliding at this instant that was introduced by Taniguchi (2002)

$$\mu_s \geq \frac{4\left[1+\left(\frac{h}{b}\right)^2\right]\frac{\ddot{u}_{g,x}}{g}+3\frac{h}{b}\left[1+\frac{\ddot{u}_{g,z}}{g}\right]}{1+4\left[\frac{h}{b}\right]^2+3\left[\frac{h}{b}\right]\frac{\ddot{u}_{g,x}}{g}+\left[4\left(\frac{h}{b}\right)^2+1\right]\frac{\ddot{u}_{g,z}}{g}}. \quad (2-9)$$

A simplified form of Eq. (2-9) obtained by neglecting the influence of $\ddot{u}_{g,z}$ was presented by Shenton (1996). Later, Pompei *et al.* (1998) adopted this simplification and proved that for slender columns (i.e., for low values of α) the sliding motion occupies a small range, even for high values of $\ddot{u}_{g,x}$. This was also proved by Housner (1963) who considered Eq. (2-7) to describe rocking initiation after neglecting the effect of $\ddot{u}_{g,z}$, and it was shown that Eq. (2-9) reduces to the well-known expression to describe prevention of sliding at the initiation of rocking motion: $\mu_s \geq b/h = \tan\alpha$. Based on these outcomes, the majority of studies on rocking dynamics assume that the value of μ_s is sufficiently large to prevent sliding at the initiation of movement.

As soon as the above conditions are satisfied, the free-standing rocking column will oscillate initially about the CR O’ with a negative rotation ($\theta < 0$) and, if the member does not overturn, it will return to the original at-rest position dissipating energy through an impact at the rocking interfaces (§2.3.1.2), thus reversing the rocking rotation to positive ($\theta > 0$), now rotating about CR

O, and so on. The Equation of Motion (EoM) during rocking under horizontal and vertical ground accelerations is derived by considering the equilibrium of moments about the corresponding CR (i.e., O' and O dependent on the direction of the movement) as it was expressed by Yim *et al.* (1980); this expression is simplified to the following form accounting for the proposals of Makris & Roussos (2000)

$$\ddot{\theta} = -p^2 \left[\text{sgn}(\theta) \left(1 + \frac{\ddot{u}_{g,z}}{g} \right) \sin(a - |\theta|) + \frac{\ddot{u}_{g,x}}{g} \cos(a - |\theta|) \right], \quad (2-10)$$

where $\text{sgn}(\theta)$ is the sign function of θ , $p = \sqrt{m \cdot g \cdot R / I_O}$ is the frequency parameter of the column, and $I_O = I_{CG} + m \cdot R^2$; for rectangular columns $I_O = 4m \cdot R^2 / 3$ and $p = \sqrt{3g/4R}$. Eq. (2-10) is valid for arbitrary values of the slenderness a . The inherent non-linearity of this problem is revealed from Eq. (2-10), not only in terms of the trigonometric functions of θ , but also due to the alternating nature of movement direction and pivot points.

Notwithstanding the above, 'pure' rocking motion is not ensured even if rocking motion has started. Almost in parallel, Scalia & Sumbatyan (1996) and Shenton (1996) indicated the existence of a slide-rock movement that can appear after rocking starts. Once the column enters rocking motion, the horizontal ($f_x(t)$) and vertical reaction forces ($f_z(t)$) fluctuate with time, which may induce sliding for certain combinations of these values. Consequently, Eq. (2-8) should apply at each time instant to avoid sliding during the entire duration of rocking motion. Zhang & Makris (2001) developed the necessary condition for a free-standing column to avoid slide-rock motion, showing the dependence of this mode not only on the width-to-height ratio ($\tan a$) and the static CoF (μ_s), but also on the magnitude of the base acceleration ($\ddot{u}_{g,x}$). However, the influence of $\ddot{u}_{g,z}$ was neglected. Soon afterwards, Taniguchi (2002) and Jeong *et al.* (2003) included this effect and presented at the same time the complete expression to describe the necessary condition for avoiding the slide-rock component in a free-standing rocking column

$$\mu_s \geq \left| \frac{-\text{sgn}(\theta) \frac{h}{b} \frac{6g}{p^2} \dot{\theta}^2 \sin(a - |\theta|) + [5 - 3 \cos(2a - 2|\theta|)] \ddot{u}_{g,x}}{+3 \text{sgn}(\theta) \frac{h}{b} \sin(2a - 2|\theta|) [g + \ddot{u}_{g,z}]} \right|, \quad (2-11)$$

$$\left| \frac{-\frac{6g}{p^2} \dot{\theta}^2 \cos(a - |\theta|) + 3 \text{sgn}(\theta) \frac{h}{b} \sin(2a - 2|\theta|) \ddot{u}_{g,x}}{+ [5 + 3 \cos(2a - 2|\theta|)] [g + \ddot{u}_{g,z}]} \right|,$$

where $\dot{\theta}$ describes the angular velocity of the column, and it shows that the slide-rock component is directly related to the movement of the column during rocking.

2.3.1.2 Modelling of Impact in Free-standing Rocking Columns

When a column resting on a rigid foundation as shown in Fig. 2-6 starts and sustains a ‘pure’ rocking motion without overturning, Eq. (2-10) describes the response-history of its angle of rotation (θ). The moment-rotation relation during rocking motion follows the curve shown in Fig. 2-5 without enclosing any area and, therefore, energy is only dissipated during the impacts at the rocking interfaces (when $\theta = 0$). Several proposals can be found in the literature for modelling this impact (i.a., Prieto *et al.* 2004, Giouvanidis & Dimitrakopoulos 2017b), the most commonly adopted being the concept adopted by Housner (1963). This model assumes a Coefficient of Restitution (CoR) η that is always lower than unity to express attenuation of movement (inelastic impact), and it is determined as the ratio of the kinetic energy of the column just after the impact to that just before the impact

$$\eta^2 = \frac{\frac{1}{2} I_{CG} \dot{\theta}_{II}^2}{\frac{1}{2} I_{CG} \dot{\theta}_I^2} = \left[\frac{\dot{\theta}_{II}}{\dot{\theta}_I} \right]^2 \Leftrightarrow \eta = \left| \frac{\dot{\theta}_{II}}{\dot{\theta}_I} \right| < 1, \quad (2-12)$$

where $\dot{\theta}_I$ and $\dot{\theta}_{II}$ are the angular velocities of the column just before and after the impact, respectively. Thus, the ratio of energy loss due to impact is equal to $1 - \eta^2$. In this regard, the lower the value of η , the larger is the energy loss due to impact. This has been confirmed experimentally for free-standing rocking columns by Aslam *et al.* (1980), who showed that columns with larger contact surface and constant height (leading to lower values of η) have enhanced performance against overturning compared to equivalent members with smaller contact surface.

Unlike the kinetic energy of the column that is not conserved after each impact at the rocking interfaces, Housner considered that the angular momentum is conserved. This is based on the assumption of smooth change of rotation without bouncing or sliding that is valid for slender columns (Cheng 2007) and for large values of μ_s (Di Egidio & Contento 2009). To this end, and by assuming that the CR changes from O' to O (see Fig. 2-6), the angular momentum about O immediately before and after impact is conserved, leading to the following expression

$$[I_O - 2mbR \sin a] \dot{\theta}_I = I_O \dot{\theta}_{II}. \quad (2-13)$$

The above equation is derived by assuming that the impact forces are applied exactly at the imminent CR O , as shown in Fig. 2-7A. Substitution of Eq. (2-13) into Eq. (2-12) returns the expression for η as presented for the first time by Housner (1963)

$$\eta = 1 - \frac{mR^2}{I_O} [1 - \cos 2a], \quad (2-14)$$

and Eq. (2-14) simplifies to $\eta = 1 - 1.5\sin^2 a$ for rectangular columns. Eq. (2-14) shows that each impact at the rocking interfaces is expressed through a constant value of η , which is not the case in real structures. However, Thomaidis *et al.* (2018) demonstrated numerically that free-standing rocking columns (and relevant frames) of different slenderness may have a substantial discrepancy in the values of η at each impact at the rocking interfaces, but the average CoR value is similar to that determined analytically by Housner (1963), especially for slender members. This is also confirmed numerically by Ceh *et al.* (2018) who showed that the overturning stability of a rocking column is not affected by the variations in the value of η at each impact at the rocking interfaces.

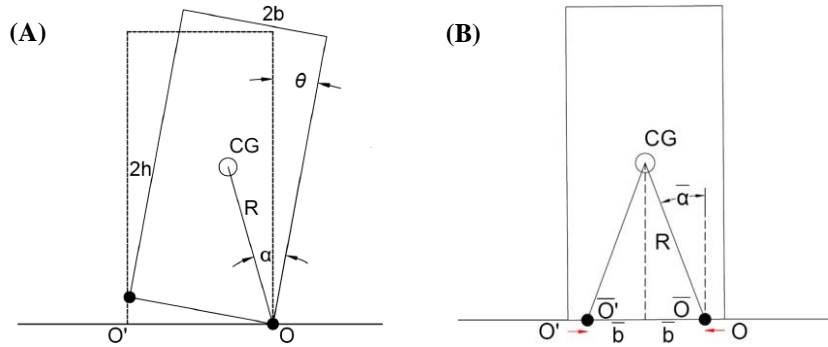


Fig. 2-7 Schematic of a free-standing rocking column tilting (A) about the CR O, and (B) about a migrating kinematic CR. (figure taken from Kalliontzis *et al.* 2016)

Considering that the impact at the rocking interfaces is the only source of energy dissipation for a free-standing rocking structure, discussion has been generated recently on Housner's approach (e.g., Ceh *et al.* 2018, Avgenakis & Psycharis 2020), resulting in several energy dissipation models. One of the better-known extended models of the rocking impacts is the one that considers a more realistic location for the CR, accounting for the potential migration of the resultant force towards the centre of the pier base due to an extended contact surface as shown in Fig. 2-7B. This approach has been adopted by Kalliontzis *et al.* (2016) and Chatzis *et al.* (2017), and the former proposed an equivalent to the Housner's expression for η . In this regard, the expression for η proposed by Kalliontzis *et al.* extends that presented by Housner by taking into account the effect of the extended contact surface during impact, and this is done by means of a constant k , leading to the following expression

$$\eta = \frac{1 + \frac{mR^2}{I_{CG}} \left[1 - (\sin a)^2 (1 + k^2) \right]}{1 + \frac{mR^2}{I_{CG}} \left[1 - (\sin a)^2 (1 - k^2) \right]}, \quad (2-15)$$

where $k = \bar{b}/b$ takes values $0 \sim 1$, and the value of η is constant for each impact at the rocking interfaces; Eq. (2-15) reduces to $\eta = [4 - 3\sin^2 a \cdot (1 + k^2)] / [4 - 3\sin^2 a \cdot (1 - k^2)]$ for rectangular columns.

Table 2-2 compares the CoR values for rectangular columns that were determined experimentally in different studies with those obtained from Eqs. (2-14) and (2-15), respectively; it is noted that the experimental values of η are derived from free vibration tests where the columns are allowed to rock in all the cases with initial rotation $\theta_{init.} = \alpha$ that is the maximum available, while in Eq. (2-15) k is set equal to 0.72 as proposed in Kalliontzis *et al.* (2016). In general, Table 2-2 shows that the squatter the column, the lower is the value of η regardless of the approach adopted. Additionally, and for slender columns ($h/b > 3$), the effect of the interface material on the $\eta_{exp.}$ value is minimal, and similar values are shown for different interface materials of same slenderness (α). This observation is in line with the analytical approaches of Housner and Kalliontzis *et al.* where the effect of the interface material is not taken into account. Exceptions exist, though, as in the case of rubber with RC(3) and RC(5) (see further discussion with regard to this material as interface in §2.4.1.2 and §2.4.1.3).

Table 2-2 Experimental studies determining the CoR values at the rocking interfaces ($\eta_{exp.}$) for rectangular free-standing rocking columns with different aspect ratio (h/b), slenderness (α) and interface materials. The values of η are calculated according to the analytical approaches of Housner (1963) ($\eta_{Hous.}$) and Kalliontzis *et al.* (2016) ($\eta_{Kall.}$). The effect of the CR in Eq. (2-15) is equal to $k = 0.72$.

Study where it was determined	h/b [-]	α [rad]	Column-to-Base	$\eta_{exp.}$ [-]	$\eta_{Hous.}$ [-]	$\eta_{Kall.}$ [-]
Ogawa (1977)	2	0.5	Wood-to-Steel	0.79	0.66	0.81
Priestley <i>et al.</i> (1978)	2	0.5	Concrete-to-Aluminium	0.87	0.66	0.81
Pena <i>et al.</i> (2007)	2.85	0.35	Granite-to-Granite	0.93	0.82	0.9
Ogawa (1977)	3	0.33	Wood-to-Steel	0.88	0.84	0.91
ElGawady <i>et al.</i> (2011)	3	0.33	Concrete-to-Concrete	0.82	0.84	0.91
ElGawady <i>et al.</i> (2011)	3	0.33	Timber-to-Concrete	0.84	0.84	0.91
ElGawady <i>et al.</i> (2011)	3	0.33	Rubber-to-Concrete	0.79	0.84	0.91
Ogawa (1977)	4	0.25	Wood-to-Steel	0.94	0.91	0.95
Fielder <i>et al.</i> (1997)	4	0.25	Concrete-to-Steel	0.93	0.91	0.95
Pena <i>et al.</i> (2007)	4	0.25	Granite-to-Granite	0.94	0.91	0.95
Fielder <i>et al.</i> (1997)	4	0.25	Wood-to-Aluminium	0.95	0.91	0.95
Lipscombe & Pellegrino (1993)	4	0.25	Steel-to-Steel	0.92	0.91	0.95
Muto <i>et al.</i> (1960)	4.33	0.23	Steel-to-Wood	0.96	0.92	0.96
ElGawady <i>et al.</i> (2011)	5	0.2	Concrete-to-Concrete	0.94	0.94	0.97
ElGawady <i>et al.</i> (2011)	5	0.2	Timber-to-Concrete	0.95	0.94	0.97
ElGawady <i>et al.</i> (2011)	5	0.2	Rubber-to-Concrete	0.85	0.94	0.97
Pena <i>et al.</i> (2007)	5.88	0.17	Granite-to-Granite	0.97	0.96	0.98
Pena <i>et al.</i> (2007)	8.03	0.12	Granite-to-Granite	0.98	0.98	0.99

Fig. 2-8 presents the ratios of the experimental CoR values ($\eta_{exp.}$) to those predicted from the analytical coefficients of Housner and Kalliontzis *et al.* ($\eta_{anal.}$) shown in Table 2-2; each case is denoted using the initial letter of the column material followed by that of the base, while the aspect ratio (h/b) is mentioned in parenthesis. Fig. 2-8 indicates that Kalliontzis *et al.* predict a CoR value that is larger (i.e., lower energy dissipation) than the experimental value in fourteen out of the seventeen examined cases and, therefore, this approach is considered as conservative from the stability point of view. This is not the case in Housner's approach that is conservative only in three cases compared to the experimental values (Ceh *et al.* 2018). Going into more details, it is observed that the analytical expression by Kalliontzis *et al.* gives a better prediction for the CoR value for an aspect ratio up to 2.85 (i.e., for squatter columns) with an average difference with the experimental values of only 2% compared to 16% found for Housner's one. The opposite occurs for aspect ratios close to 3, with Housner's approach showing an average difference of 0.7% compared to 7% that was found for Kalliontzis *et al.*. For slenderer columns ($h/b > 3$) that is often the case with bridge piers, both expressions match the experimental values in the same way (i.e., average differences of 10% and 12% for Housner and Kalliontzis *et al.*, respectively). In that respect, and for the concrete-to-concrete surface (i.e., CC(3) and CC(5)) that is the type of interface considered in this thesis, the Housner's approach matches almost perfectly the experimental value.

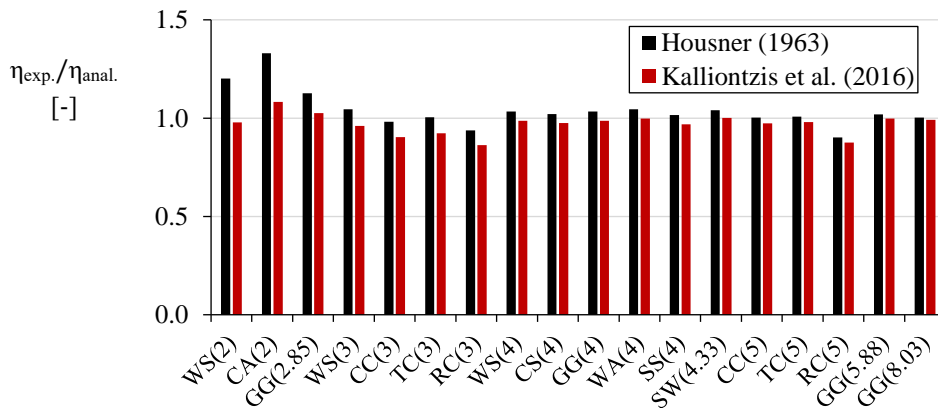


Fig. 2-8 Ratios of the experimental values of the CoR at the rocking interfaces ($\eta_{exp.}$) to those obtained from the analytical approaches ($\eta_{anal.}$) of Housner (1963) and Kalliontzis *et al.* (2016). Results obtained for rectangular free-standing rocking columns with different aspect ratio (h/b) and interface materials.

The CoR values determined from Eqs. (2-14) and (2-15) depend mainly on the contact surface of the column that is expressed through the slenderness (α). However, the influence of the impact at the rocking interfaces depends on three more factors that are not directly considered in Table 2-2, and are (i) the angular velocity just before the impact (Jankowski 2007), (ii) the inelastic behaviour of the interface material at the instant of impact (Roh & Reinhorn 2010a) and (iii) the imperfections of the contact surfaces (ElGawady *et al.* 2011). From the previous discussion, condition (i) is taken into account to some extent in the values presented in Table 2-2, considering that the free-standing rocking columns develop considerably high velocity just before the impact under the examined free vibration tests. However, conditions (ii) and (iii) are totally ignored in

Eqs. (2-14) and (2-15). Therefore, the actual value of η will be lower than the one computed from Eqs. (2-14) and (2-15), and higher energy dissipation is expected in reality, constituting analytical derivations of this type as conservative (see §3.2.5, §4.2.5, §5.2.3).

2.3.1.3 Key Findings about Free-standing Rocking Columns

The seismic performance of rocking columns has been mainly examined by considering only the horizontal ground motion ($\ddot{u}_{g,x}$), thus ignoring the vertical component ($\ddot{u}_{g,z}$); the effect of the latter in free-standing rocking columns is discussed in §2.3.1.4.

The first experimental works on the rocking response of free-standing columns (Aslam *et al.* 1980, Tso & Wong 1989a and 1989b) showed significant variations in the response and, therefore, the problem has often been tackled from a stochastic perspective (Yim & Chopra 1984, Spanos & Koh 1984, Taniguchi 2002) to find consistent trends in the overturning behaviour and/or provide probabilistic predictions. Another way of illustrating the overturning stability of rocking structures is through spectra constructed for the minimum acceleration amplitude (a_p) of a ground motion with given circular frequency ($\omega_p = 2\pi/T_p$) that is able to overturn a rocking column with certain slenderness (α) and frequency parameter (p). This spectrum was introduced by Shi *et al.* (1996), and it is referred to as Overturning Minimum Acceleration Spectrum (OMAS) (shown in Fig. 2-10). The resulting graph divides the possible combinations of the earthquake intensity and the structural characteristics in two areas, one wherein the structure fails and the other one that delineates a safe area. These graphs are generalised by utilising dimensionless variables (ω_p/p , $a_p/g \cdot \tan\alpha$) using Buckingham's Π -theorem, which offer a physically self-similar description of the response (Dimitrakopoulos & DeJong 2012a, Makris & Vassiliou 2012, Voyagaki *et al.* 2012, Makris & Kampas 2016b). Consequently, the OMAS allows for general prediction of rocking response for a wide range of rocking configurations with equivalent characteristics, even if the structural response is nonlinear.

Pulse-type motions facilitate the construction of OMAS, considering that they can be described by their a_p and ω_p values only. To this end, several pulse type-motions like single-lobe, sine, cosine, symmetric and antisymmetric Ricker pulses have been used to create OMAS (i.a., Makris & Roussos 2000, Zhang & Makris 2001, Dimitrakopoulos & Fung 2016, Ther & Kollár 2017). Additionally, some pulse-type motions have shown good agreement with near-fault earthquakes (Makris & Roussos 2000, Mavroeidis *et al.* 2004, Vassiliou & Makris 2011, Makris & Vassiliou 2013). The vulnerability of rocking columns to near-fault excitations has been observed since the early work of Kirkpatrick (1927), and this result has been confirmed experimentally by Tso & Wong (1989b) and later by Pena *et al.* (2007). Hence, pulse-type motions have emerged as a useful tool not only in terms of providing simple mathematical expressions for the ground motions, but also because they can capture the main characteristics of near-fault ground motions, if the appropriate parameters of the pulse are introduced.

The prediction of the rocking response using pulse-type motions is not completely reliable, though. Acikgoz & DeJong (2014) compared the response under historic and pulse-type earthquakes and concluded that there are cases wherein the use of pulse-type motions can be

unconservative. These authors proposed regions in terms of ω_p/p and $\alpha_p/g \cdot \tan\alpha$ where pulse-like records are likely to give reliable results, as shown in Fig. 2-9. The reason behind this difference is that pulse-type motions usually ignore the first part of the real earthquake motion, and they can capture only the strong part of it (see i.a. Makris & Vassiliou 2013). This initial part, although not strong enough to induce overturning by itself, can induce small rotations that are very important in terms of overturning stability due to the fact that when the main part of the ground motion comes, uplift has already occurred.

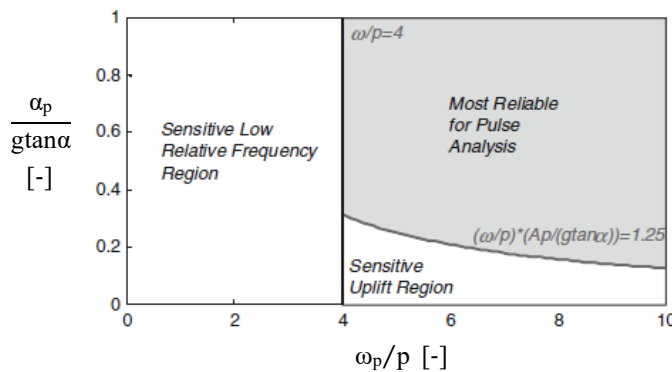


Fig. 2-9 Dimensionless intensity regions in terms of ω_p/p and $\alpha_p/g \cdot \tan\alpha$ highlighting where analysis with pulse-type motions is more reliable and where it is more sensitive, when rocking structures are examined. (figure taken from Acikgoz & DeJong 2014)

In any case, the OMAS with pulse-type motions is a valuable tool to identify general trends in the rocking response. Fig. 2-10A, B, C show OMAS for a free-standing rocking column when subject to sine, symmetric and antisymmetric Ricker pulses, respectively. The main research findings from OMAS of free-standing rocking columns under several pulse-type motions are summarised in the following;

- Slender columns obtained by reducing the value of α while keeping b constant are less stable, because they are more prone to uplift that fosters overturning.
- Large columns obtained by increasing the value of R while keeping b constant lead to safer configurations in a seismic performance context due to the influence of I_0 .
- From the previous remarks, it can be concluded that there is a contrasting effect of α and R in the rocking columns. Makris & Kampas (2016b) stated that the prevailing factor depends only on the frequency range of the ground motion, which is uncertain when the ground motion is unknown.
- Rocking columns are more prone to overturn when subject to near-fault ground motions due to their low-frequency range (see the term ‘uplifted resonance’ in Acikgoz & DeJong 2012).

- Columns can overturn with distinct failure modes under pulse-type motions, that is either by experiencing no impact prior to overturning (Mode 0), or one (Mode 1) or more impacts (Mode 2), as shown in Fig. 2-10.
- Deformable rocking columns show slightly larger overturning areas for Mode 0 and considerably smaller overturning areas for Mode 1 compared to rigid sections (Acikgoz & DeJong 2012, Vassiliou *et al.* 2014, Vassiliou *et al.* 2015). Overall, overturning is less likely when the deformability of the columns is considered as opposed to assuming rigid columns and, therefore, simplifying the analysis by considering that the rocking columns are rigid is conservative from the seismic performance point of view.

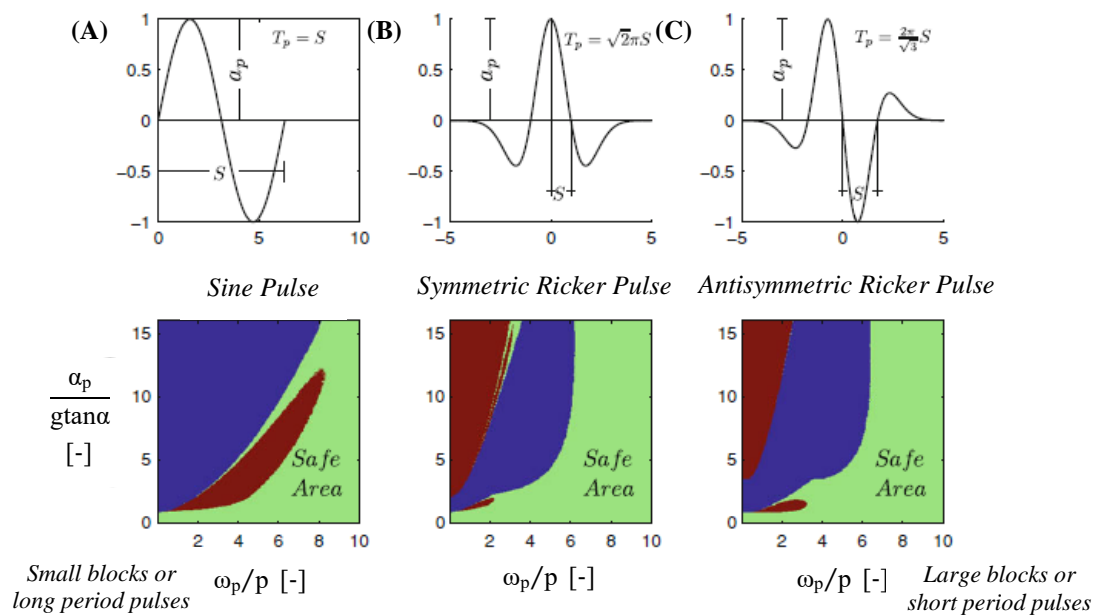


Fig. 2-10 OMAS for a free-standing rocking column with slenderness $\alpha = 14^\circ$ when subject to acceleration pulses of (A) sine, (B) symmetric and (C) antisymmetric Ricker type. Blue shapes refer always to Mode 0, while red shapes to Mode 1 and 2. (figure taken from Makris & Vassiliou 2012)

Apart from OMAS, which have shed valuable light on the seismic performance of rocking configurations, Priestley *et al.* (1978) developed a practical methodology using standard displacement and acceleration response spectra based on the representation of the rocking column as a single Degree of Freedom (DoF) oscillator with constant viscous damping ratio (ζ). The results presented therein were adopted in the pre-standard FEMA 356 (2000). Additionally, Makris & Konstantinidis (2003) introduced the concept of rocking spectrum to predict the maximum rotation angles (θ) and maximum angular velocities ($\dot{\theta}$) of free-standing rocking columns with specific slenderness (α) under a specific ground motion. An example of this is shown in Fig. 2-11A, B for the Pacoima Dam record from the 1971 San Fernando earthquake. This procedure could be extended to more complex structures such as two-block assemblies and frames based on similarity laws presented by DeJong & Dimitrakopoulos (2014) for these structures and the corresponding rocking column. However, the rocking spectrum has not received enough attention, apparently due

to the fact that each graph is constructed for a specific ground motion and, therefore, it cannot be extended to a wide range of ground motions as is the case in OMAS.

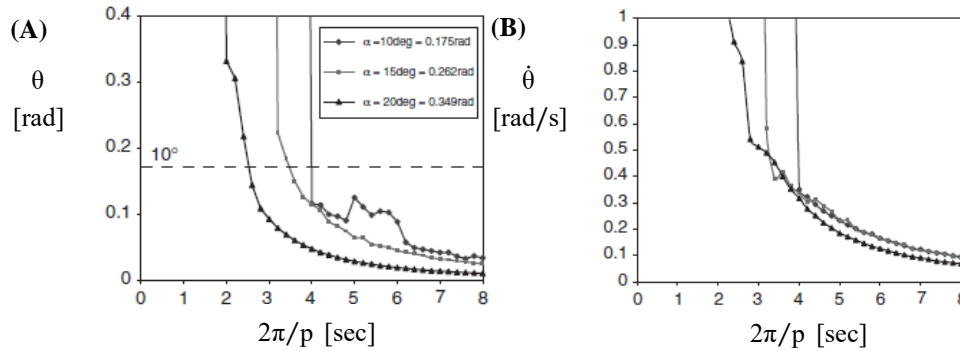


Fig. 2-11 Rocking spectrum in terms of (A) relative rotation (θ) and (B) angular velocity ($\dot{\theta}$) for free-standing rocking columns with different slenderness (α), when subject to the Pacoima Dam motion recorded during the 1971 San Fernando earthquake. (figure taken from Makris & Konstantinidis 2003)

2.3.1.4 Effect of Vertical Component of Ground Motion on Free-standing Rocking Columns

The vertical component of the earthquake has proved to be a significant obstacle in the study of the rocking behaviour. Yim *et al.* (1980) were the first who noticed the high ambiguity in rocking response due to the vertical ground motion. They observed that its effect could be either positive or negative, but the conditions for each case were not determined. Hao & Zhou (2011) tried to explain numerically this effect by examining cases with vertical acceleration amplitude more than 1 g that forces the block to upthrow. These authors observed that the effect of upthrow would reduce the possibility of overturning. However, the block may be displaced with respect to its initial position at the end of earthquake, which is crucial for the seismic performance.

Makris & Kambas (2016b) suggested that the vertical ground motion has a marginal effect on the rocking response. This was justified by the factors that multiply each ground motion component as can be seen in Eq. (2-10). Specifically, the $\ddot{u}_{g,x}$ value is multiplied by $\cos(\alpha - |\theta|)$, whereas $\ddot{u}_{g,z}$ is multiplied by $\sin(\alpha - |\theta|)$. The sinusoidal function maximises its value when full contact is achieved ($\theta = 0$), and Fig. 2-12 presents the effect of slenderness (α) on both trigonometric functions at this position. It is observed that the vertical ground motion participates marginally in the rocking response of slender free-standing columns, contrary to the horizontal component that contributes significantly to the response. Less importantly in bridge configurations, this difference diminishes for stocky members that are affected the same way from both ground motion components. Notwithstanding the above, the effect of the vertical component of ground motion should not be underestimated in a seismic performance context due to the potential lack of recentring of the vertical members when this component is taken into account in the analysis (Hao & Zhou 2011).

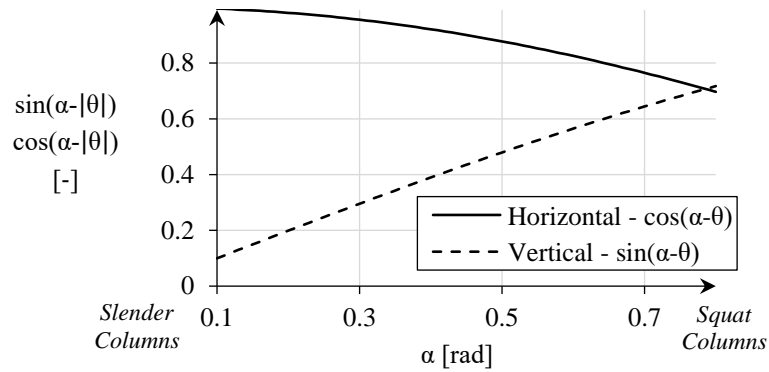


Fig. 2-12 Effect of horizontal ($\ddot{u}_{g,x}$) and vertical components of ground motion ($\ddot{u}_{g,z}$) expressed through the trigonometric functions of cosine and sine type, respectively, accounting for the influence of the slenderness (α). Results obtained when $\theta = 0$.

2.3.1.5 Alternative Configurations for Rocking Columns

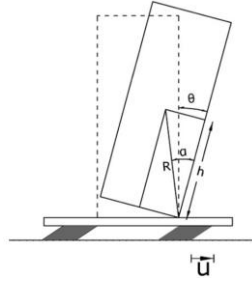
The rocking response of free-standing columns has been the stimulus for studying a number of more complex configurations. Table 2-3 summarises the principles and main findings from different analytical studies in the topic of enhancing the seismic performance of the free-standing rocking column (§2.3.1.3) through supplemental devices, while the main findings are derived mainly from OMAS; it is noted that the proposed inerters produce resisting forces proportional to the relative acceleration between their terminals, and the additional clutch ensures that their rotational inertia is only employed to oppose the motion (Smith 2002, Marian & Giaralis 2014).

Table 2-3 Rocking columns supplemented with additional devices to improve the seismic performance of the free-standing configuration. Principles and main findings.

Additional Device Studies where it was used	Schematic	Principles and Main Findings
<u>Dissipating Device</u> Makris & Zhang (2001) Makris & Black (2002) Dimitrakopoulos & DeJong (2012a) Ceravolo <i>et al.</i> (2017) Pecorelli & Ceravolo (2017)		<ul style="list-style-type: none"> - Pre-yielding stiffness is positive. - Post-yielding stiffness depends on the strain hardening of the spring. More effective when negative. - The additional energy that is dissipated through the supplemental devices is beneficial for small columns, while for large columns this effect is negligible.
<u>Unbonded Tendon</u> Aslam <i>et al.</i> (1980) Dimitrakopoulos & DeJong (2012a) Vassiliou & Makris (2015)		<ul style="list-style-type: none"> - Post-uplift stiffness varies from negative to positive depending on the axial stiffness of the tendon. - Tendons are effective in suppressing the rocking response of small columns, while this effect is negligible for large ones. - Increasing the strength of the tendon leads to ambiguous results due to the fact that energy is stored in the system.

Isolated Base

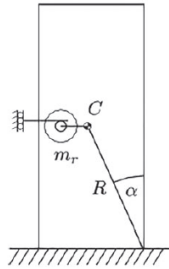
Vassiliou & Makris (2012)
 Roussis & Odysseos (2017)
 Harvey (2017)



- CoR at the rocking interfaces is always smaller compared to that in the free-standing column.
- Base isolation enhances the seismic performance of small columns, while it is detrimental for large columns due to the fact that it lengthens the duration of the pulses.

Inerter

Thiers-Moggia & Málaga-Chuquitaype (2018)
 Thiers-Moggia & Málaga-Chuquitaype (2020a)
 Thiers-Moggia & Málaga-Chuquitaype (2020b)



- The inerters reduce the frequency parameter of the block resulting in lower seismic demands.
- The use of inerters in free-standing and anchored columns increases the overturning capacity of the corresponding member without inerters.
- The addition of a clutch further improves the resistance to overturning.

2.3.2 Frames with Rocking Columns

2.3.2.1 Dynamics and Modelling of Impact in Frames with Free-standing Rocking Columns

The impressive seismic performance of rocking columns promoted the examination of rocking behaviour in structural framing systems without fixed joints between the individual members (a very common system in ancient monuments). The dynamics of a frame with two free-standing rocking columns was first studied by Allen *et al.* (1986). This study was extended by Makris & Vassiliou (2013) who integrated in the formulation multiple supporting members (N) with equal dimensions ($2h$ and $2b$) as shown in Fig. 2-13. The EoM of this symmetric system subject to horizontal ($\ddot{u}_{g,x}$) and vertical ground motions ($\ddot{u}_{g,z}$) was formulated using the rotation of the column θ as the only DoF, and the following expression applies after using an energy approach through a Lagrangian formulation

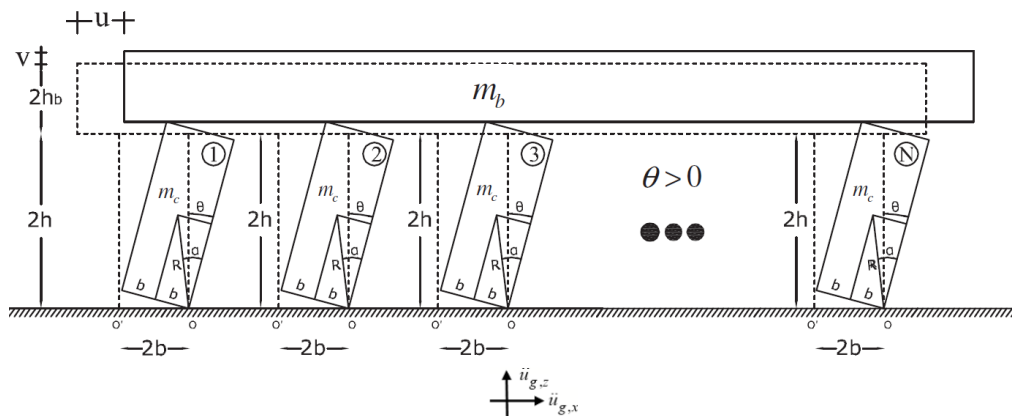


Fig. 2-13 Schematic of a frame with free-standing rocking columns of equal height (symmetric) during rocking motion. (figure taken from Makris & Vassiliou 2013)

$$\ddot{\theta} = -\frac{1+2\gamma}{1+3\gamma} p^2 \left[\text{sgn}(\theta) \left(1 + \frac{\ddot{u}_{g,z}}{g} \right) \sin(a - |\theta|) + \frac{\ddot{u}_{g,x}}{g} \cos(a - |\theta|) \right], \quad (2-16)$$

where $\gamma = m_b/N \cdot m_c$ is the superstructure mass effect that is introduced as the ratio of the mass of the superstructure (m_b) to that of the substructure ($N \cdot m_c$).

It is observed that Eq. (2-16) differs from the corresponding EoM for a rocking column (Eq. (2-10)) only through the constant $1+2\gamma/1+3\gamma$. Makris & Vassiliou (2013) pointed out this difference, and they proposed the following relationship between the single rocking column with slenderness α , and the symmetric frame that is supported on N rocking columns with slenderness α and superstructure mass effect γ

$$\hat{p} = \sqrt{\frac{1+2\gamma}{1+3\gamma}} p, \quad (2-17)$$

and by solving Eq. (2-17) with respect to the size of the pier ($p = \sqrt{m \cdot g \cdot R/I_O}$, where $I_O = f(R^2)$), the relationship between a rocking column and a relevant frame is derived

$$\hat{R} = \frac{1+3\gamma}{1+2\gamma} R. \quad (2-18)$$

Thus, the rocking response of a symmetric frame with rocking columns can be described by that of a rocking column with slenderness α and size \hat{R} . In this regard, the frame with rocking columns experiences a ‘pure’ rocking motion without sliding, upthrow and slide-rock movements according to the conditions described in §2.3.1.1 accounting for the difference in size of the member.

Similarly to Housner’s approach presented in §2.3.1.2, Makris & Vassiliou (2013) expressed the energy that is dissipated at each impact at the rocking interfaces by means of a CoR value. This expression of η was formulated based on the conservation of angular momentum at the instant of the impact, and by assuming that the impact forces are concentrated at the imminent pivot point (see Fig. 2-7A), leading to the following expression

$$\hat{\eta} = \left| \frac{\dot{\theta}_{II}}{\dot{\theta}_I} \right| = \frac{1 - \frac{3}{2} \sin^2 a + 3\gamma \cos 2a}{1 + 3\gamma}, \quad (2-19)$$

and Eq. (2-19) applies to frames with rectangular rocking columns and is different from that for the corresponding rocking columns (Eq. (2-14)).

The frame with rocking columns of equal height is not the usual case in real structures, especially in bridges (e.g., valley crossings). DeJong & Dimitrakopoulos (2014) and, later,

Dimitrakopoulos & Giouvanidis (2015) presented the dynamics of a frame that is supported on two rocking columns with different height and same width, shown in Fig. 2-14B. In both studies, the dynamic motion of this asymmetric system was derived using a Lagrangian formulation, and it was described by using only one DoF that is different from that selected for the corresponding symmetric system. Specifically, this DoF describes the angle that is defined by the diagonal of the tall column and by the horizontal X-axis (φ) as shown in Fig. 2-14A, C. In this case, the supporting members exhibit a different rotation (i.e., φ for the tall column and φ_{CD} for the short one) due to their difference in height, which leads to an additional rotation angle at the bridge deck (φ_{BC}). As a result, the EoM is very different from that presented in Eq. (2-16) for the symmetric case. Additionally, the impact at the rocking interfaces was expressed by using the usual concept of CoR, and after following an impulse formulation a totally different expression from that shown in Eq. (2-19) was derived. Therefore, the symmetric and asymmetric frames with rocking columns show very different kinematics, and this is attributed to the different height of the supporting members that leads to differential rotations (i.e., the shorter or squatter piers are forced to larger rotations that taller or slenderer members) and to the resulting rotation of the superstructure.

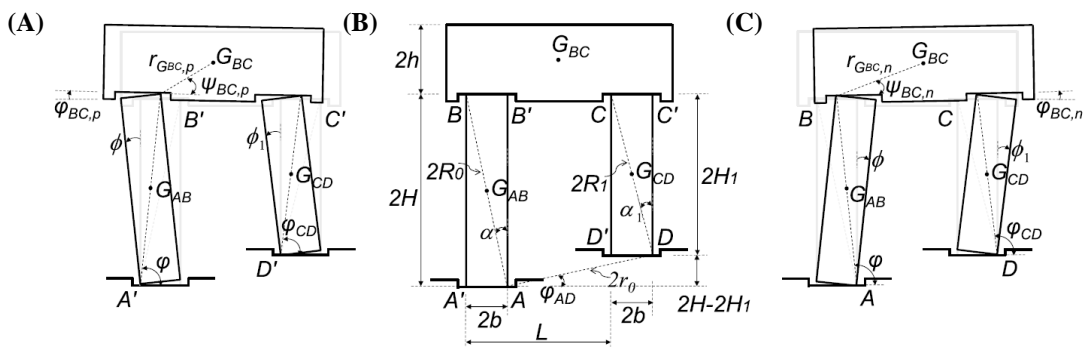


Fig. 2-14 Schematic of a frame with free-standing rocking columns of unequal height (asymmetric) (A) when sustaining counter-clockwise rotation of the columns, (B) at the at-rest position, and (C) when sustaining clockwise rotation of the columns. (figure taken from Dimitrakopoulos & Giouvanidis 2015)

2.3.2.2 Key Findings about Frames with Free-standing Rocking Columns

Eqs. (2-18) and (2-19) show that the symmetric frame with N free-standing rocking columns of slenderness α and effect of superstructure γ can be described by an equivalent rocking column with slenderness α , size \widehat{R} and CoR $\widehat{\eta}$. Fig. 2-15A presents the influence of γ on the ratio \widehat{R}/R as determined from Eq. (2-18) assuming columns with rectangular section and common slenderness ($\alpha = 0.1$ rad), and this is done by increasing the γ value (i.e., the mass of the superstructure is increased by keeping constant that of the substructure for illustration reasons). Accordingly, Fig. 2-15B compares the values of η for rocking columns (Eq. (2-14)) with those obtained for equivalent frames (Eq. (2-19)) for the same rectangular rocking columns. It is shown that the larger the value of γ (i.e., the larger the mass of the superstructure), the larger is the size of the equivalent column to describe the rocking response of the frame, and the lower is the value of η . Therefore, following §2.3.1.3 and §2.3.1.2, larger γ leads to more stable configurations in terms of overturning. For this reason, the

system consisting of rocking columns with a cap beam on top shows enhanced seismic performance compared to the corresponding single rocking column with same slenderness. In this regard, Makris & Vassiliou (2014b) state that ‘the heavier the freely supported cap beam, the more stable is the rocking frame, regardless of the rise of the centre of gravity of the cap beam’.

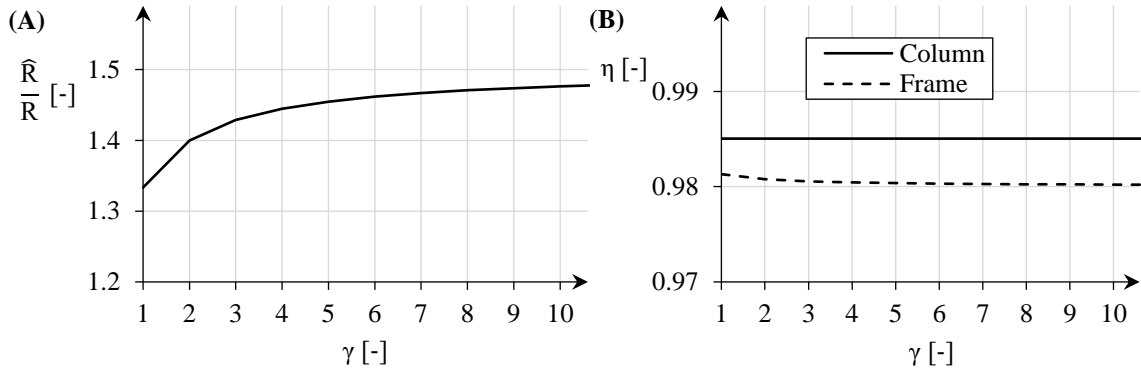


Fig. 2-15 (A) Ratio \widehat{R}/R as described by Eq. (2-18) and (B) CoR at the rocking interfaces (η) for free-standing rocking columns (Housner 1963) and for relevant symmetric frames (Makris & Vassiliou 2013), accounting for the influence of the superstructure mass effect (γ). Results obtained when $\alpha = 0.1$ rad.

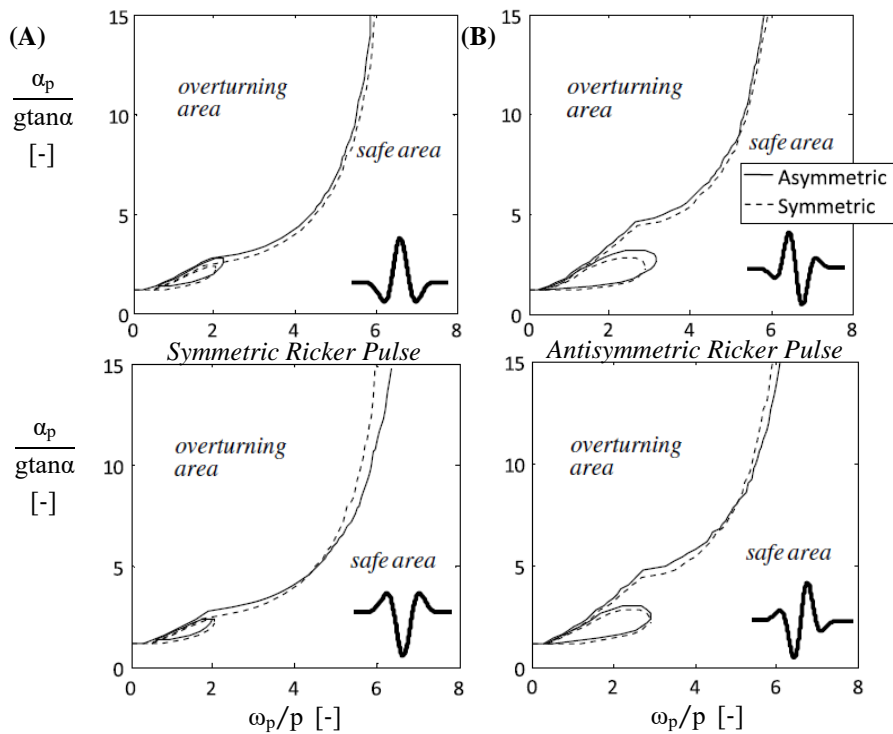


Fig. 2-16 OMAS for a symmetric frame with free-standing rocking columns and for the corresponding asymmetric configuration. Results obtained when subject to positive and negative acceleration pulses of (A) symmetric and (B) antisymmetric Ricker type. (figure taken from Dimitrakopoulos & Giouvanidis 2015)

Dimitrakopoulos & Giouvanidis (2015) compared the seismic performance of asymmetric frames with two rocking piers of same width and different height with respect to the corresponding symmetric configuration. This was done by deriving OMAS for symmetric and antisymmetric

Ricker pulses as shown in Fig. 2-16A, B, respectively. It was noticed that the two configurations show equivalent seismic performance against overturning for a wide range of frequencies and acceleration amplitudes. Therefore, the overturning stability is not affected by the irregularity in the height of the piers, despite the different kinematics of the two systems, as well as the delay in the initiation of rocking motion that was observed for the asymmetric frame.

2.3.2.3 Alternative Configurations for Frames with Rocking Columns

Due to the uncertain effect of the vertical ground motion (§2.3.1.4) and to the minimal damping that is offered from a ‘bare’ configuration (§2.4.1.2), different researchers proposed the use of supplemental devices to enhance the frame with free-standing rocking columns (i.a., Mander & Cheng 1997, Ou *et al.* 2007, ElGawady *et al.* 2010). In most cases, these were an unbonded (post-tensioned) tendon located at the centroid of the rocking column to give recentring capacity, and mild steel at the pier base to provide damping. The configuration that combines both devices can be found in the literature as frame with rocking columns and Flag-Shaped Hysteretic Behaviour (FSHB). This was initially proposed by Mander & Cheng (1997) and, simultaneously, by Stanton *et al.* (1997), and soon enough this proposal has attracted the attention of several researchers that examined this configuration analytically (see relevant discussion in §2.4.2). Table 2-4 summarises the principles and main findings (mainly from OMAS) from the different analytical studies on the performance of frames with supplemental devices (including the one with FSHB) and compares them with the corresponding free-standing configurations (§2.3.2.2 and §2.3.1.3); it is noted that some of these studies treat only one supplemental device and the main findings are combined in the following table.

Table 2-4 Frames with rocking columns supplemented with additional devices to improve the seismic performance of the free-standing configuration. Principles and main findings.

Study where it was used	Makris & Vassiliou (2014a) Makris & Vassiliou (2014c) Dimitrakopoulos & Giouvanidis (2015) Giouvanidis <i>et al.</i> (2015) Giouvanidis & Dimitrakopoulos (2016) Giouvanidis & Dimitrakopoulos (2017a) Giouvanidis <i>et al.</i> (2017)		
Unbonded Tendon	Prestressing Force	Dissipating Device	FSHB
- The tendons should stay in the elastic range; fracture leads to unpredictable behaviour. - More effective for frames with small columns, while their effect becomes	- Rocking initiation is delayed compared to the free-standing configuration. - Prestressing force should be avoided, while it leads to ambiguous results due to the fact that energy is stored in the system in	- Increase is favourable regardless of the overall stiffness sign, but more pronounced for systems with negative post-uplift stiffness. - Additional damping leads to	- This configuration is much more stable in terms of overturning compared to the free-standing configuration. - Increasing the overall stiffness from negative to positive does not lead to superior performance,

immaterial in larger columns.	the form of strain energy in the tendons.	safer frame configurations.	while the efficiency of rocking isolation is reduced. This threshold is determined analytically
- Increase of stiffness from negative to positive leads to mitigated stability compared to the free-standing configuration.		- The overall behaviour is very sensitive to the fracture of the dissipating mechanism.	

2.4 Inherent Disadvantages in Free-standing Rocking Piers and Enhanced Rocking Pier Configurations

2.4.1 Inherent Disadvantages in Free-standing Rocking Piers

Rocking has been proposed as an isolation technique that can improve the seismic performance of conventional piers by eliminating damage in the pier-foundation connection and, therefore, lead to safer systems without residual displacements. Several researchers focused on this and found that the ‘bare’ rocking configuration, although it reduces substantially the damage at bottom section of the piers, lacks recentring (§2.4.1.1) and dissipating capacity (§2.4.1.2). Furthermore, the behaviour of the rocking interface highly influences the integrity of the pier, leading in some cases to detrimental effects on the overall seismic performance (§2.4.1.3). To this end, recent proposals for rocking piers tackle the three inherent disadvantages of rocking movement.

2.4.1.1 Effect of Recentring Capacity

Cheng (2008) conducted shaking table tests on free-standing rocking piers made of concrete subjected to an additional compressive force aiming to simulate the beneficial effect of the deck weight. It was found that residual displacements occur in the member under seismic excitations regardless of the material at the rocking interface. The concept of using unbonded tendons to reduce residual displacements was implemented for the first time by Sakai & Mahin (2004). These researchers compared the seismic performance of a conventionally designed concrete bridge pier with a rocking one in which half of the non-prestressed reinforcement is removed, and an unbonded post-tensioned tendon is used instead. The results showed that, although both members sustained the same drift, the residual displacements are significantly reduced for the rocking pier. Trono *et al.* (2015) and Thonstad *et al.* (2016) came also to the same conclusion using precast concrete members allowed to rock at both joints. However, the use of pre-tensioning instead of post-tensioning reduces potential fatigue or corrosion problems at the anchorages.

2.4.1.2 Effect of Energy Dissipation

Energy dissipation in the ‘bare’ rocking configuration derives mainly from the impacts at the rocking surfaces. In this regard, the total energy dissipation during rocking motion can be described

by an inherent viscous damping ratio (ζ_{in}) that is intrinsic to the structure, and an additional radiation damping ratio (ζ_{im}) that is due to the impacts. The equivalent viscous damping ratio (ζ) can be calculated by the following expression

$$\zeta = \zeta_{in} + \zeta_{im}, \quad (2-20)$$

where ζ_{in} takes values from 2% to 5% for structures vibrating in the elastic range, while several researchers have proposed relations involving ζ_{im} and the CoR η in order to have the same energy loss at the impacts. Some of these proposals are

$$\text{FEMA 356 (2000):} \quad \zeta_{im} = 0.4[1 - \eta], \quad (2-21)$$

$$\text{Makris \& Konstantinidis (2003):} \quad \zeta_{im} = -0.34 \ln \eta^2, \quad (2-22)$$

$$\text{Anagnostopoulos (2004):} \quad \zeta_{im} = \frac{-\ln \eta^2}{\sqrt{\pi^2 + (\ln \eta^2)^2}}, \quad (2-23)$$

$$\text{Cheng (2007):} \quad \zeta_{im} = \frac{1 - \eta^2}{\pi \left[1 - \frac{u_{CG}}{b} \right]}, \quad (2-24)$$

where u_{CG} in Eq. (2-24) is the lateral displacement at the CG. Table 2-5 presents the values of ζ calculated from Eqs. (2-21) to (2-24) for different interface materials with values of CoR determined experimentally in the literature (see Table 2-2). It is noted that the values shown in Table 2-5 are calculated assuming $\zeta_{in} = 3\%$ for all cases. It is observed that squat columns dissipate more energy than slender ones. This is due to the fact that the larger the contact surface, the larger is the energy dissipation. However, in all cases shown in Table 2-5, ζ is lower than 20%. More importantly for actual bridge piers, the damping associated with the slender columns ($\alpha \leq 0.25$) does not even exceed 10%, and this was confirmed experimentally by Cheng (2008) for the frame shown in Fig. 2-17 with $\alpha = 0.25$ and a steel-to-steel surface. Exceptions exist, though, for the case of rubber-to-concrete surface (i.e., $\alpha \geq 0.2$ in ElGawady *et al.* 2011) and, therefore, rubber shows high potential to be used as an interface material considering that it leads to higher energy dissipation at each impact at the rocking interfaces compared to other (stiffer) materials. In any case, conventional designs based on structural dissipation in ductile piers can achieve damping ratios of 20% for ductility ratios (μ) of 4 (Priestley & Grant 2005). Therefore, it becomes essential to increase the capacity in the energy dissipation of the ‘bare’ rocking configuration, and this is usually done through supplemental dissipating devices.

Table 2-5 Equivalent viscous damping ratio (ζ) for different models presented in the literature, accounting for experimental CoR values at the rocking interfaces ($\eta_{exp.}$) for rectangular free-standing rocking columns with different slenderness (α). Value of ζ_{in} is assumed equal to 3%.

Study where it was determined	α [rad]	$\eta_{exp.}$ [-]	$\zeta_{FEMA\ 356}$ [%]	$\zeta_{Mak.Kon.}$ [%]	$\zeta_{Anagn.}$ [%]	ζ_{Cheng} [%]
Ogawa (1977)	0.5	0.79	11.5	19.25	18.04	15.22
Priestley <i>et al.</i> (1978)	0.5	0.87	8.13	12.33	11.7	10.72
Pena <i>et al.</i> (2007)	0.35	0.93	5.91	8.13	7.8	7.5
Ogawa (1977)	0.33	0.88	7.9	11.89	11.29	10.4
ElGawady <i>et al.</i> (2011)	0.33	0.82	10.02	16.11	15.18	13.29
ElGawady <i>et al.</i> (2011)	0.33	0.84	9.3	14.64	13.84	12.32
ElGawady <i>et al.</i> (2011)	0.33	0.79	11.5	19.25	18.04	15.22
Ogawa (1977)	0.25	0.94	5.48	7.35	7.07	6.86
Fielder <i>et al.</i> (1997)	0.25	0.93	5.91	8.13	7.8	7.5
Pena <i>et al.</i> (2007)	0.25	0.94	5.48	7.35	7.07	6.86
Fielder <i>et al.</i> (1997)	0.25	0.95	5.05	6.58	6.35	6.22
Lipscombe & Pellegrino (1993)	0.25	0.92	6.12	8.53	8.17	7.82
Muto <i>et al.</i> (1960)	0.23	0.96	4.63	5.83	5.65	5.57
ElGawady <i>et al.</i> (2011)	0.2	0.94	5.26	6.96	6.71	6.54
ElGawady <i>et al.</i> (2011)	0.2	0.95	5.05	6.58	6.35	6.22
ElGawady <i>et al.</i> (2011)	0.2	0.85	9.06	14.17	13.4	12
Pena <i>et al.</i> (2007)	0.17	0.97	4.01	4.74	4.63	4.61
Pena <i>et al.</i> (2007)	0.12	0.98	3.81	4.39	4.3	4.29

In order to increase the energy dissipation on the ‘bare’ rocking configuration, Leitner & Hao (2016) provided mild steel and superelastic alloy dissipators either inside or outside of the rocking pier. The numerical results showed that the addition of dissipating devices can reduce the rocking amplitude and improve the hysteretic behaviour of the system. Additionally, Cheng & Chen (2013) included Frictional Hinge Dampers (FHD) in the rocking system shown in Fig. 2-17, and the experimental results showed that the FHD significantly improves the rocking response with ζ reaching values up to 30%. However, if the supplemental device fails, the residual displacements are usually larger than those of the ‘bare’ configuration, and this is due to the energy stored in the system.

This is a probable scenario in bridges because the weight of the superstructure is relatively large. The reduced seismic performance of rocking columns with geometric imperfections at the rocking surfaces was confirmed numerically by Mathey *et al.* (2016) who compared their rocking response with equivalent integral columns and showed that the former is more prone to rocking and to overturning.

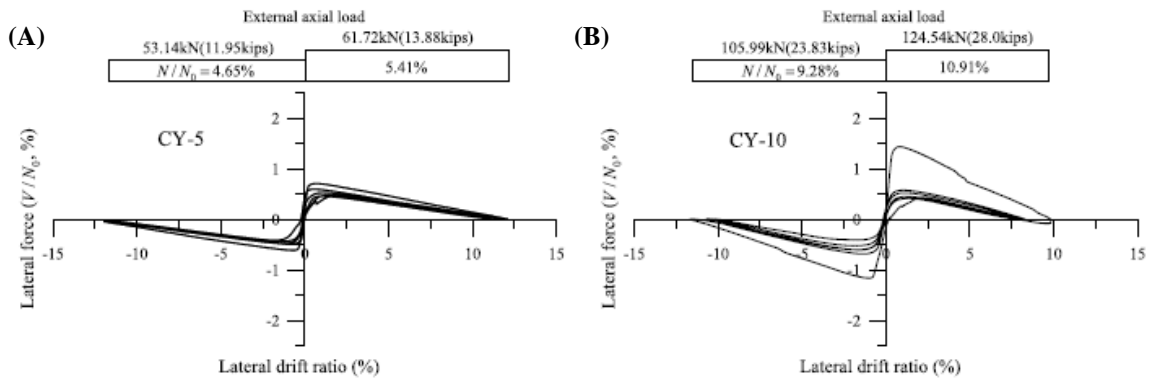


Fig. 2-18 Force-drift ($F-d$) behaviour of a free-standing rocking pier. Results obtained for a quasi-static cyclic test with (A) lower and (B) higher external axial loads. (figure taken from Roh & Reinhorn 2010b)

2.4.2 Enhanced Rocking Pier Configurations

Different proposals that combine different supplemental devices have been presented in recent years to tackle the three inherent disadvantages of ‘bare’ rocking piers as explained in §2.4.1.1, §2.4.1.2, §2.4.1.3. So far, the ones that received more interest in a numerical and experimental context are those classified in the following three categories;

- The one-segment concrete pier with FSHB.
- The segmental concrete pier with Hybrid Sliding-Rocking Behaviour (HSRB) supplemented with self-centring.
- The segmental concrete pier wrapped with Fibre-Reinforced Polymer (FRP) tubes supplemented with self-centring.

The one-segment monolithic pier with FSHB was originally proposed for precast concrete buildings (Stanton *et al.* 1997), and subsequently it was adopted for steel frames (i.a., Karavasilis *et al.* 2011). Positive stiffness is usually utilised in these systems and it goes against the fundamental advantage of rocking isolation compared to the ‘traditional’ construction methods (see Table 2-1). Recentring is achieved primarily by using unbonded tendons that are anchored to the foundation and the cap-beam with a moment-rotation ($M-\theta$) behaviour shown in Fig. 2-19A, while the dissipation capacity is obtained via internal non-prestressed bars or external dissipators according to Fig. 2-19B, leading to a particular hysteresis behaviour with ‘flag-shape’ as shown in Fig. 2-19C. The lack of bond between the tendon and the duct is intentional in all cases and it aims

at distributing the axial load uniformly along the full length of the tendon, which should remain elastic for large displacements. Rocking movement prior to fracture of the dissipative devices is (in principle) not allowed, while after the potential fracture of the tendon rocking movement is used in its ‘pure’ form as the last factor of safety. Compared to the ‘traditional’ solution in which extensive damage of the pier is expected at the plastic hinge region, in a FSHB solution the inelastic demand is accommodated at the pier-foundation interface through the yielding of the dissipative devices, and the opening and closing of an existing gap. Simple modelling procedures of FSHB connections have been presented by Palermo *et al.* (2007) and Vassiliou *et al.* (2016).

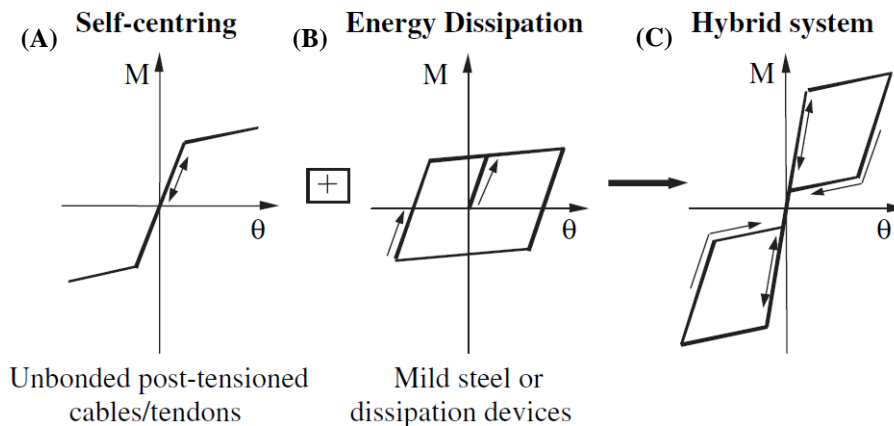


Fig. 2-19 Rocking pier with FSHB, including the moment-rotation ($M-\theta$) behaviour that is offered by (A) the unbonded tendon and (B) the dissipating devices, as well as (C) the resulting hysteresis behaviour. (figure taken from Palermo & Pampanin 2008)

Inspired by the endurance of ancient ‘multi-drum’ (segmental) columns having withstood numerous strong earthquakes with limited or no damage in ancient structures (i.a., Konstantinidis & Makris 2005), Ou *et al.* (2007) proposed piers with HSRB as an alternative of the one-segment configuration in modern structures, as shown in Fig. 2-20. Analytical studies on the free-standing column with HSRB proved that the multiple rocking surfaces provide higher energy dissipation (Kounadis & Papadopoulos 2016) and lower vulnerability against overturning (Ther & Kollár 2018) compared to the one-segment column; the former was confirmed numerically by Wiebe & Christopoulos (2009). However, residual displacements in different directions are still possible. The response can be improved by using unbonded tendons that pass through the segments providing recentring capacity. The concept of positive stiffness is also adopted in this case, but with smaller values compared to the corresponding one-segment pier with a tendon, and this is because of the multiple openings and closures of the different rocking surfaces. Alternatives for improving the behaviour of the concrete segments were made by ElGawady *et al.* (2010) and Li *et al.* (2017) by wrapping the segments with FRPs and steel jackets, respectively, in order to confine the concrete segment. Further enhancements for energy dissipation and interface behaviour were made by ElGawady & Sha’Ian (2011) using steel angles and rubber pads, respectively.

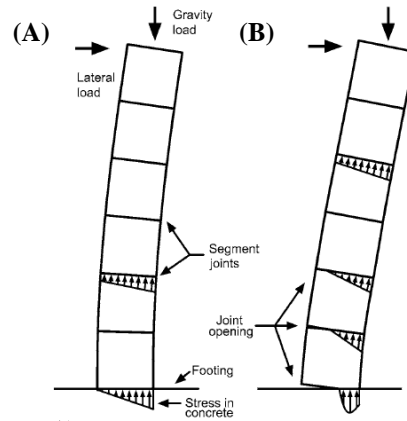
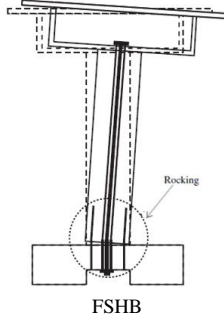
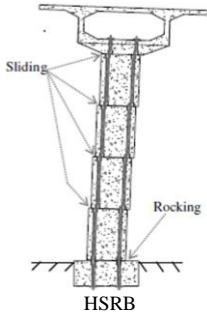
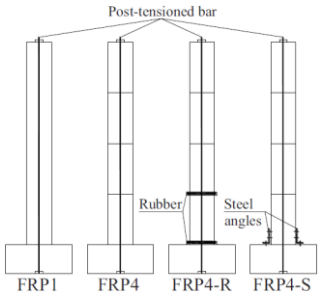


Fig. 2-20 Rocking pier with HSRB, including (A) the pre-decompression and (B) post-decompression stages. (figure taken from *Ou et al. 2007*)

Table 2-6 summarises the principles and the main findings of these three enhanced rocking pier configurations as presented in several numerical and experimental studies. In all these three configurations, post-uplift lateral stiffness is positive and recentring capacity is achieved passing unbonded tendons through the centre of the rocking pier.

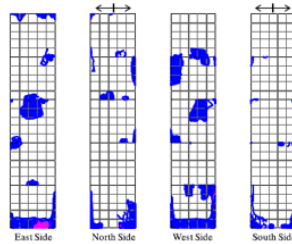
Table 2-6 Rocking piers with enhanced configurations. Principles and main findings.

	Mander & Cheng (1997)	Ou <i>et al.</i> (2007)	
	Palermo <i>et al.</i> (2004)	Sideris (2012)	ElGawady <i>et al.</i> (2010)
Study where it was used	Palermo <i>et al.</i> (2005)	Sideris <i>et al.</i> (2014a)	ElGawady & Sha'Ian (2011)
	Palermo <i>et al.</i> (2007)	Sideris <i>et al.</i> (2014b)	ElGawady & Dawood (2012)
	Marriott <i>et al.</i> (2009)	Sideris <i>et al.</i> (2015)	
	Kam <i>et al.</i> (2010)	Sideris (2015)	
	Andisheh <i>et al.</i> (2018)	Salehi <i>et al.</i> (2017)	
Schematic			
Interface Material	Concrete-to-concrete	Concrete-to-concrete	Concrete-to-concrete Rubber-to-concrete
Main Findings	- Rocking piers with FSHB utilising internal mild steels or external viscous dissipators lead to similar maximum drift compared to the monolithic configuration (i.e., 15 ~ 20%, and even more dependent on the number	- Rocking piers with HSRB reach drift values up to 15% with ξ being around 17% at the highest drift value. - Small permanent displacements occur due to sliding (easily reversible).	- Maximum drift around the same level for all the different configurations (i.e., 15-20%), despite the higher elongation of the tendon that was observed in the segmental members. However, ξ does not exceed 8% in any case

and the characteristics of the devices).

- Despite the identical drifts, no residual drifts occur for the piers with FSHB.
- Damage is concentrated at the dissipating device. Mild steel across the joint drastically increases the concrete damage compared to the external dissipators which show minimal damage at the surrounding concrete; furthermore, inspection of devices located externally is easier, considering the crucial effect of corrosion on the behaviour of the dissipating device.

- Rocking motion occurs primarily at the bottom joint, while in the rest of the joints sliding prevails. Significant damage can be observed in the bottom joint in the form of concrete spalling and crushing, while negligible damage can be detected in the rest of the joints in the form of spalling of the concrete cover:



with the highest values being met for FRP4-S.

- Higher residual displacements of the segmental configurations compared to FRP1.
- Damage is concentrated at the rocking surfaces in FRP1 and FRP4 with simultaneous fracture of the FRP.
- The rubbers increase the displacement demand in FRP4-R compared to FRP4. However, the damage in the rocking surface and the FRP are reduced.
- Damage is concentrated in the steel angles in FRP4-S keeping the rocking surface and the FRP tube integral. However, residual displacements occur.

2.5 Studies Specific to Bridges with Rocking Pier Isolation

Makris & Vassiliou (2013) studied analytically the planar seismic response of bridges with free-standing rocking piers of equal height using real ground motions. This was done by integrating step-by-step Eq. (2-16), and by expressing the attenuation of movement through impacts at the rocking interfaces using Eq. (2-19). The results showed that the heavy rigid superstructure experiences significant horizontal and vertical displacements reaching peak values up to 500 and 80 mm, respectively. However, although the assumption of rigidity can be accepted for deriving some primary outcomes on the response of bridges with rocking piers, this work neglects the effect of the abutments and, therefore, it reduces the problem to the extensively studied symmetric frame with rocking columns (§2.3.2).

From the numerical and experimental points of view, the majority of works on bridges with rocking pier isolation focus on a single pier or a frame system and take into account some of the assumptions that have been found essential for the analytical derivations (e.g., sliding effects at the rocking interfaces). In this regard, previous numerical and experimental works on (entire) bridges with rocking piers can be classified into three basic categories;

- When a monolithic connection is assumed between the rocking pier and the superstructure, single DoF models with a large mass at the top are usually adopted in numerical (Palermo *et al.* 2004, Titirla *et al.* 2017) and experimental studies (Sakai & Mahin 2004, Chen *et al.* 2006, Trono *et al.* 2015).

- When a joint is assumed between the rocking pier and the superstructure, models with a compressive force at the top of the piers are developed by utilising numerical (Ou *et al.* 2007, ElGawady & Dawood 2012, Sideris 2015, Leitner & Hao 2016, Wang *et al.* 2018) or experimental tools (Palermo *et al.* 2005, Palermo *et al.* 2007, Roh & Reinhorn 2008, Marriott *et al.* 2009, ElGawady *et al.* 2010, Sideris *et al.* 2014b). In these models, the compressive force represents the (beneficial) effect of the superstructure weight (Makris & Vassiliou 2014b).
- Similarly, models of rocking piers capped with a massive beam have been developed numerically (Roh & Reinhorn 2009, Agalianos *et al.* 2017, Psychari *et al.* 2017) or experimentally (Cheng 2007, Cheng 2008, ElGawady & Sha'Ian 2011, Cheng & Chen 2013, Du *et al.* 2019).

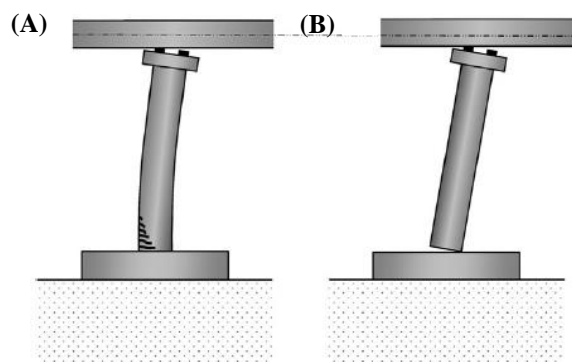


Fig. 2-21 Schematic of a bridge with (A) conventional seismic isolation through elastomeric bearings and (B) rocking pier isolation. (*figure taken from Agalianos et al.* 2017)

In the same context, Agalianos *et al.* (2017) compared numerically the seismic performance of a 5-span bridge with equal pier heights employing two different isolation techniques: (i) conventional seismic isolation and (ii) rocking pier isolation. Fig. 2-21A, B show these two alternatives where the piers are disconnected from the deck through simple bearings, thus rendering system (ii) as a ‘hybrid’ rocking solution. The performance of the systems was studied by considering pairs of ten strong ground motions that significantly exceed the design spectrum by two to seven times, while pier failure (i.e., overturning for the rocking case) was the only failure criterion considered in the comparison. The results revealed that the bridge with rocking pier isolation avoided collapse in more cases than the conventionally isolated system. Moreover, the maximum Bending Moment (BM) at the pier foundation for the rocking system was much lower than in the conventionally isolated structure, hence a smaller foundation could have been used; in soft soils, the reduction of the design moment at the base of the piers could result in avoiding costly pile foundations. Another positive aspect observed in the rocking system was that the residual displacements were negligible and, therefore, the structure is resilient and indeed ready-to-use even after the strongest earthquakes. However, this can be attributed to the special contact elements used in that work to prevent sliding ($\mu_s = 10$ was assumed). Furthermore, it was observed that the uplift of the rocking piers causes an increase in the BMs at the end spans of the superstructure compared to the conventionally isolated system, hence increase in the flexural capacity of the conventionally

designed bridge deck may be required. This was not observed in the intermediate spans, though, considering that the examined structure is fully symmetric, thus the piers are forced to uplift the same way (see §2.3.2.1).

2.6 Identified Gaps in the State-of-the-Art

The analytical models that can approach the behaviour of bridges with rocking piers are presented in §2.3.2, and they treat the rocking system as a frame without end supports (see Fig. 2-13 for the symmetric system, and Fig. 2-14 for the asymmetric one). In some studies (Makris & Vassiliou 2013, see §2.5), the frame model without end supports was considered as able to capture the behaviour of an actual bridge. However, it has been found that the abutment-backfill system affects significantly the response (i.a., Aviram *et al.* 2008, Wilson & Elgamal 2010) leading in some cases to a different collapse hierarchy when significant pier drifts are developed, potentially rendering the abutments and/or the backfill as the most vulnerable component of the bridge system (Kappos *et al.* 2007); this can also be the case in rocking structures, as shown in Fig. 2-18. This research gap is addressed in Chapters 3 (for symmetric bridges) and 4 (for asymmetric bridges).

Recent proposals on rocking pier configurations try to mitigate the inherent disadvantages of ‘bare’ rocking technique as stated in §2.4.1.1, §2.4.1.2 and §2.4.1.3, and this is achieved through supplemental devices/elements. However, the inherent advantages that are offered by rocking motion in free-standing piers along with the concept of Accelerated Bridge Construction (ABC) and, therefore, prefabrication have not been exploited so far from the pier shape point of view. These are briefly: (i) the rocking piers sustain negligible flexural and shear strains during the free rocking motion, considering that rigid body motion is predominant (i.a., Agalianos *et al.* 2017), and (ii) no firm connection is required at either end of the piers. Therefore, earlier design considerations for the rocking piers than those presented in §2.4.2 are worth revisiting with a view to enhancing the seismic performance of the free-standing ‘traditional’ (or rectangular in elevation and square in cross-section) rocking piers. This is addressed in Chapter 5.

The vast majority of numerical and experimental studies presented in §2.5 examine rocking pier isolation in bridges based on some core assumptions that are: (i) the effect of the abutments and the dynamic interaction between deck and abutments are ignored (Aviram *et al.* 2008) and, therefore, the problem is reduced to a frame with rocking columns, (ii) the superstructure is usually modelled as a high compressive force that benefits the rocking behaviour of the system (Makris & Vassiliou 2014b), but the overall behaviour of the superstructure and the resulting effects on the substructure are neglected, and (iii) the asymmetry in the height of the piers is ignored and, therefore, all the potential detrimental effects of rocking motion on the superstructure cannot be revealed (§2.3.2.2). Additionally, a limited number of studies (i.a., Agalianos *et al.* 2017) compared the seismic performance of bridges with conventional seismic and rocking pier isolation, without establishing the superiority of each approach. These research topics are addressed in Chapter 6 using rigorous FE models.

Chapter 3

Analytical Modelling of Symmetric Bridges with Rocking Piers

3.1 Introduction

Chapter 3 expands the initial studies on bridges with rocking piers modelled as frames (Makris & Vassiliou 2013) to represent bridge configurations with realistic end support conditions. This is done by means of an additional structural member that is integrated at either end of the superstructure to represent the most common form of deck support, the seat-type abutment and the backfill behind it. Seat-type abutments and embankments are often considered as earth-retaining systems designed to provide only traffic access to and from the bridge. However, it has been found that the abutment characteristics and the stiffness of the backfill/embankment can influence significantly the global response of bridges under moderate to strong ground motions (Aviram *et al.* 2008), and this is due to the reduction of displacement demand in the piers (Wilson & Elgamal 2010); this is the case for both integral and seat-type abutments, in the latter when the end gap closes. More importantly, in a performance assessment context, collapse of the frames with rocking columns is triggered only due to overturning of the vertical members. However, this is considered as an extreme scenario when realistic bridge configurations are examined, even in the analytical context adopted therein. The proposed analytical model includes the following *modifications and advancements* compared to the frame mechanism without end supports proposed by Makris & Vassiliou (2013);

- Extension of the current configuration for symmetric bridges with rocking piers to a more complete structural system accounting for differences in the span lengths, the end joint between the superstructure and the abutment, the effect of the supports at the abutment seats aiming to allow the free rocking motion of the system, and the effect of the abutment and the backfill at each end of the superstructure.
- Derivation of EoM during longitudinal rocking accounting for the stages before and after the closure of the end gap, when the longitudinal stiffness of the structure is increased due to the presence of the abutment-backfill system.
- Integration of energy dissipation provided by the impact between the superstructure and the abutment backwall (i.e., pounding).

- Derivation of a new expression for the CoR to describe the attenuation of rocking motion when an impact at the rocking interfaces occurs, considering that the abutment seats carry vertically part of the deck weight as well as the influence of each span length.
- Adoption of a failure criterion to describe failure of the abutment-backfill system in a performance assessment context.

In this respect, the proposed bridge configuration is described in §3.2 followed by basic kinematics (§3.2.1), and by the analytical expression to determine the initiation of the rocking motion (§3.2.2). The EoM accounting explicitly for the effect of the abutment-backfill system is derived in §3.2.3 based on an energy approach. The energy dissipation associated with pounding of the superstructure on the abutment backwall is accounted for through a CoR in §3.2.4. The development of the CoR to describe attenuation of rocking motion when an impact at the rocking interfaces takes place is explained in §3.2.5 following an impulse formulation. The analysis framework (§3.3) adopted herein includes different rocking configurations (§3.3.1) and different types of ground motions (§3.3.2) to establish in more detail the effect of the abutment-backfill system in free-standing frames in a performance assessment context (§3.3.3). Parametric analyses are conducted in §3.3.4 to better understand the effect of the parameters in the newly developed formulation on the rocking response of bridges with abutments. The seismic performance of bridges modelled with the proposed analytical approach is compared with that reported by Makris & Vassiliou (2013) in §3.3.5.

3.2 Analytical Model of the Rocking Response

This section examines the longitudinal rocking response of bridge structures accounting for the effect of the abutment and the backfill at each end of the deck. Fig. 3-1 shows a symmetric bridge with rocking piers at the at-rest position, subjected to a horizontal ground acceleration history \ddot{u}_g . The generic bridge has N piers and a total length $L_{tot} = 2L_1 + [N - 1] \cdot L_2$, where L_1 and L_2 denote the length of the end and the intermediate spans, respectively. The superstructure consists of a continuous box girder section with depth $2h$ and cross-sectional area A_{deck} , while the piers have a rectangular configuration with height of $2H$ and square cross-sections with a dimension of $2B$. The system is free to move longitudinally until the deck closes the end joint gap (u_{jo}) and impacts on the abutment backwall, which has a height h_{bw} . Longitudinally sliding support conditions are assumed at each abutment seat (points E and E', as shown in Fig. 3-1), and this can be materialised through low-friction ($\mu \approx 0$) sliding concave steel bearings. These support conditions at the abutment seats provide negligible constraint to the movement of the deck in the longitudinal direction, while they are assumed to follow the up-and-down (cyclic vertical) motion of the superstructure at the position of the rocking piers. The following criteria are adopted to formulate the rocking motion of the symmetric bridge structure;

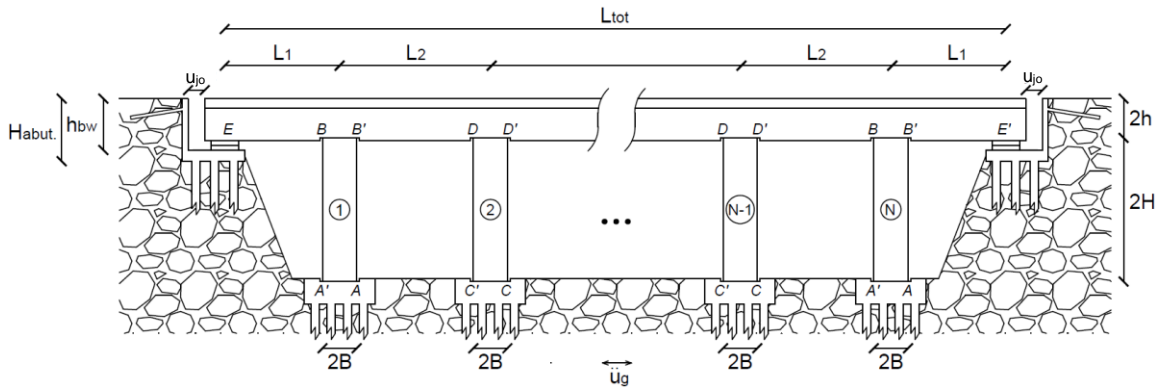


Fig. 3-1 Schematic of a symmetric bridge supported on N rectangular-in-elevation free-standing rocking piers, and on frictionless sliding bearings at the abutment seats. The bridge is at the at-rest position.

- The rocking motion is constrained within the plane of the bridge, thus ignoring three-dimensional rocking response (Chatzis & Smyth 2012, Vassiliou 2017). It is noted that the rocking response in the transverse direction is beyond the scope of the present chapter.
- The deformability of all structural members is ignored without a significant loss of accuracy (as shown i.a. by Agalianos *et al.* 2017), but with gains in simplicity and computational efficiency. In this regard, this assumption leads to identical vertical movement of the superstructure at the end supports and at the rocking piers that is feasible due to the sliding bearings with uplift capacity that were adopted at the abutment seats. However, this is not expected to be a realistic assumption when the deformability of the superstructure is taken into account, especially in bridges with long end spans as those adopted in the thesis (see §3.3.1, §4.3.1, §5.3.1). To check whether consideration of the effect of the end spans working as cantilevers would affect the analytically obtained findings of the thesis, a comparison with regard to the seismic rocking response of a bridge structure was conducted. Specifically, the analytical model in Chapter 4 (i.e., equivalent to that presented in this chapter, thus ignoring the vertical deflection at the end spans) was compared with the rigorous FE models in Chapter 6 that account for the deformability of all the structural members and, therefore, the end spans. The results revealed that the analytical model presents deck uplifts at the abutment seats that are not present in the numerical model. However, it was observed that the analytical model is fairly accurate in predicting response parameters from the statistical point of view compared to the numerical model; this is also the case in previous studies (i.e., Bachmann *et al.* 2018). More importantly, the seismic performance of the bridge structure with respect to the prevailing failure mode (i.e., abutment-backfill failure mode, see relevant discussion in §3.3.3, §4.3.3 and §6.2.2.2) remains unaffected when analysed analytically and numerically. Therefore, the effect of the end spans working as cantilevers that is ignored in the analytical models presented in the thesis is not expected to affect considerably the analytical findings of the thesis (see also relevant discussion in §7.2.1).

- The piers are designed to rock freely on the foundation (pivots A'-A- and C'-C) and the deck interfaces (pivots B-B' and D-D'), without sliding at the initiation of movement and throughout the whole motion in order for the slide-rock movement to be prevented (as described for free-standing rocking columns by Eqs. (2-9) and (2-11), respectively). From a construction perspective, this can be achieved by means of grooves provided on the top surface of the foundation and on the soffit of the deck, although a small level of sliding could occur in reality, especially for slender blocks (see §2.3.1.1).

3.2.1 Kinematics

The kinematics of the bridge with rocking piers is illustrated in Fig. 3-2, which shows the structure experiencing longitudinal and vertical motions induced by the rocking motion of the free-standing piers around the corresponding CRs at their bases (A and C) just before contacting the abutment backwall. As soon as contact is activated, the longitudinal stiffness of the system is increased due to the presence of the abutment-backfill system which is represented by spring (k) and dashpot (c) in parallel elements (Kelvin-Voigt model). Due to the symmetry of the system, all piers undergo identical movement and, therefore, the superstructure experiences a 'purely' translational motion (longitudinal, along-X, and vertical, along-Z) that is driven by the pivot points located at the top of the piers (B and D), without relative rotations about the transverse (Y) axis (see §4.2.1). Consequently, the dynamic motion of this bridge configuration can be captured with a single DoF, selected to be the relative rotation of each pier with respect to the at-rest position (θ). When the bridge structure undergoes rocking motion without toppling, the longitudinal u (along-X) and the vertical v (along-Z) relative displacements of the CG of the piers and the deck are expressed in terms of the independent variable θ according to Eqs. (3-1) and (3-2), respectively (note that u and v are relative displacements of the CG of the piers and the deck with respect to the at-rest position of the bridge)

$$\begin{aligned} u_{pier}^{CG} &= \text{sgn}(\theta) R \left[\sin a - \sin(a - |\theta|) \right] \quad \text{and} \\ v_{pier}^{CG} &= R \left[\cos(a - |\theta|) - \cos a \right], \end{aligned} \quad (3-1)$$

$$\begin{aligned} u_{deck}^{CG} &= \text{sgn}(\theta) 2R \left[\sin a - \sin(a - |\theta|) \right] \quad \text{and} \\ v_{deck}^{CG} &= 2R \left[\cos(a - |\theta|) - \cos a \right], \end{aligned} \quad (3-2)$$

where $\text{sgn}(\theta)$ is the sign function of θ , $R = \sqrt{H^2 + B^2}$ is the semi-diagonal length of the pier and $\alpha = \tan^{-1}(B/H)$ describes the slenderness of this member. The corresponding linear velocities (\dot{u} and \dot{v}) occur as the first time-derivatives of Eqs. (3-1) and (3-2), respectively, and are given by the following expressions

$$\delta u_i^{CG} = \frac{\partial u_i^{CG}}{\partial \theta} \delta \theta \quad \text{and} \quad \delta v_i^{CG} = \frac{\partial v_i^{CG}}{\partial \theta} \delta \theta, \quad (3-6)$$

where i refers to the pier and deck members, respectively. Introducing Eqs. (3-1) and (3-2) into Eq. (3-6), and subsequently into Eq. (3-5) gives the minimum ground acceleration that is required to initiate the rocking motion

$$Nm_{pier} \ddot{u}_{g,\min} \left[R \cos(\alpha - |\theta|) \delta \theta \right] + m_{deck} \ddot{u}_{g,\min} \left[2R \cos(\alpha - |\theta|) \delta \theta \right] = \mp Nm_{pier} g \left[R \sin(\alpha - |\theta|) \delta \theta \right] \mp m_{deck} g \left[2R \sin(\alpha - |\theta|) \delta \theta \right]. \quad (3-7)$$

Eq. (3-7) can be simplified by considering that the rocking motion has just started at this instant ($\theta = 0$) and by cancelling out the admissible rotation $\delta \theta$, which yields the minimum acceleration needed to uplift the bridge structure

$$\ddot{u}_{g,\min} = \mp \lambda g \tan \alpha, \quad (3-8)$$

where $\lambda = 1$ for a symmetric bridge. The double sign formulation (\mp) in Eqs. (3-7) and (3-8) denotes that the bridge will initially rock with a positive (clockwise) rotation only if the horizontal ground acceleration has a negative value (i.e., the ground is accelerating to the left in Fig. 3-1), and vice-versa. According to Eq. (3-8), the value of the ground acceleration required to initiate rocking motion of the bridge structure depends only on the slenderness of the piers (α), while it is independent of the direction of the movement, the mass of the deck (m_{deck}) and the properties of the abutment-backfill system. It is noted that this result is the same as that in the corresponding frame with rocking columns, wherein the effect of the abutments and the backfill is ignored (Eq. (2-1), similar to Makris & Vassiliou 2013). This is because their influence on the rocking motion starts only after rocking is initiated, that is when the joint gap with a non-zero value (u_{jo}) is closed and the deck impacts longitudinally on one abutment backwall, or when the deck returns to its original position and it impacts on the abutment seats.

3.2.3 Equation of Motion during Rocking

Considering that the ground motion is strong enough to initiate rocking of the bridge in Fig. 3-1 (i.e., $\max(|\ddot{u}_g|) > |\ddot{u}_{g,\min}|$), its response can be described by the energy balance using Lagrange's equation

$$\frac{d}{dt} \left(\frac{\partial T}{\partial \dot{\theta}} \right) - \frac{\partial T}{\partial \theta} + \frac{\partial V}{\partial \theta} = Q, \quad (3-9)$$

where T is the kinetic energy of the rocking system, V is the potential energy produced by the conservative forces and Q expresses the effect of the non-conservative forces. The generalised coordinate that describes the rocking motion is the pier rotation θ . The kinetic energy of the system with respect to the corresponding CG of the members can be expressed as

$$T = N \frac{1}{2} m_{pier} \left[\dot{u}_{pier}^{CG^2} + \dot{v}_{pier}^{CG^2} \right] + N \frac{1}{2} I_{pier}^{CG} \dot{\theta}^2 + \frac{1}{2} m_{deck} \left[\dot{u}_{deck}^{CG^2} + \dot{v}_{deck}^{CG^2} \right], \quad (3-10)$$

and by substituting Eqs. (3-3) and (3-4) into Eq. (3-10), the expression of the kinetic energy can be simplified to

$$T = N \frac{1}{2} m_{pier} \left[R^2 \dot{\theta}^2 \right] + N \frac{1}{2} I_{pier}^{CG} \dot{\theta}^2 + \frac{1}{2} m_{deck} \left[4R^2 \dot{\theta}^2 \right]. \quad (3-11)$$

Eq. (3-11) is rearranged to describe the total kinetic energy of the system with respect to the corresponding CR (A and C for positive - clockwise rotation or A' and C' for negative – counter-clockwise rotation)

$$T = \left[\frac{N}{2} I_{pier}^{Pivot} + 2m_{deck} R^2 \right] \dot{\theta}^2, \quad (3-12)$$

where $I_{pier}^{Pivot} = 4m_{pier} \cdot R^2/3$ is the mass moment of inertia of the rocking pier with respect to the pertinent pivot point. The total potential energy in the bridge (V) is introduced by the gravitational effects (V_{in}) and by the elastic spring forces of the abutments (V_{as}), $V = V_{in} + V_{as}$. The term V_{in} expresses the total weight of the system that tends to return the bridge with rocking piers to its equilibrium position, and it is given by

$$V_{in} = g \left[Nm_{pier} v_{pier}^{CG} + m_{deck} v_{deck}^{CG} \right], \quad (3-13)$$

where v_{pier}^{CG} and v_{deck}^{CG} are given by Eqs. (3-1) and (3-2), respectively. The term V_{as} expresses the longitudinal constraint of the abutment-backfill system to the free rocking motion of the structure, and it is active only when the deck is in contact with the abutments.

$$V_{as} = \begin{cases} 0 \\ \frac{1}{2} k \left[u_{deck}^{CG} - \text{sgn}(\theta) u_{jo} \right]^2 \end{cases} \quad \text{if} \quad \begin{cases} |u_{deck}^{CG}| < u_{jo} \\ |u_{deck}^{CG}| \geq u_{jo} \end{cases}. \quad (3-14)$$

Introducing Eq. (3-2) in Eq. (3-14) yields the following expression for the potential energy component, which expresses the effect of the elastic spring forces at the abutments.

$$V_{as} = \begin{cases} 0 & |u_{deck}^{CG}| < u_{jo} \\ 2kR^2 \begin{bmatrix} \sin^2 \alpha - 2 \sin \alpha \sin(\alpha - |\theta|) \\ + \sin^2(\alpha - |\theta|) - \sin \alpha \frac{u_{jo}}{R} \\ + \sin(\alpha - |\theta|) \frac{u_{jo}}{R} + \frac{u_{jo}^2}{4R^2} \end{bmatrix} & \text{if} \\ \end{cases} \quad \begin{cases} |u_{deck}^{CG}| < u_{jo} \\ |u_{deck}^{CG}| \geq u_{jo} \end{cases} \quad (3-15)$$

The total effect of the conservative forces on the rocking system is introduced by accounting for the contribution of both the inertia forces (Eq. (3-13)) and the elastic spring forces of the abutments (Eq. (3-15)).

$$V = \begin{cases} gR [Nm_{pier} + 2m_{deck}] (\cos(\alpha - |\theta|) - \cos a) & |u_{deck}^{CG}| < u_{jo} \\ gR [Nm_{pier} + 2m_{deck}] (\cos(\alpha - |\theta|) - \cos a) \\ + 2kR^2 \begin{bmatrix} \sin^2 a - 2 \sin a \sin(\alpha - |\theta|) + \sin^2(\alpha - |\theta|) \\ - \sin a \frac{u_{jo}}{R} + \sin(\alpha - |\theta|) \frac{u_{jo}}{R} + \frac{u_{jo}^2}{4R^2} \end{bmatrix} & \text{if} \\ \end{cases} \quad \begin{cases} |u_{deck}^{CG}| < u_{jo} \\ |u_{deck}^{CG}| \geq u_{jo} \end{cases} \quad (3-16)$$

The variation of the virtual work δW_{nc} describes the effect of the generalised non-conservative forces required for the Lagrangian Eq. (3-9)

$$\delta W_{nc} = Q\delta\theta \Rightarrow \delta W_{in} + \delta W_{ad} = [Q_{in} + Q_{ad}] \delta\theta, \quad (3-17)$$

where $\delta W_{in} = -\ddot{u}_g \cdot [N \cdot m_{pier} \cdot u_{pier}^{CG} + m_{deck} \cdot u_{deck}^{CG}]$ represents the external work introduced in the system by the ground acceleration, $\delta W_{ad} = -c \cdot \dot{u}_{deck}^{CG} \cdot [u_{deck}^{CG} - \text{sgn}(\theta) \cdot u_{jo}]$ is the energy dissipated by the interaction between the deck and the backfill through the dashpot elements used to model it, u_{pier}^{CG} and u_{deck}^{CG} are given by Eqs. (3-1) and (3-2), respectively, and \dot{u}_{deck}^{CG} is given by Eq. (3-4). The corresponding generalised forces $Q_{in} = \partial W_{in} / \partial \theta$ and $Q_{ad} = \partial W_{ad} / \partial \theta$ are given by

$$Q_{in} = -\ddot{u}_g R [Nm_{pier} + 2m_{deck}] \cos(\alpha - |\theta|), \quad (3-18)$$

$$Q_{ad} = -4cR^2 \cos^2(\alpha - |\theta|) \dot{\theta}. \quad (3-19)$$

The total effect of the generalised non-conservative forces (Q) is given by combining Eqs. (3-18) and (3-19). Introducing Eqs. (3-12), (3-16), (3-18) and (3-19) into Eq. (3-9) gives the EoM for the rocking motion of symmetric bridges with rocking piers

$$\ddot{\theta} = \overbrace{-p^2 \frac{1+2\gamma}{1+3\gamma} \left[\text{sgn}(\theta) \sin(a-|\theta|) + \frac{\ddot{u}_g}{g} \cos(a-|\theta|) \right]}^{\text{frame system}} \underbrace{-p^2 q \begin{bmatrix} k \text{sgn}(\theta) \left(\sin \alpha - \sin(a-|\theta|) - \frac{u_{jo}}{2R} \right) \\ \cos(a-|\theta|) + c(\cos^2(a-|\theta|)) \dot{\theta} \end{bmatrix}}_{\text{abutment-backfill contribution}}, \quad (3-20)$$

where $p = \sqrt{3g/4R}$ describes the dynamic characteristics of the pier, as explained in §2.3.1.1, and $\gamma = m_{deck}/N \cdot m_{pier}$ expresses the influence of the mass of the superstructure on the rocking motion (§2.3.2.1). However, $q = 4R/g \cdot [N \cdot m_{pier} + 3m_{deck}]$ is a new parameter resulting from the present study related to the longitudinal restraint of the abutment-backfill system, and it depends on the properties of the bridge. Eq. (3-20) shows that the symmetric bridge with rocking piers cannot be related from the dynamics point of view with the corresponding frame (Eq. (2-16)) as was done in the past for relevant frames and columns (§2.3.2.1, §2.3.2.2).

Two distinct parts of Eq. (3-20) contribute to the overall rocking response; the first one ('*frame system*') describes the motion before the deck contacts the abutments in the longitudinal direction ($|u_{deck}^{CG}| < u_{jo}$), and it is exactly the same as the EoM of the symmetric frame with rocking columns presented in Makris & Vassiliou (2013) (Eq. (2-16)), while the second term ('*abutment-backfill contribution*') is only active when the deck contacts the abutments longitudinally ($|u_{deck}^{CG}| \geq u_{jo}$), and it describes the constraint of the rocking motion of the frame due to the presence of the abutment-backfill system. Considering two identical bridge configurations with same properties for the abutment and the backfill at each bridge end (i.e., bridges with rocking piers of same size R and slenderness α as well as with same longitudinal gaps u_{jo} , and same values for spring stiffness k and dashpot coefficient c), the longitudinal influence of the abutment-backfill system is captured fully by the parameter q ; large values of q indicate that the rocking system interacts with the abutment and the backfill to a significant extent, while for lower values the response approaches that of the frame with rocking columns addressed in previous studies, or the '*frame system*' contribution dominates the EoM and the response follows that in Makris & Vassiliou (2013). In order to illustrate the relationship between the bridge characteristics and the effect of the abutment-backfill system in the longitudinal direction, Fig. 3-3A, B plot the value of q in terms of the size (R) and number of piers (N) as well as the superstructure mass effect (γ), assuming same parameters for the abutment and the backfill at each end of the bridge. The results indicate that larger sections of the bridge members (i.e., higher values of R and γ) and longer bridge structures (i.e., larger N) minimise the influence of the abutment-backfill system. Hence, without lack of generality, the

greater the total mass of the bridge system, the lower is the contribution of the abutment-backfill system in the longitudinal rocking response, reducing the rocking motion to that of an equivalent frame. It is also observed that for low values of all the examined parameters, small variations can change significantly the participation of the abutment-backfill system in the rocking response, while the value of q becomes almost constant when R , γ or N are relatively large.

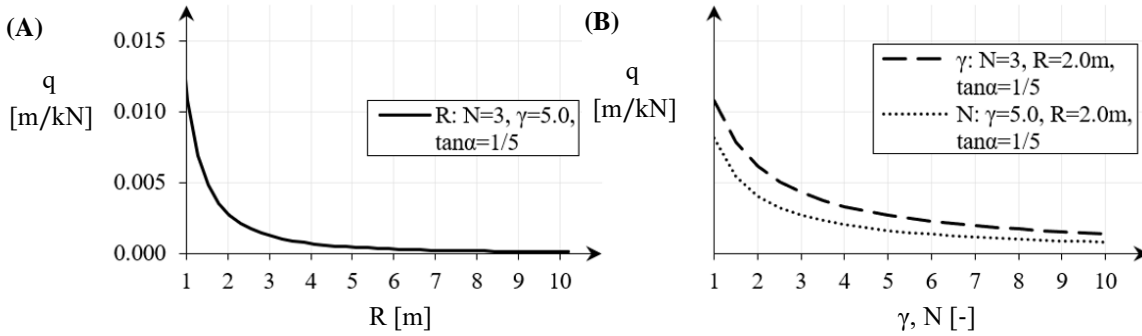


Fig. 3-3 Longitudinal influence of the abutment-backfill system (q) in symmetric bridges with rocking piers, accounting for the influence of (A) the size of the piers (R), (B) the superstructure mass effect (γ) and the number of piers (N). Results obtained when the spring stiffness (k) and the dashpot coefficient (c) are constant.

3.2.4 Impact on the Abutment Backwall

When a bridge starts rocking according to Eq. (3-8), the first part of Eq. (3-20) (i.e., ‘frame system’) describes the response-history of the angle of rotation (θ) of the piers before the deck contacts the abutments. When this contact occurs ($|u_{deck}^{CG}| = u_{jo}$), an impact on the abutment backwall follows immediately. These impacts dissipate energy instantly, and subsequently the structure either behaves as a frame system in a free rocking motion described by the first part of Eq. (3-20) (i.e., ‘frame system’) or it activates the abutment-backfill system and the response-history of angle of rotation is described by both parts of Eq. (3-20) (i.e., ‘frame system’ plus ‘abutment-backfill contribution’).

The pounding problem is modelled using several concepts (e.g., Muthukumar & DesRoches 2006, Shi & Dimitrakopoulos 2017), the key idea being to capture the attenuation of motion whenever an impact between superstructure and abutment takes place. The present adopts the ‘stereomechanical approach’ based on the conservation of linear momentum in the normal direction, as described in the study of Muthukumar & DesRoches (2006). This approach is related to a CoR e to describe pounding. Fig. 3-4A illustrates the superstructure of the rocking system just before impacting on the abutment backwall with a longitudinal velocity $\dot{u}_{deck,I}^{CG}$, while Fig. 3-4B depicts the post-pounding condition where the superstructure moves longitudinally, either towards the at-rest position or towards the abutment-backfill system, with a decreased value of the longitudinal velocity $\dot{u}_{deck,II}^{CG}$. The expression that relates the pre-pounding and the post-pounding longitudinal velocity of the superstructure is

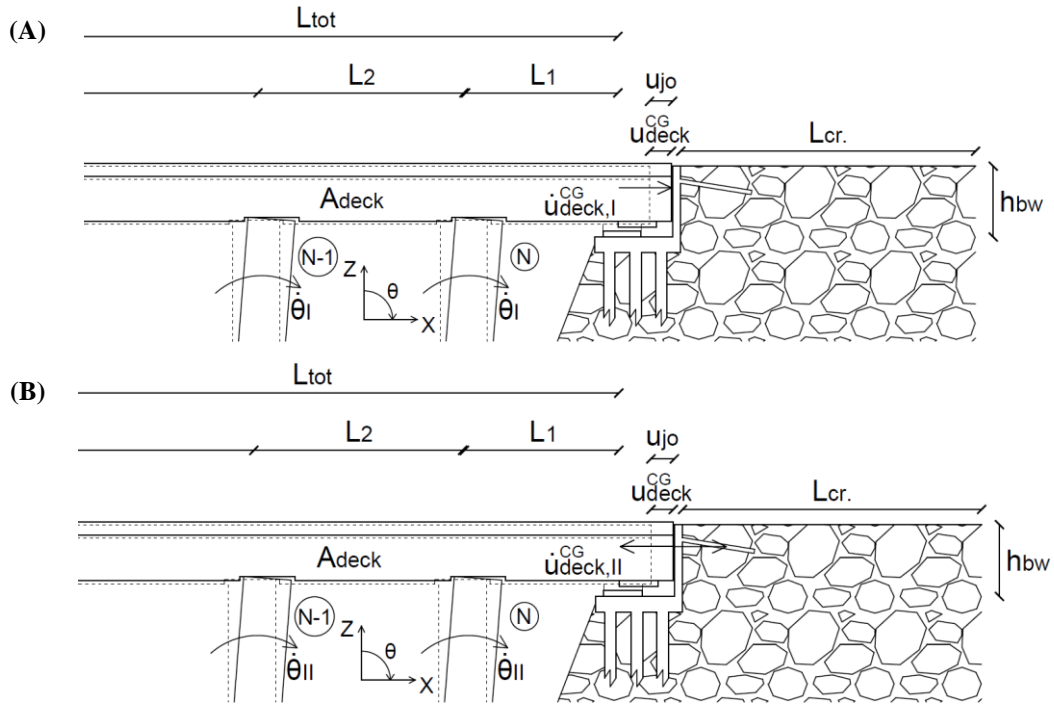


Fig. 3-4 Schematic of the pounding problem considered in the rocking motion of a symmetric bridge with rocking piers, including (A) the pre-pounding state with a longitudinal velocity of the superstructure $\dot{u}_{deck,I}^{CG}$ and (B) the post-pounding state with an associated deck velocity $\dot{u}_{deck,II}^{CG}$.

$$\dot{u}_{deck,II}^{CG} = \dot{u}_{deck,I}^{CG} - [1 + e] \frac{m_{abut.} [\dot{u}_{deck,I}^{CG}]}{m_{abut.} + m_{deck}}, \quad (3-21)$$

in which $m_{abut.} = \rho_s \cdot L_{cr.} \cdot B_{abut.} \cdot h_{bw}$ refers to the mass of the backfill related to the mass density of the soil (ρ_s), the longitudinal zone of the backfill soil that is expected to resist the impact of the superstructure on the abutment backwall ($L_{cr.}$), as well as the width ($B_{abut.}$) and the height (h_{bw}) of the abutment backwall that represent the contact surface between the deck and the abutment, finally m_{deck} is given in §3.2.1. It is noted that this definition of $m_{abut.}$ is relevant to the (usual) case of seat-type abutments with sacrificial backwalls; when this is not the case a larger mass of the abutment is resisting the deck impact (through passive pressures). Introducing Eq. (3-4) in Eq. (3-21) returns the ratio of the angular velocities of the piers ($\dot{\theta}_{II}/\dot{\theta}_{I}$) to describe the pounding effect in the abutments of bridges with rocking piers

$$\frac{\dot{u}_{deck,II}^{CG}}{\dot{u}_{deck,I}^{CG}} = \frac{2R \cos(a - |\theta_{jo}|) \dot{\theta}_{II}}{2R \cos(a - |\theta_{jo}|) \dot{\theta}_{I}} = \frac{\dot{\theta}_{II}}{\dot{\theta}_{I}} = 1 - [1 + e] \frac{m_{abut.}}{m_{abut.} + m_{deck}}, \quad (3-22)$$

where $\theta_{jo} = \text{sgn}(\theta) \cdot [a - \sin^{-1}(\sin a - u_{jo}/2R)]$ describes contact between superstructure and abutments in terms of the DoF of the system. Thus, when the superstructure impacts on the abutments, the angular velocity of the piers will be reduced according to Eq. (3-22).

3.2.5 Impact at the Rocking Interfaces

When the bridge has started rocking, on returning to the at-rest position ($\theta = 0$), impact at the rocking interfaces occurs. These impacts dissipate energy instantly, and subsequently the sign of the angle of rotation changes and its velocity reduces according to the CoR $\eta = |\dot{\theta}_{II}/\dot{\theta}_{I}|$ (Eq. (2-12)). From the point of view of the energy balance, the potential energy stored in the system (Eq. (3-16)) is zero immediately before and after the instant when impact at the rocking interfaces occurs. Hence, at these two instants, the total energy in the system is all in the form of kinetic energy (Eq. (3-12)) that is subsequently dissipated. The present study follows an impulse approach, the novelty consisting in that it integrates in the resulting formulation of η the effect of the abutments acting as vertical supports (points E and E'), as well as the length of the end spans (L_1) and the intermediate spans (L_2). To do so, the following assumptions are adopted in the impact problem considered;

- Reversal of rocking rotation at each impact at the rocking interfaces takes place smoothly without bouncing or sliding and, therefore, the angular momentum is conserved just before and after the impact. These assumptions are only valid for slender piers (Cheng 2007) and for large CoF values (Di Egidio & Contento 2009).
- A 'pointwise' approach was adopted by considering that the impact forces are concentrated at the corresponding pivot points (see Housner 1963 in Fig. 2-7A), thus ignoring the potential migration of the resultant force towards the centre of the pier base due to an extended contact surface (see Kalliontzis *et al.* 2016 in Fig. 2-7B). It is noted that the Housner's approach was found accurate in capturing attenuation of motion at each impact at the rocking interfaces for slender columns with a concrete-to-concrete surfaces, as shown in Fig. 2-8.

To assess the post-impact state in the case of rocking, the impact problem presented in Fig. 3-5 needs to be solved. The post-impact angular velocity of the piers is the variable to be determined ($\dot{\theta}_{II}$) and, therefore, the impact problem is treated in terms of impulses rather than forces. In general, the impulse at point j , Λ_j , is defined as

$$\Lambda_j = \lim_{\Delta t_i \rightarrow 0} \int_{\Delta t_i} \lambda_j dt, \quad (3-23)$$

where λ_j is the corresponding impact force at point j and Δt_i is the duration of the impact.

With reference to Fig. 3-5A, B, C consider that all piers initially rock about CR A' and C' in the counter-clockwise (negative) direction with a magnitude of the angular velocity $\dot{\theta}_{I}$, and reverse the rocking rotation smoothly to the clockwise (positive) direction with angular velocity $\dot{\theta}_{II}$, now rotating around CR A and C. For completeness, the condition corresponding to the reversal of rocking from clockwise (positive) to counter-clockwise (negative) direction is presented in Appendix A. At the intermediate condition, where the bridge is at the at-rest position, the abutments

serve as vertical supports (E and E') and carry part of the deck weight when impact is imminent. Hence, additional impulses ($\Lambda_{E,z}$ and $\Lambda_{E',z}$) originate at the abutment seats as can be seen in Fig. 3-5B, which do not occur in the frame with rocking columns. As a result, in this study there are seven unknowns that need to be determined, namely the impulses at the CR A of the two-side rocking piers in the longitudinal and vertical directions ($\Lambda_{A,x}$ and $\Lambda_{A,z}$), the impulses at the CR C of the $[N - 2]$ intermediate rocking piers in both directions ($\Lambda_{C,x}$ and $\Lambda_{C,z}$), and the vertical impulses at the two abutment seats ($\Lambda_{E,z}$ and $\Lambda_{E',z}$) as well as the angular velocity after impact ($\dot{\theta}_{II}$). Without lack of accuracy, and when the bridge with rocking piers returns to the original at-rest position (when $\theta = 0$) after rocking is initiated, the following analogies based on tributary zones are adopted instantaneously among the impulses (or reaction forces as shown in Eq. (3-23)) that are developed at the different impact points, considering the assumptions of rigid deck and prevention of sliding at all impact faces (§3.2)

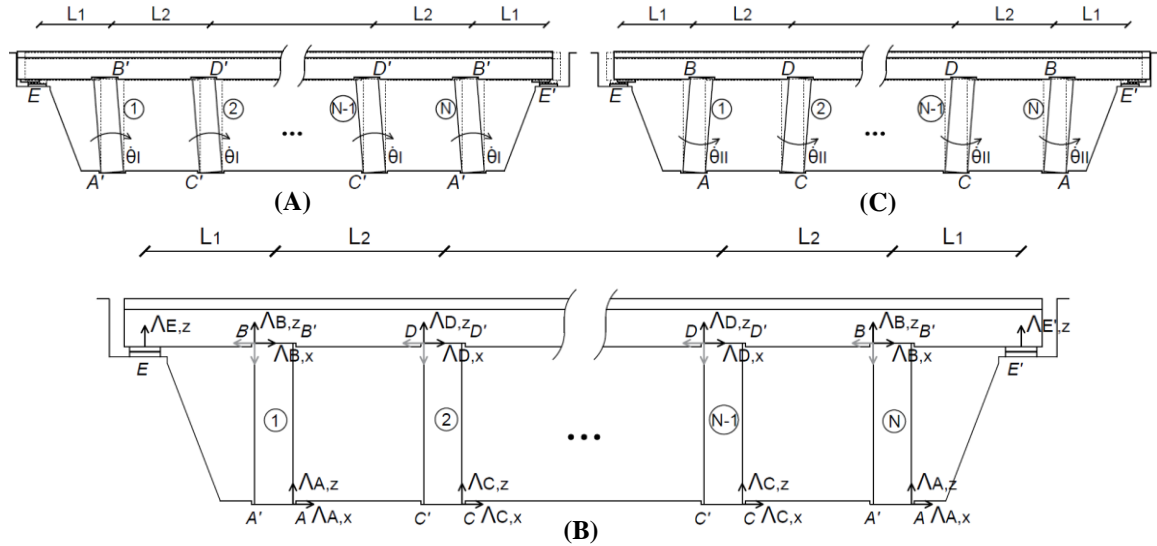


Fig. 3-5 Schematic of the impact problem considered in the rocking motion of a symmetric bridge with rocking piers that (A) undergoes counter-clockwise (negative) rotation with an angular velocity of the piers $\dot{\theta}_I$, (B) impacts at the corresponding pivot points, and then reverses to (C) clockwise (positive) rotation with an angular velocity of the piers $\dot{\theta}_{II}$.

$$\Lambda_{E,z} = \Lambda_{E',z} = \frac{L_1}{L_1 + L_2} \Lambda_{B,z}, \quad (3-24)$$

$$\Lambda_{B,x} = \frac{L_1 + L_2}{2L_2} \Lambda_{D,x} \quad \text{and} \quad \Lambda_{B,z} = \frac{L_1 + L_2}{2L_2} \Lambda_{D,z}. \quad (3-25)$$

Eqs. (3-24) and (3-25) are used separately in order to reduce the number of unknowns in the impact problem. Specifically, the utilisation of Eq. (3-24) and the conservation of linear momentum just before and after the impact along the Z axis for the side piers establishes the relationships between the vertical impulses at the points E and E' with those at CR A

$$\Lambda_{E,z} = \Lambda_{E',z} = \frac{L_1}{L_1 + L_2} \left[\Lambda_{A,z} + m_{pier} B (\dot{\theta}_I + \dot{\theta}_{II}) \right], \quad (3-26)$$

whilst Eq. (3-25) combined with the conservation of linear momentum in both directions for the side and for the intermediate piers relates the impulses at the CR C and A

$$\begin{aligned} \Lambda_{C,x} &= \frac{2L_2}{L_1 + L_2} \Lambda_{A,x} - \frac{L_2 - L_1}{L_1 + L_2} m_{pier} H (\dot{\theta}_I - \dot{\theta}_{II}) \quad \text{and} \\ \Lambda_{C,z} &= \frac{2L_2}{L_1 + L_2} \Lambda_{A,z} + \frac{L_2 - L_1}{L_1 + L_2} m_{pier} B (\dot{\theta}_I + \dot{\theta}_{II}). \end{aligned} \quad (3-27)$$

Eqs. (3-26) and (3-27) reduce the unknowns of the impact problem from seven to only three ($\Lambda_{A,x}$, $\Lambda_{A,z}$ and $\dot{\theta}_{II}$). Hence, the following equations are considered in the determination of these unknowns;

1. Linear momentum along the X axis for the entire bridge

$$2\Lambda_{A,x} + [N - 2]\Lambda_{C,x} = [Nm_{pier} + 2m_{deck}] H (\dot{\theta}_I - \dot{\theta}_{II}). \quad (3-28)$$

2. Linear momentum along the Z axis for the entire bridge

$$\Lambda_{E,z} + 2\Lambda_{A,z} + [N - 2]\Lambda_{C,z} + \Lambda_{E',z} = -[Nm_{pier} + 2m_{deck}] B (\dot{\theta}_I + \dot{\theta}_{II}). \quad (3-29)$$

3. Angular momentum at point B for a side pier

$$2H\Lambda_{A,x} + 2B\Lambda_{A,z} = [m_{pier}H^2 - I_{pier}^{CG}] (\dot{\theta}_I - \dot{\theta}_{II}) - m_{pier}B^2 (\dot{\theta}_I + \dot{\theta}_{II}). \quad (3-30)$$

Eqs. (3-28) to (3-30) describe the impact problem when the rotation changes from negative to positive. In the opposite case (i.e., rocking from positive to negative rotation), the formulation is provided in Appendix A. The CoR at the rocking interfaces (η) during the rocking motion of the bridge is obtained by solving the system of Eqs. (3-28) to (3-30)

$$\eta = \left| \frac{\dot{\theta}_{\text{II}}}{\dot{\theta}_{\text{I}}} \right| = \frac{1 - \frac{3}{2} \sin^2 a - \frac{3}{4} \gamma [\bar{L} + 1] [(\bar{L} - 1 + N) \cos 2a + \bar{L} \cos^2 a]}{-\frac{1}{8} \left[3\bar{L} + N + \frac{1}{N} (2\bar{L}^2 - 3\bar{L} + 1) \right] [1 + 3 \cos 2a]}, \quad (3-31)$$

$$1 - \frac{3}{4} \gamma [\bar{L} + 1] [(\bar{L} - 1 + N) + \bar{L} \cos^2 a]$$

$$-\frac{1}{2} \left[3\bar{L} + N + \frac{1}{N} (2\bar{L}^2 - 3\bar{L} + 1) \right]$$

and η is independent of the direction of the movement due to the symmetry of the rocking system, as shown in Appendix A. Eq. (3-31) includes an additional dimensionless factor $\bar{L} = L_1/L_2$ which is not present in the CoR at the rocking interfaces for a frame with the same number of rocking columns (Eq. (2-19)), and it describes the effect of the span arrangement in the bridge. If $L_1 = L_2$ (then $\bar{L} = 1$), the span arrangement has no effect on the impulses developed at each pier and the impulses in both directions at the foundation level are the same for all piers ($\Lambda_{C,x} = \Lambda_{A,x}$ and $\Lambda_{C,z} = \Lambda_{A,z}$). If, in addition, the vertical impulses that are developed at the abutments are ignored by introducing $\Lambda_{E,z} = \Lambda_{E',z} = 0$ in Eq. (3-29), the CoR η reduces to the simpler one utilised in previous works for frames with rocking columns as shown in Eq. (2-19) (presented first by Makris & Vassiliou 2013).

As it was mentioned previously, the differences between the value of η in bridges with rocking piers and in relevant frames stem from the impact at the vertical supports of the abutment seats and from the span arrangement in the bridge. Fig. 3-6 depicts the effect of the additional impacts at the ends of the bridge deck by ignoring the effect of the side spans ($\bar{L} = 1$) and compares η in bridges with rocking piers and relevant frames with same dimensions. The results are for structures with four rocking piers ($N = 4$) with slenderness $a = 0.165$ rad, for different values of superstructure mass effect γ . It is apparent from Fig. 3-6 that the value of the CoR at the rocking interfaces for the bridge is always higher than that for the corresponding frame for any value of γ . This means that the energy dissipation associated with each impact at the rocking interfaces is always lower in the bridge, and this is because part of the weight of the superstructure is carried by the abutments that reduces the weight supported by each pier. Furthermore, the value of η for bridges is lower for larger values of γ , confirming the beneficial effect of heavier superstructures on rocking attenuation which is consistent with previous findings (Makris & Vassiliou 2014b). It should be noted that, although the difference between the value of η in bridges and frames is relatively small (around 1% for all the examined cases), rocking performance can be considerably differentiated due to the highly non-linear nature of rocking response (Dimitrakopoulos & DeJong 2012b).

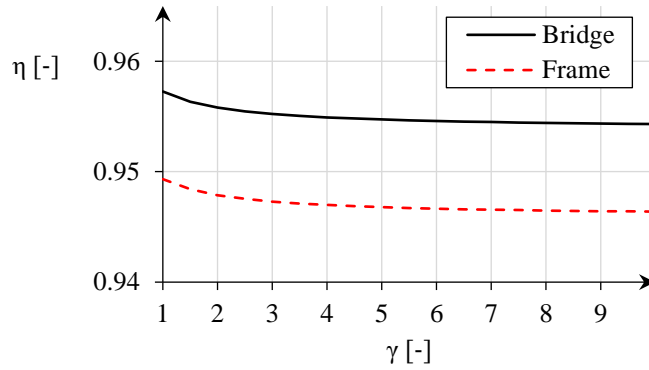


Fig. 3-6 CoR at the rocking interfaces (η) for symmetric bridges with rocking piers and for equivalent frames (Makris & Vassiliou 2013), accounting for the influence of the superstructure mass effect (γ). Results obtained when $\bar{L} = 1$.

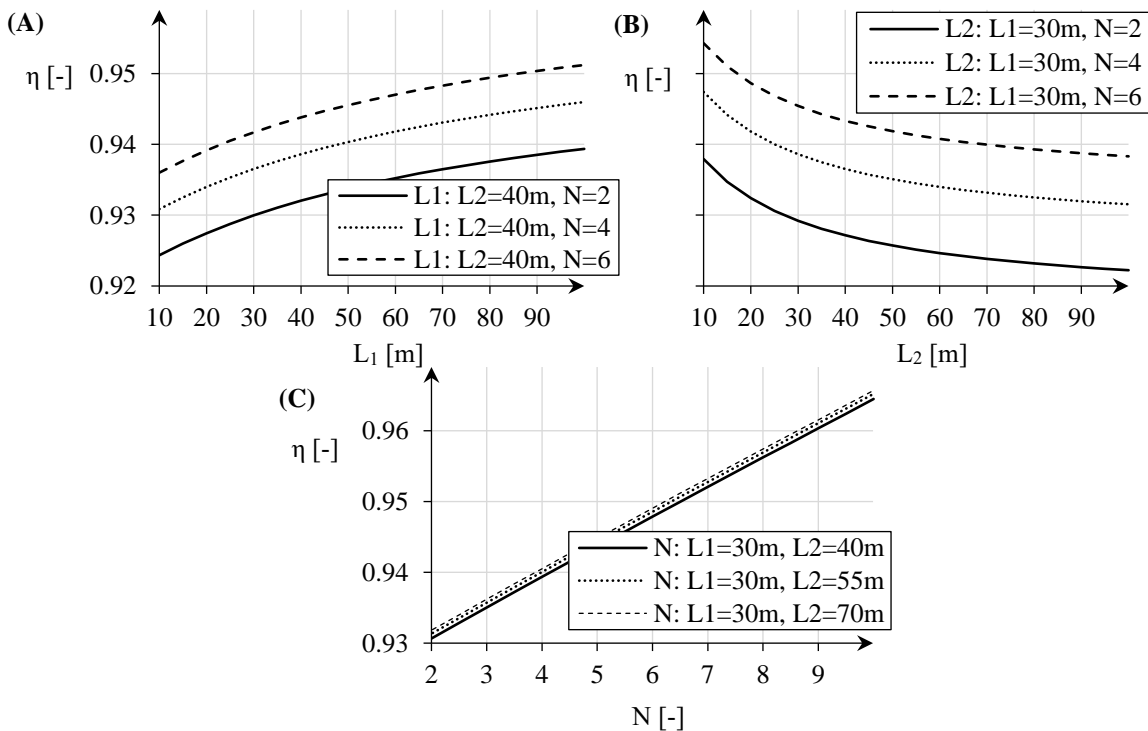


Fig. 3-7 CoR at the rocking interfaces (η) for symmetric bridges with rocking piers, accounting for the influence of (A) the length of the end spans (L_1), (B) the length of the intermediate spans (L_2), and (C) the number of piers (N). Results obtained when the deck mass is constant.

Compared to the frame case, the attenuation of the rocking motion at each impact at the rocking interfaces (η) for a bridge depends on a number of additional parameters, namely the length of the bridge spans (L_1 and L_2) as well as the number of piers (N). To better understand the effect of these parameters on the value of η , reference is made to a bridge with constant deck mass $m_{deck} = 270 \cdot 10^4$ kg that is supported on rectangular-in-elevation piers with the same dimensions $2B = 3$ m and $2H = 15$ m for all the examined cases. Fig. 3-7A shows that, considering a constant mass of the deck, longer end spans (L_1) with constant length for the intermediate spans (L_2) result in higher values of η , because the vertical reaction forces at the piers are progressively decreasing (similarly, they are increasing at the abutment seats), which reduces the energy loss at every impact at the

rocking interfaces during the rocking motion. The opposite occurs if the length of the intermediate spans (L_2) is increased keeping constant the length of the side spans (L_1), which leads to slightly larger energy dissipation and smaller η , as shown in Fig. 3-7B. The influence of the increasing number of piers keeping the deck mass constant is represented in Fig. 3-7C. It can be observed that distributing the weight of the deck to more piers leads to larger values of η based on the same reasoning. As expected, the effect of number of piers N is more significant than changing the span arrangement, as it is observed in the shifting of the curves in Fig. 3-7A, B, and the steeper slope of the curves in Fig. 3-7C. It must be noted that the proposed value of η ignores some factors that could lead to additional energy dissipation at each impact at the rocking interfaces (§2.3.1.2) and, therefore, it represents an upper bound to the total energy dissipated for a bridge system, rendering the analytical modelling presented as conservative. Additionally, the potential effect of the end spans working as cantilevers on the value of the proposed CoR value is not taken into account in Eq. (3-31) (see relevant discussion in §7.2.1).

3.3 Analysis Framework

To analyse the rocking response of the configurations studied in this chapter (§3.3.1) for any given ground motion (§3.3.2), Eq. (3-8) is used to determine the instant at which the bridge (or frame) starts rocking, and Eq. (3-20) (or Eq. (2-16) when the frame with rocking columns is examined) is integrated step-by-step using the ‘*ode45*’ solver in MATLAB (2016) with a time-step of 10^{-3} s, selected after a sensitivity analysis. The response-history solution of the EoM of the bridge structure requires identifying the instants at which $|u_{deck}^{CG}| = u_{jo}$ (or $\theta = \theta_{jo}$). At these instants, impacts on the abutment backwalls occur and Eq. (3-22) is utilised to express the attenuation of rocking motion. To do so, an iterative process is constructed in the MATLAB code with a decreasing time-step value ($5 \cdot 10^{-6}$ s) to capture this phenomenon with more accuracy. Similarly, the instants at which $\theta = 0$ after rocking initiation also need to be identified, while impacts at the rocking interfaces occur and Eq. (3-31) (or Eq. (2-19) when the frame with rocking columns is examined) is employed to account for the corresponding attenuation of the rocking motion. Failure of the systems (§3.3.3) is simply integrated in the analysis as a special condition after which the process is terminated; a more detailed representation of this procedure by means of a flowchart is shown in Appendix A (Fig. A-2). It should be noted that the overall duration for a single analysis of a symmetric bridge with rocking piers is only a few minutes with the hardware that was used for this thesis (i.e., a machine with an available RAM of 10 GB).

3.3.1 Description of the Studied Bridges

The effect of the abutment-backfill system on the seismic rocking response is addressed by examining the behaviour of two bridges with rocking piers (one with a short/light configuration and the other with a long/heavy one) and the corresponding frames resulting by neglecting the abutments. The two structures have a total length $L_{tot} = 2L_1 + 2L_2 = 2 \cdot 50 + 2 \cdot 50 = 200$ m and

$L_{tot} = 2L_1 + 6L_2 = 2 \cdot 50 + 6 \cdot 50 = 400$ m and they are supported on $N = 3$ and $N = 7$ rocking piers, respectively, of rectangular configuration and square cross-section. The total mass of the short and long configurations is equal to $m_{tot} = 310 \cdot 10^4$ kg and $m_{tot} = 720 \cdot 10^4$ kg, respectively. The superstructure in both cases consists of a single-cell box girder with depth $2h = 1.7$ m, while the width of the bottom and the top slabs of the deck are $B_{bot} = 6$ m and $B_{top} = 9.5$ m, respectively. The flange ($t_f = 0.25 \sim 0.3$ m) and the wall thicknesses ($t_w = 0.7 \sim 0.8$ m) of the box girder section were adjusted to achieving a mass ratio equal to $\gamma = 4.8$ for both structures. The deck has a constant cross-section with area $A_{deck} = 5.2$ m² and $A_{deck} = 6$ m² in the light and the heavy bridge, respectively. The rocking piers have a width $2B = 1.8$ m and a height $2H = 22$ m in both configurations. The abutment properties of an actual overpass that is part of the Egnatia Motorway (2002) (Greece) are selected as per Kappos *et al.* (2007). The same abutments are considered in both bridge configurations, with total height $H_{abut.} = 5.5$ m and width $B_{abut.} = 10.5$ m, while the height and the thickness of the backwall are $h_{bw} = 2$ m and $b_{bw} = 0.4$ m, respectively. The mechanical properties of a typical backfill are adopted from Kappos *et al.* (2007) composed from well-compacted sand with friction angle $\varphi = 40^\circ$ classified as Ground C ($V_s \approx 290$ m/s) according to Eurocode 8 (EC8) site classification (CEN 2004b). The examined structures are founded on soil C and belong to the highest seismicity zone prescribed in Southern Europe, with Peak Ground Acceleration (PGA) equal to 0.36 g. The structures are classified to importance class II ($\gamma_I = 1$).

3.3.2 Representation of Seismic Action

3.3.2.1 Single-frequency Pulse-type Ground Motions

The abutment-backfill contribution in the rocking response is studied first by utilising ground motions that are described by simple mathematical expressions. Three different single-frequency pulse-type excitations are considered that can capture both qualitatively and quantitatively the most destructive part of near-fault ground motions (Vassiliou & Makris 2012, Makris & Vassiliou 2013) to which rocking structures have shown high vulnerability (§2.3.1.3). These signals are the sine, Ricker symmetric and antisymmetric pulses, as described by Eqs. (3-32) to (3-34), respectively

$$\ddot{u}_g(t) = a_p \sin\left(\frac{2\pi}{T_p} t\right), \quad (3-32)$$

$$\ddot{u}_g(t) = a_p \left(1 - \frac{2\pi^2 t^2}{T_p^2}\right) \exp\left(-\frac{1}{2} \frac{2\pi^2 t^2}{T_p^2}\right), \quad (3-33)$$

$$\ddot{u}_g(t) = \frac{a_p}{\beta} \left(\frac{4\pi^2 t^2}{3T_p^2} - 3\right) \frac{2\pi t}{\sqrt{3}T_p} \exp\left(-\frac{1}{2} \frac{4\pi^2 t^2}{3T_p^2}\right), \quad (3-34)$$

where $T_p = 2\pi/\omega_p$ and α_p are the period and the acceleration amplitude of each pulse-type motion, respectively, and $\beta = 1.38$ in Eq. (3-34) maximises the function to the acceleration amplitude α_p .

3.3.2.2 Multi-frequency Synthetic Ground Motions

To further establish the effect of the abutment-backfill system on the rocking response, considering the potential lack of conservativeness of pulse-type motions (see Fig. 2-9), the structures are subjected to a total of ten Artificial Excitations (ARs) as presented in Gkatzogias (2017). The generation of the artificial accelerograms was based on the approach of Gasparini & Vanmarcke (1976), adopting the Saragoni & Hart (1974) envelope function with a total duration of 25 s and time step of $dt = 0.01$ s. The acceleration amplitudes of the ARs were generated to match the reference EC8 target spectrum (CEN 2004b) considering a PGA equal to 0.36 g and site conditions C (§3.3.1). Fig. 3-8 presents the fit of the individual ARs and their Geometric Mean (GM) to the target EC8 spectrum, while Table 3-1 presents the main characteristics of the ARs.

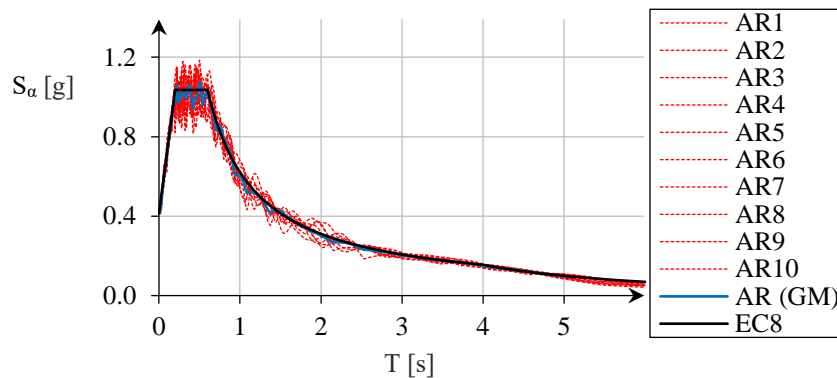


Fig. 3-8 Response acceleration spectra of the set of ARs, and matching to EC8 target spectrum with PGA = 0.36 g and site conditions C.

Table 3-1 Information for the generated ARs, including the Peak Ground Acceleration (PGA), the Peak Ground Velocity (PGV), the Peak Ground Displacement (PGD), and the Arias Intensity (I_A).

AR	PGA [g]	PGV [m/s]	PGD [m]	I_A [m/s]
AR1	0.412	0.516	0.283	3.047
AR2	0.412	0.549	0.244	3.982
AR3	0.412	0.549	0.219	3.251
AR4	0.412	0.608	0.238	2.785
AR5	0.412	0.530	0.271	3.666
AR6	0.412	0.500	0.217	2.724
AR7	0.411	0.513	0.237	3.557
AR8	0.412	0.456	0.244	3.772
AR9	0.411	0.516	0.212	3.094
AR10	0.412	0.462	0.217	3.791

3.3.3 Failure Criteria

The ‘traditional’ overturning criterion of the rocking piers $|\theta_{ov}| \geq a$ is considered for both structures (with or without abutments at the end of the superstructure), which occurs when the total mass of the system can no longer act as a restoring mechanism. In terms of linear variables, this condition is achieved when the longitudinal displacement of the pier exceeds the overturning threshold ($|u_{pier}^{CG}| \geq B$), or the displacement of the superstructure exceeds double of this value ($|u_{deck}^{CG}| \geq 2B$). However, and contrary to the frame case without abutments in which failure of the system can only occur due to overturning of the rocking piers, a new failure criterion has to be introduced for the bridge configuration based on the possibility of damage or failure related to longitudinal displacement of the deck at the abutments.

The abutment-backfill system fails if the longitudinal displacement of the superstructure (u_{deck}^{CG}) closes the end joint gap (u_{jo}), and it induces a displacement at the abutments that exceeds their capacity (u_{ab}). This failure mode can be expressed in terms of the DoF of the rocking system (θ) by rearranging Eq. (3-2)

$$|u_{deck}^{CG}| \geq u_{jo} + u_{ab} \Leftrightarrow |\theta_{ab}| \geq a - \sin^{-1} \left(\sin a - \frac{u_{jo} + u_{ab}}{2R} \right). \quad (3-35)$$

Several proposals can be found in the literature regarding the capacity of abutments and backfills/embankments. These include the collapse of the abutment-backfill system due to the exceedance of shear strength of the abutment backwall (e.g., Kwon & Elnashai 2010), the failure of the abutment foundation or ‘unrecoverable abutment damage’ (e.g., Kappos *et al.* 2007), and the unseating of the deck due to large displacements and/or inadequate seat lengths; the latter is typically prevented when bridges are designed according to modern code provisions (e.g., CEN 2005a). In the context of the present study, the failure criterion to be used for these systems needs to be comparable with the overturning criterion used for the rocking piers, which is physical collapse, and hence it relates to ‘Collapse Prevention’ in performance assessment. Simplified approaches like the exceedance of shear strength of the abutment backwall (Kwon & Elnashai 2010) can considerably underestimate the overall seismic performance of bridges compared to more pragmatic approaches like the one proposed by Kappos *et al.* (2007). This considers the behaviour of a specific abutment-backfill system in the nonlinear range using a ‘full-range’ pushover analysis up to significant drop in strength. The benefit of this approach is that it recognises that backwalls are sacrificial elements that may fail under large ground motions, but there is no system failure so long as the abutment is able to transfer the horizontal loads from the deck to the backfill. Therefore, additional horizontal loads can be accommodated by the abutment-backfill system after yielding of the backwall. On the contrary, failure of the abutment foundation (the piles, in Kappos *et al.* 2007) can be considered as system failure, broadly equivalent to overturning of the rocking piers. These point to the need of properly defining the behaviour of the abutment-backfill system in the rocking problem, while small variations in the values of spring

stiffness (k), dashpot coefficient (c) and displacement capacity of the abutment-backfill system (u_{ab}) can affect significantly the safety of bridges with rocking piers and, consequently, it is important to account for failure of these components in performance assessment. The dominant failure mode of the bridge system (i.e., pier overturning or failure of the abutment-backfill system) depends on the properties of the bridge system. Hence, the abutment-backfill member fails first as long as $|\theta_{ov}| > |\theta_{ab}|$ or $2B > u_{jo} + u_{ab}$, while overturning prevails if $|\theta_{ov}| < |\theta_{ab}|$ or $2B < u_{jo} + u_{ab}$; as expected, the simultaneous failure of the entire system occurs when $2B = u_{jo} + u_{ab}$.

3.3.4 Analysis Parameters

3.3.4.1 Modelling of the Abutment-Backfill System – Stiffness

The values for spring stiffness (k) and displacement at failure of the abutment-backfill system (u_{ab}) are derived from the pushover curve in the longitudinal direction as per Kappos *et al.* (2007), considering that subsequent to pier yielding the end gap closes and thereafter the pushover curve is dominated by the behaviour of the abutment and the backfill. Fig. 3-9 shows the bilinear behaviour of the abutment-backfill system considered and, based on this, the ultimate displacement of this member is set equal to $u_{ab} = 0.1$ m.

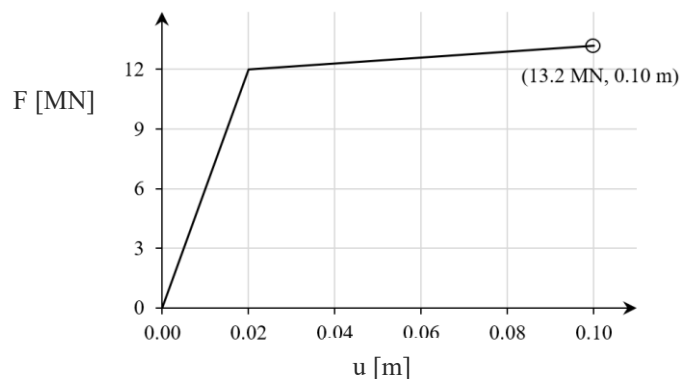


Fig. 3-9 Force-displacement (F - u) behaviour of the abutment-backfill system in the longitudinal direction (Kappos *et al.* 2007).

Since elastic response of the end springs is assumed here, the value of spring stiffness is determined using the equivalent linearisation approach based on the secant stiffness. Starting from the actual nonlinear pushover curve of the abutment-backfill system shown in Fig. 3-9, the most conservative value for secant stiffness is selected. This value corresponds to the stiffness at the ultimate displacement of the abutment-backfill system (0.1 m), resulting in $k = 132$ MN/m. It is pointed out that this value for secant stiffness is the proper one when abutment failure is triggered, while the ultimate displacement of 0.1 m is reached for the abutments. However, it is recognised that this is not the case when the abutment-backfill system maintains its integrity in the cases studied. Ideally for those cases, an iterative procedure could be used, as in a more rigorous secant stiffness procedure based on the target displacement of the abutment-backfill system. However, it is believed that the key findings regarding the importance of the abutment-backfill system in the rocking response of bridges would not change due to the underestimation of this stiffness value.

To check this, the response-history of both bridge structures (i.e., short configuration with $N = 3$ rocking piers and long one with $N = 7$ rocking piers) subject to the multi-frequency excitations (§3.3.2.2) is examined, considering three alternatives for the stiffness value of the abutment-backfill system: (i) the most conservative value for secant stiffness referring to the ultimate abutment displacement of the pushover curve shown in Fig. 3-9, (ii) a revised secant stiffness value based on the target abutment displacement from the pushover curve shown in Fig. 3-9 (iterations are required in this case assuming a 10%-tolerance in the peak superstructure displacement between consecutive iterations), and (iii) the simplified stiffness value proposed in Caltrans (2019). For the bridge structures examined, the damping coefficient is equal to $c = 48 \text{ MN}\cdot\text{s/m}$ (§3.3.4.2). Joint gaps of $u_{jo} = 100 \text{ mm}$ and $u_{jo} = 150 \text{ mm}$ are considered for the short and long bridges, respectively, (§3.3.4.3) and pounding on the abutment backwalls is expressed through a CoR $e = 0.6$ (§3.3.4.4).

Table 3-2 presents the abutment-backfill stiffness values for the three alternatives when implemented in the bridge configuration with $N = 3$ rocking piers. It is noted that procedure (ii) converged with only one iteration. It is shown that procedure (i) underestimates the stiffness values up to 4.6 times compared to the detailed case (ii), obviously because for this level of ground motion the displacement at the abutment is far from that corresponding to failure. The adopted conservative secant stiffness (i) is in a good match with that in the simplified Caltrans approach (iii).

Table 3-2 Spring stiffness values of the abutment-backfill system (k), considering three alternatives. Results obtained for the bridge configuration with $N = 3$ piers.

		Procedure			
		Kappos et al. (2007)			
		(i) Secant at Ultimate Displacement	(ii) Secant at Target Displacement	(iii) Caltrans (2019)	
N = 3	Abutment		AR2	AR4	
	k [MN/m]				
	Right	132	469	600	186
	Left		600	600	

The histories of the superstructure longitudinal displacement (u_{deck}^{CG}) of these configurations when subjected to AR2 and AR4 are presented in Fig. 3-10A, B, respectively; the values in brackets for cases (ii-blue) and (iii-red) denote the corresponding percent difference in peak superstructure displacements with the procedure adopted in this chapter (procedure i-black). It is observed that the short bridges adopting procedures (i) and (iii) to calculate the spring stiffness yield very similar response-histories throughout the whole rocking motion, with a peak difference of merely 1.5% as can be seen in Fig. 3-10A. Analogously in Fig. 3-10B, and despite the considerable difference in stiffness values, the short structures with stiffness values according to (i) and (ii) behave in a similar way, especially in terms of peak superstructure displacements, with a maximum difference of around 5%. Thus, adopting the secant stiffness value at the ultimate abutment displacement for the

short configuration is not expected to affect the main outcomes of this study compared to a more rigorous secant stiffness approach.

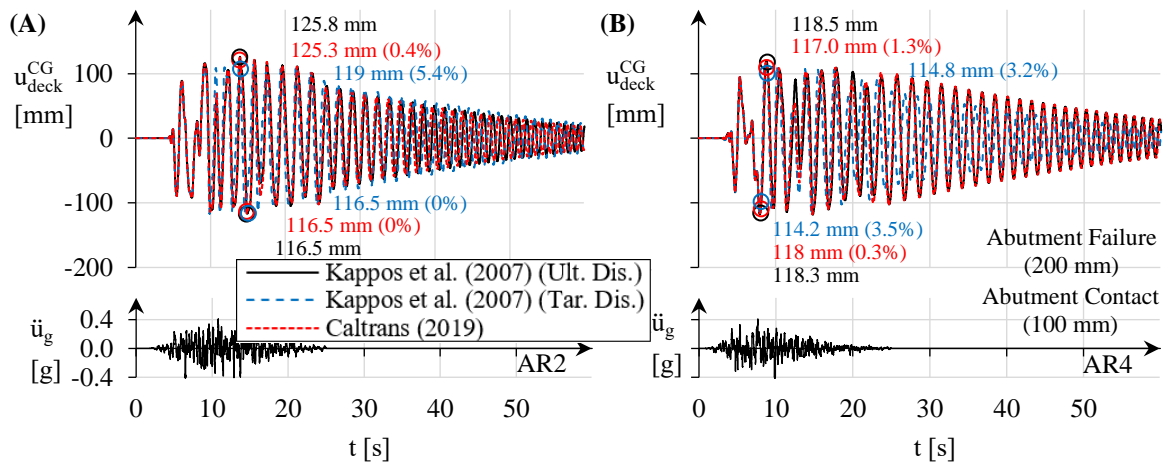


Fig. 3-10 Histories of the longitudinal displacement of the superstructure (u_{deck}^{CG}) for the symmetric bridge with $N = 3$ rocking piers, considering three alternatives for the abutment-backfill stiffness. Results obtained when subject to (A) AR2 and (B) AR4.

Table 3-3 Spring stiffness values of the abutment-backfill system (k), considering three alternatives. Results obtained for the bridge configuration with $N = 7$ piers.

N = 7		Procedure			
		Kappos et al. (2007)			
		(i) Secant at Ultimate Displacement	(ii) Secant at Target Displacement	(iii) Caltrans (2019)	
k [MN/m]	Right	132	AR5	AR8	186
	Left		279	317	
			328	376	

Accordingly, [Table 3-3](#) presents the abutment-backfill stiffness values for the three alternatives when implemented in the bridge configuration with $N = 7$ rocking piers, while [Fig. 3-11A, B](#) present the corresponding histories of the superstructure longitudinal displacement (u_{deck}^{CG}) when excited by AR5 and AR8, respectively; it is noted again that procedure (ii) converged with only one iteration leading to the stiffness values shown in [Table 3-3](#). It can be seen that the stiffness values for this configuration vary in a ratio from 1.4 to 2.8 for all the different procedures considered and, therefore, the bridges with rocking piers show similar peak and overall responses. The maximum difference shown for case (iii) is 1.4% ([Fig. 3-11A](#)), while the pertinent difference for the detailed case (ii) is around 6% ([Fig. 3-11B](#)). This is considered acceptable as it is not expected to affect the main conclusions of this study. Thus, the most conservative value for secant

stiffness is selected from the pushover curve shown in Fig. 3-9, leading to $k = 132 \text{ MN/m}$ for the soil profile considered.

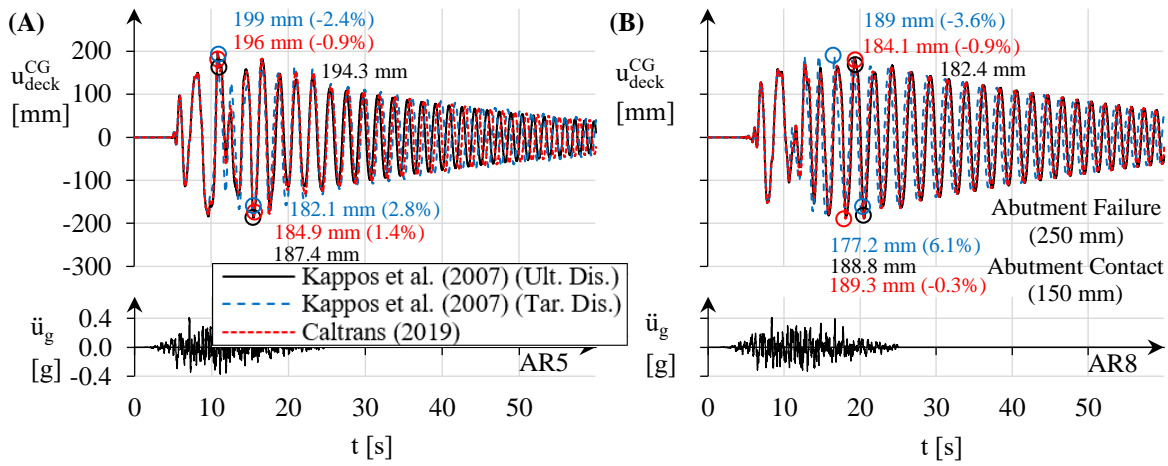


Fig. 3-11 Histories of the longitudinal displacement of the superstructure (u_{deck}^{CG}) for the symmetric bridge with $N = 7$ rocking piers, considering three alternatives for the abutment-backfill stiffness. Results obtained when subject to (A) AR5 and (B) AR8.

3.3.4.2 Modelling of the Abutment-Backfill System – Damping

The dashpot coefficient (c) accounts for the effect of both material and radiation damping of the backfill soil, and it is activated when the superstructure enforces a longitudinal displacement to the abutments. To incorporate both damping forms in the value of a dashpot coefficient, the following equation is considered after the work of Mylonakis *et al.* (2006)

$$c = \rho_s V_{La} A_{abut.} + 2 \frac{\bar{K}\beta}{\omega}, \quad (3-36)$$

where ρ_s is the mass density of the backfill soil, $V_{La} = 3.4V_s/\pi \cdot [1 - \nu_s]$ where V_s and ν_s are the shear wave velocity and the Poisson's ratio of the soil, respectively, $A_{abut.} = H_{abut.} \cdot B_{abut.}$ is the area of the abutment, $\bar{K} = K \cdot k(\omega)$ is the dynamic stiffness of the abutment-backfill system as a product of the static stiffness $K = [V_s^2 \cdot \rho_s] \cdot B_{abut.} \cdot [0.73 + 1.54(A_b/B_{abut.}^2)^{0.75}]/[1 - \nu_s]$ times the dynamic stiffness coefficient $k(\omega)$, β is the linear hysteretic damping factor of the backfill soil and $\omega = \sqrt{K/m_{abut.}}$ expresses the cyclic frequency of the abutment-backfill system; finally, $m_{abut.}$ is given in §3.2.4. Substituting $\rho_s = 1.8 \text{ tn/m}^3$, $V_s = 290 \text{ m/s}$, $\nu_s = 0.3$, $H_{abut.} = 5.5 \text{ m}$ and $B_{abut.} = 10.5 \text{ m}$, $\beta = 5\%$ and $m_{abut.} = 14 \cdot 10^4 \text{ kg}$ into Eq. (3-36) gives $c = 48 \text{ MN}\cdot\text{s/m}$ for the backfill soil considered. For the sake of completeness, the dashpot coefficient is calculated considering another recommendation from the literature, namely Zhang & Makris (2002), and the value of dashpot coefficient is equal to $c = 43 \text{ MN}\cdot\text{s/m}$. Therefore, both approaches yield similar values with the difference being below 15% despite the different procedure adopted in each method. Thus, different proposals for the value of the dashpot coefficient are not expected to affect the results

significantly and, therefore, the value derived according to Mylonakis *et al.* (2006) is utilised in this chapter.

3.3.4.3 Effect of Gap Size

The length of the end joint gaps (u_{jo}) depends on both the service actions and the seismic demands. The service actions include shrinkage and creep with a temperature increment of $\Delta T_{N,eq} = 30\text{ }^{\circ}\text{C}$, thermal expansion and contraction of the superstructure with $\Delta T_{N,exp} = \Delta T_{N,con} = 25\text{ }^{\circ}\text{C}$, respectively, and prestressing. These effects result in the requirement of minimum gap sizes at each end of the superstructure equal to 40 mm and 80 mm for the short structure with $N = 3$ rocking piers and the long one with $N = 7$ rocking piers, respectively. This section presents the effect of the joint length on the rocking motion of the long structure considering the multi-frequency excitations (§3.3.2.2). The selection of this bridge configuration is made because the effect of joint length is expected to be more apparent in the long bridge, where larger superstructure displacements are expected compared to the short bridge. This is due to the participation of the abutment-backfill system in the rocking response expressed through parameter q , which is smaller in the long bridge than in the short one ($q = 0.234 \cdot 10^{-3}\text{ m/kN}$ and $q = 0.545 \cdot 10^{-3}\text{ m/kN}$, respectively) (§3.2.3).

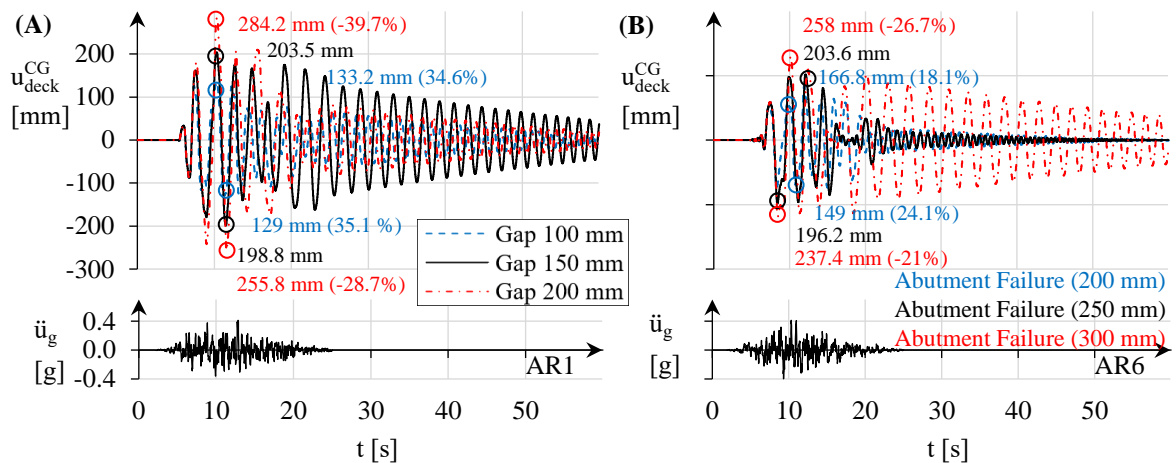


Fig. 3-12 Histories of the longitudinal displacement of the superstructure (u_{deck}^{CG}) for the symmetric bridge with $N = 7$ rocking piers, considering three alternatives for the gap size. Results obtained when subject to (A) AR1 and (B) AR6.

For the examined bridge configuration, the spring stiffness of the abutment-backfill system is $k = 132\text{ MN/m}$ (§3.3.4.1), the dashpot coefficient is equal to $c = 48\text{ MN}\cdot\text{s/m}$ (§3.3.4.2), pounding is described by a CoR $e = 0.6$ (§3.3.4.4) and three alternatives are considered for the gap size: (i) 100 mm, (ii) 150 mm and (iii) 200 mm. Fig. 3-12A, B present the histories of the deck longitudinal displacement (u_{deck}^{CG}) of these configurations when subjected to AR1 and AR6, respectively; it is noted that the values in brackets for cases (i-blue) and (iii-red) in Fig. 3-12 show the corresponding percent difference in terms of the peak superstructure displacements with respect to case (ii-black). It is observed that the effect of the end gap size on the rocking response of the long bridge is

significant. Specifically, larger end gaps lead to reduced longitudinal effective stiffness in the closed gap stage of the system and, therefore, result in larger deck displacements than smaller end gaps. The difference in the peak seismic displacements can be up to 40% as shown in Fig. 3-12A for the structure with gap size (iii) subjected to AR1. On the contrary, structures with the smallest joint length (i) show the lowest deck displacements at each examined case. However, from the performance assessment point of view, the abutment-backfill system maintains its integrity for all the examined cases, independently of the gap size. Thus, this study adopts a reasonably large value for the longitudinal joint gap which is equal to $u_{jo} = 100$ mm for the short bridge and $u_{jo} = 150$ mm for the long bridge.

3.3.4.4 Effect of Pounding

As described in §3.2.4, the attenuation of the superstructure motion when an impact between the superstructure and the abutment backwall takes place is achieved through a CoR e . Several proposals can be found in the literature for the value of this parameter to describe a concentric impact between two concrete objects, and it usually ranges between 0.4 and 0.8 (e.g., Jankowski 2007). This section examines the effect of the CoR value to describe pounding on the seismic response of the long structure with $N = 7$ rocking piers subject to the synthetic ground motions (§3.3.2.2). Note that this bridge configuration is selected because it is expected to give the largest superstructure displacements as explained in §3.3.4.3.

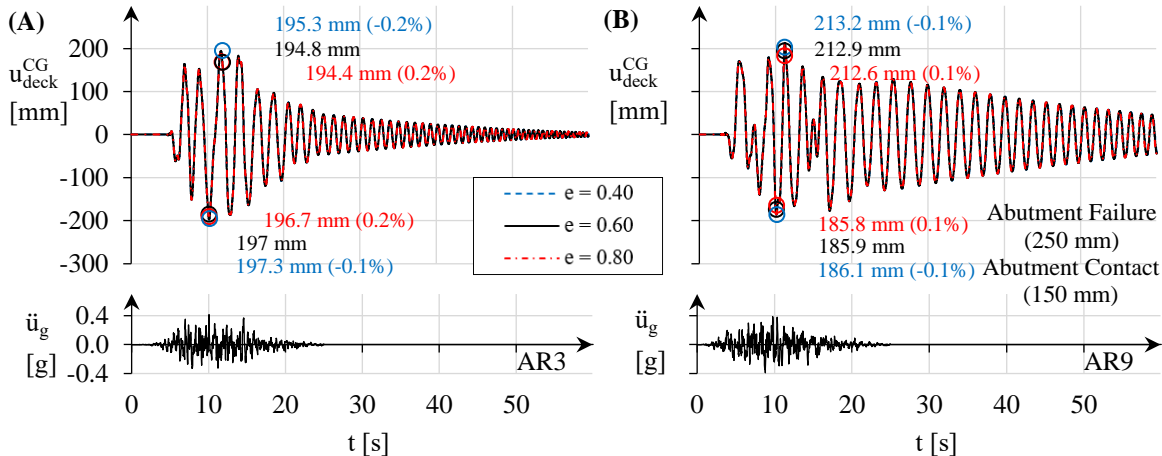


Fig. 3-13 Histories of the longitudinal displacement of the superstructure (u_{deck}^{CG}) for the symmetric bridge with $N = 7$ rocking piers, considering three alternatives for the CoR value to describe pounding. Results obtained when subject to (A) AR3 and (B) AR9.

For the structure examined, and following the justification provided in the previous sections, the spring stiffness of the abutment-backfill system is $k = 132$ MN/m (§3.3.4.1), the dashpot coefficient is equal to $c = 48$ MN·s/m (§3.3.4.2) and the joint length for the long bridge $u_{jo} = 150$ mm (§3.3.4.3). Three alternatives are considered for the CoR value e : (i) 0.4, (ii) 0.6 and (iii) 0.8. Fig. 3-13A, B present the histories of the deck longitudinal displacement (u_{deck}^{CG}) of these configurations when subjected to AR3 and AR9, respectively. The values in brackets for cases (i-

blue) and (iii-*red*) describe the corresponding percent difference in peak superstructure displacements with respect to case (ii-*black*). It can be seen that the smaller the CoR, the more suppressed is the rocking response of the structure. However, this difference is marginal for all the examined cases, showing a maximum difference of approximately 0.2% for cases (ii) and (iii) subject to AR3 (Fig. 3-13A). This outcome is in line with previous findings based on Athanassiadou *et al.* (1994), who showed that variations in the value of this CoR in the range of 0.2 to 0.8 have negligible effect on the overall seismic response of structures. Thus, this study considers a CoR value of $e = 0.6$ to describe pounding.

3.3.5 Effect of the Abutment-Backfill System on Bridges with Rocking Piers

3.3.5.1 Rocking Response under Single-frequency Pulse-type Ground Motions

This section addresses the effect of the abutment-backfill system on the seismic performance of symmetric frames with rocking columns (§3.3.1) by considering pulse-type excitations (§3.3.2.1). The analysis parameters for the spring model as well as the collapse of the abutment-backfill system, the dashpot model, the gap size and the pounding model are defined following §3.3.4.1, §3.3.4.2, §3.3.4.3 and §3.3.4.4, respectively. As described in §2.3.1.3 a useful way of illustrating the vulnerability of rocking structures in such pulses is through OMAS, considering that overturning was defined as the only failure mechanism of the rocking blocks and relevant frames. However, an additional failure criterion is adopted in bridges with rocking piers (§3.3.3), hence the term OMAS cannot describe the more complex nature of failure in bridges with rocking piers and a broader term is used in the following to capture this effect: Failure Minimum Acceleration Spectra (FMAS).

Fig. 3-14A, B, C present the FMAS for the analysed bridges and their equivalent frames when subjected to the sine, Ricker symmetric and antisymmetric pulses, respectively. The bridges are more susceptible to fail due to high demand of longitudinal displacement at the abutments than due to overturning of the piers (§3.3.3); this is because $2B = 1.8 \text{ m} > u_{jo} + u_{ab} = 0.2 \text{ m}$ and $2B = 1.8 \text{ m} > u_{jo} + u_{ab} = 0.25 \text{ m}$ in the short and long bridges, respectively. However, in order to examine the influence of the abutment-backfill system on the rocking response of bridges in more detail, both failure modes for bridges (i.e., abutment failure as per Kappos *et al.* 2007 described in §3.3.4.1 and overturning) are plotted in the failure graphs of Fig. 3-14, and they are compared with the overturning condition of the equivalent frames without abutments. It is noted that the unsafe area will not be examined with respect to the number of impacts before failure as described in §2.3.1.3. The FMAS in Fig. 3-14 are constructed by obtaining the response-history of the pier rotation (θ) (§3.3) for different values of the dimensionless parameters ω_p/p and $\alpha_p/g \cdot \tan\alpha$. A wide range of pulse durations and acceleration amplitudes are considered to obtain a broad view of the likelihood of failure for different scenarios. The ground motion parameters are scaled gradually with respect to the rocking properties, or for pulses of constant angular frequency $\omega_p = [0.1 \sim 6] \cdot p$ (and $p = 0.82 \text{ rad/s}$), the acceleration amplitude $\alpha_p = [0.1 \sim 15] \cdot g \cdot \tan\alpha$ (and $g \cdot \tan\alpha = 0.082 \text{ g}$) is gradually increased to determine the minimum acceleration that induces failure.

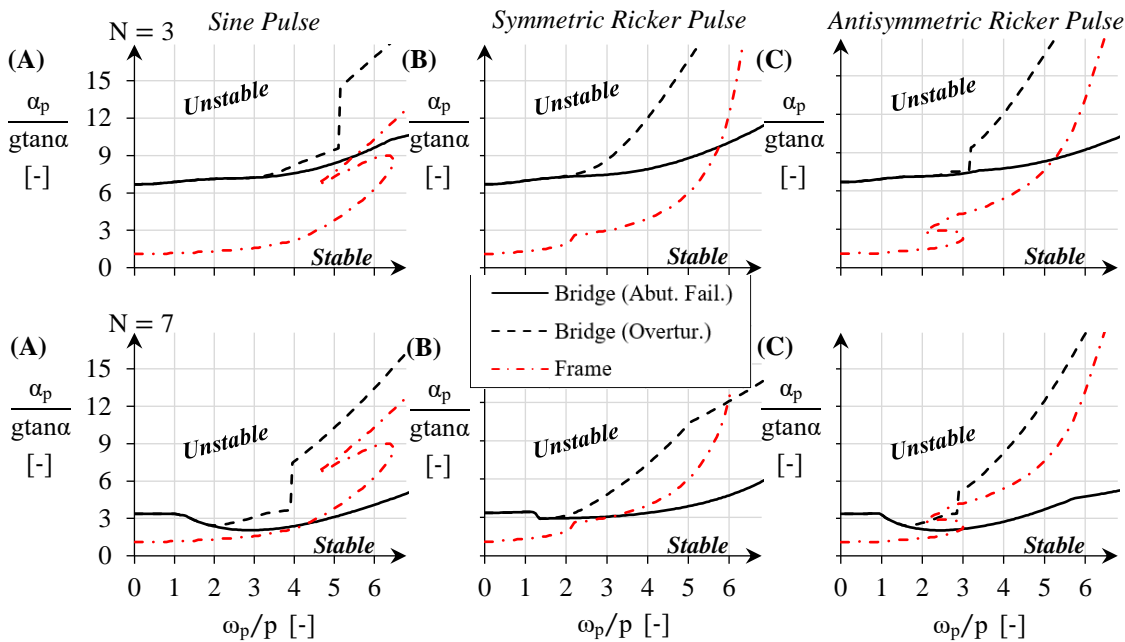


Fig. 3-14 FMAS for the symmetric bridges and for the equivalent frames with $N = 3$ and $N = 7$ rocking piers. Results obtained when subject to acceleration pulses of (A) sine, (B) symmetric and (C) antisymmetric Ricker type.

As expected, the overturning behaviour of frames with rocking columns is predictable, showing high vulnerability to low-frequency acceleration pulses, which is gradually decreased for medium- and high-frequency pulses as also found in previous works (see Fig. 2-10). However, and compared to frames, although the seismic performance of the short bridge with $N = 3$ rocking piers against pier overturning is slightly differentiated by revealing a plateau in the medium-frequency pulses (1 ~ 3 Hz, depending on the shape of the pulse-type motion), the corresponding failure mode for the long bridge with $N = 7$ rocking piers shows the highest sensitivity within this frequency range. Moreover, the hitherto ignored failure mode at the abutments modifies the failure spectrum of rocking structures to one that can be described as ‘sickle’ shaped. Specifically, the curves representing collapse of the bridge systems show that failure of the abutments and overturning coincide over a considerable range of frequency pulses (up to approximately 3 Hz for the bridge with $N = 3$ rocking piers and up to 2 Hz for the bridge with $N = 7$ rocking piers), implying that the same pulse-like ground motion is able to induce either failure mode. Interestingly, within this low-frequency range, the FMAS for the bridges present a straight branch (up to 1 Hz for both bridges, independently of the pulse type), which is followed by a zone wherein the critical acceleration either is insensitive or decreases with increasing ω_p/p . The results suggest that lower values of q ($q = 0.234 \cdot 10^{-3}$ m/kN for the bridge with $N = 7$ rocking piers) lead to a decreasing zone, while larger values of q ($q = 0.545 \cdot 10^{-3}$ m/kN for the bridge with $N = 3$ rocking piers) keep the value of α_p almost constant, thus the shape of the failure spectrum for the bridge depends on the level of influence of the abutment-backfill system. This type of behaviour is not observed in the corresponding frames. The straight branch in the FMAS for bridges shows critical acceleration amplitudes that are up to six and three times higher than those for the frames corresponding to the short and the long structures, respectively, while the plateau and decreasing zones of the bridge

FMAS are more similar to the overturning failure of the frames. After that point and as expected from the foregoing discussions about the prevailing failure mode of the bridges, the minimum acceleration amplitude that activates pier overturning increases with ω_p/p at a much higher rate than that for abutment failure, which is less sensitive to the dimensionless frequency parameter ω_p/p . For this reason, the minimum acceleration that induces overturning in the piers is up to five times larger than that for abutment failure in the high-frequency region, for both bridge configurations. Interestingly, the abutment failure mode precedes overturning in the range of medium and high-frequency acceleration pulses (after 5 Hz for the short structure and after 3 Hz for the long one, depending on the type of pulse-type motion). Hence, there are cases where the overturning mode of the frame model overestimates the bridge safety compared to the abutment failure, and the present thesis establishes the need for accounting for all expected failure modes in bridges with rocking piers. Nevertheless, by examining pier overturning of the bridge structures notwithstanding abutment failure, the beneficial influence of the abutment-backfill system in preventing overturning in bridges with rocking piers compared to equivalent frames is also observed. However, opposite trends are observed for the long system when high-frequency symmetric Ricker pulses of large magnitude are considered (Fig. 3-14B), but they only occur for extreme situations and do not change the main observation that bridges have better seismic performance than corresponding frames.

Fig. 3-14 also indicates that a ‘self-similar response’ (Makris & Vassiliou 2013) is achieved for the frame systems when subjected to pulses of the same form. In other words, with $B = 0.9$ m, $H = 11$ m and $\gamma = 4.8$ for both frame configurations, the overturning curves are exactly the same regardless of the total length or mass of the structure. However, the overturning curves of the short and the long bridges are different when pulses of the same type are examined, which is attributed to the influence of the total mass of the system on the abutment-backfill parameter q . Specifically, a larger overturning zone appears for the long bridge than for the short one. According to Fig. 3-3, the short bridge is expected to interact to a higher extent with the abutment-backfill system than the long bridge because its parameter q is lower ($q = 0.545 \cdot 10^{-3}$ m/kN in the short bridge and $q = 0.234 \cdot 10^{-3}$ m/kN in the long one), which implies that the long bridge response is closer to that of the frame. Accordingly, the short bridge is safer from the point of view of abutment failure than the long one considering the same type of pulse ground motion. Hence, self-similarity in bridge structures can be accomplished only if different properties for the abutment and the backfill are selected in relation to the weight of the corresponding configuration (e.g., for the heavy bridge examined, larger abutment dimensions should be selected in the first place, leading to larger values of k and c to counteract the decreased value of q compared to the light system). To this end, joint gaps (u_{jo}) with the same length are also required for the different configurations, highlighting even more the complexity of the rocking problem in bridges. Consequently, bridges with rocking piers cannot achieve self-similar response in the context adopted so far (i.e., structures with same values for B , H and γ independently of the total length or mass of the structure) due to the fact that different values must be selected for the spring stiffness (k) and the dashpot coefficient (c), which should be directly proportional to the influence of the abutment-backfill system (q). Thus, the FMAS for

bridges differs in principle from that for frames due to the presence of the abutment-backfill system, making the rocking response of the bridge configuration more non-linear.

3.3.5.2 Rocking Response under Multi-frequency Synthetic Ground Motions

This section extends the seismic performance analysis of the same symmetric bridges with rocking piers and relevant frames (§3.3.1, §3.3.4.1, §3.3.4.2, §3.3.4.3, §3.3.4.4) subject to the acceleration histories composed of a wide range of frequencies (§3.3.2.2). Fig. 3-15A, B illustrate the peak responses of the superstructure longitudinal displacement (u_{deck}^{CG}) in the structures with $N = 3$ and $N = 7$ rocking piers, respectively; the displacement at the contact with the abutments (dotted line) and the ultimate displacement demand in the abutment-backfill systems (dashed line) are also shown for the bridge structures.

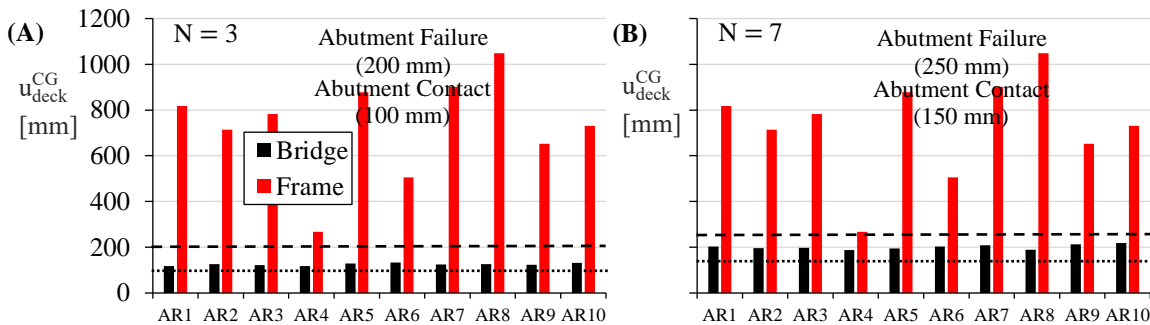


Fig. 3-15 Peak responses of the longitudinal displacement of the superstructure (u_{deck}^{CG}) for the symmetric bridges and for the equivalent frames with (A) $N = 3$ and (B) $N = 7$ rocking piers. Results obtained when subject to ARi.

As expected, due to self-similarity in rocking response, the frame models for the short and long configurations present the same peak responses, independently of the total length or mass of the structure as shown in Fig. 3-15. It is observed that the frame system develops longitudinal displacements that are significantly larger compared to those in a bridge with abutments. On average, the frame system overestimates the rocking amplitudes in the corresponding short structure by 439% (Fig. 3-15A), and in the long structure approximately by 228% (Fig. 3-15B). The reduced overestimation for the long structure is attributed to the stabilising effect of the abutments, directly proportional to the decreased value of q , confirming the decreased contribution of the abutment-backfill system to the rocking performance of heavy bridges. Moreover, comparison in a performance assessment context reveals that the bridge and frame models do not trigger the prevailing failure modes of abutment-backfill system and overturning, respectively, in any case. The lowest safety margin against the corresponding prevailing failure mode of each system is found for the long bridges against abutment failure and it is about 31% for AR10, while in the frame models and the short bridges the corresponding values are 42% against overturning (1800 mm ultimate superstructure capacity) for AR8 and 66% against the abutment failure for AR6, respectively. Thus, slightly stronger ground motions could trigger abutment failure for the long bridges, while the frame models could maintain their integrity, confirming that the frame system without end supports misses potential failure modes, thus overestimating bridge safety.

Additionally, superstructure longitudinal displacements higher than 700 mm as those met for the frame models are considered as extreme for the considered bridge structures under seismic actions meaningful for design. It is also observed that the record-to-record variability of the response is much more significant in the frames than in the bridges, for which the peak response is almost unaffected by the randomness in the AR, particularly in the short bridge. Thus, it can be concluded that the frame model without abutments is unconservative for predicting in a comprehensive way the rocking response of real bridges, as the contribution of the abutment-backfill system is crucial for assessing their performance.

Fig. 3-16A, B show the histories of the longitudinal displacement of the deck (u_{deck}^{CG}) for the structures with $N = 3$ and $N = 7$ rocking piers, respectively when subjected to two of the ARs. Again, the displacements describing the contact between the deck and the abutments (dotted line) and the failure of the abutment-backfill systems (dashed line) are illustrated. It is observed that rocking initiates at $t \approx 6$ s for both bridge and frame structures, independently of the effect of the abutments (i.e., rocking initiation is the same for bridges and frames following Eq. (3-8)). Similarly, and after rocking initiation, the results show that in the very first rocking cycles (up to $t \approx 8$ s) the two structures behave in the same way while the abutment-backfill system has not been activated and the free rocking motion prevails (i.e., only the term ‘frame system’ in Eq. (3-20) is active in the EoM of the bridge structure).

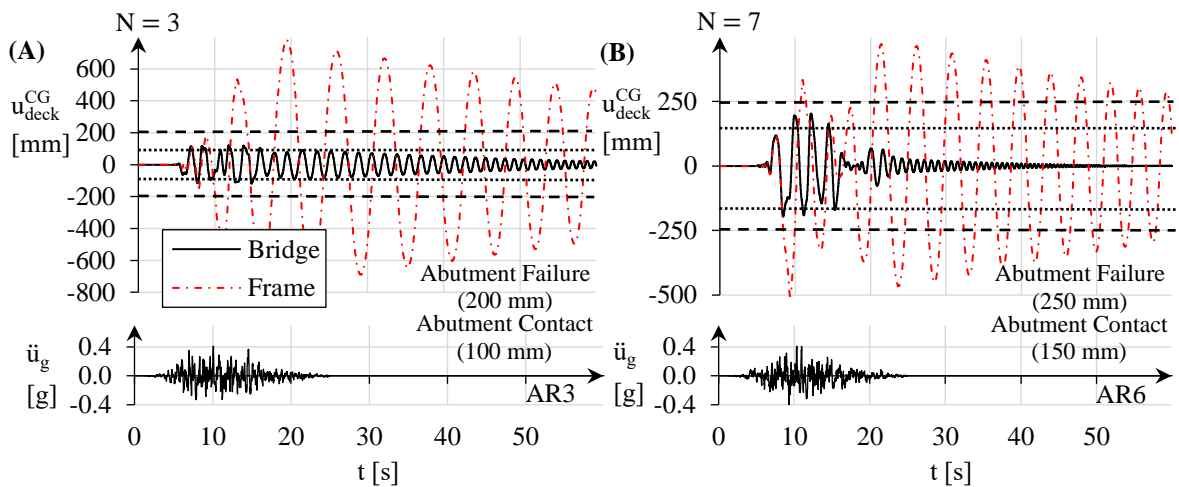


Fig. 3-16 Histories of the longitudinal displacement of the superstructure (u_{deck}^{CG}) for the symmetric bridges with rocking piers and for the equivalent frames. Results obtained for (A) the structure with $N = 3$ piers when subject to AR3 and for (B) the structure with $N = 7$ piers when subject to AR6.

Fig. 3-16 shows that, after the first rocking cycles, the history of the superstructure displacement in the frames has significantly larger rocking amplitudes than those in the bridges, and the rocking movement also lasts much longer. In fact, the rocking motion of the bridges almost stops when the ground motion finishes at $t \approx 25$ s, while at the same time the corresponding frames experience some of the highest rocking amplitudes for the entire dynamic response. The improved seismic behaviour of the bridges is attributed to the effect of the abutment and the backfill from $t \approx 8$ s to the end of the record ($t \approx 25$ s), when the longitudinal movement of the deck is large

enough to close the gap at the joints. In this interval, the bridge systems impact on the abutment systems which force them to return to the at-rest position and, at the same time, dissipate energy, whereas the frame systems are free to experience some large rocking amplitudes, exceeding 500 mm and 350 mm for the frames with $N = 3$ and $N = 7$ rocking piers, respectively. Thus, despite the slightly lower energy dissipation at each impact at the rocking interfaces for the bridges compared to the frames (i.e., the CoR at the rocking interfaces are around $\eta = 0.986$ and $\eta = 0.99$ for frame and bridge systems, respectively), the rocking motion of the systems accounting for the abutment-backfill behaviour is considerably suppressed compared to the frames. It is noted, though, that when the abutment-backfill effect is considered, additional energy is dissipated at each contact of the deck with the abutments through pounding and also the radiation and material damping of the backfill soil simulated by the dashpot elements at each end of the superstructure. For this reason, the total energy dissipated by a bridge structure is considerably higher than that for a simple frame model. It is also important to note that the number of impacts at the rocking interfaces during the rocking motion is significantly reduced in the bridge structures compared to their corresponding frames, which reduces the potential damage in the rocking interface and the risk of rocking instability (Mathey *et al.* 2016).

3.4 Closing Remarks

Chapter 3 extended the study on the dynamic response and the seismic performance of free-standing symmetric frames with rocking columns presented in Makris & Vassiliou (2013) by including in the formulation the abutment-backfill system at each end of the superstructure. In this respect, the rocking motion of a bridge with rocking piers can be described by a sequence of events. Specifically, the rectangular piers enter longitudinal rocking about their CR and force the superstructure to move; this movement of the deck is a pure translation due to the symmetric configuration of the system. If the movement of the superstructure is sufficient to close the end joint gaps (u_{jo}), pounding takes place through a CoR value e and, afterwards, the abutment-backfill system is activated. This is modelled through the parallel effect of a linear spring (k) and a linear dashpot (c) element that are located at each end of the superstructure. Impacts at the rocking interfaces occur when the bridge returns at the at-rest position, and the energy dissipation is described by means of another CoR value η .

To formulate this motion, a Lagrangian formulation was followed to derive the EoM in the longitudinal direction of the bridge with rocking piers, a ‘stereomechanical’ approach to represent pounding, whilst the impact at the rocking interfaces was expressed through an impulse formulation. The latter is based on the conservation of momentum assuming that the impact forces (or impulses) are applied at the imminent pier pivots (i.e., Housner’s approach, see §2.3.1.2), while the impulses developed at the soffit of the deck and at the abutment seats are related through their tributary zones. The influence of each span length (L_1 and L_2) is also taken into account in the formulation to model realistic span arrangements.

The following conclusions were drawn for the proposed bridge model compared to the frame configuration adopted so far for modelling bridges (Makris & Vassiliou 2013)

- Initiation of rocking motion occurs at the same time-instant for the two systems. This is done considering that the frictionless sliding bearings at the abutment seats of the bridge do not restrain the longitudinal movement of the superstructure, and a non-zero joint length is assumed at each end of the superstructure (u_{jo}), thus allowing the free rocking motion of the bridge system till closure of the end gap.
- The EoM accounts for the stages before and after the closure of the gap at the bridge end joints. The former is the EoM of the frame system without abutments studied in previous works, while the latter expresses the resistance of the spring (k) and dashpot (c) elements at each end of the deck to the free rocking motion of the structure. In this regard, the EoM of the symmetric bridge with rocking piers cannot be related with the corresponding frame in the context adopted so far for relevant frames and columns.
- The level of resistance of the abutment-backfill system to the free rocking motion of the structure depends on a new parameter q which appears in the EoM of the bridge. The results indicate that the lower the total mass of the system, the higher the value of q is, indicating a stronger interaction with the spring (k) and dashpot (c) elements of the abutment-backfill system.
- The CoR to describe attenuation of rocking motion when an impact at the rocking interfaces occurs (η) is derived based on the impulses developed at the different impact points, including the impulses at the abutment seats, and accounting for the length of the end (L_1) and the intermediate spans (L_2), as well as the number of piers (N) in the bridge, which are parameters that do not affect the value of the corresponding frame without abutments presented in Makris & Vassiliou (2013). The dissipated energy at each impact at the rocking interfaces for a bridge structure is always lower than that of a frame with equivalent characteristics due to the influence of the vertical supports of the abutments which carry part of the weight of the superstructure, thus reducing the weight that goes to the piers.
- The frame model without abutments cannot capture the energy dissipation associated with the impact of the deck on the abutment backwall (e) and, subsequently, the activation of the dashpot element (c) at each bridge end. Hence, the total energy dissipated by the bridge system is higher compared to the corresponding frame without abutments.
- An additional failure criterion is introduced to describe the failure of the abutment-backfill system. This is defined in a way that is consistent with the failure due to overturning of the rocking piers.

- The joint length (u_{jo}) highly influences the performance of the proposed bridge configuration. Large gap sizes reveal low longitudinal effective stiffness in the closed gap stage of the system, thus resulting in increased superstructure displacements compared to the same structure with small joint lengths. On the contrary, the response of the suggested model remains almost unaffected by the choice of the spring stiffness (k), the dashpot coefficient (c) and the CoR to describe pounding (e).
- To incorporate failure of the abutment-backfill system in the assessment of bridges with rocking piers, the existing overturning spectra for pulse-type motions (OMAS) were extended in this work to so-called FMAS. The FMAS differ from the corresponding OMAS in terms of the failure modes considered and on the basic rules on which the seismic stability of rocking structures is assessed.
- Structures with equivalent characteristics (i.e., same B , H and γ) and the same properties for the abutment, the backfill and the end joint at each bridge end (i.e., same k , c , e and u_{jo}), but with different level of interaction with the abutment-backfill system (i.e., different value for q) yield different rocking responses. Thus, self-similarity in bridge structures cannot be achieved in the context adopted so far for frame models.
- The failure mode of the bridge structure can be determined a priori based on the mechanical properties of the structure. This is confirmed by the FMAS obtained for two conventional bridges which are more prone to fail the abutment-backfill system than to overturn.
- The FMAS for the two conventional bridges and same frames without abutments suggest that the bridge system is more stable against overturning compared to the frame system. The consideration of the abutment failure of the bridge structure in the FMAS results in a ‘sickle’ shaped diagram; the shape of this spectrum depends on the level of influence of the abutment-backfill system, with lower values of q resulting in higher vulnerability in medium-frequency pulses. This failure mode is not observed in frames and it can precede the overturning of piers in the medium-to-high frequency range. Hence, the frame model can be more conservative in some cases than the model accounting for the abutment-backfill system.
- The frame model predicts longitudinal displacements of the superstructure that are extremely large under the action of design spectrum-compatible ground motions. The results indicate that the frame model is not realistic enough to assess the rocking motion of bridges, because it considerably overestimates their seismic response in terms of rocking amplitudes, duration of the rocking response and, as a result, the number of impacts at the rocking interfaces. The more pragmatic behaviour predicted by the proposed model is due to accounting for the beneficial contribution of the abutment-backfill system in suppressing the free rocking motion of the structure.

Chapter 4

Analytical Modelling of Asymmetric Bridges with Rocking Piers

4.1 Introduction

Chapter 4 examines the complex dynamics and the seismic performance of bridges with rocking piers that have an irregular configuration (i.e., consisting of piers with unequal height), which is the rule case in bridges (in ravine or valley crossings). In this regard, the proposed analytical model extends the asymmetric frame presented in the work of Dimitrakopoulos & Giouvanidis (2015) (see also §2.3.2), and it includes the same *modifications and advancements* compared to the frame approach as those presented in §3.1 for the symmetric configuration. Additionally, this work extends/generalises the analytical model presented in §3 by addressing the issue of asymmetry (§2.3.2.1 and Fig. 2-14) in rocking motion of bridges, and it includes the following *modification*;

- Generalisation of the regular configuration with N rocking piers of the same height that was presented in §3 to an irregular system with two rocking piers of unequal height.

In this respect, the dynamics of the asymmetric bridge is described in §4.2 followed by the complex kinematics of this configuration (§4.2.1). The condition to describe rocking initiation for the irregular structure is given in §4.2.2, followed by the development of the EoM for the free rocking stage and the consideration of the increased longitudinal stiffness of the system due to the presence of the abutment-backfill system in §4.2.3. The energy dissipation due to impacts on the abutment backwall and at the rocking interfaces constitute two inherent stability mechanisms of the rocking system, and these are captured through a corresponding CoR as discussed in §4.2.4 and §4.2.5, respectively. From the response analysis point of view (§4.3), this chapter investigates bridges with rocking piers of different configuration (§4.3.1) under ‘extreme’ earthquake conditions (§4.3.2), and it assesses their seismic behaviour in a performance assessment context (§4.3.3). In an effort to reduce the computational cost when asymmetric bridges are analysed, the complex equations that govern their response are simplified in §4.3.4. Finally, the seismic performance of symmetric (§3) and asymmetric bridges is compared in §4.3.5 to evaluate the effect of irregularity in pier height in the rocking motion of bridges.

4.2 Analytical Model of the Rocking Response

This section presents an analytical model to describe the longitudinal rocking motion of straight bridges supported by two piers with the same rectangular section in elevation and different height,

accounting for the effect of the abutment and the backfill. Fig. 4-1 illustrates the bridge configuration at the at-rest position of equilibrium subject to a horizontal ground acceleration history \ddot{u}_g . The deck consists of a continuous box girder section with depth $2h$, cross-sectional area A_{deck} and total length $L_{tot} = 2L_1 + L_2$. The deck is free to move longitudinally until the joint gap between one of its ends and the abutments is closed (u_{jo}). At this instant, an impact on the abutment backwall with height h_{bw} occurs. The superstructure is supported on frictionless sliding bearings at the abutment seats E and E' (§3.2) and on the two free-standing rocking piers ($N = 2$). The piers have a width $2B$ and unequal heights $2H_1$ and $2H_2$ for the tall and short piers, respectively. The semi-diagonals of both piers are given by $R_1 = \sqrt{H_1^2 + B^2}$ and $R_2 = \sqrt{H_2^2 + B^2}$, while the slenderness parameters are $\alpha_1 = \tan^{-1}(B/H_1)$ and $\alpha_2 = \tan^{-1}(B/H_2)$, respectively. Special grooved caps are introduced at the bottom and the top surfaces of both piers to allow free rocking on the base (CR A'-A for the tall pier and CR C'-C for the short pier) and the deck interfaces (accordingly, points B-B' and points D-D'), while preventing sliding in these faces. With reference to the symmetric system (§3.2), two new parameters are integrated in the rocking formulation which are the distance between the CR of the piers at the foundation level $2r_{AC} = \sqrt{(2H_1 - 2H_2)^2 + L_2^2}$, and the angle between this line and the horizontal $\phi_{AC} = \tan^{-1}((2H_1 - 2H_2)/L_2)$. Furthermore, an additional criterion is adopted to address the complex dynamics of the asymmetric system;

- The free-standing rocking piers are assumed to have same longitudinal (along-X) displacements despite their different height. This assumption is in line with the work of Dimitrakopoulos & Giouvanidis (2015), where the dynamics of asymmetric frames with rocking columns was studied. Additionally, the asymmetric rocking configurations that are analysed numerically in §6.4.1.3 and §6.4.2.3 using the commercial FE analysis software ABAQUS CAE (2018) without the mentioned kinematic constraint verify the validity of this assumption.

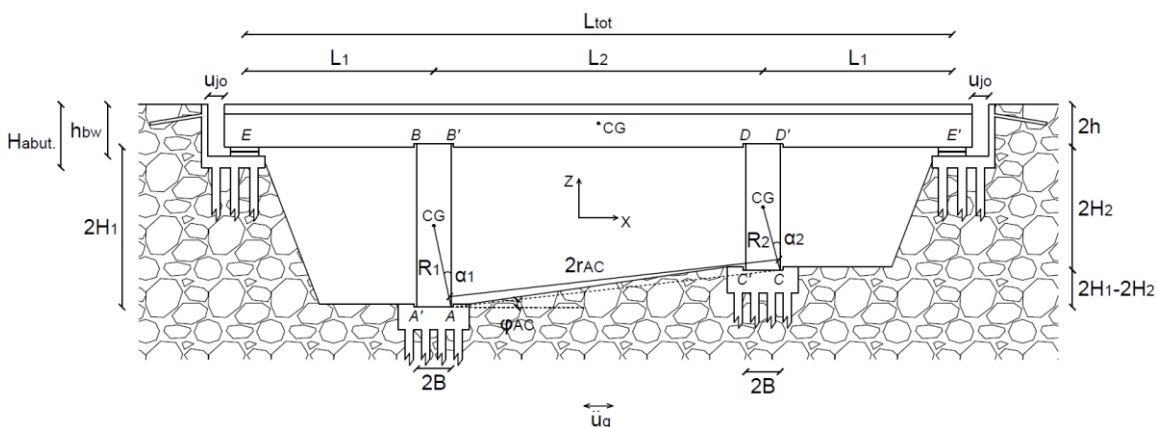


Fig. 4-1 Schematic of an asymmetric bridge supported on two rectangular-in-elevation free-standing rocking piers, and on frictionless sliding bearings at the abutment seats. The bridge is at the at-rest position.

4.2.1 Kinematics

Fig. 4-2A, B illustrate the rocking motion of the asymmetric bridge for counter-clockwise (positive, superscript p) and clockwise (negative, superscript n) rotations, respectively; it is noted that the positive rotation in the asymmetric system is opposite to that adopted in the symmetric configuration (§3.2.1). The effect of the abutment and the backfill at each end of the bridge is modelled through a Kelvin-Voigt system (spring (k) and dashpot (c) in parallel elements).

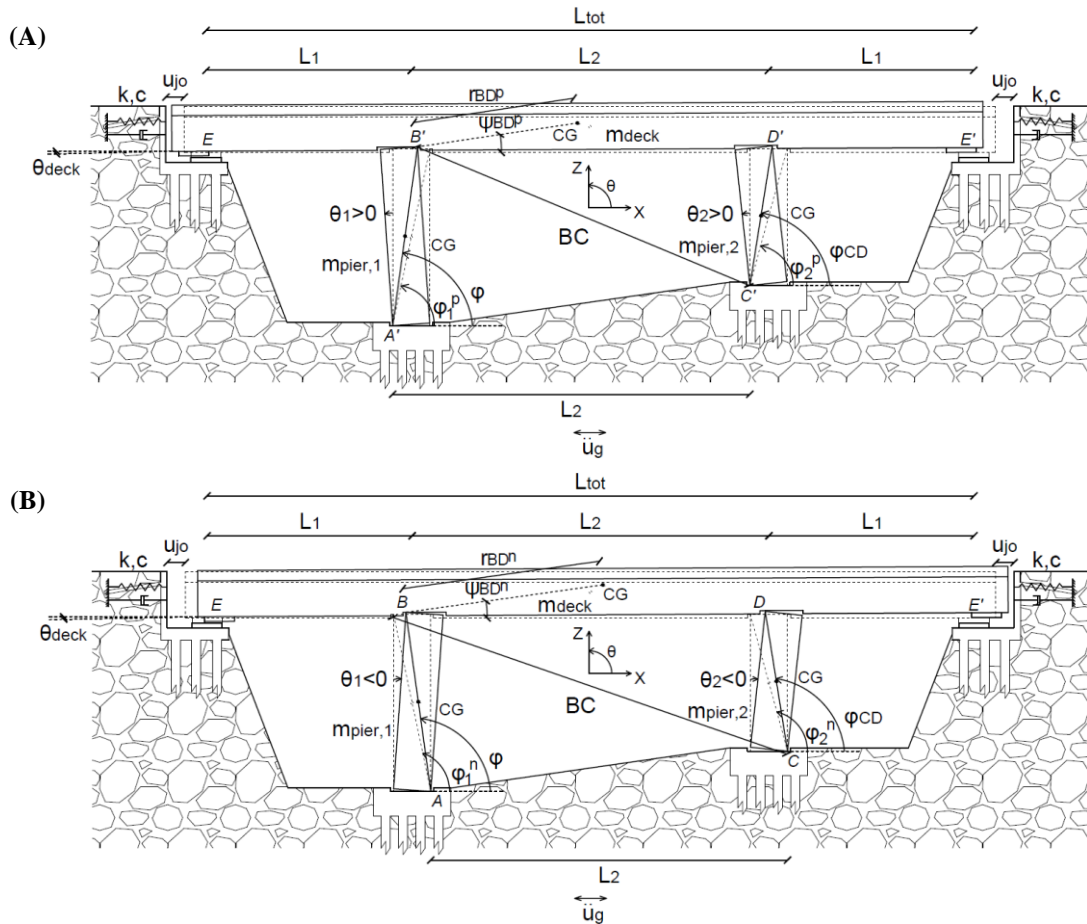


Fig. 4-2 Schematic of an asymmetric bridge with rocking piers during rocking motion. The structure sustains (A) counter-clockwise (positive) rotation of the piers, and (B) clockwise (negative) rotation of the piers.

Despite the complexity of the system, the longitudinal rocking motion of the bridge can be described by a single DoF. This is selected as the angle ϕ formed between the horizontal (X) axis and the diagonal of the tall pier (starting from the CR at its base). Consequently, the relative rocking rotation of the tall pier (θ_1) is given by the following expression

$$\theta_1 = \phi - \varphi_1^{p/n}, \quad (4-1)$$

where $\varphi_1^{p/n} = \pi/2 \mp \alpha_1$ represents the angle at the at-rest position of the tall pier. It is noted that the diagonal that is required for determining φ_1^p (i.e., the angle at the at-rest position for positive

relative rotation of the piers) and φ_1^n (i.e., the angle at the at-rest position for negative relative rotation of the piers) is different depending on the direction of the movement and, therefore, it is determined in each case by the pivot points that drive the rocking motion of the tall pier, as shown in Fig. 4-2. To this end, the double sign formulation (\mp) describes the different directions of movement, with the top sign referring to positive relative rotation of the piers and vice-versa for the bottom one. This convention is maintained in the remainder of Chapter 4.

Similarly, the rocking tilt for the short pier is simply expressed by $\theta_2 = \varphi_{CD} - \varphi_2^{p/n}$, where $\varphi_2^{p/n} = \pi/2 \mp \alpha_2$ is the angle at the at-rest rotation. With this notation the dependent variable φ_{CD} is a function of the geometrical properties of the rocking configuration

$$\varphi_{CD} = \pi + \tan^{-1} \left(\frac{R_1 \sin \varphi - r_{AC} \sin \varphi_{AC}}{R_1 \cos \varphi - r_{AC} \cos \varphi_{AC}} \right) - \cos^{-1} \left(\frac{BC^2 + 4R_2^2 - L_2^2}{4R_2 BC} \right), \quad (4-2)$$

where $BC = \sqrt{(2R_1)^2 + (2r_{AC})^2 - 8R_1 \cdot r_{AC} \cdot \cos(\varphi - \varphi_{AC})}$ is the length from point B' to point C' (or from B to C) as shown in Fig. 4-2. Contrary to the symmetric bridge (§3.2.1), and due to the irregular arrangement of the piers, the deck is forced to have a translational movement in the longitudinal and vertical directions (along the X and the Z axes, respectively) that occurs simultaneously with a rotational movement (about the Y axis). The rocking rotation of the deck is given by the following expression

$$\theta_{deck} = \tan^{-1} \left(\frac{-R_1 \sin \varphi + r_{AC} \sin \varphi_{AC} + R_2 \sin \varphi_{CD}}{-R_1 \cos \varphi + r_{AC} \cos \varphi_{AC} + R_2 \cos \varphi_{CD}} \right). \quad (4-3)$$

The longitudinal (u) and the vertical (v) relative displacements of the CG of the tall and the short piers are expressed in terms of the DoF φ in Eqs. (4-4) and (4-5), with the corresponding displacements of the CG of the deck being related to φ in Eq. (4-6)

$$\begin{aligned} u_{pier,1}^{CG} &= R_1 \cos \varphi \mp B && \text{and} \\ v_{pier,1}^{CG} &= R_1 \sin \varphi - H_1, \end{aligned} \quad (4-4)$$

$$\begin{aligned} u_{pier,2}^{CG} &= R_2 \cos \varphi_{CD} \mp B && \text{and} \\ v_{pier,2}^{CG} &= R_2 \sin \varphi_{CD} - H_2, \end{aligned} \quad (4-5)$$

$$\begin{aligned} u_{deck}^{CG} &= 2R_1 \cos \varphi + r_{BD}^{p/n} \cos(\theta_{deck} + \psi_{BD}^{p/n}) \mp B - \frac{L_2}{2} && \text{and} \\ v_{deck}^{CG} &= 2R_1 \sin \varphi + r_{BD}^{p/n} \sin(\theta_{deck} + \psi_{BD}^{p/n}) - 2H_1 - h, \end{aligned} \quad (4-6)$$

in which $r_{BD}^{p/n} = \sqrt{h^2 + (L_2/2 \mp B)^2}$ is the distance from the CR of the tall pier B' or B (i.e., depending on the direction of the movement) to the CG of the deck, and $\psi_{BD}^{p/n} = \tan^{-1}(h/(L_2/2 \mp B))$ describes the angle between the horizontal axis (X) and the line that connects B' (or B) and the CG of the deck. The convention for positive displacements is shown in Fig. 4-2.

The linear velocities of the piers and the deck in the longitudinal and the vertical directions (\dot{u} and \dot{v}) can be found as the first time-derivatives of Eqs. (4-4) to (4-6) in the following expressions

$$\begin{aligned} \dot{u}_{pier,1}^{CG} &= [-R_1 \sin \varphi] \dot{\varphi} & \text{and} \\ \dot{v}_{pier,1}^{CG} &= [R_1 \cos \varphi] \dot{\varphi}, \end{aligned} \quad (4-7)$$

$$\begin{aligned} \dot{u}_{pier,2}^{CG} &= \left[-R_2 \sin \varphi_{CD} \frac{\partial \varphi_{CD}}{\partial \varphi} \right] \dot{\varphi} & \text{and} \\ \dot{v}_{pier,2}^{CG} &= \left[R_2 \cos \varphi_{CD} \frac{\partial \varphi_{CD}}{\partial \varphi} \right] \dot{\varphi}, \end{aligned} \quad (4-8)$$

$$\begin{aligned} \dot{u}_{deck}^{CG} &= \left[-2R_1 \sin \varphi - r_{BD}^{p/n} \sin(\theta_{deck} + \psi_{BD}^{p/n}) \frac{\partial \theta_{deck}}{\partial \varphi} \right] \dot{\varphi} & \text{and} \\ \dot{v}_{deck}^{CG} &= \left[2R_1 \cos \varphi + r_{BD}^{p/n} \cos(\theta_{deck} + \psi_{BD}^{p/n}) \frac{\partial \theta_{deck}}{\partial \varphi} \right] \dot{\varphi}, \end{aligned} \quad (4-9)$$

where $\dot{\varphi} = \dot{\theta}_1$ describes the angular velocity of the tall pier. During the free rocking motion of the system, the translational masses of the tall ($m_{pier,1} = 8\rho \cdot B^2 \cdot H_1$) and the short piers ($m_{pier,2} = 8\rho \cdot B^2 \cdot H_2$) as well as that of the deck ($m_{deck} = 2\rho \cdot A_{deck} \cdot L_{tot}$) tend to restore the bridge to the at-rest position. Additionally, and considering that all members rotate with respect to the Y axis, the rotational masses of all members resist the induced rotational movement. The expressions for the rotational inertia with respect to the CG of the tall and the short rectangular piers are $I_{pier,1}^{CG} = m_{pier,1} \cdot R_1^2/3$ and $I_{pier,2}^{CG} = m_{pier,2} \cdot R_2^2/3$, respectively. Accordingly, the rotational inertia of the box girder section of the deck is calculated according to the parallel axis theorem, $I_{deck}^{CG} = \sum m_{deck,i} \cdot r_i^2$, where $m_{deck,i}$ is the mass of a small element of the box girder section and r_i is the perpendicular distance from the CG of the element to the CG of the whole deck section.

4.2.2 Initiation of Rocking Motion

The asymmetric bridge enters rocking motion due to a lateral ground motion ($\ddot{u}_{g,min}$) that is capable of inducing uplift in the entire system. At that instant, from the application of the principle of virtual work to the bridge the following expression can be determined

$$m_{pier,1}\ddot{u}_{g,\min}\delta u_{pier,1}^{CG} + m_{pier,2}\ddot{u}_{g,\min}\delta u_{pier,2}^{CG} + m_{deck}\ddot{u}_{g,\min}\delta u_{deck}^{CG} = m_{pier,1}g\delta v_{pier,1}^{CG} + m_{pier,2}g\delta v_{pier,2}^{CG} + m_{deck}g\delta v_{deck}^{CG}, \quad (4-10)$$

where $\delta u_{pier,1}^{CG}$, $\delta v_{pier,1}^{CG}$, $\delta u_{pier,2}^{CG}$, $\delta v_{pier,2}^{CG}$, δu_{deck}^{CG} and δv_{deck}^{CG} are calculated by introducing Eqs. (4-4) to (4-6) into Eq. (3-6). Substituting the relative rotations of the piers (θ_1 and θ_2) into Eq. (4-10) gives

$$\begin{aligned} & m_{pier,1}\ddot{u}_{g,\min} \left[R_1 \sin(\theta_1 + \varphi_1^{p/n}) \delta\varphi \right] + m_{pier,2}\ddot{u}_{g,\min} \left[R_2 \sin(\theta_2 + \varphi_2^{p/n}) \frac{\partial\varphi_{CD}}{\partial\varphi} \delta\varphi \right] \\ & + m_{deck}\ddot{u}_{g,\min} \left[2R_1 \sin(\theta_1 + \varphi_1^{p/n}) + r_{BD}^{p/n} \sin(\theta_{deck} + \psi_{BD}^{p/n}) \frac{\partial\theta_{deck}}{\partial\varphi} \delta\varphi \right] = \\ & m_{pier,1}g \left[R_1 \cos(\theta_1 + \varphi_1^{p/n}) \delta\varphi \right] + m_{pier,2}g \left[R_2 \cos(\theta_2 + \varphi_2^{p/n}) \frac{\partial\varphi_{CD}}{\partial\varphi} \delta\varphi \right] \\ & + m_{deck}g \left[2R_1 \cos(\theta_1 + \varphi_1^{p/n}) + r_{BD}^{p/n} \cos(\theta_{deck} + \psi_{BD}^{p/n}) \frac{\partial\theta_{deck}}{\partial\varphi} \delta\varphi \right]. \end{aligned} \quad (4-11)$$

Taking into account that the rocking motion has just started at this instant, hence $\theta_1 = \theta_2 = \theta_{deck} = 0$, and by cancelling out the rotation $\delta\varphi$, Eq. (4-11) is simplified to the following form after rearranging appropriately

$$\ddot{u}_{g,\min} = \pm \lambda g \tan \alpha_1 = \pm \frac{m_{pier,1} + m_{pier,2}\bar{h} + m_{deck} \left[1 + \bar{h} - 2\bar{b}(\pm\bar{h} \mp 1) \right]}{m_{pier,1} + m_{pier,2} + 2m_{deck} \left[\frac{\bar{b}\bar{h}}{H_1}(\pm\bar{h} \mp 1) + 1 \right]} g \tan \alpha_1, \quad (4-12)$$

where $\bar{h} = H_1/H_2$ is a ratio that indicates the asymmetry in the height of the rocking piers, and $\bar{b} = B/L_2$. Eq. (4-12) shows that the minimum ground acceleration amplitude that starts rocking of the bridge is different in the field of positive (referring to top sign) and negative rotations (referring to bottom sign). This is expected due to the asymmetric configuration of the system, and it is a key difference from the symmetric bridges with rocking piers, in which the initiation of the structural motion described in Eq. (3-8) is insensitive to the direction of movement. It is noted that when asymmetry is ignored ($\bar{h} = 1$ or $H_1 = H_2$) and by taking into account the different convention for positive rotations in the symmetric (§3.2.1) and in the asymmetric bridge (§4.2.1), Eq. (4-12) reduces to Eq. (3-8). As expected, and based on the foregoing discussion for the symmetric case (§3.2.2), this result is the same as in the corresponding frame with rocking columns (Dimitrakopoulos & Giouvanidis 2015), wherein the effect of the abutments and the backfill was ignored; this is because the effect of the end conditions does not affect the initiation of rocking considering a non-zero gap. It is also known that the factor λ , which is always greater than unity in the asymmetric bridge (§3.2.2), increases with the asymmetry in the height of the piers (higher

value of \bar{h}) (§2.3.2.2). Therefore, the more asymmetric the bridge, the longer is the delay in rocking initiation of the irregular system compared to the corresponding regular case.

4.2.3 Equation of Motion during Rocking

The rocking response of the asymmetric bridge is formulated using the Lagrangian Eq. (3-9), where the generalised coordinate (θ) and its first time-derivative ($\dot{\theta}$) are substituted by the corresponding generalised coordinates selected for this system (φ and $\dot{\varphi}$). The kinetic energy of the system with respect to the corresponding CG of the members that compose the bridge can be expressed as

$$T = \frac{1}{2} m_{pier,1} \left[\dot{u}_{pier,1}^{CG^2} + \dot{v}_{pier,1}^{CG^2} \right] + \frac{1}{2} I_{pier,1}^{CG} \dot{\varphi}^2 + \frac{1}{2} m_{pier,2} \left[\dot{u}_{pier,2}^{CG^2} + \dot{v}_{pier,2}^{CG^2} \right] + \frac{1}{2} I_{pier,2}^{CG} \dot{\varphi}_{CD}^2 + \frac{1}{2} m_{deck} \left[\dot{u}_{deck}^{CG^2} + \dot{v}_{deck}^{CG^2} \right] + \frac{1}{2} I_{deck}^{CG} \dot{\theta}_{deck}^2, \quad (4-13)$$

where $\dot{u}_{pier,1}^{CG}$, $\dot{v}_{pier,1}^{CG}$, $\dot{u}_{pier,2}^{CG}$, $\dot{v}_{pier,2}^{CG}$, \dot{u}_{deck}^{CG} and \dot{v}_{deck}^{CG} are given by Eqs. (4-7) to (4-9), respectively, while the angular velocities of the short pier ($\dot{\varphi}_{CD} = \dot{\theta}_2$) and the deck ($\dot{\theta}_{deck}$) are found from

$$\dot{\varphi}_{CD} = \frac{d\varphi_{CD}}{dt} = \frac{\partial\varphi_{CD}}{\partial\varphi} \frac{d\varphi}{dt} = \frac{\partial\varphi_{CD}}{\partial\varphi} \dot{\varphi}, \quad (4-14)$$

$$\dot{\theta}_{deck} = \frac{d\theta_{deck}}{dt} = \frac{\partial\theta_{deck}}{\partial\varphi} \frac{d\varphi}{dt} = \frac{\partial\theta_{deck}}{\partial\varphi} \dot{\varphi}. \quad (4-15)$$

Eqs. (4-14) and (4-15) are substituted into Eq. (4-13), which is subsequently rearranged to describe the total kinetic energy of the system with respect to the active CR

$$T = \left[\frac{1}{2} I_{pier,1}^{Pivot} + \frac{1}{2} I_{pier,2}^{Pivot} \left(\frac{\partial\varphi_{CD}}{\partial\varphi} \right)^2 + \frac{1}{2} I_{deck}^{Pivot} \left(\frac{\partial\theta_{deck}}{\partial\varphi} \right)^2 + m_{deck} \left(2R_1^2 + 2R_1 r_{BD}^{p/n} \cos(\varphi - \theta_{deck} - \psi_{BD}^{p/n}) \frac{\partial\theta_{deck}}{\partial\varphi} \right) \right] \dot{\varphi}^2, \quad (4-16)$$

wherein $I_{pier,1}^{Pivot} = 4 m_{pier,1} \cdot R_1^2/3$ is the mass moment of inertia of the tall rectangular pier with respect to the CR A' (or A), $I_{pier,2}^{Pivot} = 4 m_{pier,2} \cdot R_2^2/3$ refers to the short rectangular pier with respect to the CR C' (or C) and $I_{deck}^{Pivot} = I_{deck}^{CG} + m_{deck} \cdot r_{BD}^{p/n^2}$ refers to the deck section and the points B'-D' (or B-D). The potential energy components that describe the gravitational effects (V_{in}) and the elastic spring forces of the abutments (V_{as}) are given by

$$V_{in} = g \left[m_{pier,1} v_{pier,1}^{CG} + m_{pier,2} v_{pier,2}^{CG} + m_{deck} v_{deck}^{CG} \right], \quad (4-17)$$

$$V_{as} = \begin{cases} 0 \\ \frac{1}{2} k \left[u_{deck}^{CG} \pm u_{jo} \right]^2 \end{cases} \quad \text{if} \quad \begin{cases} |u_{deck}^{CG}| < u_{jo} \\ |u_{deck}^{CG}| \geq u_{jo} \end{cases}. \quad (4-18)$$

The total potential energy of the free-standing asymmetric system is derived by combining Eqs. (4-17) and (4-18), and after substituting Eqs. (4-4) to (4-6) it is simplified to

$$V = g \left[\begin{aligned} & m_{pier,1} (R_1 \sin \varphi - H_1) + m_{pier,2} (R_2 \sin \varphi_{CD} - H_2) \\ & + m_{deck} \left(2R_1 \sin \varphi + r_{BD}^{p/n} \sin(\theta_{deck} + \psi_{BD}^{p/n}) - 2H_1 - h \right) \end{aligned} \right] \\ + \frac{1}{2} k \left[\begin{aligned} & 4R_1^2 \cos^2 \varphi + r_{BD}^{p/n 2} \cos^2(\theta_{deck} + \psi_{BD}^{p/n}) + B^2 + \frac{L_2^2}{4} \\ & + 4R_1 r_{BD}^{p/n} \cos \varphi \cos(\theta_{deck} + \psi_{BD}^{p/n}) \mp 2B r_{BD}^{p/n} \cos(\theta_{deck} + \psi_{BD}^{p/n}) \pm BL_2 \\ & \mp 4R_1 B \cos \varphi - 2R_1 L_2 \cos \varphi - r_{BD}^{p/n} L_2 \cos(\theta_{deck} + \psi_{BD}^{p/n}) \\ & + \left(\pm 4R_1 \cos \varphi \pm 2r_{BD}^{p/n} \cos(\theta_{deck} + \psi_{BD}^{p/n}) - 2B \mp L_2 \right) u_{jo} + u_{jo}^2 \end{aligned} \right]. \quad (4-19)$$

It is noted that Eq. (4-19) accounts for the contact of the superstructure with the abutment ($|u_{deck}^{CG}| \geq u_{jo}$). Before contact is activated ($|u_{deck}^{CG}| < u_{jo}$), the term expressed by the spring stiffness k should be excluded from the calculation. The generalised forces $Q_{in} = \partial W_{in} / \partial \varphi$ and $Q_{ad} = \partial W_{ad} / \partial \varphi$ are given by the variation of the virtual work $\delta W_{in} = -\ddot{u}_g \cdot [m_{pier,1} \cdot u_{pier,1}^{CG} + m_{pier,2} \cdot u_{pier,2}^{CG} + m_{deck} \cdot u_{deck}^{CG}]$ and $\delta W_{ad} = -c \cdot \dot{u}_{deck}^{CG} \cdot [u_{deck}^{CG} \pm u_{jo}]$, respectively. Substituting Eqs. (4-4) to (4-6) and Eq. (4-9) in the expressions of the generalised forces results in

$$Q_{in} = \ddot{u}_g \left[\begin{aligned} & \left(m_{pier,1} + 2m_{deck} \right) R_1 \sin \varphi + m_{pier,2} R_2 \sin \varphi_{CD} \frac{\partial \varphi_{CD}}{\partial \varphi} \\ & + m_{deck} r_{BD}^{p/n} \sin(\theta_{deck} + \psi_{BD}^{p/n}) \frac{\partial \theta_{deck}}{\partial \varphi} \end{aligned} \right], \quad (4-20)$$

$$Q_{ad} = -4cR_1^2 \left[\sin \varphi + \bar{r}^{p/n} \sin(\theta_{deck} + \psi_{BD}^{p/n}) \frac{\partial \theta_{deck}}{\partial \varphi} \right]^2 \dot{\varphi}, \quad (4-21)$$

where $\bar{r}^{p/n} = r_{BD}^{p/n} / 2R_1$. The total effect of the generalised non-conservative forces (Q) is given by the sum of Eqs. (4-20) and (4-21). Introducing Eqs. (4-16), (4-19), (4-20) and (4-21) into Eq. (3-9) yields the EoM for the asymmetric bridge structure during rocking

$$\ddot{\varphi} = -\frac{g}{R_1} \left[\overbrace{-\frac{R_1}{g} \left(\frac{T_{f2}(\varphi)}{T_{f1}(\varphi)} \right) \dot{\varphi}^2 + \left(\frac{V_{inf}(\varphi)}{T_{f1}(\varphi)} \right) - \frac{\ddot{u}_g}{g} \left(\frac{Q_{inf}(\varphi)}{T_{f1}(\varphi)} \right)}^{\text{frame system}} \right] \underbrace{- \frac{g}{R_1} q \left[k \left(\frac{V_{asf}(\varphi)}{T_{f1}(\varphi)} \right) + c \left(\frac{Q_{adf}(\varphi)}{T_{f1}(\varphi)} \right) \dot{\varphi} \right]}_{\text{abutment-backfill contribution}}, \quad (4-22)$$

where

$$\begin{aligned} T_{f1}(\varphi) &= \frac{I_{pier,1}^{Pivot}}{R_1^2} + \frac{I_{pier,2}^{Pivot}}{R_1^2} \left(\frac{\partial \varphi_{CD}}{\partial \varphi} \right)^2 + m_{deck} \left[4 + 8\bar{r}^{p/n} \cos(\varphi - \theta_{deck} - \psi_{BD}^{p/n}) \frac{\partial \theta_{deck}}{\partial \varphi} \right] \\ &\quad + \frac{I_{deck}^{Pivot}}{R_1^2} \left(\frac{\partial \theta_{deck}}{\partial \varphi} \right)^2 \\ T_{f2}(\varphi) &= \frac{I_{pier,2}^{Pivot}}{R_1^2} \frac{\partial \varphi_{CD}}{\partial \varphi} \frac{\partial^2 \varphi_{CD}}{\partial \varphi^2} + 4m_{deck} \bar{r}^{p/n} \left[\cos(\varphi - \theta_{deck} - \psi_{BD}^{p/n}) \frac{\partial^2 \theta_{deck}}{\partial \varphi^2} \right. \\ &\quad \left. - \sin(\varphi - \theta_{deck} - \psi_{BD}^{p/n}) \frac{\partial \theta_{deck}}{\partial \varphi} \left(1 - \frac{\partial \theta_{deck}}{\partial \varphi} \right) \right] \\ &\quad + \frac{I_{deck}^{Pivot}}{R_1^2} \frac{\partial \theta_{deck}}{\partial \varphi} \frac{\partial^2 \theta_{deck}}{\partial \varphi^2} \\ V_{inf}(\varphi) &= \left[m_{pier,1} + 2m_{deck} \right] \cos \varphi + m_{pier,2} \bar{R} \cos \varphi_{CD} \frac{\partial \varphi_{CD}}{\partial \varphi} \\ &\quad + 2m_{deck} \bar{r}^{p/n} \cos(\theta_{deck} + \psi_{BD}^{p/n}) \frac{\partial \theta_{deck}}{\partial \varphi} \\ Q_{inf}(\varphi) &= \left[m_{pier,1} + 2m_{deck} \right] \sin \varphi + m_{pier,2} \bar{R} \sin \varphi_{CD} \frac{\partial \varphi_{CD}}{\partial \varphi} \\ &\quad + 2m_{deck} \bar{r}^{p/n} \sin(\theta_{deck} + \psi_{BD}^{p/n}) \frac{\partial \theta_{deck}}{\partial \varphi} \\ V_{asf}(\varphi) &= \left[m_{pier,1} + m_{pier,2} + 3m_{deck} \right] \left[\begin{aligned} &-\cos \varphi - \bar{r}^{p/n} \cos(\theta_{deck} + \psi_{BD}^{p/n}) \\ &\pm \frac{B}{2R_1} + \frac{L_2}{4R_1} \mp \frac{u_{jo}}{2R_1} \end{aligned} \right] \\ &\quad \left[\sin \varphi + \bar{r}^{p/n} \sin(\theta_{deck} + \psi_{BD}^{p/n}) \frac{\partial \theta_{deck}}{\partial \varphi} \right] \\ Q_{adf}(\varphi) &= \left[m_{pier,1} + m_{pier,2} + 3m_{deck} \right] \left[\sin \varphi + \bar{r}^{p/n} \sin(\theta_{deck} + \psi_{BD}^{p/n}) \frac{\partial \theta_{deck}}{\partial \varphi} \right], \end{aligned}$$

and $\bar{R} = R_2/R_1$. The terms ‘frame system’ and ‘abutment-backfill contribution’ in Eq. (4-22) describe the same conditions as those explained in §3.2.3. It is noted that when there is no contact between the superstructure and the abutments at the ends of the deck ($|u_{deck}^{CG}| < u_{jo}$), the spring

stiffness (k) and the dashpot coefficient (c) of the end supports must be neglected, and the EoM reduces to that of an asymmetric frame without end restraints, coinciding in this particular case with the equation by Dimitrakopoulos & Giouvanidis (2015). It is noted that Eq. (4-22) drops to Eq. (3-20) for the case with $N = 2$ rocking piers with same height ($\bar{h} = 1$ and $m_{pier,1} = m_{pier,2}$) and the same rocking behaviour ($\varphi = \varphi_{CD} = \theta_1 + \varphi_1^{p/n}$ forcing the superstructure to translate only, or $\theta_{deck} = 0$), and after rearranging appropriately by integrating the following parameters in the EoM: (i) $\ddot{\varphi} = \ddot{\theta}_1$, (ii) $\dot{\varphi} = \dot{\theta}_1$, (iii) $p = \sqrt{3g/4R_1}$ and (iv) $\gamma = m_{deck}/2m_{pier,1}$.

The level of longitudinal influence of the abutment-backfill system in rocking response is expressed through the parameter $q = 4R_1/g \cdot [m_{pier,1} + m_{pier,2} + 3m_{deck}]$, which is analogous to that in §3.2.3. To this effect, high values of q indicate a significant importance of the abutments and the backfills in the rocking motion, while for low values the influence of the spring and dashpot elements representing the abutment and the backfill is reduced and the response of the bridge system approaches that of its equivalent frame. In order to establish the effect of the level of asymmetry on the contribution of the abutment-backfill system, reference is made to a bridge structure with rectangular rocking piers of dimension $2B = 2.6$ m and height of the tall pier $2H_1 = 26$ m, thus resulting in $m_{pier,1} = 44 \cdot 10^4$ kg, and a constant mass of the deck $m_{deck} = 200 \cdot 10^4$ kg. Fig. 4-3 plots the value of q with respect to the mass of the second pier ($m_{pier,2}$). The variation of $m_{pier,2}$ is obtained by changing the height of the short pier ($2H_2$), resulting in values of the asymmetry ratio ranging from $\bar{h} = 1$ (symmetric) to $\bar{h} = 5$ (the largest asymmetry considered here). The results in Fig. 4-3 indicate that the bridges wherein the mass of the short pier is much smaller than that of the long one (with a higher level of asymmetry) show larger interaction with the abutment-backfill system due to the reduction in the total mass of the system. On the contrary, in the symmetric structure ($\bar{h} = 1$) the generally beneficial contribution of the abutments and the backfills in the rocking response (§3.4) is smaller. However, the difference between the two extreme cases (highly asymmetric with $\bar{h} = 5$ and symmetric with $\bar{h} = 1$) is only 4% and, therefore, the contribution of the abutment-backfill system to the rocking response is not expected to be influenced significantly by the asymmetry in the height of the piers.

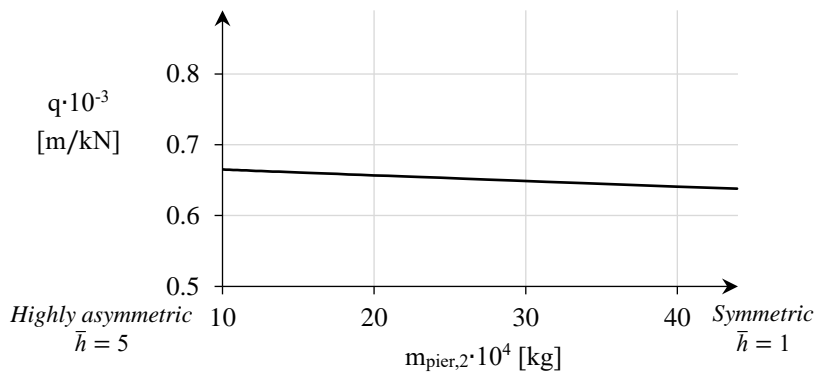


Fig. 4-3 Longitudinal influence of the abutment-backfill system (q) in bridges with rocking piers of different degree of asymmetry, accounting for the influence of the mass of the short pier ($m_{pier,2}$). Results obtained when the tall pier section and the deck mass are constant.

4.2.4 Impact on the Abutment Backwall

Following the justification provided in §3.2.4, the attenuation of rocking motion due to an impact of the superstructure on the abutment backwall (when $|u_{deck}^{CG}| = u_{jo}$) is described through the CoR *e*. Fig. 4-4A, B illustrate the asymmetric bridge rocking for positive rotation just before pounding on the abutment backwall with longitudinal velocity of the superstructure $\dot{u}_{deck,I}^{CG}$ and just after pounding with $\dot{u}_{deck,II}^{CG}$, respectively.

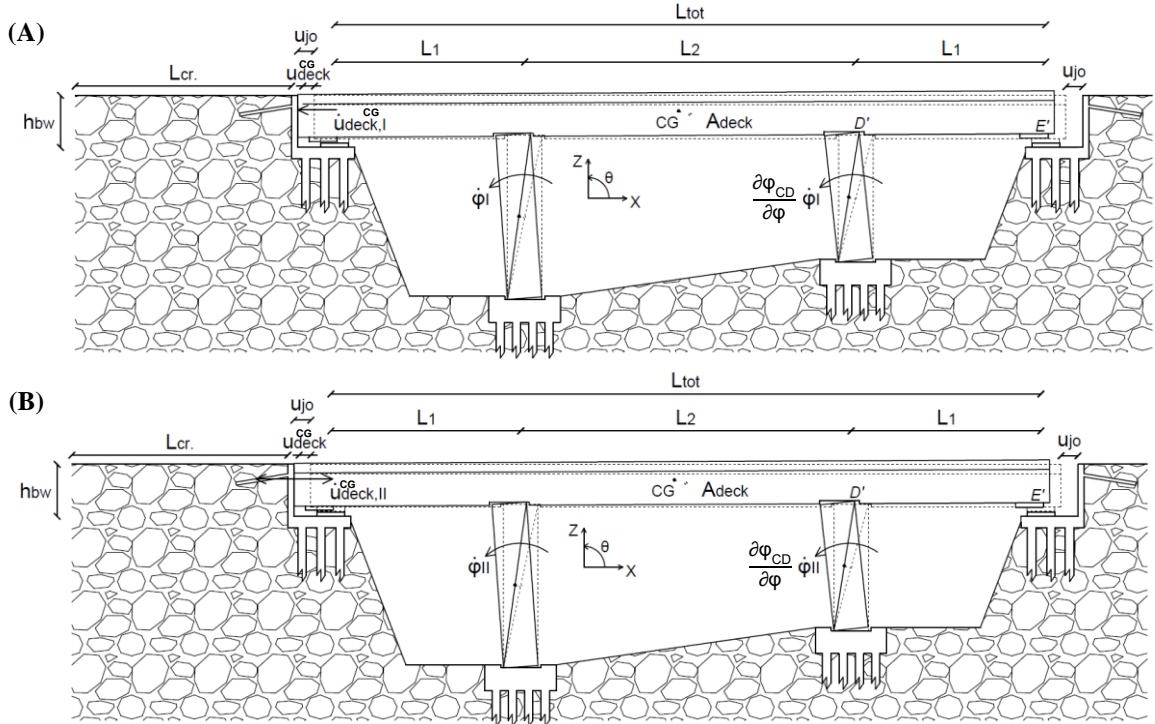


Fig. 4-4 Schematic of the pounding problem considered in the rocking motion of an asymmetric bridge with rocking piers, including (A) the pre-pounding state with a longitudinal velocity of the superstructure $\dot{u}_{deck,I}^{CG}$, and (B) the post-pounding state with an associated deck velocity $\dot{u}_{deck,II}^{CG}$.

The relationship between the longitudinal velocities of the superstructure after and before this impact was described in Eq. (3-21). Introducing Eq. (4-9) and simplifying gives the ratio of the corresponding angular velocities of the tall pier ($\dot{\phi}_I$ and $\dot{\phi}_{II}$)

$$\frac{\dot{u}_{deck,II}^{CG}}{\dot{u}_{deck,I}^{CG}} = \frac{\left[-2R_1 \sin \varphi - r_{BD}^{p/n} \sin(\theta_{deck} + \psi_{BD}^{p/n}) \frac{\partial \theta_{deck}}{\partial \varphi} \right] \dot{\phi}_{II}}{\left[-2R_1 \sin \varphi - r_{BD}^{p/n} \sin(\theta_{deck} + \psi_{BD}^{p/n}) \frac{\partial \theta_{deck}}{\partial \varphi} \right] \dot{\phi}_I} \Leftrightarrow \frac{\dot{\phi}_{II}}{\dot{\phi}_I} = 1 - [1 + e] \frac{m_{abut.}}{m_{abut.} + m_{deck}}, \quad (4-23)$$

where $m_{abut.}$ and m_{deck} are given in §3.2.4 and §4.2.1, respectively.

4.2.5 Impact at the Rocking Interfaces

The bridge with rocking piers dissipates energy after each impact at the rocking interfaces when the structure returns to the at-rest position of equilibrium ($\theta_1 = \theta_2 = \theta_{deck} = 0$ or $\varphi = \varphi_1^{p/n}$) after rocking starts. This energy dissipation is described by means of a CoR $\eta = |\dot{\varphi}_{II}/\dot{\varphi}_I|$ which relates the independent variable of the angular velocity of the tall pier in the pre-impact ($\dot{\varphi}_I$) and the post-impact ($\dot{\varphi}_{II}$) field. The present study follows an impulse formulation based on the assumptions presented in §3.2.5, and it extends the work by Dimitrakopoulos & Giouvanidis (2015) by integrating in the formulation the effect of the abutments acting as vertical supports, as well as the length of the end spans (L_1).

To solve the impact problem, let the displaced position of the bridge change from counter-clockwise (positive) to clockwise (negative) as shown in Fig. 4-5A, B, C; the condition corresponding to the opposite rocking reversal is treated in Appendix B for completeness. Considering that additional reaction forces (or impulses) are developed at the abutment seats compared to the corresponding frame without abutments, there are seven unknowns that need to be determined, namely, the impulses $\Lambda_{A,x}$ and $\Lambda_{A,z}$ at CR A of the tall pier, $\Lambda_{C,x}$ and $\Lambda_{C,z}$ at CR C of the short pier, $\Lambda_{E,z}$ as well as $\Lambda_{E',z}$ at the two abutment seats E and E', respectively, and the angular velocity of the tall pier after the impact at the rocking interfaces $\dot{\varphi}_{II}$. However, only five equations can be used to describe the impact problem. For this reason, two additional relationships between the impulses at the abutment seats and those at the pier-deck interfaces are introduced according to the rationale presented in §3.2.5

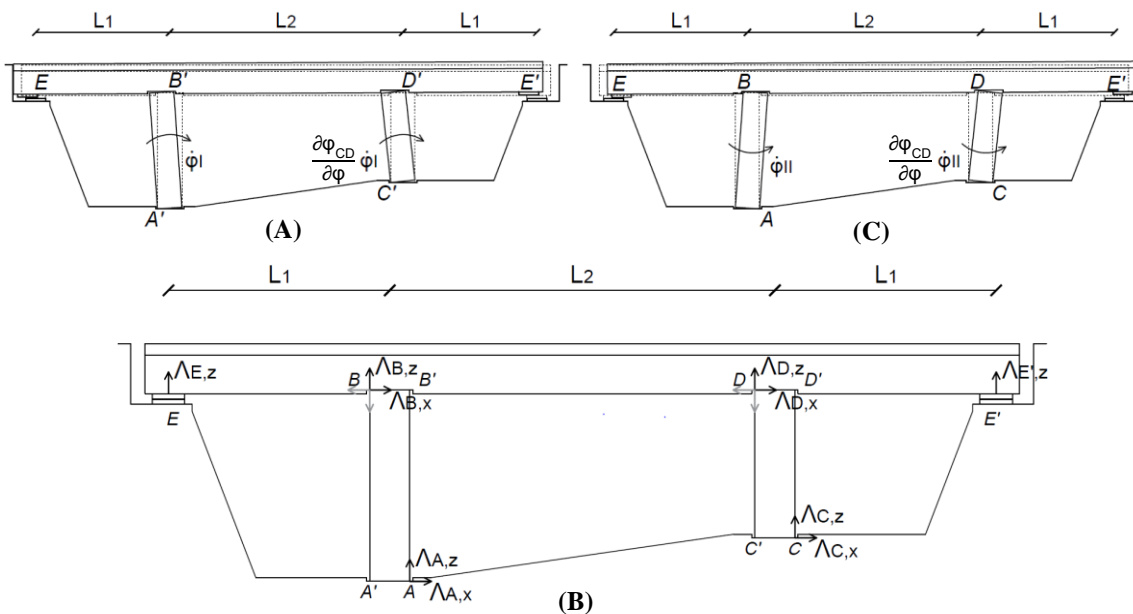


Fig. 4-5 Schematic of the impact problem considered in the rocking motion of an asymmetric bridge with rocking piers that (A) undergoes counter-clockwise (positive) rotation with an angular velocity of the tall pier $\dot{\varphi}_I$, (B) impacts at the corresponding pivot points, and then reverses to (C) clockwise (negative) rotation with an angular velocity of the tall pier $\dot{\varphi}_{II}$.

$$\Lambda_{E,z} = \frac{L_1}{L_1 + L_2} \Lambda_{B,z}, \quad (4-24)$$

$$\Lambda_{E',z} = \frac{L_1}{L_1 + L_2} \Lambda_{D,z}. \quad (4-25)$$

Introducing the conservation of linear momentum just before and after the impact at the rocking interfaces along the Z axis for the tall pier into Eq. (4-24) relates the impulses at point E with those at CR A

$$\Lambda_{E,z} = \frac{L_1}{L_1 + L_2} \left[\Lambda_{A,z} + m_{pier,1} B (\dot{\phi}_I + \dot{\phi}_{II}) \right]. \quad (4-26)$$

Similarly, Eq. (4-25) combined with the conservation of linear momentum for the short pier establishes the relationship between the impulses at point E' and those at CR C

$$\Lambda_{E',z} = \frac{L_1}{L_1 + L_2} \left[\Lambda_{C,z} + m_{pier,2} B \bar{h} (\dot{\phi}_I + \dot{\phi}_{II}) \right]. \quad (4-27)$$

Eqs. (4-26) and (4-27) reduce the unknowns of the impact problem from seven to five ($\Lambda_{A,x}$, $\Lambda_{A,z}$, $\Lambda_{C,x}$, $\Lambda_{C,z}$ and $\dot{\phi}_{II}$), and the following equations are considered in the determination of these unknowns;

1. Linear momentum along the X axis for the entire bridge

$$\Lambda_{A,x} + \Lambda_{C,x} = \left[m_{pier,1} + m_{pier,2} + 2m_{deck} \right] H_1 (\dot{\phi}_I - \dot{\phi}_{II}) + 2m_{deck} \bar{b} \bar{h} [\bar{h} - 1] (\dot{\phi}_I + \dot{\phi}_{II}). \quad (4-28)$$

2. Linear momentum along the Z axis for the entire bridge

$$\Lambda_{E,z} + \Lambda_{A,z} + \Lambda_{C,z} + \Lambda_{E',z} = 2m_{deck} B \bar{b} [\bar{h} - 1] (\dot{\phi}_I - \dot{\phi}_{II}) - \left[m_{pier,1} B + m_{pier,2} B \bar{h} + m_{deck} B (\bar{h} + 1) \right] (\dot{\phi}_I + \dot{\phi}_{II}). \quad (4-29)$$

3. Angular momentum about B for the tall pier

$$2H_1 \Lambda_{A,x} + 2B \Lambda_{A,z} = \left[m_{pier,1} H_1^2 - I_{pier,1}^{CG} \right] (\dot{\phi}_I - \dot{\phi}_{II}) - m_{pier,1} B^2 (\dot{\phi}_I + \dot{\phi}_{II}). \quad (4-30)$$

4. Angular momentum about D for the short pier

$$2H_2\Lambda_{C,x} + 2B\Lambda_{C,z} = \left[m_{pier,2}H_1H_2 - I_{pier,2}^{CG}\bar{h} \right] (\dot{\phi}_I - \dot{\phi}_{II}) - m_{pier,2}B^2\bar{h} (\dot{\phi}_I + \dot{\phi}_{II}). \quad (4-31)$$

5. Angular momentum about A for the entire bridge

$$\begin{aligned} & -[L_1 + B]\Lambda_{E,z} - [2H_1 - 2H_2]\Lambda_{C,x} \\ & + L_2\Lambda_{C,z} + [L_1 + L_2 - B]\Lambda_{E',z} = \\ & \left[\begin{array}{l} -m_{pier,1}H_1^2 - I_{pier,1}^{CG} - m_{pier,2}H_1(2H_1 - H_2) - I_{pier,2}^{CG}\bar{h} \\ -2m_{deck}H_1(2H_1 + h) + 2m_{deck}\left(\frac{L_2}{2} - B\right)B\bar{b}(\bar{h} - 1) \end{array} \right] (\dot{\phi}_I - \dot{\phi}_{II}) \\ & + \left[\begin{array}{l} m_{pier,1}B^2 - m_{pier,2}B\bar{h}(L_2 - B) - 2m_{deck}(2H_1 + h)\bar{b}h(\bar{h} - 1) \\ -m_{deck}\left(\frac{L_2}{2} - B\right)B(\bar{h} + 1) - I_{deck}^{CG}2\bar{b}(\bar{h} - 1) \end{array} \right] (\dot{\phi}_I + \dot{\phi}_{II}) \end{aligned} \quad (4-32)$$

Eqs. (4-26) and (4-27) are substituted in the system formed by Eqs. (4-28) to (4-32), and its solution returns the four impulses ($\Lambda_{A,x}$, $\Lambda_{A,z}$, $\Lambda_{C,x}$, $\Lambda_{C,z}$) and the post-impact angular velocity of the tall pier ($\dot{\phi}_{II}$). The CoR at the rocking interfaces $\eta = |\dot{\phi}_{II}/\dot{\phi}_I|$ is given by the following expression

$$\begin{aligned} \eta^{p/n} = \left| \frac{\dot{\phi}_{II}}{\dot{\phi}_I} \right| = & \frac{\alpha_1 [H_1^2 - B^2] m_{pier,1} + \alpha_1 I_{pier,1}^{CG} + \alpha_1 [H_1^2 - \bar{h}^2 B^2] m_{pier,2} + \alpha_1 \bar{h}^2 I_{pier,2}^{CG} \\ & + \left[\begin{array}{l} 4\alpha_1 H_1^2 \pm 4\alpha_2 H_1 h \bar{b} (\bar{h} - 1) - 4\alpha_3 h^2 \bar{b}^2 (\bar{h} - 1)^2 \\ -B^2 (\alpha_4 (\bar{h} + 1)^2 - 4\alpha_5 \bar{b}^2 (\bar{h} - 1)^2) \mp 2\alpha_6 \bar{b} (\bar{h}^2 - 1) \end{array} \right] m_{deck} \\ & - 4\alpha_3 \bar{b}^2 [\bar{h} - 1]^2 I_{deck}^{CG}}{\alpha_1 [H_1^2 + B^2] m_{pier,1} + \alpha_1 I_{pier,1}^{CG} + \alpha_1 [H_1^2 + \bar{h}^2 B^2] m_{pier,2} + \alpha_1 \bar{h}^2 I_{pier,2}^{CG} \\ & + \left[\begin{array}{l} 4\alpha_1 H_1^2 \mp 4\alpha_7 H_1 h \bar{b} (\bar{h} - 1) + 4\alpha_3 h^2 \bar{b}^2 (\bar{h} - 1)^2 \\ + B^2 (\alpha_4 (\bar{h} + 1)^2 + 4\alpha_5 \bar{b}^2 (\bar{h} - 1)^2) \pm 2\alpha_8 \bar{b} (\bar{h}^2 - 1) \end{array} \right] m_{deck} \\ & + 4\alpha_3 \bar{b}^2 [\bar{h} - 1]^2 I_{deck}^{CG}} \end{aligned} \quad (4-33)$$

where

$$\begin{aligned} \alpha_1 &= 4\bar{L}^3 + 6\bar{L}^2 + 4\bar{L} + 1 & \alpha_2 &= 4\bar{L}^3 + 4\bar{L}^2 + \bar{L} & \alpha_3 &= 2\bar{L}^2 + 3\bar{L} + 1 \\ \alpha_4 &= 2\bar{L}^3 + 4\bar{L}^2 + 3\bar{L} + 1 & \alpha_5 &= [\bar{L} + 1]^2 & \alpha_6 &= 2\bar{L}^3 + 3\bar{L}^2 + \bar{L} \end{aligned}$$

$$\alpha_7 = 4\bar{L}^3 + 8\bar{L}^2 + 7\bar{L} + 2$$

$$\alpha_8 = 2\bar{L}^3 + 5\bar{L}^2 + 5\bar{L} + 2$$

and $\bar{L} = L_1/L_2$ describes the effect of the span arrangement. It is observed that Eq. (4-33) depends on the direction of rocking reversal; the value of η obtained with the upper signs corresponds to the movement in which the rotation of the rocking piers changes from positive to negative, and vice-versa for the lower signs. The impulse formulation that leads to the bottom signs of Eq. (4-33) is given in Appendix B. It must be noted that, although Eq. (4-33) is more complex than the corresponding Eq. (3-31) for the symmetric system, both expressions of Eq. (4-33) (i.e., for upper and lower signs) reduce to the CoR at the rocking interfaces of the symmetric bridges with $N = 2$ rocking piers when both have the same height. This can be verified by simplifying Eq. (4-33) under the following conditions: (i) $H_1 = H_2$, hence $\bar{h} = 1$, (ii) $I_{pier,1}^{CG} = I_{pier,2}^{CG} = m_{pier,1} \cdot R_1^2/3$ for rectangular rocking piers, and (iii) introducing parameter $\gamma = m_{deck}/2m_{pier,1}$ to express the effect of the mass of the deck. The simpler expression results after rearranging appropriately

$$\eta = \frac{\left| \frac{\dot{\phi}_{II}}{\dot{\phi}_I} \right|}{\left| \frac{\dot{\theta}_{II}}{\dot{\theta}_I} \right|} = \frac{8 - 12 \sin^2 a_1 - 6\gamma \left[(\bar{L} + 1)^2 \cos 2a_1 + \bar{L}(\bar{L} + 1) \cos^2 a_1 \right] - \left[\bar{L}^2 + 1.5\bar{L} + 2.5 \right] [1 + 3 \cos 2a_1]}{8 - 6\gamma \left[(\bar{L} + 1)^2 + \bar{L}(\bar{L} + 1) \cos^2 a_1 \right] - 4 \left[\bar{L}^2 + 1.5\bar{L} + 2.5 \right]}. \quad (4-34)$$

Eq. (4-33) is different from the corresponding CoR η in asymmetric frames with rocking columns (Dimitrakopoulos & Giouvanidis 2015) due to the additional impulses developed at the abutment seats. If such impulses are neglected ($\Lambda_{E,z} = \Lambda_{E',z} = 0$) in Eqs. (4-28) to (4-32), the solution of this system of equations gives exactly the CoR developed by Dimitrakopoulos & Giouvanidis (2015) for asymmetric frames. To this end, and to establish the effect of the additional impacts at the end of the superstructure in the value of η , Fig. 4-6 compares the values obtained using Eq. (4-33) with those from the corresponding expression for asymmetric frames. The bridge considered in this comparison has three spans of equal length ($\bar{L} = 1$) in order to make the expression proposed by Dimitrakopoulos & Giouvanidis (2015) applicable. The bridge has rectangular piers with width $2B = 2.5$ m, height of the tall pier $2H_1 = 30$ m and a height of the short pier $2H_2$ that ranges from 6 m ($\bar{h} = 5$) to 30 m ($\bar{h} = 1$) in order to evaluate the influence of the asymmetry on the results. The superstructure in the bridges and frames has length $L_{tot} = 2L_1 + L_2 = 2 \cdot 45 + 45 = 135$ m and consists in a simplified single-cell box girder with depth $2h = 2$ m, width of the bottom and the top slabs $B_{bot} = 6.5$ m and $B_{top} = 10$ m, respectively, and flange and wall thicknesses $t_f = 0.35$ m and $t_w = 0.9$ m, respectively, thus resulting in $A_{deck} = 7$ m². The mass of the tall pier is equal to $m_{pier,1} = 47 \cdot 10^4$ kg and that of the superstructure is $m_{deck} = 240 \cdot 10^4$ kg, while the mass moment of inertia of the box girder section of the deck is approximated to $I_{deck}^{CG} = 360 \cdot 10^7$ kg·m². The results presented in Fig. 4-6 show that the value of η is always larger in the bridge than in the corresponding frame with the same dimensions. This indicates that the presence of the abutment (vertical) supports reduces the energy dissipation as they carry part of the deck

weight, and it is in line with the results observed for symmetric bridges in Fig. 3-6. The percentage of increase in the value of η for the bridges with rocking piers with respect to the equivalent frames ranges from 0.5% for the symmetric configuration ($\bar{h} = 1$) to 12.5% for the highly asymmetric configuration ($\bar{h} = 5$). Thus, compared to the corresponding frames without abutments, the presence of the end supports reduces the energy dissipation more in highly asymmetric bridges. This is expected taking into account that the reduction in the deck weight due to the presence of the end supports is more significant when short piers are examined (i.e., as in highly asymmetric configurations) than tall ones (i.e., as in symmetric configurations), considering that for the latter the total weight impacting on the rocking interfaces is already large due to the self-weight of the pier. Furthermore, it is shown that the larger the height of the short pier ($2H_2$) by keeping constant the rest of the bridge parameters, the higher is the value of η (or the lower the energy dissipation), which confirms previous studies that observed that slender blocks dissipate less energy than the stocky ones due to impact at the rocking interfaces (e.g., Housner 1963).

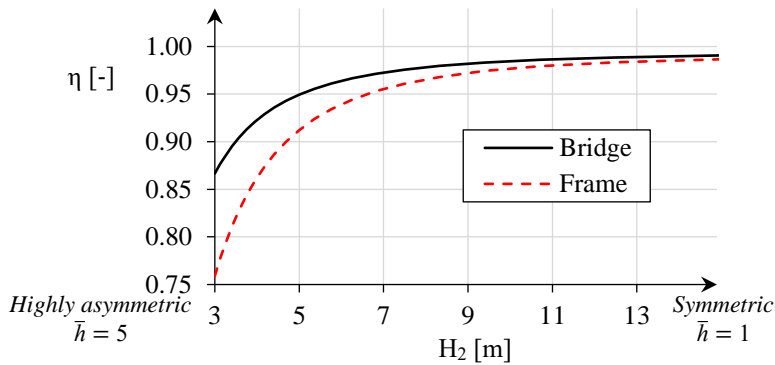


Fig. 4-6 CoR at the rocking interfaces (η) for bridges with rocking piers of different degree of asymmetry and for equivalent frames (Dimitrakopoulos & Giouvanidis 2015), accounting for the influence of the short pier height (H_2). Results obtained when the tall pier section and the deck mass are constant.

The value of the CoR at the rocking interfaces in Eq. (4-33) is influenced by the length of the spans L_1 and L_2 . The effect of these parameters on the value η is shown in Fig. 4-7, considering the same bridge dimensions as in the previous paragraph, apart from the height of the short pier which is set equal to $2H_2 = 20$ m ($\bar{h} = 1.5$). The mass of the deck is kept constant for comparison purposes and equal to $m_{deck} = 240 \cdot 10^4$ kg independently of the fluctuating length of the superstructure. The results in Fig. 4-7A show that by increasing the length of the end spans (L_1) while keeping constant the length of the intermediate spans (L_2) the CoR η increases slightly, leading to lower energy dissipation. This is due to the higher impulses that are developed at the abutment seats, and the explanation is analogous to that provided in §3.2.5 based on the results obtained for symmetric rocking structures in Fig. 3-7A. On the other hand, higher amount of energy is dissipated when the length of the central span (L_2) is increased while keeping constant the length of the end spans (L_1), and the justification is based on the same reasoning (§3.2.5). Additionally, and similarly to the symmetric configuration, the proposed value of η is conservative and it does not take into account the effect of the end spans, based on the justification provided in §3.2.5.

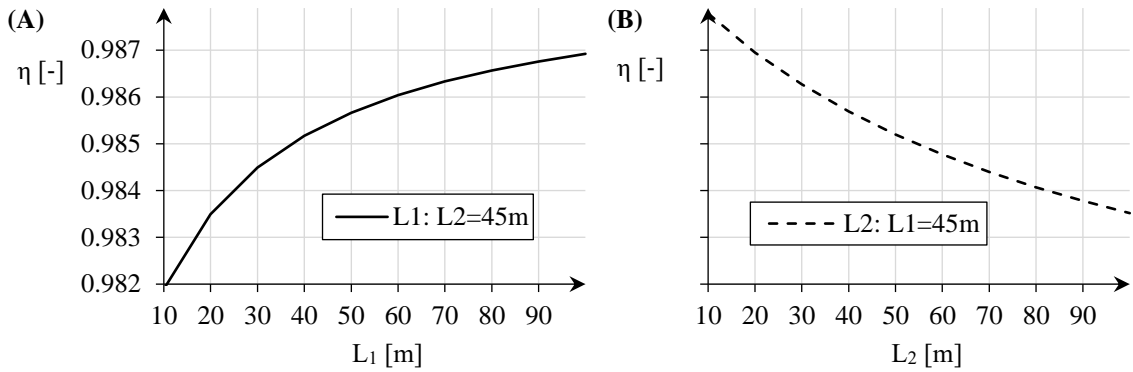


Fig. 4-7 CoR at the rocking interfaces (η) for asymmetric bridges with rocking piers, accounting for the influence of (A) the length of the end spans (L_1) and (B) the length of the intermediate spans (L_2). Results obtained when the deck mass is constant.

4.3 Analysis Framework

Chapter 4 addresses the seismic response of symmetric ($\bar{h} = 1$) and asymmetric ($\bar{h} > 1$) bridges with rocking piers. The rocking response analysis of the symmetric configurations is given in detail in §3.3, while for the corresponding asymmetric bridges addressed in this chapter (§4.3.1) when subject to a ground motion (§4.3.2), rocking initiation starts as described in Eq. (4-12) and, after this happens, Eq. (4-22) is integrated step-by-step using the ‘ode45’ solver in MATLAB (2016) with a time-step of 10^{-3} s to simulate the rocking motion of the structure. The response-history solution of the EoM that governs the seismic response of the asymmetric bridges with rocking piers requires identifying the instants at which pounding with the abutment backwall occurs ($|u_{deck}^{CG}| = u_{jo}$), and the instants when impacts at the rocking interfaces occur ($\varphi = \varphi_1^{p/n}$). To this effect, Eqs. (4-23) and (4-33) are employed to account for the corresponding attenuation of the rocking motion with respect to the DoF of the system ($\dot{\varphi}$). Failure of the rocking structures is defined as a special condition that is checked in every time-step and, if met, the analysis is terminated. The failure criteria are given in §4.3.3. The logic of the MATLAB code follows that presented in Fig. A-2 with the required adjustments due to the different equations that are utilised for the asymmetric bridge.

The response-history solution of the EoM is based on an iterative process implemented in MATLAB; a relatively large time-step value (i.e., 10^{-3} s) is selected to start with, and this value is decreased (i.e., $5 \cdot 10^{-6}$ s) when an impact phenomenon is detected to capture this instant with higher accuracy. This adaptive time-stepping did not affect significantly the computational cost of the symmetric configurations because a single analysis requires only a few minutes to be conducted (§3.3), but it considerably reduces the analysis duration of the asymmetric systems which are much more computationally expensive. This is attributed to the high complexity of the equations that are needed to be integrated step-by-step (see Eq. (4-22)), for which selection of a small time-step (e.g., $5 \cdot 10^{-6}$ s) leads to a duration of around 20 hours for a single analysis with the hardware that was used for this thesis (i.e., a machine with an available RAM of 10 GB). Therefore, an analysis with a time-step equal to 10^{-3} s which is adjusted when an impact is detected leads to reduction of

computational cost by approximately 50% (i.e., around 10 hours for a single analysis) compared to the same analysis with a very small time-step of $5 \cdot 10^{-6}$ s without affecting the accuracy, thus further comparisons are not conducted in that respect. In order to further reduce computation time for asymmetric rocking structures, §4.3.4 presents a new analytical technique based on a model that simplifies the step-by-step integration of the complex equations that have been found to cost computationally in the response analysis of these systems.

4.3.1 Description of the Studied Bridges

Three bridges with two rocking piers and different levels of asymmetry in their height are analysed to establish the effect of pier irregularity on the seismic response. The structures have a continuous single-cell box girder concrete section with length $L_{tot} = 2L_1 + L_2 = 2 \cdot 38 + 60 = 136$ m, depth $2h = 1.7$ m, width of the bottom and the top slabs $B_{bot} = 6$ m and $B_{top} = 9.5$ m, respectively, and flange and wall thicknesses $t_f = 0.3$ m and $t_w = 0.8$ m, respectively. With these dimensions the cross-section area of the deck is $A_{deck} = 6$ m². The substructure consists of two rectangular rocking piers with dimension $2B = 2.6$ m and constant height of the left pier $2H_1 = 26$ m. Asymmetry is introduced through the height of the right pier (H_2). Three different heights are considered in this pier to give (i) a symmetric configuration with $2H_2 = 26$ m, hence $\bar{h} = 1$, (ii) a moderately asymmetric configuration with $2H_2 = 0.8 \cdot 2H_1 = 20.8$ m, hence $\bar{h} = 1.25$ and (iii) a highly asymmetric configuration with $2H_2 = 0.5 \cdot 2H_1 = 13$ m, hence $\bar{h} = 2$.

Table 4-1 gives further details of each bridge structure. Although the parameter $\gamma = m_{deck}/(m_{pier,1} + m_{pier,2})$ that relates the mass of the deck to that of the piers (§3.2.3) is not present in the EoM of the asymmetric bridge as shown in Eq. (4-22), the effect of the deck mass is explored here as a factor of stability in the seismic rocking response (Makris & Vassiliou 2014b). Interestingly, the more asymmetric the bridge configuration, the higher are the values of the deck mass ratio (γ) and of the longitudinal influence of the abutments and the backfills (q) in the EoM. This is due to the reduction in mass of the substructure ($m_{pier,1} + m_{pier,2}$), thus implying the increased contribution of these stabilising factors in rocking response of asymmetric structures compared to the corresponding symmetric systems examined herein. It is also noted that the longitudinal influence of the abutment-backfill system (q) is relatively large for all the systems examined in this chapter, in comparison with the corresponding values obtained for the symmetric configurations in §3.3.4.3. This is expected taking into account that this part of the study considers bridges that are lighter than those studied in §3.3.1.

The abutment and the backfill properties are obtained from Kappos *et al.* (2007) (§3.3.1) and they are kept the same for all the different bridge configurations. This results in a spring stiffness of the abutment-backfill system equal to $k = 132$ MN/m with a capacity of the abutment-backfill equal to $u_{ab} = 0.1$ m (§3.3.4.1), and a dashpot coefficient to represent material and radiation damping of the backfill $c = 48$ MN·s/m (§3.3.4.2). Based on the justification provided in §3.3.4.4, pounding is described through a CoR in the longitudinal direction $e = 0.6$. Considering that the longitudinal influence of the abutment-backfill system (q) is relatively large (Table 4-1), the abutment-backfill system is expected to suppress considerably the longitudinal displacement of the

deck during rocking. This would make it difficult to study the differences in the seismic responses of bridges with rocking piers with different levels of asymmetry. For this reason, a relatively large gap size equal to $u_{jo} = 120$ mm is selected between the superstructure and the abutments to reduce the longitudinal effective stiffness in the closed gap stage of the systems (§3.4). The structures are founded on soil C and belong to a seismicity zone with PGA equal to 0.36 g, which is the same as in the study of the symmetric systems (§3.3.1). All the structures are classified to importance class II ($\gamma_I = 1$).

Table 4-1 Information for the bridges with rocking piers of different degree of asymmetry, including the deck mass (m_{deck}), the pier masses ($m_{pier,1}$ and $m_{pier,2}$), and the total mass (m_{tot}) as well as the stabilising factors of the superstructure mass effect (γ) and the longitudinal influence of the abutment-backfill system (q).

Degree of Asymmetry	$m_{deck} \cdot 10^4$ [kg]	$m_{pier,1} \cdot 10^4$ [kg]	$m_{pier,2} \cdot 10^4$ [kg]	$m_{tot} \cdot 10^4$ [kg]	γ [-]	$q \cdot 10^{-3}$ [m/kN]
Symmetric ($\bar{h} = 1$)	204	44	44	292	2.3	0.761
Moderately asymmetric ($\bar{h} = 1.25$)	204	44	35	283	2.6	0.771
Highly asymmetric ($\bar{h} = 2$)	204	44	22	270	3.1	0.786

4.3.2 Representation of Seismic Action

The effect of the pier height irregularity on the rocking response of bridges is studied by representing the seismic action with ten ARs generated for different conditions than those in the study of symmetric bridges (§3.3.2.2). This is because the larger abutment/backfill suppression of the rocking motion (q) in the structures examined in this chapter (see Table 4-1) makes it necessary to increase the seismic demand of displacements in order to detect potential differences in the responses of the proposed configurations. To this end, the ARs were generated to match the Type 1 EC8 reference spectrum for site conditions C (CEN 2004b) and for a PGA equal to 0.6 g, thus considerably exceeding the design conditions (PGA = 0.36 g). Fig. 4-8 shows the good matching of the individual ARs, and their GM to the EC8 spectrum for PGA = 0.6 g

4.3.3 Failure Criteria

The criteria to describe collapse of the asymmetric bridges are the same as those in the symmetric structure, which were explained in §3.3.3. Assuming that the longitudinal displacement of the CG of both piers is the same (§4.2), both supporting members overturn simultaneously when $|u_{pier,1}^{CG}| = |u_{pier,2}^{CG}| \geq B$. This failure condition is described in terms of the DoF of the system with the inequalities $\varphi \geq \pi/2$ and $\varphi \leq \pi/2$ for positive and negative relative rotations of the piers,

respectively. Additionally, the abutment-backfill system fails when $|u_{deck}^{CG}| \geq u_{jo} + u_{ab}$. However, solving this inequality with respect to the DoF φ using Eq. (4-6) is complicated and, therefore, the failure of the abutment-backfill system is integrated in the MATLAB code in terms of the linear variable u_{deck}^{CG} , and after calculating its value in each time-step. To this end, the dominant failure mode of the asymmetric system cannot be addressed in the context presented for the symmetric structures in §3.3.3. However, the contribution of the rotational movement of the superstructure (θ_{deck}) in the longitudinal displacement of the superstructure (u_{deck}^{CG}) is marginal (as will be shown in §4.3.5), and for this reason θ_{deck} can be neglected and Eq. (4-6) can be simplified to Eq. (3-2). Therefore, the dominant failure mode of the asymmetric bridges is failure of the abutment/backfill system if $2B > u_{jo} + u_{ab}$, while overturning of the piers prevails if $2B < u_{jo} + u_{ab}$. Both failure modes would occur simultaneously if $2B = u_{jo} + u_{ab}$.

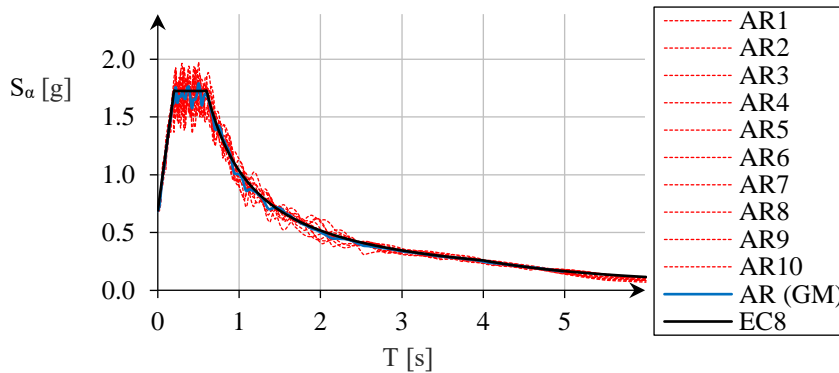


Fig. 4-8 Response acceleration spectra of the set of ARs, and matching to EC8 target spectrum with PGA = 0.6 g and site conditions C.

4.3.4 Simplification of Analysis Procedure

This section proposes a simplified procedure with respect to the equations required to be integrated step-by-step in the EoM of the asymmetric bridges (Eq. (4-22)) and have been found to cost computationally in the response analysis; it is noted that this simplification procedure is also applicable to the corresponding asymmetric frames with rocking columns presented by Dimitrakopoulos & Giouvanidis (2015). The idea behind the proposed method is to avoid obtaining the full expressions of the first and the second partial derivatives in Eq. (4-2) with respect to the DoF φ ($\partial\varphi_{CD}/\partial\varphi$ and $\partial^2\varphi_{CD}/\partial\varphi^2$) and also the first and second partial derivatives in Eq. (4-3) ($\partial\theta_{deck}/\partial\varphi$ and $\partial^2\theta_{deck}/\partial\varphi^2$), which take a significant amount of time due to their complexity and length. Instead, these expressions can be substituted by simpler equations that depend on φ , which speed up the solution of the EoM in each time-step of the analysis.

To elaborate more on this procedure, Fig. 4-2A shows that the DoF that describes the rocking system can take values from $\varphi = \pi/2 - \alpha_1$ to $\varphi = \pi/2$, describing the angle at the at-rest position and overturning of the tall pier, respectively, in the field of positive rocking tilt of the piers; similarly, Fig. 4-2B shows that φ ranges from $\pi/2 + \alpha_1$ to $\pi/2$ representing the corresponding angle at the at-rest position and overturning condition of the tall pier, respectively, in the field of negative rocking tilt of the piers. Looking at the full rocking amplitude, the possible values of φ

range from $\pi/2 - \alpha_1$ to $\pi/2 + \alpha_1$. Considering the properties for the moderately asymmetric bridge presented in §4.3.1 (with $\bar{h} = 1.25$ and $\alpha_1 = 0.1$ rad), substitution of this φ -range into $\partial\varphi_{CD}/\partial\varphi$, $\partial^2\varphi_{CD}/\partial\varphi^2$, $\partial\theta_{deck}/\partial\varphi$ and $\partial^2\theta_{deck}/\partial\varphi^2$ obtained as the derivatives of Eqs. (4-2) and (4-3), returns the range of these variables with respect to the DoF of the system (φ) and leads to simple shapes (i.e., linear and second-order parabolic). Without lack of accuracy, these curves can be approximated by much simpler equations that are unique for this specific case. To this end, each of the dependent variables $\partial\varphi_{CD}/\partial\varphi$, $\partial^2\varphi_{CD}/\partial\varphi^2$, $\partial\theta_{deck}/\partial\varphi$ and $\partial^2\theta_{deck}/\partial\varphi^2$ can be expressed with respect to the DoF of the asymmetric system (φ) according to a simplified model that is expressed through Eqs. (4-35) to (4-38), respectively.

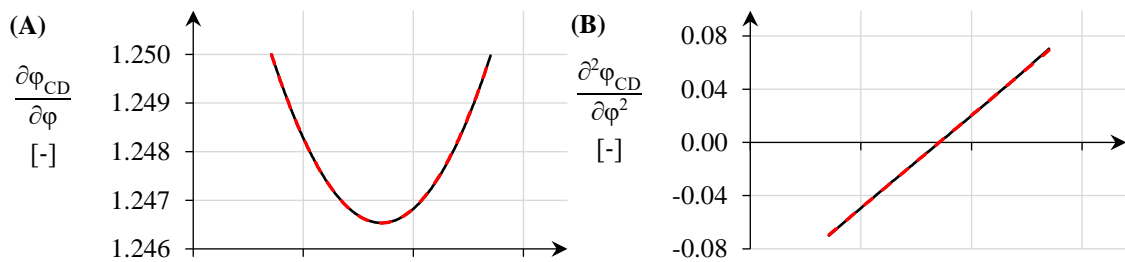
$$\frac{\partial\varphi_{CD}}{\partial\varphi}_{sim.} = 0.3486 \left[\varphi - \frac{\pi}{2} \right]^2 + 1.2465, \quad (4-35)$$

$$\frac{\partial^2\varphi_{CD}}{\partial\varphi^2}_{sim.} = 0.697 \left[\varphi - \frac{\pi}{2} \right] - 1.1787 \cdot 10^{-4}, \quad (4-36)$$

$$\frac{\partial\theta_{deck}}{\partial\varphi}_{sim.} = -0.1085 \left[\varphi - \frac{\pi}{2} \right] + 1.8333 \cdot 10^{-5}, \quad (4-37)$$

$$\frac{\partial^2\theta_{deck}}{\partial\varphi^2}_{sim.} = -0.4024 \left[\varphi - \frac{\pi}{2} \right]^2 - 0.1074. \quad (4-38)$$

Fig. 4-9A, B, C, D compare the curves derived from these equations (simplified model) and those from Eqs. (4-2) and (4-3) (rigorous model). It is observed that the curves depicting the derivatives of the functions given by the rigorous model and those using the simplified model are almost identical, with the maximum difference being 3% for the variable $\partial^2\varphi_{CD}/\partial\varphi^2$ at values of φ that are close to the overturning threshold ($\varphi = \pi/2$). Therefore, the simplified equations capture accurately the values of the dependent variables before the structure overturns (which is the main focus of this thesis), and they are reasonably accurate even for rocking movements close to the overturning of the piers.



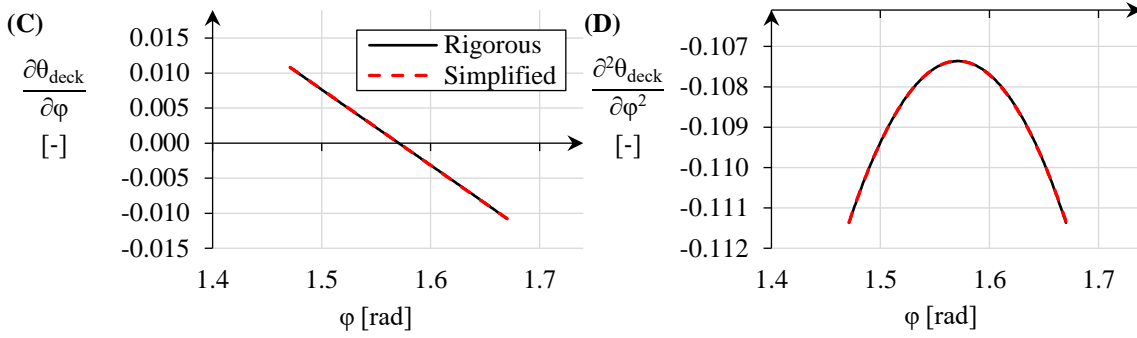


Fig. 4-9 Comparison of the rigorous and simplified models for the range of the dependent variables (A) $\partial\varphi_{CD}/\partial\varphi$, (B) $\partial^2\varphi_{CD}/\partial\varphi^2$, (C) $\partial\theta_{deck}/\partial\varphi$ and (D) $\partial^2\theta_{deck}/\partial\varphi^2$ with respect to the DoF φ . Results obtained for the moderately asymmetric bridge with rocking piers of $\bar{h} = 1.25$ and $\alpha_1 = 0.1$ rad.

Similarly to the system with $\bar{h} = 1.25$, Eqs. (4-39) to (4-42) show the unique expressions for the simplified model that approximate the values of the dependent variables $\partial\varphi_{CD}/\partial\varphi$, $\partial^2\varphi_{CD}/\partial\varphi^2$, $\partial\theta_{deck}/\partial\varphi$ and $\partial^2\theta_{deck}/\partial\varphi^2$ in the range $\varphi = [\pi/2 - 0.1, \pi/2 + 0.1]$ for the highly asymmetric structure with $\bar{h} = 2$ (§4.3.1).

$$\frac{\partial\varphi_{CD}}{\partial\varphi}_{sim.} = 2.919 \left[\varphi - \frac{\pi}{2} \right]^2 + 1.9709, \quad (4-39)$$

$$\frac{\partial^2\varphi_{CD}}{\partial\varphi^2}_{sim.} = 5.8309 \left[\varphi - \frac{\pi}{2} \right] - 9.8688 \cdot 10^{-4}, \quad (4-40)$$

$$\frac{\partial\theta_{deck}}{\partial\varphi}_{sim.} = -0.4326 \left[\varphi - \frac{\pi}{2} \right] + 7.3339 \cdot 10^{-5}, \quad (4-41)$$

$$\frac{\partial^2\theta_{deck}}{\partial\varphi^2}_{sim.} = -3.6266 \left[\varphi - \frac{\pi}{2} \right]^2 - 0.4228. \quad (4-42)$$

Fig. 4-10A, B, C, D present the curves of $\partial\varphi_{CD}/\partial\varphi$, $\partial^2\varphi_{CD}/\partial\varphi^2$, $\partial\theta_{deck}/\partial\varphi$ and $\partial^2\theta_{deck}/\partial\varphi^2$, respectively, with respect to the DoF φ obtained with the rigorous and with the simplified models. It is observed that the proposed simplified expressions return curves that are very close to the exact ones, with the highest difference being approximately 8% for the variable $\partial^2\varphi_{CD}/\partial\varphi^2$. However, this deviation also occurs close to the overturning threshold and, therefore, it is not expected to affect considerably the rocking response of the proposed rocking structures, especially if their responses do not approach the overturning limit. It should be noted though that for the determination of the equations for the simplified model, the full derivatives of Eqs. (4-2) and (4-3) need to be produced one time.

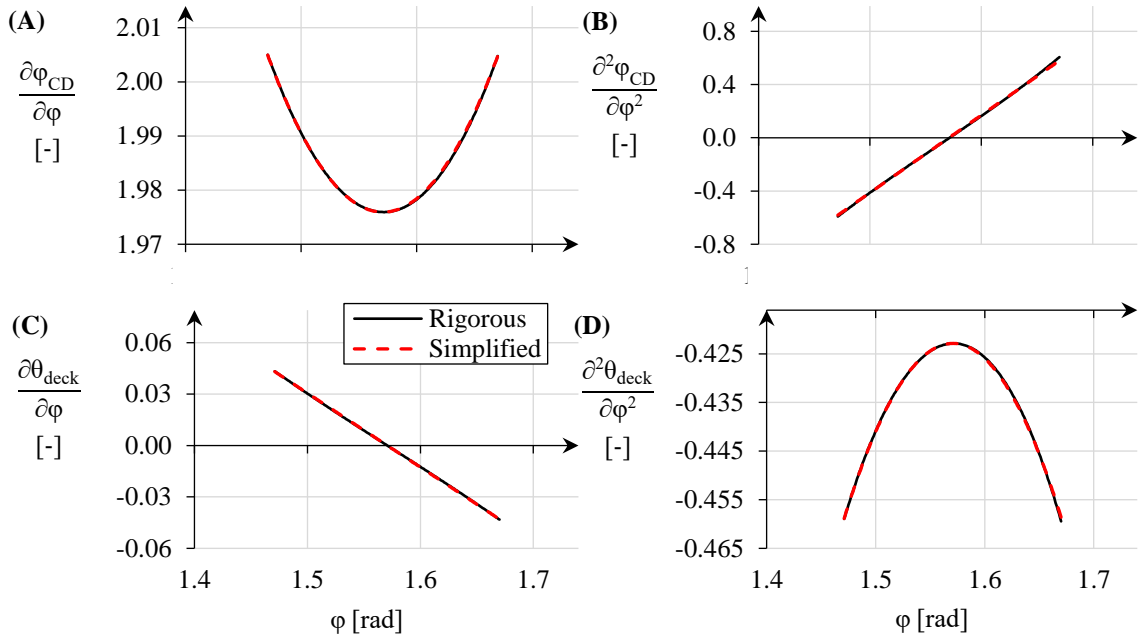


Fig. 4-10 Comparison of the rigorous and simplified models for the range of the dependent variables (A) $\frac{\partial \varphi_{CD}}{\partial \varphi}$, (B) $\frac{\partial^2 \varphi_{CD}}{\partial \varphi^2}$, (C) $\frac{\partial \theta_{deck}}{\partial \varphi}$ and (D) $\frac{\partial^2 \theta_{deck}}{\partial \varphi^2}$ with respect to the DoF φ . Results obtained for the highly asymmetric bridge with rocking piers of $\bar{h} = 2$ and $\alpha_1 = 0.1$ rad.

Despite the accuracy of the simplified expressions in the corresponding model compared to the full expressions in the rigorous one as shown in Fig. 4-9 and Fig. 4-10, it is recognised that the rocking response can vary considerably considering that the equations are needed to be integrated twice at each time-step in the EoM of the system (Eq. (4-22)) accounting for different initial conditions at each case. In order to assess the accuracy of the proposed procedure, the response-history of both asymmetric structures is examined by utilising the two different models.

Fig. 4-11A, B show the histories of the superstructure longitudinal (u_{deck}^{CG}) and vertical displacements (v_{deck}^{CG}) as well as rotation (θ_{deck}) for the moderately asymmetric configuration (with $\bar{h} = 1.25$) when excited by AR8 and AR10, respectively. Selection of these variables to describe rocking response is made considering that they can capture all the salient features of rocking piers in asymmetric bridges and, therefore, this comparison is considered adequate to determine the accuracy of the proposed procedure examined. The values in round brackets for the simplified model (ii-red) indicate the difference in percentage between the peak response obtained with this method and that obtained with the rigorous model in the determination of the EoM (procedure i-black). It is noted that the computational time when the simplified model is utilised in the response analysis reduces approximately 90% compared to the rigorous one (i.e., the duration for a single analysis is around 1 hour for a machine with an available RAM of 10 GB when the simplified model is selected). The results in Fig. 4-11 indicate that both methods give almost identical rocking responses. The maximum difference corresponds to a 0.02% error in terms of the peak longitudinal displacements (u_{deck}^{CG}) for the AR10, while this difference disappears for the rest of superstructure variables (v_{deck}^{CG} and θ_{deck}). Therefore, adopting the simplified model proposed herein to analyse rocking response of moderately asymmetric bridges shrinks considerably the computational cost

without affecting the response-history compared to the rigorous model that includes the full expressions for the examined dependent variables.

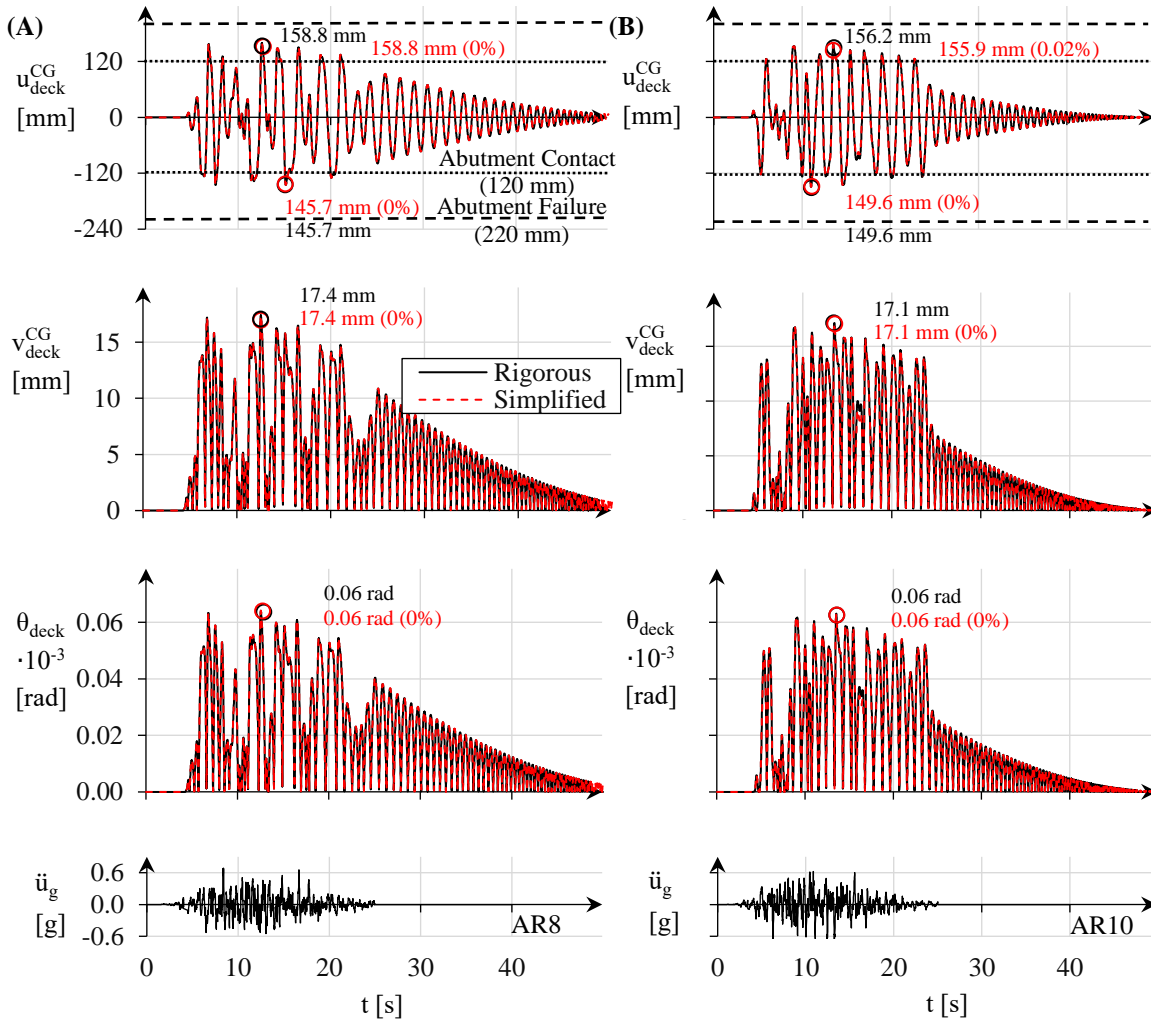


Fig. 4-11 Histories of the longitudinal (u_{deck}^{CG}) and vertical displacements of the superstructure (v_{deck}^{CG}) as well as superstructure rotation (θ_{deck}) for the moderately asymmetric bridge with rocking piers of $\bar{h} = 1.25$, considering the rigorous and simplified models for $\partial\varphi_{CD}/\partial\varphi$, $\partial^2\varphi_{CD}/\partial\varphi^2$, $\partial\theta_{deck}/\partial\varphi$ and $\partial^2\theta_{deck}/\partial\varphi^2$. Results obtained when subject to (A) AR8 and (B) AR10.

Fig. 4-12A, B present the same comparison between the rigorous and simplified models in the response-history of the highly asymmetric bridge (with $\bar{h} = 2$) when subject to AR2 and AR3, respectively. The error introduced by the proposed simplification is larger in the highly asymmetric system than in the corresponding moderately asymmetric system, but the differences in the peak responses are still relatively minor (i.e., 1.3% in u_{deck}^{CG} as well as 0.4% in v_{deck}^{CG} and θ_{deck} for the AR3 motion). These small deviations are accepted as they are not expected to affect the main conclusions of this chapter. It is noted that the same reduction in computational cost was met for this case as that shown for the moderately asymmetric system (i.e., 90% for the machine utilised for this thesis). Thus, the computationally cheap simplified model is utilised to describe $\partial\varphi_{CD}/\partial\varphi$, $\partial^2\varphi_{CD}/\partial\varphi^2$, $\partial\theta_{deck}/\partial\varphi$ and $\partial^2\theta_{deck}/\partial\varphi^2$, which returns same response-histories compared to the

same analysis by utilising the full expression of these variables as derive from Eqs. (4-2) and (4-3).

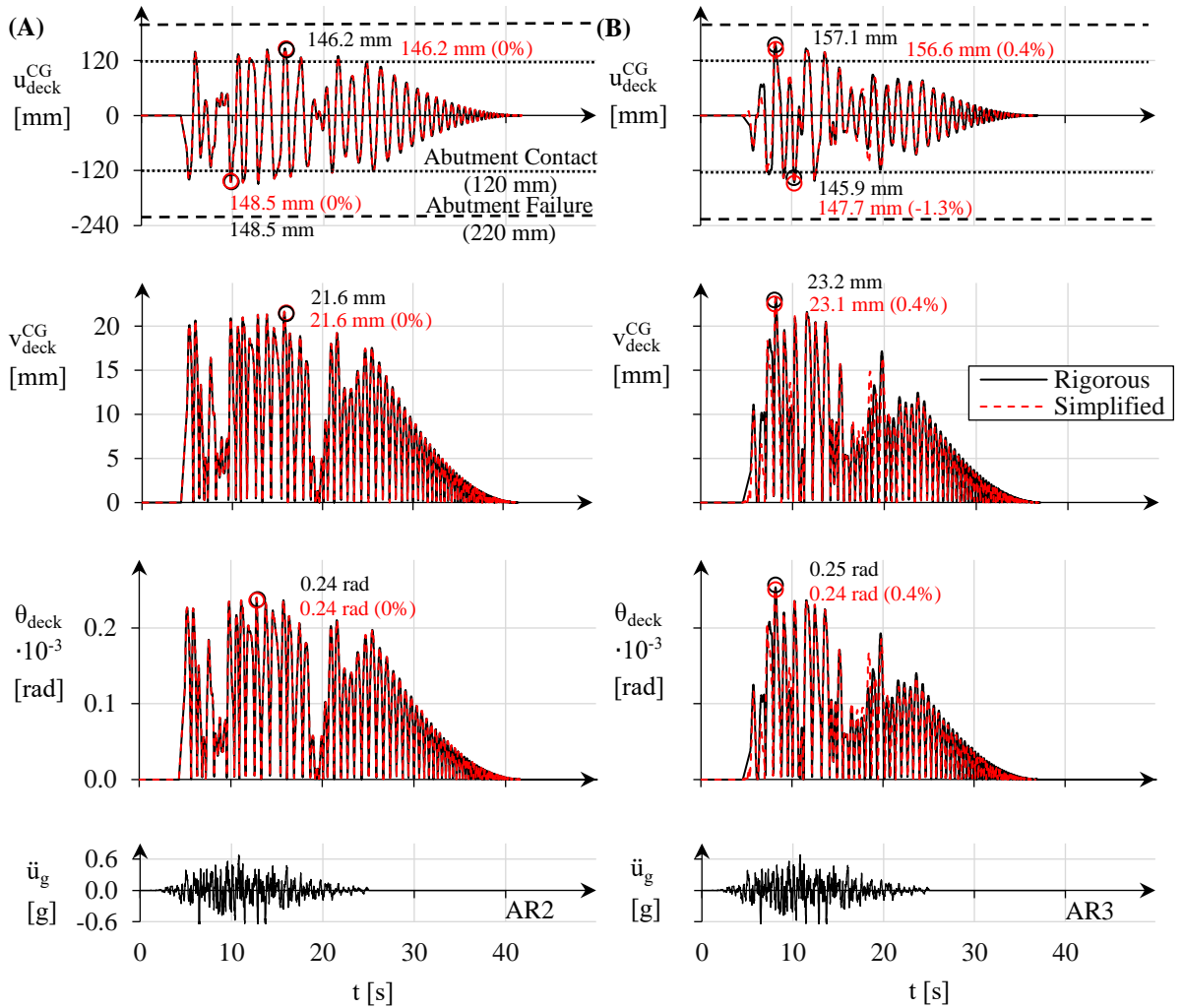


Fig. 4-12 Histories of the longitudinal (u_{deck}^{CG}) and vertical displacements of the superstructure (v_{deck}^{CG}) as well as superstructure rotation (θ_{deck}) for the highly asymmetric bridge with rocking piers of $\bar{h} = 2$, considering the rigorous and simplified models for $\partial\varphi_{CD}/\partial\varphi$, $\partial^2\varphi_{CD}/\partial\varphi^2$, $\partial\theta_{deck}/\partial\varphi$ and $\partial^2\theta_{deck}/\partial\varphi^2$. Results obtained when subject to (A) AR2 and (B) AR3.

4.3.5 Effect of the Degree of Asymmetry on Bridges with Rocking Piers

This section addresses the effect of asymmetry on the seismic performance of the bridges with rocking piers (§4.3.1) when excited by the synthetic ground motions (§4.3.2). All the examined structures are more vulnerable to the abutment-backfill failure mode than to pier overturning because $2B = 2.6 \text{ m} > u_{jo} + u_{ab} = 0.12 \text{ m}$ (§4.3.3). The response analysis of the asymmetric systems is carried out using the simplified model as described in §4.3.4.

Fig. 4-13A, B, C illustrate the peak responses of the superstructure longitudinal (u_{deck}^{CG}) and vertical displacements (v_{deck}^{CG}) as well as rotation (θ_{deck}), respectively, for the structures with different degree of irregularity. In addition, Fig. 4-13A includes the longitudinal displacement of

the deck for which contact with the abutments start (dotted line), and the ultimate longitudinal deck displacement for which the abutment-backfill system fails (dashed line). It is interesting to note that none of the bridges fail under the strong ground motions applied (§4.3.2), despite their relatively large gaps at the joints and the resulting low effective stiffness in the closed gap stage (§4.3.1). The results among the different structures are similar for the maximum longitudinal displacement of the deck (u_{deck}^{CG}). Specifically, the highly asymmetric system ($\bar{h} = 2$) shows the lowest longitudinal displacements in six out of ten cases, thus being in line with the increased stabilising factors of the deck effect (γ) and the participation of the abutment-backfill system in longitudinal rocking (q) (see Table 4-1). However, for the remaining cases, the less asymmetric systems show the lowest longitudinal deck displacements (i.e., in three cases for the symmetric system with $\bar{h} = 1$ and in one case for the moderately asymmetric system with $\bar{h} = 1.25$); therefore, a general trend cannot be derived easily. From the point of view of assessing of the seismic performance of the bridges, it is observed that the symmetric bridge reaches the largest value of its capacity against the governing failure (i.e., failure of the abutment-backfill system), which is around 46% for the AR6, while in the moderately and highly asymmetric systems the corresponding values are 44.5% and 42%, respectively, again for the same earthquake. The slightly larger value of its abutment capacity value of the symmetric structure (which is also the heaviest as it can be seen in Table 4-1) compared to the asymmetric configurations can be attributed to its slightly lower value of q . However, this difference is negligible and, therefore, it can be concluded that the overall performance of bridges with rocking piers is not significantly affected by variations in the degree of irregularity in the supporting members, which was also observed for frame structures by Dimitrakopoulos & Giouvanidis (2015).

Due to the rigidity of the structural members and based on the foregoing discussion for superstructure longitudinal displacements, analogous peak values may be expected for the vertical movement of the superstructure (v_{deck}^{CG}). However, Fig. 4-13B shows that the more unsymmetrical the configuration, the larger is the maximum uplift. Thus, the superstructure vertical displacements of the moderately and highly asymmetric systems are up to 14% and 52% larger than those of the symmetric structure, respectively. This can be explained by the rotation of the superstructure (θ_{deck}) which, although zero in the symmetric configuration due to the same rocking behaviour of the piers (§3.2.1), takes non-zero values for the asymmetric configurations (§4.2.1) with maxima of $0.07 \cdot 10^{-3}$ rad for the moderately asymmetric system subject to the AR6 motion and $0.26 \cdot 10^{-3}$ rad for the highly asymmetric system subject to AR7 as shown in Fig. 4-13C. Therefore, particular attention is required when rocking is implemented in irregular bridges while significant uplifts occur due to the rotation of the superstructure. It is noted that the contribution of the rotational movement of the superstructure (θ_{deck}) to the longitudinal movement of this member (u_{deck}^{CG}) is marginal, while the values of u_{deck}^{CG} are identical in the structures with different degree of asymmetry; on the contrary, the values of θ_{deck} influence considerably those of v_{deck}^{CG} , thus leading to higher uplifts for higher rocking-induced rotation of the superstructure.

The rotation of the deck during the rocking response of the asymmetric bridges is attributed to the differential rotations of their piers (θ_1 and θ_2), as shown in Fig. 4-13D, E, respectively. It is

observed that the rotation of the left pier remains almost unaffected by the degree of irregularity in rocking structures (around $6 \cdot 10^{-3}$ rad for all the examined cases), which can be explained by the fact that the height of this pier is the same in all the proposed bridges. However, the variation of the height of the right pier among the proposed bridges with different irregularity levels affects the peak demand of rotation at this member (θ_2). The results show that the shorter the pier (and therefore the more stocky it becomes), the higher is its rotation demand; θ_2 is up to 100% larger for the shortest pier examined (i.e., for the highly asymmetric bridge) than for the tallest one (i.e., for the symmetric structure). Hence, the superstructure uplifts and rotates more in highly irregular systems and this is due to the irregularity in the height of the piers (§2.3.2.1).

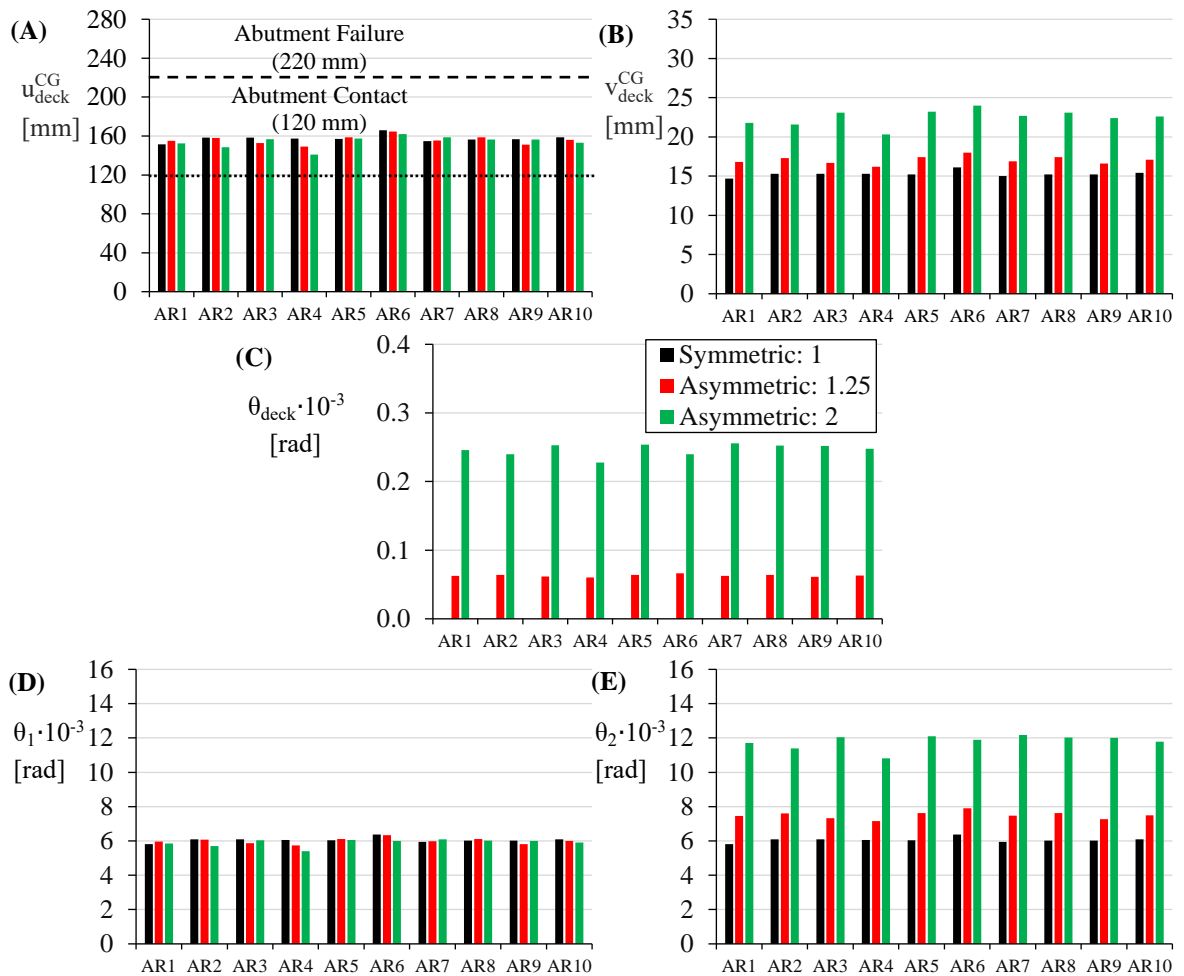


Fig. 4-13 Peak responses of the (A) longitudinal (u_{deck}^{CG}) and (B) vertical displacements of the superstructure (v_{deck}^{CG}) as well as (C) superstructure rotation (θ_{deck}), (D) relative rotation of the left rocking pier (θ_1) and (E) relative rotation of the right rocking pier (θ_2) for the bridges with rocking piers of different degree of asymmetry. Results obtained when subject to ARi.

To examine the effect of asymmetry on the overall rocking response, Fig. 4-14 shows response-histories of the superstructure and the piers for the three different configurations subject to AR7. It is observed that the highly asymmetric bridge ($\bar{h} = 2$) starts rocking later than the other configurations. In fact, the asymmetric bridge just starts rocking at $t \approx 7$ s for this record, and at

the same instant the moderately asymmetric ($\bar{h} = 1.25$) and symmetric structures ($\bar{h} = 1$) already closed their end gaps due to significant rocking (with three and four rocking cycles, respectively) and interaction takes place between abutment-backfill and the deck (see dotted line in Fig. 4-14A). This is explained from the discussion provided in §4.2.2, where it was shown that the higher the degree of irregularity in a bridge with rocking piers, the larger is the minimum base acceleration required to initiate rocking. After rocking initiates, as it can be seen in Fig. 4-14A, the superstructure moves longitudinally in a similar way for all the different configurations for the remainder of the ground motion, showing similar amplitudes and the same number of rocking cycles, with small differences. Therefore, the longitudinal behaviour of the superstructure is not affected considerably due to the different analytical dynamics of symmetric (§3.2) and unsymmetric bridges (§4.2).

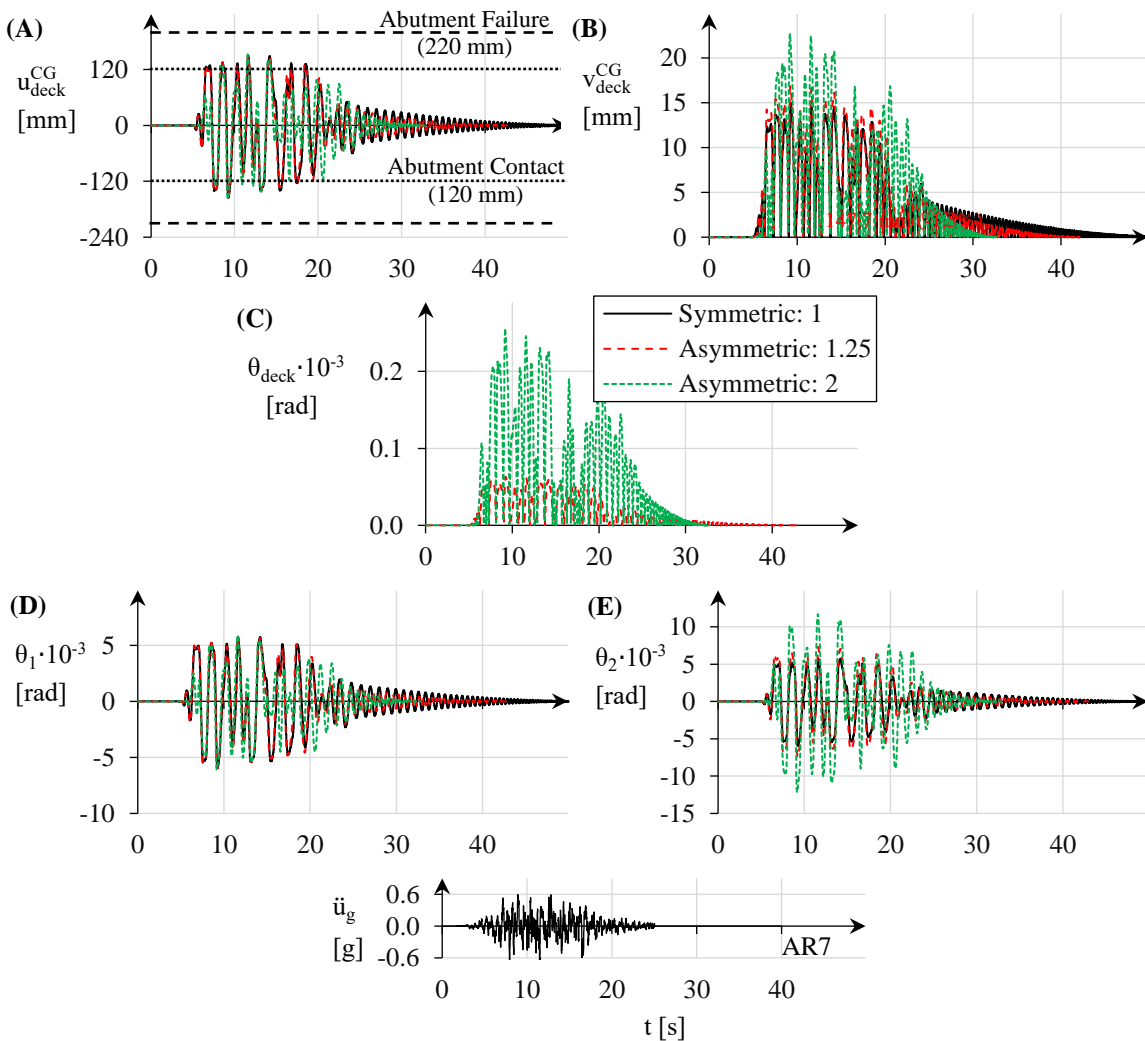


Fig. 4-14 Histories of the (A) longitudinal (u_{deck}^{CG}) and (B) vertical displacements of the superstructure (v_{deck}^{CG}) as well as (C) superstructure rotation (θ_{deck}), (D) relative rotation of the left rocking pier (θ_1) and (E) relative rotation of the right rocking pier (θ_2) for the bridges with rocking piers of different degrees of asymmetry. Results obtained when subject to AR7.

The irregular structures present substantially larger vertical displacements (v_{deck}^{CG}) and rotations (θ_{deck}) in the girder than the symmetric bridge, as shown in Fig. 4-14B, C, respectively. This is more significant in the highly asymmetric configuration due to the differential rotations of its two piers, with large differences in height. To this effect, Fig. 4-14D, E show the histories of the rocking rotations of the two piers θ_1 and θ_2 , respectively. It is shown that the left rocking pier, having the same height in all the bridges, has almost the same response at each rocking cycle regardless of the height of the right pier. However, the response of the right pier is significantly increased with the irregularity of the bridge, because its height is reduced. This is observed at each rocking cycle and it reaches a maximum difference at $t \approx 12$ s, when the right pier in the highly asymmetric bridge has a rotation demand that is 140% larger than the one corresponding to the same pier in the symmetric configuration. Nevertheless, the rocking movement decays faster in asymmetric structures. This is particularly clear after $t \approx 24$ s, and it is due to the higher energy dissipation introduced by the impacts at the rocking interfaces in the asymmetric configurations. This is explained by the values of the CoR η , which are equal to 0.986, 0.982 and 0.96 in the symmetric, moderately and highly asymmetric bridges (see Fig. 4-6), respectively. The longitudinal influence of the abutment-backfill system (q) is also slightly higher in the asymmetric structures (see Table 4-1) and, in combination with the lower value of η gives to the structures with more unequal piers the capacity to dissipate more energy during the earthquake than the corresponding symmetric systems. Finally, it is observed that the irregularity in pier height reduces the number of impacts during the earthquake, which can improve the structural integrity of the rocking interfaces in the bridge (e.g., Mathey *et al.* 2016).

4.4 Closing Remarks

Chapter 4 presented the dynamics of asymmetric bridges with rocking piers which extends previous work on asymmetric frames (Dimitrakopoulos & Giouvanidis 2015), by including the end spans (L_1) and the end joint gaps (u_{jo}) that activate the abutment and the backfill behind it when closed. As in the case of symmetric bridges (§3), the abutment-backfill system is modelled through a spring (k) - dashpot (c) Kelvin-Voigt system, and pounding of the deck on the abutment backwall (e) was also included. The following key remarks apply for the proposed analytical model compared to the corresponding asymmetric frame model with rocking columns (Dimitrakopoulos & Giouvanidis 2015);

- Rocking motion initiates at the same instant for both asymmetric bridges and frames. This is because of the frictionless sliding bearings considered at the abutment seats of the bridge, which do not restrain the longitudinal movement of the superstructure, so long as the end gap (u_{jo}) does not close.
- The EoM of bridges with rocking piers includes a new term that is not present in equivalent frames without end supports and expresses the resistance of the spring (k) and dashpot (c)

elements at the bridge ends when the longitudinal end joint gap (u_{jo}) is closed. The parameter (q) introduced in §3 represents the level of longitudinal resistance of the abutment/backfill and it depends on the total mass of the system.

- Modelling of impact at the rocking interfaces accounts for the additional vertical impulses developed at the abutment seats. This is done by incorporating in the formulation the end spans (L_1) that are of different length than the central span (L_2). The vertical supports at the abutment seats increase the value of the CoR at the rocking interfaces (η), leading to lower energy dissipation by the bridge compared to the equivalent frame. This is due to the reduction of the deck weight that is transmitted to the piers, and it becomes more noticeable the more irregular is the height of the piers in the bridge.
- The analytical model incorporates the energy dissipation due to pounding of the superstructure on the abutment backwall by means of a CoR value (e). In addition, a new failure mode associated with the collapse of the abutment-backfill system due to excessive longitudinal displacements induced by the superstructure on the abutment backwall is defined. This failure mode is more critical than the classical pier overturning in the rocking response of bridges with conventional dimensions.

It is noted that, similarly to Dimitrakopoulos & Giouvanidis (2015) where ignoring asymmetry reduces the rocking solution to that of the corresponding symmetric frame presented by Makris & Vassiliou (2013), the analytical model presented in Chapter 4 simplifies to the corresponding symmetric bridge presented in §3 after considering two rocking piers of same height. After studying the effect of the abutment/backfill and the pier irregularity in the analytical formulation of the EoM, three conventional bridges with different levels of asymmetry and relatively large end gaps were subjected to ground motions, stronger than the design earthquake. The following conclusions were drawn for the effect of asymmetry in the rocking of bridges;

- The computational cost of integrating step-by-step the full EoM of asymmetric bridges with rocking piers is very high. A significant reduction of this calculation time was achieved by using a simplified model where the expressions of the derivatives of the governing DoF of the rocking system are substituted by simple linear and quadratic expressions, without affecting the accuracy of the results.
- All the bridges with rocking piers considered herein resisted a very high seismic excitation that is almost two times larger than the design one in the considered seismic zone, with a reserve capacity against the prevailing failure mode of approximately 50%, regardless of the degree of irregularity.
- The level of asymmetry in bridges with rocking piers does not affect significantly the demand of longitudinal displacements in the deck and the rotation of the tallest pier (whose height is kept the same in all studied bridges). However, in a performance assessment context, the lower

the asymmetry in a rocking configuration, the more likely is the prevailing failure mode to be activated (i.e., abutment-backfill failure mode when realistic bridge configurations are examined). This is attributed to the lower value of the stabilising effect of the abutment-backfill system (q) in configurations of lower irregularity.

- The more different the height of the piers, the larger is the uplift of the deck during the rocking motion and, this has to be accounted for when rocking is implemented in irregular structures. This is due to the larger rotation demand in the shorter pier.
- The configurations with higher level of asymmetry experience less impacts at the rocking interfaces due to (i) the delay in the initiation of the rocking motion, and (ii) the slightly larger attenuation of the rocking motion. The latter is explained because bridges with higher degree of asymmetry in rocking piers height dissipate more seismic energy because they have a slightly lower CoR at the rocking interfaces (η) and higher levels of participation of the abutment/backfill (q).

Chapter 5

Non-conventional Pier Configurations in Bridges with Rocking Piers

5.1 Introduction

Chapter 5 examines the dynamics and the seismic performance of bridges with free-standing rocking piers of non-conventional configuration. The focus is on the effect of the shape of the piers in cross-section and in elevation, studied using the analytical model developed in §3. This study is motivated by the fact that the flexural and the shear strains are negligible in the piers during the free rocking motion (rigid body motion is predominant as shown i.a. by Agalianos *et al.* 2017), and therefore new, more efficient, rocking pier configurations are worth exploring, with a view to reducing the overall cost and the seismic forces in the structure without affecting its performance. Additionally, the free-standing conditions of the piers (i.e., no firm connection is required at either end of the piers as described in §3), along with the possibility of devising piers with relatively complex geometries, make prefabrication suitable, and hence speed up the construction process. This is well aligned with the concept of ABC that has gained significant attention worldwide due to the advantages that it offers over the ‘traditional’ construction methods, such as substantial reduction of onsite construction time and lower cost (Doolen *et al.* 2011). It is noted that, although a broad range of pier shapes are offered offsite, so far the research community has favoured conventional pier sections in ABC applications, such as rectangular (e.g., Zhang *et al.* 2018) or circular (e.g., Tucker & Ibarra 2016). However, by reducing the mass of the rocking piers, the designer is also reducing the inherent restoring mechanisms of the bridge (i.e., the mass and mass moment of inertia of the piers are reduced when less solid sections are utilised). This is carefully explored in this chapter by introducing the following *modifications and advancements* to the bridge model presented in §3;

- Extension of the studied configuration of symmetric bridges supported on rectangular rocking piers to a system with piers of ‘non-rectangular’ shape.
- Derivation of a general expression for the EoM to describe the longitudinal rocking motion of the bridge accounting for ‘non-rectangular’ pier sections.
- Derivation of a general expression for the CoR to describe the attenuation of rocking motion when an impact at the rocking interfaces takes place, considering the potential reduction in the restoring capability of the vertical members due to their reduced mass with respect to the ‘traditional’ rectangular piers.

In this respect, two ‘non-rectangular’ pier configurations are proposed in §5.2. The kinematics of the rocking motion in §5.2.1 is presented with emphasis on the differences between the translational and rotational resistances of piers with conventional (rectangular) and non-conventional shapes. The general forms of the EoM and the expression for CoR to describe the energy dissipation at each impact at the rocking interfaces are given in §5.2.2 and §5.2.3, respectively. The analysis framework adopted herein (§5.3) includes a symmetric bridge with different pier configurations (§5.3.1) under design and ‘extreme’ earthquake conditions (§5.3.2), and an assessment of its seismic performance (§5.3.3). Finally, the seismic behaviour of symmetric bridges with rocking piers of conventional and non-conventional configurations is compared in §5.3.4, both from the economy and seismic performance points of view.

5.2 Analytical Model of the Rocking Response

The bridge configurations follow the schematic shown in Fig. 3-1. Specifically, the superstructure has a total length $L_{tot} = 2L_1 + [N - 1] \cdot L_2$. The frictionless sliding bearings located at the abutment seats allow the deck to move freely in the longitudinal direction until the gap at one of the end joints is closed (u_{j0}) and the deck impacts on the corresponding abutment backwall. Thereafter, the abutment-backfill system is activated through spring (k) and dashpot (c) elements that are arranged in parallel (Kelvin-Voigt model). The superstructure consists of a single-cell box girder section with constant depth ($2h$) and constant cross-section (A_{deck}) throughout length. The structure is supported on N free-standing rocking piers with slenderness $\alpha = \tan^{-1}(B/H)$ and size $R = \sqrt{H^2 + B^2}$ that are designed to rock freely on the foundation (CR A'-A for a side pier and C'-C for an intermediate pier) and the deck interfaces (accordingly, points B-B' and D-D').

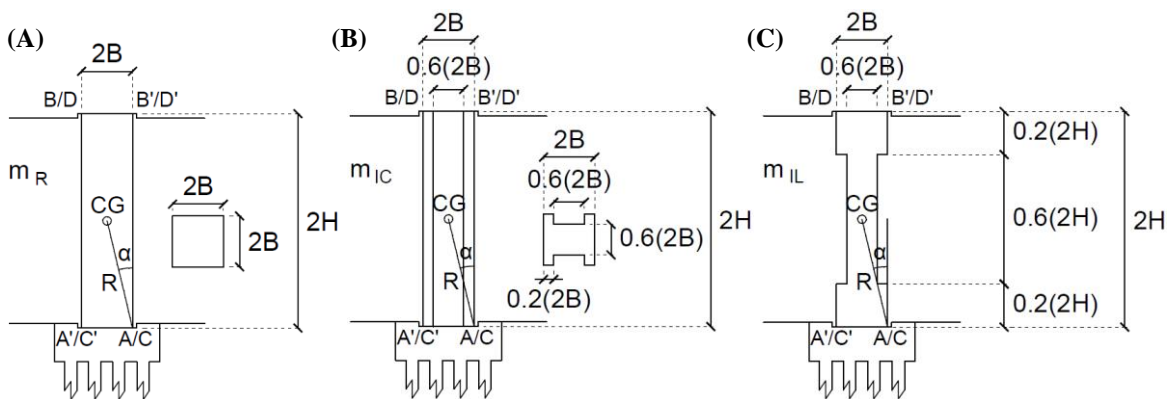


Fig. 5-1 Schematic of rocking piers with (A) rectangular section (or R), (B) I-shaped cross-section (or IC) and (C) I-shaped longitudinal section (or IL). The piers are at the at-rest position.

The alternative pier shapes are presented in Fig. 5-1A, B, C, ranging from the most to the least massive section. These are, respectively, a conventional rectangular section (referred in the following as R), an I-shaped cross-section (IC) and an I-shaped longitudinal section or ‘barbell’ (IL). The ‘non-rectangular’ shapes are inscribed in the rectangular one and their dimensions were

selected aiming to give a reasonably low value for the normalised axial force (v) at the critical sections of each pier configuration (CEN 2004a) assuming realistic dimensions for the bridge system; it is noted that the dimensions of the piers with non-conventional section lead to an increase of v_{Ed} approximately 2.5 times with respect to the compact R section. Similarly to §3.2, the same criteria are adopted to formulate the rocking motion when non-conventional sections are selected for the piers.

5.2.1 Kinematics

Fig. 5-2A, B, C show the rocking piers with different configuration rotating around the CR A (or C) in the clockwise direction. Taking into account that all piers have the same height, the superstructure is forced to translate only through top pivot B (or D) without experiencing out-of-plane rotation (§4.2.1). The same DoF is selected for the bridges with different pier shapes, namely the relative rotation of each pier with respect to the at-rest position (θ) (§3.2.1). Considering that the proposed pier shapes have the same slenderness (α) and size (R), the longitudinal (u) and vertical (v) relative displacements of the CG of the piers and the deck remain unaffected by the shape of the pier section. These movements are described by Eqs. (3-1) and (3-2) for u and v , respectively. Similarly, the corresponding linear velocities (\dot{u} and \dot{v}) are given by Eqs. (3-3) and (3-4), respectively. Thus, the changes in the pier shape do not affect the conditions describing rocking initiation of the bridge (§3.2.2) and Eq. (3-8) can be used to calculate $\ddot{u}_{g,\min}$. In addition, the energy dissipation due to an impact of the superstructure on the abutment backwall (§3.2.4) is not affected by the piers shape and Eq. (3-22) captures this phenomenon.

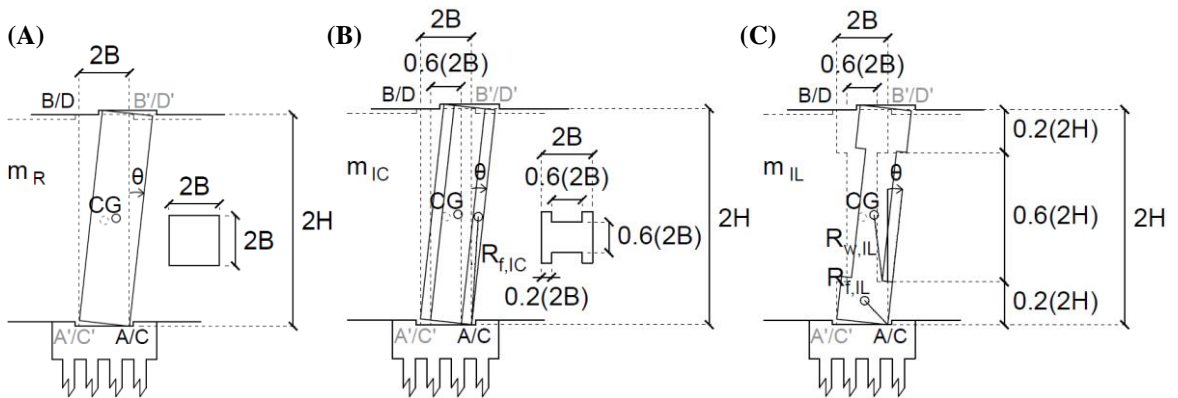


Fig. 5-2 Schematic of rocking piers with (A) R, (B) IC and (C) IL configurations during rocking motion.

The restoring capability of the entire system comes from the mass of the superstructure ($m_{deck} = 2\rho \cdot A_{deck} \cdot L_{tot}$) and the substructure ($N \cdot m_{pier}$), as well as the mass moment of inertia of each pier (I_{pier}^{CG}). The mass of each pier can be easily determined by the dimensions shown in Fig. 5-1A, B, C, and it is given by the following expressions, respectively

$$m_R = 8\rho B^2 H, \quad (5-1)$$

$$m_{IC} = 6.08\rho B^2 H , \quad (5-2)$$

$$m_{IL} = 4.928\rho B^2 H , \quad (5-3)$$

where ρ is the mass density of the pier material. For the dimensions shown in Fig. 5-1, the IC pier is heavier than the IL pier. The mass reduction for a non-conventional pier with respect to the circumscribed rectangular one is 24% and 38.4% for the IC and IL sections, respectively. Fig. 5-3 illustrates the total mass of the bridge (m_{tot}) in terms of the number of piers (N) considering different pier shapes. To this effect, reference is made to a Reinforce Concrete (RC) bridge ($\rho = 2500 \text{ kg/m}^3$) with end span length $L_1 = 43 \text{ m}$, intermediate span length $L_2 = 65 \text{ m}$ and cross-sectional area $A_{deck} = 6 \text{ m}^2$ throughout the whole length that is supported on concrete piers with width $2B = 2.2 \text{ m}$ and height $2H = 28 \text{ m}$. In general, more piers with non-conventional shape lead to larger reductions of the bridge mass, which results in savings compared to the solution with conventional R piers. The total mass reduction for the case of IC piers with respect to the R piers ranges from 5% for short bridges (low number of N) to 6% for long multi-span bridges (high number of N), while the corresponding difference for the IL configuration assumes values between 8% and 10%.

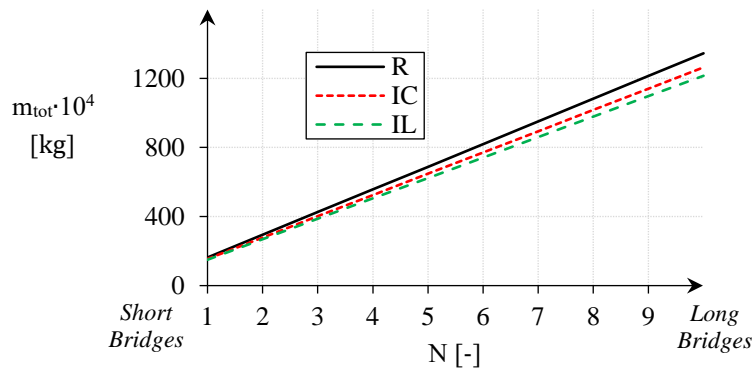


Fig. 5-3 Total mass (m_{tot}) of bridges with rocking piers of different configuration, accounting for the influence of number of piers (N). Results obtained when the pier dimensions and the deck section are constant.

The rotational movement of the piers is resisted through the mass moment of inertia of each member that depends on the shape of the section. The following expressions give the value of I_{pier}^{CG} for each pier configuration

$$I_R^{CG} = m_R R^2 / 3, \quad (5-4)$$

$$I_{IC}^{CG} = I_R^{CG} \left[0.4\bar{R}_{f,IC}^2 + 0.5376 \sin^2 a + 0.36 \right], \quad (5-5)$$

$$I_{IL}^{CG} = I_R^{CG} \left[0.4\bar{R}_{f,IL}^2 + 0.216\bar{R}_{w,IL}^2 + 0.768 \cos^2 a \right], \quad (5-6)$$

where $\bar{R}_{f,IC} = R_{f,IC}/R$ and $R_{f,IC} = \sqrt{H^2 + 0.04B^2}$ refers to the IC pier and is the distance from the active CR (A'-A for a side pier, and C'-C for an intermediate pier) to the CG of the flange as shown in Fig. 5-2B, $\bar{R}_{f,IL} = R_{f,IL}/R$ and $R_{f,IL} = \sqrt{0.04H^2 + B^2}$ is the corresponding distance for the bottom flange of the IL pier, while $\bar{R}_{w,IL} = R_{w,IL}/R$ and $R_{w,IL} = \sqrt{0.36H^2 + 0.36B^2}$ refers to the semi-diagonal of the web for the IL configuration, as shown in Fig. 5-2C. It is noted that Eqs. (5-5) and (5-6) are calculated according to the parallel axis theorem and are simplified to the preceding forms after rearranging. These expressions show that the mass moment of inertia of the piers with 'non-rectangular' shape depends on the slenderness (α) of the section. The effect of α can be visualised by varying the height of the piers (H) and maintaining a constant width $2B$ as shown in Fig. 5-4 for concrete ($\rho = 2500 \text{ kg/m}^3$) piers with $2B = 2.2 \text{ m}$. As expected, the slenderer the pier is (the higher the value of H or R), the larger I_{pier}^{CG} regardless of its section. Comparing different pier configurations, it is noticed that the non-conventional piers have less rotational resistance than the conventional one. However, the IL piers, despite being the lightest section examined, have larger values of I_{pier}^{CG} than the IC piers. Therefore, the opposite trend occurs for the reduction in I_{pier}^{CG} compared to the reduction in m_{pier} discussed before. Specifically, the percentage reduction for the piers with IL shape compared to the R piers ranges from 18.6% to 14% for short to tall sections, respectively, while the pertinent quantity for IC piers assumes values between 22.4% and 24%, thus showing that this difference diminishes for stocky members. This indicates that the I-shape is preferably used longitudinally than in cross-sections when the rotational resistance of the pier is the variable to be addressed, especially for tall piers.

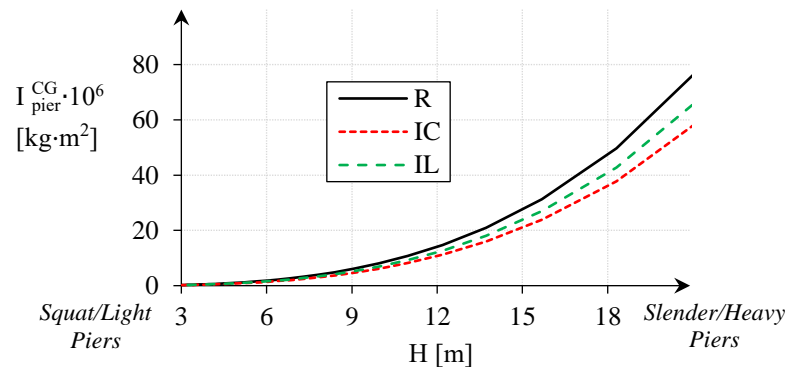


Fig. 5-4 Mass moment of inertia of a rocking pier with respect to its CG (I_{pier}^{CG}) for different pier configurations, accounting for the influence of pier height (H). Results obtained when the pier width is constant.

Consequently, rocking piers with non-conventional IC and IL shapes decrease the restoring capability of a bridge compared to conventional R rocking piers. Thus, the IC and IL rocking piers are in principle worse candidates than the R piers for bridges, notwithstanding the reduction of the horizontal inertial forces of at least 5% and 8% (for the dimensions examined herein) compared to the R configuration, respectively, and the economic and environmental implications of the decreasing use of concrete.

5.2.2 Equation of Motion during Rocking

The ground acceleration threshold for which a symmetric bridge starts rocking is given by Eq. (3-8) regardless of the rocking pier configuration. The prediction of the rocking response stems from the Lagrangian formulation in Eq. (3-9), and the EoM is based on the procedure presented in §3.2.3. To account for the effect of the different pier shapes on the rocking motion of bridges, Eqs. (5-1) to (5-6) are substituted into Eqs. (3-11), (3-16) and (3-18), and the general form of the EoM is derived after rearranging

$$\ddot{\theta} = \overbrace{-p^2 \frac{1+2\gamma}{p_{sec,1} + 3\gamma} \left[\text{sgn}(\theta) \sin(a - |\theta|) + \frac{\ddot{u}_g}{g} \cos(a - |\theta|) \right]}^{\text{frame system}} - \overbrace{p^2 q \left[\begin{array}{l} k \text{sgn}(\theta) \left(\sin \alpha - \sin(a - |\theta|) - \frac{u_{jo}}{2R} \right) \\ \cos(a - |\theta|) + c(\cos^2(a - |\theta|)) \dot{\theta} \end{array} \right]}^{\text{abutment-backfill contribution}}, \quad (5-7)$$

where $\gamma = m_{deck}/N \cdot m_{pier}$ describes the effect of the mass of the superstructure accounting for the mass of the different substructure configurations (m_{pier}) according to Eqs. (5-1) to (5-3), and $q = 4R/g \cdot [p_{sec,1} \cdot N \cdot m_{pier} + 3m_{deck}]$ expresses the contribution of the abutment-backfill system.

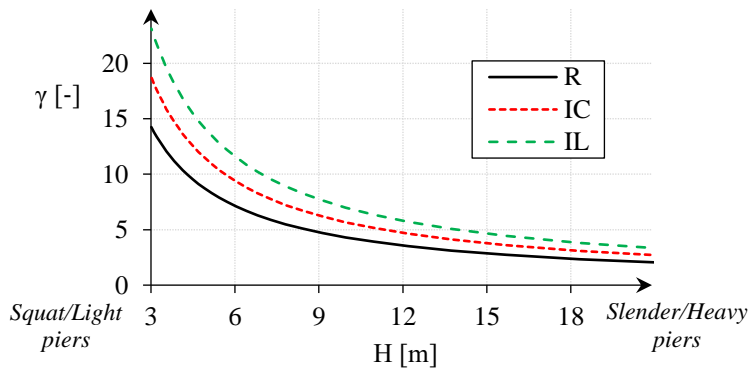


Fig. 5-5 Superstructure mass effect (γ) for bridges with rocking piers of different configuration, accounting for the influence of pier height (H). Results obtained when the pier width and the deck mass are constant.

The mass of the deck enters in the coefficient $\gamma = m_{deck}/N \cdot m_{pier}$, and it stabilises the seismic rocking response of the bridge as it increases (Makris & Vassiliou 2014b). This is verified here by considering a bridge with superstructure mass $m_{deck} = 519 \cdot 10^4$ kg that is supported on $N = 5$ rocking piers with width $2B = 2.2$. Fig. 5-5 plots the value of γ with respect to the height of the piers (H). As expected, if the mass of the superstructure (m_{deck}) does not change, reduction of the mass of the substructure increases the value of γ . Compared to the structures that are supported on R piers, in bridges with IC and IL piers γ increases by approximately 30% and 60%, respectively,

for all the examined cases. Therefore, the higher value of γ in bridges with rocking piers of non-conventional shape is expected to result in enhanced rocking performance than those supported by R rocking piers.

Compared to Eq. (3-20) that describes the EoM of a symmetric bridge with R rocking piers, Eq. (5-7) shows a new dimensionless constant $p_{sec,1}$ that depends on the shape of the piers and influences the term ‘*frame system*’ as well as the value of q . Table 5-1 gives the formulae for this constant with respect to the different pier configurations, and Fig. 5-6 plots the value of the shape factor $p_{sec,1}$ for rocking piers with constant width $2B = 2.2$ m and different heights (H). In general, the IC sections show values of $p_{sec,1}$ that are close to unity. This is also the case with R piers and, therefore, the component of the EoM attributed to the ‘*frame system*’ as well as the effect of the abutment-backfill system (q) have similar participation in the rocking response of bridges with IC or R rocking piers. However, the value of $p_{sec,1}$ is reduced in bridges with IL rocking piers; $p_{sec,1}$ is 4.7% lower in the tallest IL piers compared to the conventional R ones with the same H and B , and this reduction becomes 6.5% in the shortest piers considered. For this reason, bridges with IL rocking piers are expected to show increased rocking amplitudes before the deck contacts the abutments and, accordingly, a more significant suppression of the longitudinal motion due to the contribution of the abutment-backfill system when the end joint gap is closed compared to the bridges that are supported on heavier rocking piers. This effect is more pronounced in bridges with short IL rocking piers.

Table 5-1 Formulae for the shape factor $p_{sec,1}$ for piers of different configuration.

Shape Factor	Pier Configuration	Formula
$p_{sec,1}$	R	1
	IC	$0.1316 \cdot \bar{R}_{f,IC}^2 + 0.1768 \cdot \sin^2\alpha + 0.8684$
	IL	$0.1623 \cdot \bar{R}_{f,IL}^2 + 0.0877 \cdot \bar{R}_{w,IL}^2 + 0.3117 \cdot \cos^2\alpha + 0.6039$

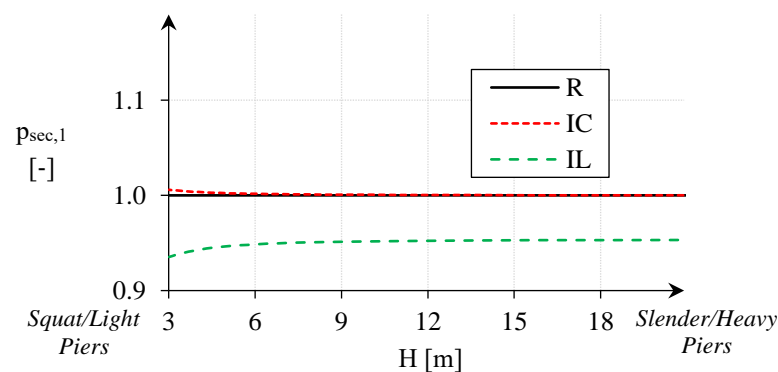


Fig. 5-6 Shape factor $p_{sec,1}$ for rocking piers of different configuration, accounting for the influence of pier height (H). Results obtained when the pier width is constant.

In order to establish the effect of pier configuration on the contribution of the abutment-backfill system (q), the bridge properties used for constructing Fig. 5-5 are also used in Fig. 5-7. The plots

include the value of q with respect to the height of the pier (H). It is observed that the bridges with rocking piers of non-conventional shape show larger values of q than those with conventional R piers. This is expected considering that the proposed piers with non-conventional shapes are lighter than those with conventional configuration. The largest increment of q for the structures with IC and IL piers with respect to those with R piers is observed in the tallest piers considered (with $H = 20$ m) and is equal to 3.6% and 6.4%, respectively. However, differences are smaller in the shortest piers with $H = 3$ m (0.5% and 1%, respectively). The variation in terms of q is directly proportional to the height of the piers, and therefore to their mass. Specifically, when light-weight piers are considered, the IC and IL configurations reduce the total mass of the bridge with respect to the structure with R piers by 1.5% and 2.5%, respectively, but this reduction is up to 8.1% and 13%, respectively, in the bridge with the tallest piers. Consequently, the denominator in the expression for q reduces more in structures with heavy (or tall) non-conventional piers, which are expected to develop a more significant interaction with the abutment-backfill system than in bridges with conventional R piers. This is more significant for the piers with IL configuration.

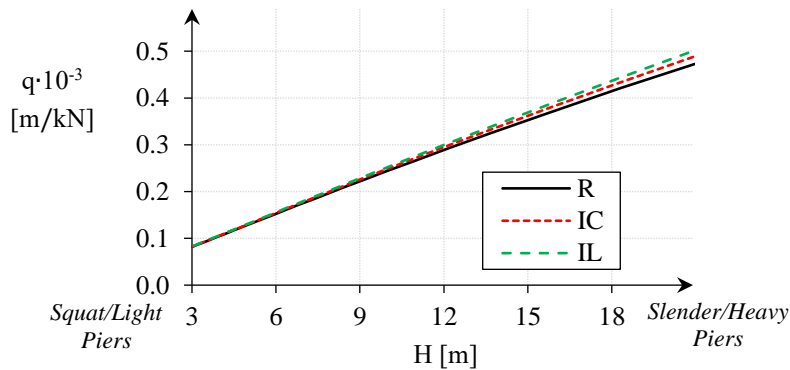


Fig. 5-7 Longitudinal influence of the abutment-backfill system (q) for bridges with rocking piers of different configuration, accounting for the influence of pier height (H). Results obtained when the pier width and the deck mass are constant.

Consequently, although the non-conventional pier shape leads to a reduction in the horizontal (m_{pier}) and rotational resistance (I_{pier}^{CG}) to their rocking motion when considered in isolation, the effect of their shape on the overall rocking behaviour of bridges can be favourable through the increased values of γ and q compared to structures supported on conventional piers.

5.2.3 Impact at the Rocking Interfaces

The impact problem in bridges with rocking piers of non-conventional shape is treated analogously to §3.2.5 and attenuation of rocking motion is expressed via a CoR at the rocking interfaces $\eta = |\dot{\theta}_{II}/\dot{\theta}_I|$. The general expression for η accounting for the effect of the different pier shapes is achieved by substituting Eqs. (5-1) to (5-6) into Eqs. (3-26) to (3-30), and is given by the following expression

$$\eta = \left| \frac{\dot{\theta}_{II}}{\dot{\theta}_I} \right| = \frac{p_{sec,2} - \frac{3}{2} \sin^2 a - \frac{3}{4} \gamma [\bar{L} + 1] [(\bar{L} - 1 + N) \cos 2a + \bar{L} \cos^2 a]}{-\frac{1}{8} \left[3\bar{L} + N + \frac{1}{N} (2\bar{L}^2 - 3\bar{L} + 1) \right] [p_{sec,3} + 3 \cos 2a]} , \quad (5-8)$$

$$p_{sec,2} - \frac{3}{4} \gamma [\bar{L} + 1] [(\bar{L} - 1 + N) + \bar{L} \cos^2 a]}{-\frac{1}{8} [p_{sec,3} + 3] \left[3\bar{L} + N + \frac{1}{N} (2\bar{L}^2 - 3\bar{L} + 1) \right]}$$

where the span arrangement is described through $\bar{L} = L_1/L_2$ and, as expected, η is independent of the direction of the movement due to the symmetry of the rocking system regardless of the pier configuration. With respect to Eq. (3-31) that describes η for symmetric bridges that are supported on R rocking piers, Eq. (5-8) includes two additional dimensionless parameters ($p_{sec,2}$ and $p_{sec,3}$) that depend on the shape of the pier, as it can be seen in Table 5-2. Fig. 5-8A, B plot the values of $p_{sec,2}$ and $p_{sec,3}$, respectively, for different values of the pier height (H), considering a constant width $2B = 2.2$ m. Similarly to conventional piers, the IC piers assume values of $p_{sec,2}$ and $p_{sec,3}$ that are close to unity. Therefore, these constants are not expected to affect considerably the dissipated energy at each impact at the rocking interfaces when IC or R rocking piers are utilised. On the contrary, bridges with IL piers have significantly higher values of $p_{sec,2}$ and $p_{sec,3}$ that is on average 9.3% and 37%, respectively. However, the effect of this difference is not expected to influence considerably the value of η considering that these two factors influence both the numerator and the denominator in Eq. (5-8).

Table 5-2 Formulae for the shape factors $p_{sec,2}$ and $p_{sec,3}$ for piers of different configuration.

Shape Factor	Pier Configuration	Formula
$p_{sec,2}$	R	1
	IC	$0.1316 \cdot \bar{R}_{f,IC}^2 + 0.1768 \cdot \sin^2 \alpha + 0.8684$
	IL	$0.1623 \cdot \bar{R}_{f,IL}^2 + 0.0877 \cdot \bar{R}_{w,IL}^2 + 0.3117 \cdot \cos^2 \alpha + 0.75$
$p_{sec,3}$	R	1
	IC	$0.5263 \cdot \bar{R}_{f,IC}^2 + 0.7074 \cdot \sin^2 \alpha + 0.4737$
	IL	$0.6494 \cdot \bar{R}_{f,IL}^2 + 0.3506 \cdot \bar{R}_{w,IL}^2 + 1.2468 \cdot \cos^2 \alpha$

Fig. 5-9 illustrates the effect of the different pier configurations on the CoR at the rocking interfaces and compares η in bridges with R, IC and IL rocking piers as a function of their height (H). The results shown are for a deck with mass $m_{deck} = 519 \cdot 10^4$ kg and a span length ratio $\bar{L} = 0.66$ that is supported on five rocking piers ($N = 5$) with width $2B = 2.2$ m. It is observed that slenderer piers have lower energy dissipation (higher value of η), echoing the work of Housner (1963). Comparison among the bridges with piers of different configuration in Fig. 5-9 shows that,

although lighter structures (bridges with IC and IL piers) are expected to dissipate less energy at each impact at the rocking interfaces than heavier ones (bridges with R piers) (Makris & Vassiliou 2014b), the value of η remains virtually unaffected by the configuration of the piers in cross-section and in elevation; it is noted that the differences are below 0.01% for all the examined cases. This is attributed to the considerable increase in the value of the parameter γ for bridges with non-conventional rocking piers compared to the structures supported on R rocking piers (see Fig. 5-5), which counteracts the reduction in the total mass of the corresponding structures. Therefore, non-conventional piers increase the overall energy dissipated during rocking because, even though the energy at each impact at the rocking interfaces (η) is not affected, their interaction with the abutment/backfill (q) is more significant (see Fig. 5-7) and they dissipate more energy through radiation and material damping of the backfill (c).

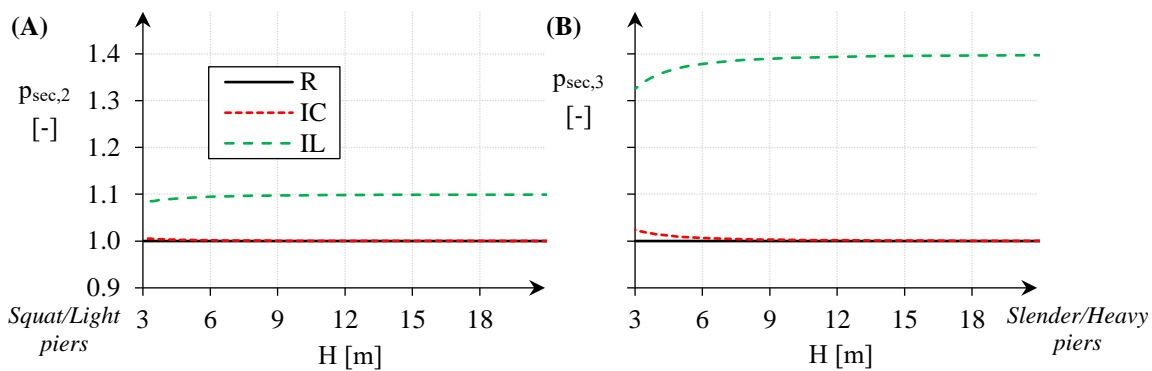


Fig. 5-8 Shape factors (A) $p_{sec,2}$ and (B) $p_{sec,3}$ for rocking piers of different configuration, accounting for the influence of pier height (H). Results obtained when the pier width is constant.

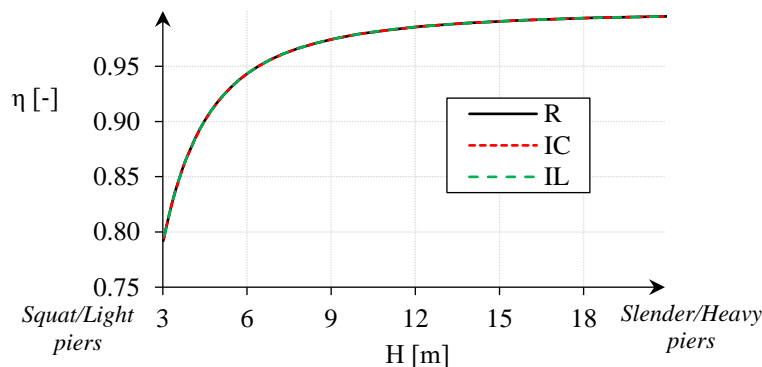


Fig. 5-9 CoR at the rocking interfaces (η) for bridges with rocking piers of different configuration, accounting for the influence of pier height (H). Results obtained when the pier width and the deck mass are constant.

5.3 Analysis Framework

This section examines symmetric bridges with rocking piers of conventional and non-conventional configurations (§5.3.1) when subjected to ground motions of different frequency content (§5.3.2).

The emphasis is on the response of non-conventional piers and on the comparison with conventional solutions; the reader is referred to §3.3 for a detailed discussion on the rocking response analysis of the latter. The analysis of the bridges with non-conventional piers starts by obtaining the ground acceleration threshold beyond which rocking is initiated using Eq. (3-8). Afterwards, the rocking motion of the structure is obtained from Eq. (5-7) that is integrated step-by-step using the ‘ode45’ solver in MATLAB (2016) with a typical time-step of 10^{-3} s. This time-step is reduced to $5 \cdot 10^{-6}$ s when impacts on the abutment-backwalls and at the rocking interfaces are close to occur (when $\theta = \theta_{jo}$ or $\theta = 0$, respectively); the adaptive time-stepping defined in MATLAB is explained in §4.3. The effects of the impacts on the abutment backwalls and at the rocking interfaces are introduced by means of Eqs. (3-22) and (5-8), respectively. The failure criteria of the bridges with piers of non-conventional configuration will be described in §5.3.3, and this condition is simply integrated in the analysis as a special case that terminates the analysis process if satisfied. For a more detailed representation of this procedure, the reader is referred to Fig. A-2 taking into account the adjustments that are needed due to the different equations that are utilised for bridges with rocking piers of non-conventional configuration.

5.3.1 Description of the Studied Bridges

The effect of the different pier configurations on the seismic performance of bridges with rocking piers is established considering three similar structures with straight decks. Each substructure consists of rocking piers having one of the configurations shown in Fig. 5-1. A span of total length $L_{tot} = 2L_1 + 4L_2 = 2 \cdot 43 + 4 \cdot 65 = 346$ m needs to be bridged and $N = 5$ rocking piers are used to achieve it with width $2B = 2.2$ m and height $2H = 28$ m. In a practical context, the five piers used for each bridge are transferred in precast segments to the construction site and they are installed with monolithic connection between the segments, while seating conditions are established at the rocking interfaces. The deck section consists of a single-cell box girder with height $2h = 1.7$ m, bottom flange width equal to $B_{bot} = 6$ m, top flange width equal to $B_{top} = 9.5$ m, as well as flange and wall thicknesses are set equal to $t_f = 0.3$ m and $t_w = 0.8$ m, respectively. These dimensions result in a cross-sectional area $A_{deck} = 6$ m², constant throughout the length of the deck. The longitudinal gap between the superstructure and the abutments is set equal to $u_{jo} = 0.1$ m, and when this gap is closed pounding takes place that is expressed through a CoR $e = 0.6$ (§3.3.4.4). The abutment and the backfill properties are obtained from Kappos *et al.* (2007) as discussed in §3.3.1. This leads to a spring stiffness $k = 132$ MN/m (§3.3.4.1) and a dashpot coefficient $c = 48$ MN·s/m (§3.3.4.2), with the displacement capacity of this member being $u_{ab} = 0.1$ m (§3.3.4.1). The examined structures are classified to importance class II ($\gamma_I = 1$), are founded on soil C and belong to the highest seismicity zone prescribed in Southern Europe with PGA equal to 0.36 g. Table 5-3 shows further information for each bridge related to the pier configuration. This table shows the progressive reduction in the total mass of the bridge system with the conventional R solution to IC rocking piers (approximately 6% lighter than R) and IL configurations (approximately 9% lighter than R). Table 5-3 also includes the normalised axial load ($v_{Ed} = N_{Ed}/A_c \cdot f_{cd}$) that is developed at

the critical section of each pier under self-weight conditions and adopting a concrete grade C35/45, indicating a significant capacity for additional vertical loads.

Table 5-3 Information for the bridges with rocking piers of different configuration, including the deck mass (m_{deck}), the pier mass (m_{pier}) and the total mass (m_{tot}) as well as the critical section of the pier (A_c) and the induced normalised axial load (v_{Ed}).

Pier Configuration	$m_{deck} \cdot 10^4$ [kg]	$m_{pier} \cdot 10^4$ [kg]	$m_{tot} \cdot 10^4$ [kg]	A_c [m ²]	v_{Ed} [-]
R	519	34	688	2.2·2.2=4.8	0.08
IC	519	26	648	1.3·1.3=1.7	0.23
IL	519	21	623	1.3·1.3=1.7	0.23

Table 5-4 shows the values of γ and q , the stability factors in the rocking seismic response of the three bridges. Specifically, the superstructure mass effect (γ) is higher for the bridges with rocking piers of non-conventional configuration than in the bridge with conventional pier shape, as was also observed in Fig. 5-5. The percentage increase in the value of γ compared to the structure on R rocking piers is approximately 31.6% and 62.3% for the bridges with IC and IL rocking piers, respectively. Accordingly, the level of longitudinal influence of the abutment-backfill system (q) increases slightly for bridges with non-conventional piers compared to the structure with R piers (see Fig. 5-7). This is due to the reduction in the total mass for the structures with IC and IL piers, and also the reduction in $p_{sec,1}$ for the latter as it was observed in Fig. 5-6. However, the variation among the participation factors q in different piers is small, and it takes values of 2% and 4% for the structures with IC and IL rocking piers compared to the conventional ones for which q is the smallest. It is also noted that the value of q in the proposed bridges is close to the lowest value shown in §3.3.4.3, which implies that the abutment-backfill system is vulnerable to the seismic rocking response (§3.4).

Table 5-4 Stabilising factors for the bridges with rocking piers of different configuration, including the superstructure mass effect (γ) and the longitudinal influence of the abutment-backfill system (q).

Pier Configuration	γ [-]	$q \cdot 10^{-3}$ [m/kN]
R	3.1	0.332
IC	4	0.340
IL	5	0.346

5.3.2 Representation of Seismic Action

5.3.2.1 Single-frequency Pulse-type Ground Motions

The effect of pier shape on the rocking response of bridges is studied by first applying ground motions simulated with the simplified sine, Ricker symmetric and antisymmetric pulses described in §3.3.2.1 (see Eqs. (3-32) to (3-34)).

5.3.2.2 Multi-frequency Synthetic Ground Motions

The next stage of the study includes the analysis of the three bridges under the ten ARs matching the design earthquake spectrum (PGA = 0.36 g) that were justified in §3.3.2.2. Additionally, ten ARs were also generated to match a spectrum that is larger than the design one in order to address the effect of pier shape in ‘extreme’ seismic events. To this end, the records were generated to match the Type 1 EC8 reference spectrum for site conditions C (CEN 2004b) and for a PGA equal to 0.72 g as shown in Fig. 5-10.

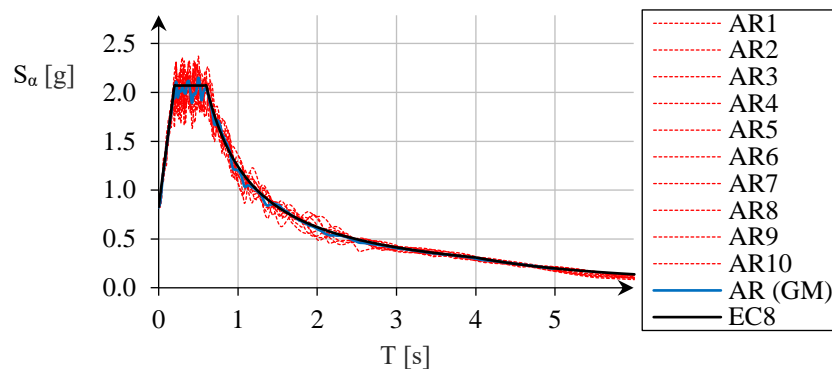


Fig. 5-10 Response acceleration spectra of the set of ARs, and matching to EC8 target spectrum with PGA = 0.72 g and site conditions C.

5.3.3 Failure Criteria

The failure modes considered for the bridges with rocking piers of non-conventional shape are the same as those in structures with R rocking piers, namely overturning and abutment-backfill failure as explained in detail in §3.3.3. Therefore, overturning occurs when $|u_{deck}^{CG}| \geq 2B$ and the abutment-backfill fails if $|u_{deck}^{CG}| \geq u_{jo} + u_{ab}$. Since the expressions for the longitudinal displacement of the deck (u_{deck}^{CG}) is not affected by the shape of the piers (§5.2.1), the failure criteria can be expressed in terms of the DoF of the system (θ) as in §3.3.3.

5.3.4 Effect of the Non-conventional Pier Configurations on Bridges with Rocking Piers

5.3.4.1 Rocking Response under Single-frequency Pulse-type Ground Motions

This section examines the seismic performance of bridges with rocking piers of different configuration (§5.3.1) by considering pulse-type excitations (§5.3.2.1), and this is done in terms of FMAS shown in Fig. 5-11. Although all bridge configurations are more prone to fail due to the abutment-backfill failure mode than due to pier overturning ($2B = 2.2 \text{ m} > u_{jo} + u_{ab} = 0.2 \text{ m}$), both failure modes are plotted in the failure spectra of Fig. 5-11 to examine in more detail the effect of pier shape. The FMAS are calculated for a wide range of pulse durations ($\omega_p = [0.1 \sim 6] \cdot p$ and $p = 0.72 \text{ rad/s}$) and acceleration amplitudes ($\alpha_p = [0.1 \sim 15] \cdot g \cdot \tan \alpha$ and $g \cdot \tan \alpha = 0.079 \text{ g}$) to obtain a complete view of the minimum acceleration that induces either failure mode.

Fig. 5-11A, B, C show that the shape of both failure curves for the bridges with rocking piers of non-conventional configuration is not differentiated compared to the structures supported on the conventional R rocking piers (discussed in detail in §3.3.5.1) regardless of the pulse-type motion. Specifically, it is shown that all bridge configurations have the ‘sickle’ shaped behaviour for the abutment failure mode, while the higher vulnerability of the three bridges for the medium-frequency pulses is attributed to their relatively low value of q (see Table 5-4, Fig. 3-14 and discussion in §3.3.5.1). Additionally, the curve representing the overturning failure coincides with the curve for the abutment failure mode in the low-frequency range, while the value of α_p increases progressively for $\omega_p/p > 2$ compared to the corresponding value for the abutment failure mode; this difference shows values at least three times larger in the high-frequency range for all the different configurations and types of ground motion.

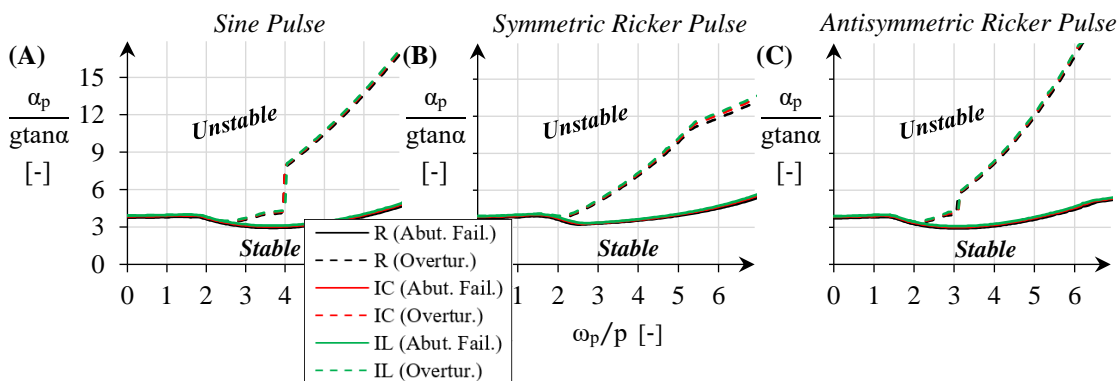


Fig. 5-11 FMAS for the bridges with rocking piers of different configuration. Results obtained when subject to acceleration pulses of (A) sine, (B) symmetric and (C) antisymmetric Ricker type.

Comparison among the different configurations in Fig. 5-11 shows that the failure spectra for the bridges with non-conventional rocking piers are slightly shifted upwards compared to those for the structures with R rocking piers. Specifically, in bridges with IC piers the value of α_p that induces abutment failure and overturning increases compared to the structures with solid R piers up to 3.1% and 2.3%, respectively, for all the mathematical excitations. The corresponding increase in the case of bridges with IL piers with respect to those with R piers is approximately 5% and 3.7%,

respectively. The increase in the value of α_p for both failure modes in the structures with non-conventional piers is attributed to their reduction in the total mass of the bridge (i.e., recall that the total mass in bridges with IC and IL piers is 6% and 9% smaller than that with R piers, respectively). This results in (i) lower horizontal forces in the structures with IC and IL piers, (ii) improved performance that is expressed through the increased value of the superstructure mass effect (γ), and (iii) larger longitudinal influence of the abutments and the backfills (q). These effects overcome the decreased restoring capability (inertia) of rocking piers with non-conventional configuration, which eventually gives slightly enhanced behaviour in a performance assessment context to bridges with these members. This is more significant in the IL piers, and it results in bridges with the best seismic performance and the least use of material.

From the foregoing discussion about the increase in the value of α_p with respect to the bridges with R piers, it is also observed that structures with IC and IL piers have larger increments of α_p for the abutment failure mode than for the overturning condition. This implies that non-conventional pier shapes protect to a higher extent the abutment integrity than the overturning condition. This can be explained because there is no stabilising effect from the abutment-backfill system (q) for the abutment that has failed. Therefore, the system is transformed from a bridge to a frame-type mechanism (i.e., the abutment-backfill system is participating in longitudinal rocking response in one or none of the two ends). In this regard, the lower restoring mechanisms of the piers with non-conventional configuration (m_{pier} reduces for a single pier approximately by 24% and 38.4% when IC and IL shapes are employed for this member with respect to the R shape, respectively, and in the same way I_{pier}^{CG} reduces by 23.9% and 14.1% according to Fig. 5-4, respectively) seem to dominate in the rocking system, implying that piers with non-conventional shape may not be adequate for rocking structures without end supports (i.e., frames with rocking columns).

5.3.4.2 Rocking Response under Multi-frequency Synthetic Ground Motions

This section presents the seismic response of the three bridges (§5.3.1) when they are subject to the accelerograms that apply to the design and the ‘extreme’ earthquake conditions (§5.3.2.2). Fig. 5-12 illustrates the peak responses of the superstructure longitudinal displacement (u_{deck}^{CG}) for all bridge configurations in the design context. The displacement demand at the contact with the abutments (dotted line) and the ultimate displacement capacity in the abutment-backfill systems (dashed line) are also shown.

Fig. 5-12 shows that all bridge configurations survived the design ground motions with substantial margin before the prevailing failure mode (i.e., abutment-backfill) is activated. In general, bridges with different rocking pier configurations have slightly lower rocking amplitudes in terms of the longitudinal movement of the superstructure compared to the bridge on R rocking piers. Specifically, the value of u_{deck}^{CG} decreases for the bridge with IC piers compared to the structure with R piers up to 1.4% for the AR4. Analogously, the structures with IL piers reduce the value of u_{deck}^{CG} approximately by 2.3% for the AR4. However, the response of the bridges with R piers is not always enhanced as can be seen for the structure with IC piers subject to the AR7

motion (i.e., the difference is around 1%). Thus, the value of u_{deck}^{CG} generally decreases by reducing the total mass of the structure, which is mainly explained by the corresponding increase in the effect of the abutment-backfill system (q) (see Table 5-4). This introduces a larger restriction to the free longitudinal rocking motion as well as higher energy dissipation when contact with the abutments occurs. Therefore, the bridges with rocking piers of non-conventional shape show slightly improved rocking response in a design context with respect to those with conventional piers, and this improvement is more noticeable in the case of the IL pier configuration.

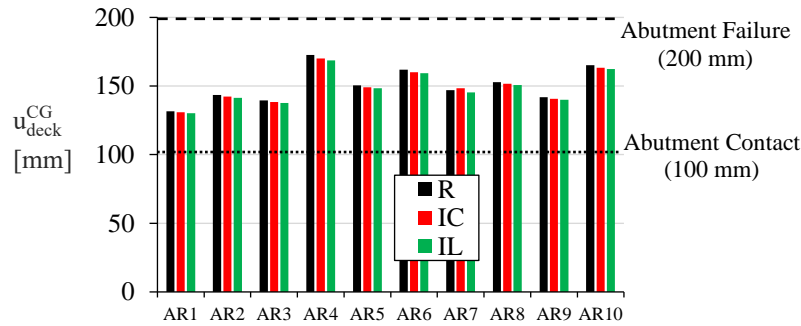


Fig. 5-12 Peak responses of the longitudinal displacement of the superstructure (u_{deck}^{CG}) for the bridges with rocking piers of different configuration. Results obtained when subject to ARi applying to the design earthquake conditions (PGA = 0.36 g).

To illustrate the effect of pier configuration on the overall rocking response, Fig. 5-13A, B show the histories of the longitudinal displacement of the deck (u_{deck}^{CG}) under the design spectrum-compatible AR3 and AR9. Again, the displacements describing the contact between the deck and the abutments (dotted line) and the failure of the abutment-backfill systems (dashed line) are illustrated. Initially, it is observed that all the studied bridges start rocking motion exactly at the same time instant (at $t \approx 6$ s and $t \approx 3$ s when subject to AR3 and AR9, respectively), which is expected because the value of $\ddot{u}_{g,min}$ in Eq. (3-8) does not depend on the pier shape. Similarly, and after rocking starts, all the bridge structures show identical response-histories by having the same number of deck-abutment contacts and similar rocking amplitudes at each rocking cycle until nearly the end of the ground motion (at $t \approx 22$ s). Therefore, non-conventionality in pier shape does not affect the response-history of the bridge when the excitation is active compared to the same structure with R piers.

The effect of the pier configuration in the response-histories in Fig. 5-13A, B becomes apparent after the earthquake almost finishes and the bridge continues moving in free rocking response. This is observed in Fig. 5-13A after $t \approx 21$ s, and when the piers with non-conventional configuration lead to larger rocking amplitudes due to their lower mass and mass moment of inertia, resulting in additional contacts of the superstructure with the abutment backwall while, at the same time, the structure with R piers behaves as a frame system in free rocking motion. These contacts dissipate energy through pounding (e) as well as through radiation and material damping of the backfill soil (c). Therefore, the bridges with rocking piers of non-conventional configuration show lower rocking amplitudes in the following cycles and dissipate the rocking motion slightly faster, with less impacts at the rocking interfaces than the structure with R rocking piers. This is not observed

in AR9 in Fig. 5-13B. Specifically, after $t \approx 22$ s there is no impact at the abutments in any configuration and the bridges with non-conventional rocking piers have slightly higher rocking motions due to their reduced values of m_{pier} and I_{pier}^{CG} . This effect is more apparent for the lightest system (with IL piers), and this can be explained by the decreased value of $p_{sec,1}$ (i.e., approximately by 4.7% compared to the R and IC cases as shown in Fig. 5-6) that increases the free rocking motion of this system more than the other configurations. This results in the bridges with non-conventional rocking piers having slightly longer rocking motions and, therefore, a larger number of impacts (part of this is shown in Fig. 5-13B). It should be noted though that the crucial for the integrity of the piers issue of number of impacts that take place throughout the whole rocking motion is not differentiated considerably in the case of bridges with piers of non-conventional and R shapes as can be seen in Fig. 5-13A, B. This can be particularly relevant to the fact that all the bridge configurations dissipate energy at the same pace at each impact at the rocking interfaces (i.e., $\eta = 0.989$ for all the cases as shown in Fig. 5-9). Therefore, the non-conventional in shape piers protect the integrity of the rocking interfaces in the same way to more compact piers, notwithstanding the economy in material use described before.

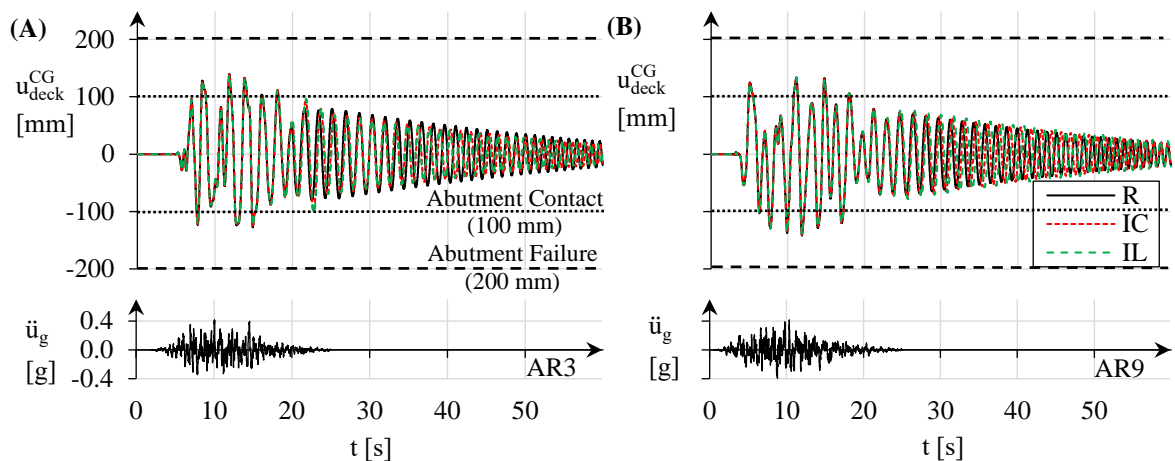


Fig. 5-13 Histories of the longitudinal displacement of the superstructure (u_{deck}^{CG}) for the bridges with rocking piers of different configuration. Results obtained when subject to (A) AR3 and (B) AR9 applying to the design earthquake conditions (PGA = 0.36 g).

The seismic performance of the three bridges under the ‘extreme’ earthquake scenario described in §5.3.2.2 is considered now, and Fig. 5-14A, B show the peak longitudinal displacements of the superstructure (u_{deck}^{CG}). This is done separately in the positive and negative directions, in order to identify in more detail the cases where abutment-backfill failure mode is activated. However, the analysis continues after abutment failure (i.e., beyond superstructure displacements of 100 mm) by assuming that the actual capacity of the abutment is higher than that assumed in the thesis, in an effort to address the rocking response of the structures that are transformed from a bridge to a frame-type mechanism. Overall, failure in the abutments in bridges with R and IC rocking piers is observed for 20% of the ground motions for both directions (three records induce failure of this member in the positive direction and 1 in the negative direction), while this type of failure is observed in 15% of the records in the structure with IL piers (two

records make the abutment fail in the positive direction and one in the negative direction). The difference for the lightest IL section is due to the protection of the abutment in the positive direction subject to AR3 that is not met for the other pier configurations. Therefore, the lightest structure protects the integrity of the abutment in more cases than the heavier configurations, suggesting the beneficial effect that non-conventionality in pier shape has in the rocking of bridges. Considering now the responses for the records in which the abutments do not fail, the mass reduction associated with non-conventional piers enhances slightly the seismic performance compared to bridges using R. This is observed in all the ground motions, with reductions of the peak longitudinal deck displacements that are on average 1.2% and 2.1% in IC and IL bridges, respectively. Nevertheless, it is interesting to note that the highest rocking amplitude is observed for the IC bridge (622.6 mm when subject to AR3 in the positive direction). This value develops after the abutment fails or, in other words, during the free rocking motion of the system, indicating that non-conventional piers may lead to more unstable rocking responses when the structure behaves as a frame.

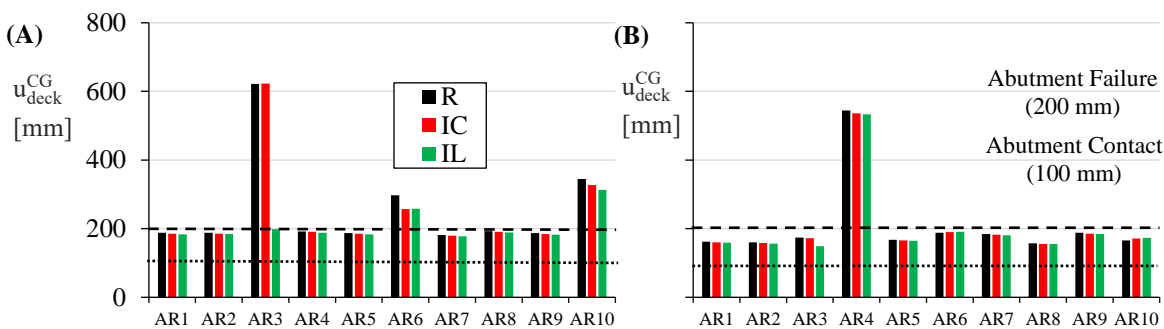


Fig. 5-14 Peak responses of the longitudinal displacement of the superstructure (u_{deck}^{CG}) for the bridges with rocking piers of different configuration. Results obtained when subject to ARi applying to the ‘extreme’ earthquake conditions (PGA = 0.72 g).

Fig. 5-14A, B also indicate that the piers of the studied bridges do not overturn for any of the ground motions. Considering the largest response of the R and the IC bridges (i.e., in the positive direction when subject to AR3), these two structures reach a maximum of 28.2% and 28.3%, respectively, of their pier rotation capacity (which in terms of the longitudinal deck displacement is 2200 mm). On the other hand, the bridge with IL piers reaches a lower peak of 24.2% of its pier overturning capacity in the negative direction under AR4. This shows that the three bridges with rocking piers have a significant reserve capacity against overturning, even in ‘extreme’ earthquake conditions (PGA = 0.72 g), especially for the case with rocking piers of IL configuration.

5.4 Closing Remarks

Chapter 5 considered the effect of the shape of the piers on the rocking response of bridges. In this regard, piers with ‘non-rectangular’ configurations, including an I shape in cross-section and a barbell shape in elevation were put forward. The motivation for these proposals is based on the inherent advantages of rocking pier isolation in an ABC context, that is (i) rocking piers show

negligible flexural strains during rocking motion, and (ii) the lack of firm connections at the rocking interfaces is suitable for ABC and, in that sense, prefabrication allows for selecting complex pier shapes that are not usually adopted in earthquake-resistant bridges. Looking ahead, considering that several studies propose the use of post-tensioned unbonded tendons to minimise sliding (§2.4.1.1, Table 2-3, Table 2-4), the use of tendons seems also important given that the rocking prefabricated piers will in practice be segmental. The following conclusions were drawn for the proposed non-conventional configurations of the rocking piers compared to the conventional rectangular in shape rocking piers in bridges;

- The non-conventional rocking pier configurations can reduce the use of concrete in the bridge examined herein up to approximately 8% in short bridges and 10% in multi-span long bridges compared to the same structures supported on rectangular rocking piers.
- The EoM during longitudinal rocking of the bridge and the COR at the rocking interfaces (η) in the bridges with non-conventional piers are distinguished from those with conventional piers by means of shape factors ($p_{sec,1}, p_{sec,2}, p_{sec,3}$), for which analytical expressions were provided.
- The value of η remains unaffected by variations in the pier configuration returning equivalently stable structures in that respect. However, bridges with non-conventional piers show higher overall energy dissipation through the material and the radiation damping of the backfill soil (c), and this is due to the increased contribution of the abutment-backfill system (q) in these structures.
- The bridges with non-conventional piers present slightly improved rocking response in a design context. The level of improvement is proportional to the reduction in the total mass of the system. The higher the mass reduction in the rocking piers, the lower the seismic forces that are developed during rocking, the higher the superstructure mass effect (γ) that contributes to the structural stability, and the higher the participation of the abutments and the backfills (q) in the rocking mechanism that counteract the decreased restoring capability of bridges with non-conventional rocking piers.
- The number of impacts during the rocking motion is not significantly affected by the shape of the rocking piers, implying that the integrity of their rocking interfaces is in the same conditions as in the conventional piers; further examination is required though regarding this crucial issue. This can be particularly relevant to the same initiation of rocking motion and the same energy dissipation when an impact at the rocking interfaces takes place for the bridges with piers of different configuration.
- In a performance assessment context for pulse-type motions, results obtained from FMAS show that the structures with rocking piers of non-conventional configuration enhance slightly the seismic performance by protecting to higher extent the integrity of the abutments, and by avoiding pier overturning (i.e., the curves are shifted slightly upwards). This is also confirmed

for the most economic (lightest) pier section examined when strong multi-frequency ground motions are utilised.

- Overturning of the piers in the longitudinal direction is practically impossible to occur, regardless of the piers shape; even under earthquakes that exceed the design PGA by two times, the reserve capacity against pier overturning is around 75%. This outcome should be related to the importance of the abutment-backfill system in rocking response and the relevant comparison with frames (see §3.3.5).
- The results suggest that the largest rocking motions of the bridges with non-conventional piers occur when the bridge is transformed into a frame-type mechanism (i.e., after one or both abutments fail), thus implying the reason why these sections were not used in frame systems in the past. This is due to their lower restoring mechanisms (inertia), which are more important in the rocking response of structures without longitudinal end supports.

Chapter 6

Comparative Assessment of Conventional Seismic and Rocking Pier Isolation

6.1 Introduction

Chapter 6 compares the seismic performance of bridges with rocking pier isolation with those controlled through a conventional seismic isolation technique. An existing overpass bridge with unequal height piers is selected for the comparison. This is because the asymmetry of the piers may have a significant influence in the rocking response, as shown in §4. In addition, a modified version of the actual geometry of the structure by increasing pier heights is considered to explore the influence of taller piers (or piers with lower slenderness) on the seismic response. The comparison is based on the results of analyses using rigorous FE models in the general-purpose software ABAQUS CAE (2018).

Seismic performance of asymmetric bridges with rocking piers was examined in §4.3.5 based on some essential assumptions that facilitated the analytical formulation of the rocking response; these are stated in §3.2 and are briefly: (i) the rocking problem is examined in two dimensions neglecting transverse rocking, (ii) all the structural members are considered rigid and (iii) there is no sliding at any instant during the entire rocking motion. However, the two-dimensional analysis restrains the response to an impact-like motion, neglecting the phenomena of wobbling and rolling (Vassiliou 2017) or twisting of the bridge piers, which might occur during biaxial excitations, while the assumptions of no sliding at the rocking interfaces (Mohamad *et al.* 2015) and rigidity of all members (i.a., Roh & Reinhorn 2009, Sideris 2015) may lead to failing to properly capture the actual effect of rocking in all structural members. These assumptions have been studied in the past using numerical or experimental tools, but other simplifications were adopted in those studies (§2.5). Chapter 6 addresses the effect of these assumptions, and extends the numerical studies described in §2.5 by using rigorous FE models to simulate contact of the rocking interfaces and the dynamic interaction between the deck and the abutments.

Moreover, Chapter 6 extends the work of Agalianos *et al.* (2017), which is one of the most complete works on FE analysis of bridges with rocking pier isolation to date (§2.5). The following *modifications and advancements* are introduced here with respect to the 3D numerical models developed by Agalianos *et al.* (2017);

- Consideration of an irregular bridge configuration, wherein rocking pier isolation is expected to be less beneficial than in a system with piers of equal height.
- Examination of rocking pier isolation in its ‘pure’ original form (i.e., no firm connection of the superstructure at any support location) as opposed to the ‘hybrid’ rocking solution adopted by

Agalianos *et al.* (2017) where the superstructure is bearing-supported on the piers and the abutments.

- Use of ground motion more realistic than the ‘extreme’ earthquake conditions considered by Agalianos *et al.* (2017) that led to overturning of the rocking alternative. It is noted that the abutment failure mode was ignored in that study, despite the fact that it typically precedes pier overturning (see §2.5, §3.3.3, §4.3.3).
- More realistic interface conditions at both ends of the rocking piers are considered herein associated with a reasonable value for the static CoF at the rocking interfaces μ_s , contrary to the special contact elements used in Agalianos *et al.* (2017) to prevent sliding ($\mu_s = 10$).

The two isolation techniques are implemented on an actual overpass (§6.2.1), and rigorous 3D numerical models of the entire bridge system are developed in ABAQUS CAE (2018) introducing deformable sections for all structural elements. The bridge with conventional isolation has Lead Rubber Bearings (LRBs) (§6.2.2.1) and is designed according to the current EC8 provisions (CEN 2005b); the latter is done separately for the actual bridge with short piers in §6.2.2.1.1 and for its modified configuration with taller piers in §6.2.2.1.2. The piers in the bridge with rocking pier isolation are allowed to rock and slide freely at both interfaces, and the superstructure is not restrained in both horizontal directions at the abutment seats (i.e., ‘purely’ free-standing system) as described in §6.2.2.2. The seismic performance of the bridges is examined considering eleven natural ground motions that are properly scaled to exceed a code spectrum (§6.2.3). The details of the FE analysis are included in §6.2.4, with the parametric study being presented in §6.3. Finally, the seismic responses obtained with the two isolation techniques are compared in §6.4 in terms of displacements of the structural members, BMs developed at the different deck spans and the piers, as well as the recentering capability of the entire system. This is done separately for the actual bridge with short piers and for the modified configuration with tall piers in §6.4.1 and §6.4.2, respectively.

6.2 Description of the Bridge Model and Analysis Outline

6.2.1 Original Bridge Overpass

A typical overpass bridge (Fig. C-1 in Appendix C), part of Egnatia Motorway located in Northern Greece, is used as case study; some modifications of the actual structural characteristics are made, depending on the analysed design alternative (i.e., conventional seismic isolation and rocking pier isolation). The actual bridge is a 3-span 99-m long structure with a central span of 45 m and two end spans of 27 m. The longitudinal slope of the deck is approximately 7%. The superstructure is a 10-m wide prestressed concrete box girder with a total depth of 2 m. More solid cross-sections are used for the deck towards the abutments ($A_{deck} = 12.6 \text{ m}^2$) and the piers ($A_{deck} = 9.2 \text{ m}^2$), while a lighter box girder is selected for the spans ($A_{deck} = 5.9 \text{ m}^2$) (Fig. C-2), thus resulting in $m_{deck} = 187 \cdot 10^4 \text{ kg}$. The actual substructure consists of cylindrical piers with diameter $D_{pier} = 2 \text{ m}$ and

heights equal to $h_{P1} = 5.4$ m and $h_{P2} = 7.4$ m (Fig. C-1 and Fig. C-3A). The pier-to-deck connection is monolithic, while the superstructure rests on each abutment through two elastomeric bearings (Fig. C-3B).

The superstructure is initially free to move at the abutments in both horizontal directions, while longitudinal and transverse displacements are restrained whenever a 100 mm (Fig. C-4) and a 150 mm gap (Fig. C-3B) between the deck and the abutment is closed, respectively. The abutments consist of a wall system with total height above the foundation of 5.3 m for Abutment 1 (Fig. C-3B) and 5.7 m for Abutment 2 (Fig. C-4), while the height of the backwall is 2 m. The soil conditions correspond to stiff formations categorised as Ground B according to the EC8 site classification (CEN 2004b). The piers and the abutments are supported on footings with dimensions $9 \times 8 \times 2$ m (Fig. C-1 and Fig. C-3A) and $12 \times 4.5 \times 1.5$ m (Fig. C-1 and Fig. C-3B), respectively. The deck and the piers are made in concrete grade C30/37 (CEN 2004a), while this grade is C16/20 in the abutments and in the foundations.

The original bridge was designed according to the provisions of the Greek Seismic Code that was applicable at the time of design (EAK 2003, similar to CEN 2005a). Additional dead loads were considered equal to 58.4 kN/m. The traffic actions correspond to the LM1 adopted by CEN (2004b), including a uniformly distributed load equal to 38 kN/m and point loads equal to 327.2 kN, with 20% of this action being considered in the seismic analysis. The thermal actions for the considered location of the bridge were based on $T_{e,\min} = -12$ °C and $T_{e,\max} = 42$ °C (Egnatia Motorway 2002, Paraskeva & Kappos 2010). The seismic design spectrum was constructed based on $PGA = 0.16$ g, site conditions of Class B, importance factor $\gamma_I = 1$ and behaviour factors along the longitudinal and transverse directions $q_{(X,Y)} = 2$.

6.2.2 Finite Element Modelling

The general-purpose software ABAQUS CAE (2018) is selected for the FE analyses due to the fact that it can properly deal with impact problems (as shown i.a. by Ou *et al.* 2007, ElGawady & Dawood 2012, Sideris 2015, Li *et al.* 2017). The modelling approach for both isolation alternatives and both pier schemes short and tall) is presented in the following sections. The same concrete grades as those used in the actual bridge are assigned to the different structural elements in all bridge configurations and isolation alternatives examined. Inelasticity effects are ignored in all RC members in both isolation approaches, considering that these members are expected to stay in the elastic range during the whole response. In this respect, concrete grade C16/20 is described by the characteristic compressive strength $f_{ck} = 16$ MPa and the mean Young's Modulus $E_{cm} = 29$ GPa (CEN 2004a). The material properties of C30/37 concrete are $f_{ck} = 30$ MPa and $E_{cm} = 33$ GPa. The mass density and Poisson's ratio are 2500 kg/m³ and 0.2 for both concrete grades.

6.2.2.1 Bridge with Conventional Seismic Isolation

The Conventional Seismic Isolation (CSI) is applied to a slightly modified version of the existing bridge, which is shown in Fig. 6-1. The structure with CSI has the dimensions of the actual bridge, but the deck is resting on the piers and the abutments through LRBs, while same joint lengths are

considered in both horizontal directions that are equal to 150 mm. Additionally, the cross-section of the piers is converted to a square one as explained in §6.2.2.2. The adopted square cross-section of the piers has 1.5-m side in order to give a reasonable value for the normalised axial force at the piers under all the dead and imposed loads (CEN 2004a), thus resulting in $v_{Ed} = N_{Ed}/A_c \cdot f_{cd} = 0.28$. The longitudinal slope of the superstructure is also ignored to simplify the model.

The FE model of the bridge uses beam elements with linear interpolation of the curvature (B31 in ABAQUS CAE) for the deck that are located at the centroid of the box girder, while rigid elements are utilised to connect the deck with the LRBs at the supports, as shown in Fig. 6-1A. The 99-m long superstructure is discretised in 32 elements to capture with more accuracy the BM distribution and the variation in the deck cross-section along its length. The latter is shown in Fig. 6-1B, in which a transition zone of 4 m is introduced to connect the different cross-sections of the box girder (Fig. 6-1A). Simulation of each box girder shape is achieved through their mechanical properties that are integrated in the ‘Profile’ option offered in ABAQUS CAE.

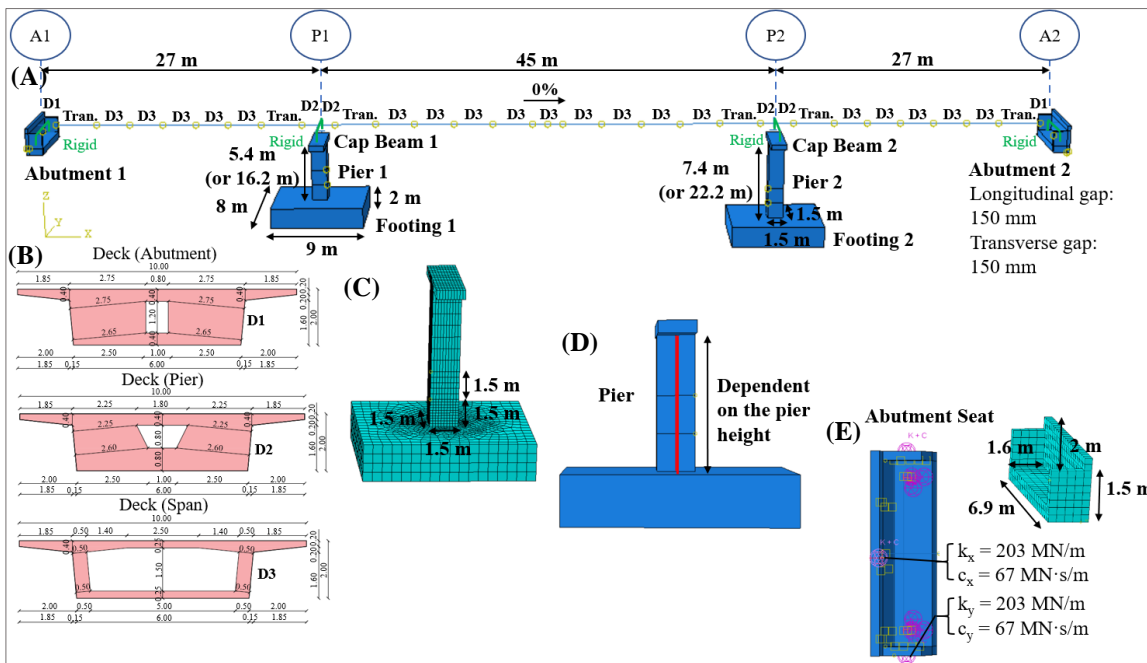


Fig. 6-1 Bridge with CSI that is supported on short and tall piers: (A) layout in the longitudinal direction, (B) different cross-sections of the superstructure, (C) generated mesh in the foundation-pier-cap beam, (D) beam element embedded in the piers, and (E) layout of the abutment-backfill system as well as mesh generation in the abutment seat.

The mesh of the system foundation-pier-cap beam is shown in Fig. 6-1C. The piers are monolithically connected to their footings that consist of linear brick first-order elements with reduced integration (C3D8R) of typical size 0.5 m; selection of this type of element is made with a view to reducing the computational cost without affecting the results in the model considered (Baker 2018). The piers are meshed with increasing size of the elements from bottom to top to match the corresponding mesh scheme of the rocking model (§6.2.2.2, §6.3.1), in an effort to compare in a better way the two FE models. Special care is put when meshing the transition between regions of different element sizes in the pier (Baker 2018); to this end, the element sizes

in regions should be smooth and not differ by more than a factor of two to four in their volume. In this regard, for a height of 1.5 m (i.e., the dimension of the square cross-section of the pier) cubic *C3D8R* elements of size 0.15 m are utilised, while a transition zone of 1.5 m height with equivalent elements of size 0.3 m is used to pass to the coarsest mesh for the rest of the pier utilising the same type of element with size 0.6 m. A cap beam with dimensions 1.5×5.2×1.2 m and concrete grade C30/37 is introduced on top of each pier to support the LRBs (Gkatzogias 2017), and it follows the coarsest mesh of the pier (i.e., *C3D8R* with size 0.6 m).

A *B31* beam element with length equal to the height of the corresponding pier and negligible mass and stiffness compared to the rest of the structural members to avoid affecting the response of the structure is integrated at the centroid of each pier as shown in Fig. 6-1D, in an effort to capture the BM distribution of the pier that is not directly available in brick elements. The beam element is meshed according to the surrounding solid (zones with elements of 0.15 m for height 1.5 m, 0.3 m for height 1.5 m and 0.6 m for the rest of the pier height). The beam element is embedded into the host element (the surrounding solid), and the translational DoFs of the former are constrained to those of the latter.

The abutment has the dimensions of the actual bridge but only the seat of the abutment is modelled in detail with *C3D8R* elements. The typical size of these elements is 0.3 m as shown in Fig. 6-1E. The contribution of the abutment-backfill system is modelled in a simplified way through a linear spring with $k = 203$ MN/m (Caltrans 2013) and a linear dashpot element with $c = 67$ MN·s/m (Mylonakis *et al.* 2006) in the longitudinal and the transverse directions (Zhang & Makris 2002). It is considered that the abutment is not expected to fail under the design ground motions considered in Chapter 6. The horizontal interaction between the deck and the abutments is activated when the 150-mm longitudinal and transverse gaps, respectively, at the two ends of the deck are closed. This contact is defined in the FE model by establishing contact interaction between the adjacent members at each time-step, considering that sliding is allowed in the tangential direction through a Coulomb friction $\mu_s = 0.9$ (Mohamad *et al.* 2015). In the normal direction, penetration of the adjacent members is not allowed in any case. The bottom surfaces of the abutments and the footings are restrained vertically (along-Z axis), and the ground motions are applied synchronously by imposing the corresponding accelerations to the entire footings of the piers in the longitudinal (X) and the transverse (Y) directions.

The bridges with CSI are redesigned according to the current EC8 provisions (CEN 2005a) separately for the cases of short (§6.2.2.1.1) and tall piers (§6.2.2.1.2) with seismic action Type 1 spectrum (high seismicity areas), site conditions B and importance factor $\gamma_I = 1$ (class II), as it was the case in the original bridge. However, the PGA is increased to 0.24 g due to the fact that the actual bridge was overdesigned for the original PGA (0.16 g), as explained in Gkatzogias (2017). The behaviour factors for the longitudinal and the transverse directions are taken as $q_{(X,Y)} = 1$, as the Code requires for seismically isolated systems. Furthermore, the additional dead loads, traffic and thermal actions are the same as in §6.2.1.

6.2.2.1.1 Bridge with Short Piers

The actual overpass bridge is supported on two short piers with heights $h_{P1} = 5.4$ m and $h_{P2} = 7.4$ m (Fig. 6-1A). The design procedure focuses on the LRB configuration and mechanical properties, while for the piers it is assumed that they are designed to remain elastic under the design ground motions. To this effect, the isolators are verified against (i) vertical load, (ii) shear strain due to horizontal and vertical displacement as well as rotation, (iii) stability (buckling) and (iv) restoring capability; this is done separately for the Lower Bound (LB) and the Upper Bound (UB) mechanical properties of the isolators (CEN 2005b). The design resulted in two identical circular LRBs located at each support (i.e., altogether eight LRBs in the bridge). These are spaced transversely at a distance of 5.2 m (centre to centre). The dimensions of the isolators are 750x410 mm with elastomer thickness $t_R = 170$ mm. The shear moduli of the elastomer and of the lead core are taken from the LRB manufacturer (Freyssinet) as $G_R = 0.8$ MPa and $G_L = f_{Ly} \cdot t_R / u_y = 256$ MPa, respectively; the latter applies to the initial stiffness of the lead with $f_{Ly} = F_{Ly} / A_L = 378$ kN/12272 mm² = 31 MPa being the yield stress of the lead core with diameter $D_L = 125$ mm, and $u_y = 20.5$ mm being the yield displacement of the isolator as given by the manufacturer.

The results from the modal analysis for the CSI bridge with short piers indicate that the first two vibration modes are translational and describe a rigid body motion of the deck in the transverse and in the longitudinal directions with natural periods equal to $T_1 = 1.81$ s and $T_2 = 1.8$ s, respectively. The mass participation factor is approximately 90% in both modes.

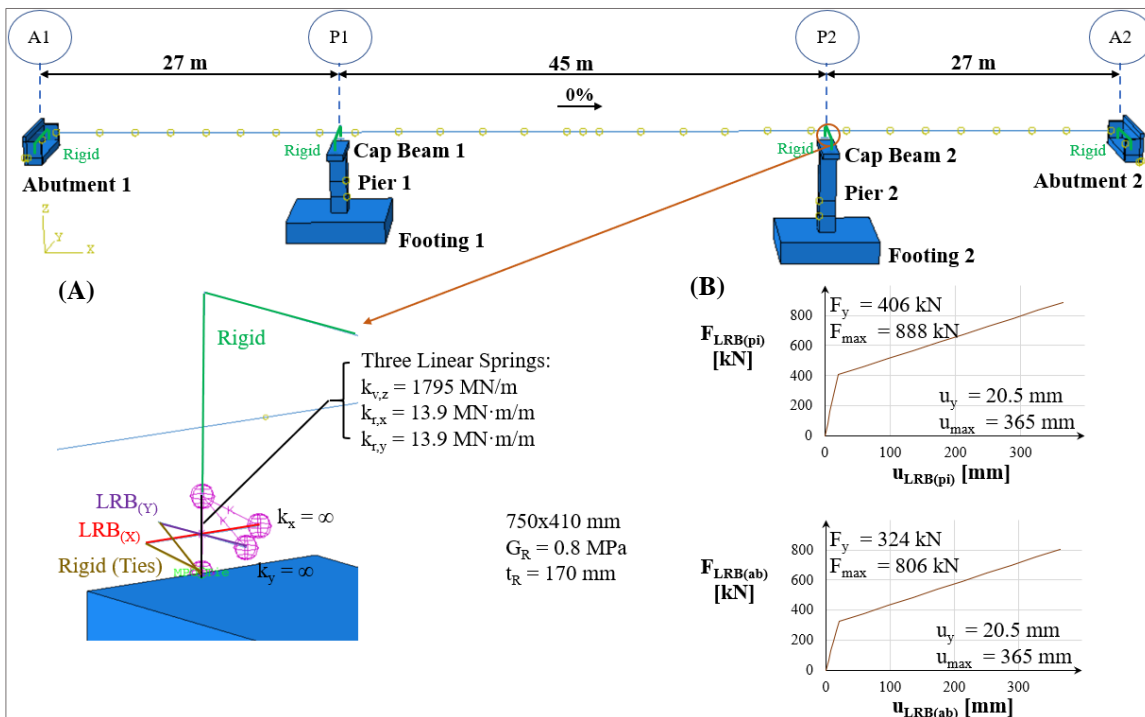


Fig. 6-2 Bridge with CSI that is supported on short piers: (A) modelling of the LRBs, and (B) bilinear force-displacement behaviour of the LRBs located at the piers and at the abutments.

The vertical response of each LRB is introduced in the FE model by means of one axial linear spring in the Z direction (this is shown in black colour in Fig. 6-2A). Additionally, and with the same visual representation, the rotational response of these devices is modelled with two rotational springs with respect to the longitudinal and the transverse axes. The horizontal (shear) response of the LRBs in the longitudinal and the transverse directions is described with two horizontal truss elements (T3D2) that are shown in red and in purple in Fig. 6-2A, respectively. Selection of truss elements (instead of e.g. linear springs) was made to incorporate the nonlinear material response of the LRB in the FE model. In this case the shear behaviour of the LRBs is assumed to be bilinear, and it allows to detect potential permanent displacements of the superstructure after the seismic action. It is noted that the torsional resistance of the isolators is considered negligible and, therefore, it is not included in the numerical model of the LRBs.

The three linear springs have a length of 0.41 m (the total height of the LRB) and connect the cap beam at the pier top with the rigid element representing the diaphragm of the deck, and they are introduced in the model with the axial (k_v) and rotational (k_r) stiffnesses that are given by the following expressions (Naeim & Kelly 1999)

$$k_{v,z} = \frac{E_c A_R''}{t_R} \quad \text{and} \quad k_{r,x/y} = 0.329 \frac{E_c I_R''}{t_R}, \quad (6-1)$$

where A_R'' and I_R'' are the effective area and the moment of inertia of the effective section, and E_c is the compression modulus. Eq. (6-1) shows that the expressions for k_r about the longitudinal (X) and transverse directions (Y) are the same, and this is due to the circular configuration of the LRB. The expressions for A_R'' and I_R'' are given as functions of the effective diameter (D_R'') after subtracting the area of the lead core (Constantinou *et al.* 2011)

$$D_R = 750 = D_R'' + 10, \quad (6-2)$$

$$A_R'' = \frac{\pi [D_R'' - D_L]^2}{4}, \quad (6-3)$$

$$I_R'' = \frac{\pi [D_R'' - D_L]^4}{64}. \quad (6-4)$$

The value of E_c is calculated according to the following suggestion made by Van Engelen & Kelly (2015) for circular pads

$$\frac{1}{E_c} = \frac{1}{6G_R S^2} + \frac{4}{3E_b}, \quad (6-5)$$

where $E_b = 2000$ MPa is the bulk modulus of the elastomer (CEN 2005b). The shape factor S represents the ratio of the loaded (bonded) area to the area of the elastomer that is free to bulge in a single elastomer layer of thickness $t_i = 17$ mm, and it is given by the following expression

$$S = \frac{D_R'^2 - D_L^2}{4D_R't_i}, \quad (6-6)$$

where $D_R' = 730$ mm is the bonded diameter of the isolator. Substitution of Eqs. (6-2) to (6-6) into Eq. (6-1) returns the stiffness values for the one axial and two rotational linear springs that are shown in Fig. 6-2A.

The two truss elements representing the bidirectional shear response of the LRB have a length 0.75 m (the diameter of the LRB). They are arranged longitudinally ($LRB_{(x)}$) and transversely ($LRB_{(y)}$) in order to simulate the shear behaviour of each isolator in each direction without coupling (see Fig. 6-2A). Connection of the cap beam with the truss elements is achieved through constraints that do not allow relative motion between them in order to transfer the pier movement to the LRBs; this is done through 'Ties' available in ABAQUS CAE. Accordingly, the truss elements transfer their movement to the superstructure through linear springs of infinite stiffness that work only in the corresponding direction (k_x and k_y , respectively, as shown in Fig. 6-2A). To account for the low confinement of the lead in the LRBs located at the abutments due to the lower axial loads applied from the deck at this location, the shear resistance $F_0 = F_{Ly}$ of the LRBs at the abutments was reduced by assuming a 25% decrease in the yield stress of the lead core f_{Ly} (Ryan *et al.* 2005, Constantinou *et al.* 2011). Therefore, two different force-displacement ($F-u$) curves are applied for the LRBs along the deck as shown in Fig. 6-2B. The curves are constructed according to the manufacturer guidelines and follow the EC8 provisions (CEN 2005b), considering for the LRBs at the piers post-elastic stiffness equal to $k_p = G_R \cdot A_R'' / t_R = 1.4$ MN/m, stiffness of the lead equal to $k_L = F_{Ly} / u_y = 18.5$ MN/m, thus resulting in an elastic stiffness equal to $k_e = k_p + k_L = 19.9$ MN/m, whereas the yield and ultimate displacements are $u_y = 20.5$ mm and $u_{max} = 365$ mm, respectively. The corresponding values for the LRBs at the abutments are $k_p = 1.4$ MN/m, $k_L = 14.5$ MN/m, $k_e = 15.9$ MN/m, $u_y = 20.5$ mm and $u_{max} = 365$ mm.

6.2.2.1.2 Bridge with Tall Piers

This configuration is a modification of the actual bridge by multiplying the original height of the piers by three, thus resulting in the following heights: $h_{P1} = 16.2$ m and $h_{P2} = 22.2$ m (see Fig. 6-1A). The design and modelling approaches for the isolators of the CSI bridge with tall piers are the same as those in the structure with short piers presented previously (§6.2.2.1.1), while the piers are again assumed to remain elastic. The design of the isolators in the structure with tall piers resulted in two circular LRBs with dimensions 600×332 mm and elastomer thickness $t_R = 144$ mm (Freyssinet) that are located at each support spaced at 5.2 m. The shear moduli of the elastomer and of the lead core are equal to $G_R = 0.8$ MPa and $G_L = 256$ MPa, respectively (§6.2.2.1.1).

The first two natural modes of the CSI bridge with tall piers are translational, as in the short pier configuration (i.e., pier height does not affect these modes that involve the deck ‘floating’ on the LRBs). The first one is a longitudinal rigid body motion of the deck with vibration period $T_1 = 2.32$ s, and the second one is a transverse motion with $T_2 = 2.28$ s. Similarly to the bridge with short piers (§6.2.2.1.1), 90% of the total mass of the system is activated (i.e., these modes dominate the seismic response of the structure).

The three linear springs representing the restraint offered by the LRB to the relative movements between the pier top and the deck have a length of 0.332 m. Their stiffnesses are calculated from the previous expressions Eqs. (6-1) to (6-6) considering $D_R = 600$ mm, $D_R' = 580$ mm, $t_R = 144$ mm, $D_L = 100$ mm, $E_b = 2000$ MPa and $t_i = 14$ mm for the isolators (Freyssinet). The resulting values are $k_{v,z} = 1289$ MN/m, $k_{r,x} = 6.4$ MN·m/m, $k_{r,y} = 6.4$ MN·m/m. The two truss (T3D2) elements of each LRB have a length of 0.6 m and show a different force-displacement behaviour at the locations of the piers and the abutments, as explained in §6.2.2.1.1; these are shown in Fig. 6-3A, B, respectively. The curves are drawn considering that the elastic stiffness for the LRBs at the piers is $k_e = 15$ MN/m and that the post-elastic stiffness is $k_p = 1.1$ MN/m, the yield and the ultimate displacements being $u_y = 17.3$ mm and $u_{max} = 310$ mm, respectively (§6.2.2.1.1). The corresponding values for the LRBs at the abutments are $k_e = 12$ MN/m, $k_p = 1.1$ MN/m, $u_y = 17.3$ mm and $u_{max} = 310$ mm (§6.2.2.1.1).

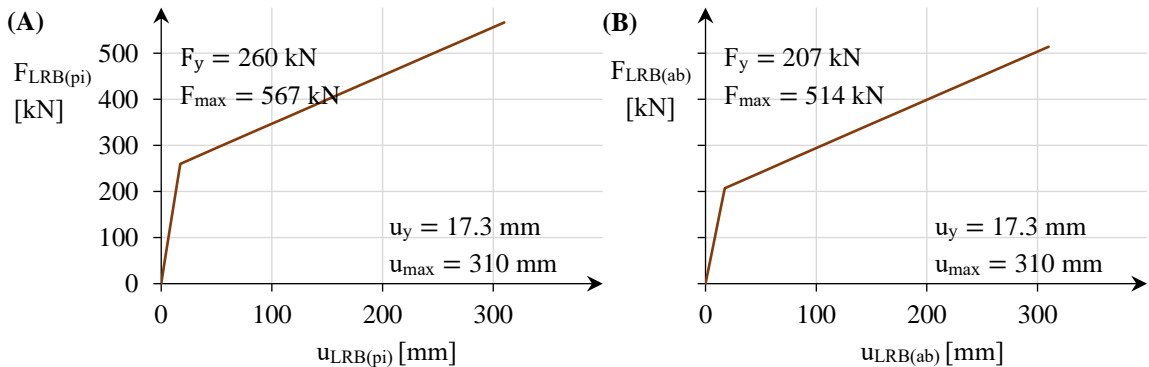


Fig. 6-3 Bilinear force-displacement behaviour of the LRBs located (A) at the piers and (B) at the abutments for the bridge with CSI that is supported on tall piers.

6.2.2.2 Bridge with Rocking Pier Isolation

The bridges with rocking pier isolation (referred in the following as RPI) have the same deck and pier dimensions as the ones with CSI (§6.2.2.1). Selection of square cross-section of the piers was made in order to avoid wobbling and rolling effects that rocking piers with circular cross-section can reveal (Vassiliou 2017), compared to square cross-section of the piers that can only twist with respect to their initial position. A high value of the superstructure mass effect for the bridge with short piers is found $\gamma = 29.3$ (§4.3.1), and this value reduces to $\gamma = 9.8$ for the tall pier configuration. The two RPI bridges differ only in the height of the piers and, therefore, the FE modelling approach is the same. It is noted that in both RPI configurations the abutment-backfill

is expected to fail before any of the piers overturn, as it can be easily determined according to the analytical approach presented in §4.3.3.

Some necessary modifications are introduced due to the differences between the two isolation techniques. Fig. 6-4A shows the bridge with rocking pier isolation where no additional devices are inserted between the substructure and the superstructure. To this effect, the cap beam is removed, and the deck is modelled with solid elements in order to define the interface surface between the soffit of the superstructure and the top surface of the rocking pier. All the different structural members of the rocking system are modelled with solid elements. However, and contrary to the *C3D8R* elements used for the CSI bridges, fully integrated *C3D8* elements are used for this model to improve the accuracy of the contact problem (Baker 2018). Additionally, the section arrangement in the deck varies slightly with respect to that in the CSI bridge by substituting the transition zone with the span section (see Fig. 6-1A), with a view to reducing the computational effort associated with the analysis of these structures without affecting the results. The dimensions of the shallow footings are also modified to 3×3×1.2 m for computational reasons, considering that decreased BMs occur at this member and smaller sections can be used compared to a conventionally isolated system (Agalianos *et al.* 2017).

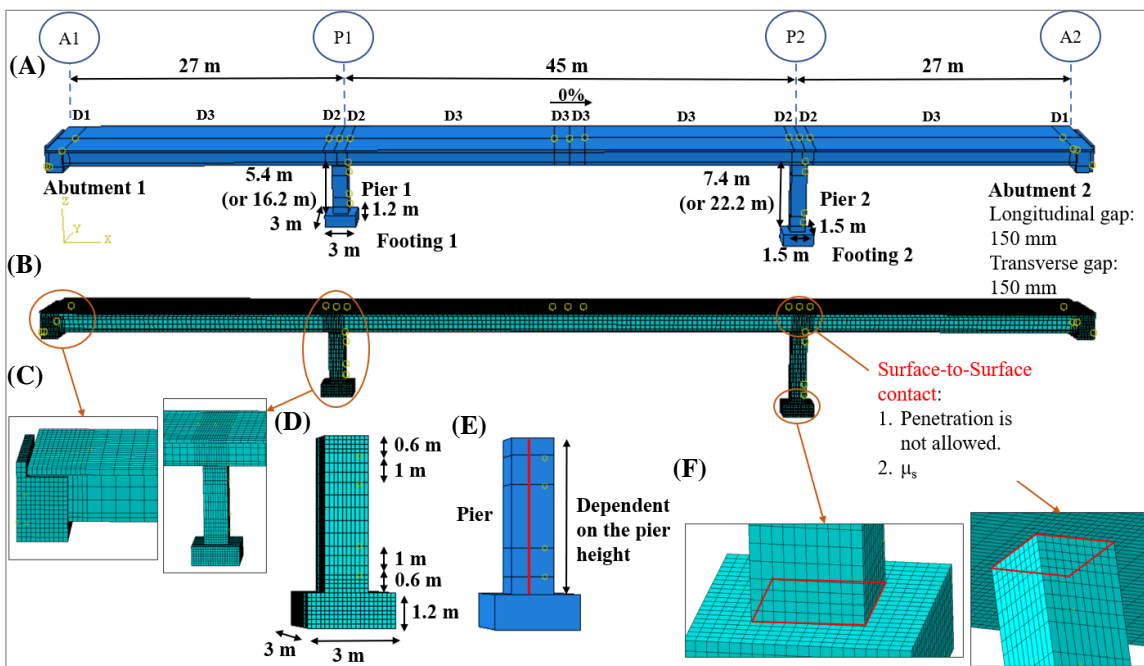


Fig. 6-4 Bridge with RPI that is supported on short and tall piers: (A) layout in the longitudinal direction, (B) mesh for the whole bridge, (C) generated mesh in the superstructure at the contact regions, (D) generated mesh in the foundation-rocking pier, (E) beam element embedded in the piers, and (F) contact interactions at the rocking interfaces.

Fig. 6-4B shows the generated mesh for the entire bridge with rocking pier isolation. Specifically, the deck is modelled with *C3D8* elements of size 0.45 m along its length, with the exception of the zones where it is in contact with the abutments and the piers, in which a smaller element size of 0.15 m is selected to capture the contact phenomena with sufficient accuracy, as shown in Fig. 6-4C. The abutments are also modelled with *C3D8* elements of size 0.15 m to match

the corresponding discretisation of the deck by activating a node-to-node matching. The mesh for the system foundation-rocking pier is presented in Fig. 6-4D, with the pier footings being meshed with *C3D8* elements of size 0.15 m, and the pier presenting a gradation in the mesh size that is finer towards the two rocking interfaces (Baker 2018). Specifically, *C3D8* elements of size x that is determined after the sensitivity analysis in §6.3.1 are utilised for a height of 0.6 m at both rocking interfaces to model with more accuracy the impact problem; in the adjacent segment with 1-m height larger *C3D8* elements with size $2 \cdot x$ are selected to connect gradually with the coarsest mesh of size $3 \cdot x$ in the central part of the pier height.

The same modelling procedure as in the CSI structures (§6.2.2.1) is used to capture the BMs in the rocking piers using embedded *B31* beam elements without mass and stiffness as shown in Fig. 6-4E. However, the size of the beam elements at the piers are different than in the CSI bridges because of the different surrounding mesh in the solid piers; for this reason, the beam elements have a length of x for the first 0.6 m from the rocking interface, $2 \cdot x$ for the following 1-m segment, and $3 \cdot x$ for the rest of pier, where x is determined from the sensitivity analysis in §6.3.1. Additionally, the contribution of the abutment-backfill system that is equivalent to a linear spring and a dashpot element, and the interaction with the superstructure are modelled according to §6.2.2.1. It is noted that the abutment-backfill failure mode is not expected to be activated for the RPI system under the design earthquake conditions adopted herein (§3.3.5, §4.3.5); this can be also justified by the large values of the abutment-backfill contribution (q), which are approximated to $0.757 \cdot 10^{-3}$ m/kN and $0.778 \cdot 10^{-3}$ m/kN (see §4.2.3 and Table 4-1) for the short and tall rocking configurations, respectively. The boundary conditions are identical to those presented for the CSI system.

Fig. 6-4F highlights the contact interactions among the piers and the adjacent members (foundations and superstructure) to capture rocking and slide motions of the piers. Specifically, a surficial contact that is adjusted at each time-step is defined at both rocking interfaces (i.e., Ou *et al.* 2007, ElGawady & Dawood 2012). The contact relationship between the adjacent interfaces has no tensile resistance and in compression it is represented with a relationship that avoids penetration of the pier nodes (slave surface) in the corresponding surface defined by the nodes of the footings or the superstructure (master surfaces). The ‘*Augmented Lagrange*’ constraint enforcement method is selected to facilitate the solution of the rocking problem (Thomaidis *et al.* 2018). In the tangential direction, the sliding effect is simulated through a static CoF μ_s ; this value is determined from the parametric analyses in §6.3.2. It is noted that a modal analysis in the bridges with RPI is meaningless considering the negative stiffness of the systems.

6.2.3 Representation of Seismic Action

The seismic action is introduced in the form of recorded ground motions that exceed the EC8 target spectrum for $\text{PGA} = 0.24$ g and soil conditions of type B. The selection of natural records was made from the PEER NGA-West 2 database (Ancheta *et al.* 2013) using the following preliminary search criteria;

- Moment magnitude (M_w) ranging from 6.5 to 7.
- Closest distance from the recording site to the ruptured area (R_{rup}) between 20 km and 40 km.
- Average shear wave velocity in the top 30 m of soil ($V_{s,30}$) corresponding to site conditions B according to the EC8 site classification (CEN 2004b) (ranging from 360 to 800 m/s).
- The maximum number of ground motions from a single event is limited to three.
- The scale factor should be between 0.25 and 4.

Table 6-1 presents the main characteristics of eleven recorded ground motions that satisfy the aforementioned criteria, along with the scale factors that are determined according to the basic scaling approach (Haselton *et al.* 2017) where each ground motion is scaled such that the average from all ground motions should not fall below 90% of the target spectrum for any period within the range of interest ($0.2T \sim 2T$ where T is the fundamental translational period of the structure, resulting in $0.3 \sim 3.6$ s for the short bridge and $0.4 \sim 4.7$ s for the tall one).

Table 6-1 Information for the Ri ground motions selected for the dynamic analyses, including the Record Sequence Number (RSN) (PEER NGA-West 2 database, Ancheta *et al.* 2013), the scale factors selected, the earthquake event, the moment magnitude (M_w), the mechanism of the seismic event, the closest distance from the recording site to the ruptured area (R_{rup}), and the average shear wave velocity to a depth of 30 m ($V_{s,30}$).

Record	RSN	Scale Factor	Earthquake	M_w [-]	Mechanism	R_{rup} [km]	$V_{s,30}$ [m/s]
R1	57	3.03	San Fernando 1971	6.6	Reverse	22.6	450
R2	88	3.57	San Fernando 1971	6.6	Reverse	24.9	389
R3	190	3.93	Imperial Valley-06 1979	6.5	Strike Slip	24.6	362
R4	288	3.10	Irpinia 1980	6.9	Normal	22.6	561
R5	739	2.85	Loma Prieta 1989	6.9	Reverse Oblique	20.3	489
R6	974	3.48	Northridge-01 1994	6.7	Reverse	22.2	371
R7	990	2.97	Northridge-01 1994	6.7	Reverse	36.6	365
R8	4214	3.36	Niigata 2004	6.6	Reverse	32.4	375
R9	5267	2.85	Chuetsu-oki 2007	6.8	Reverse	29.8	419
R10	5776	3.05	Iwate 2008	6.9	Reverse	25.2	478
R11	6971	2.53	Darfield 2010	7.0	Strike Slip	29.9	390

Fig. 6-5 shows the time-histories of the individual scaled ground motions, and their acceleration response spectra, as well as their GM compared to the EC8 target spectrum; it is noted that the ground motions used included no long-period pulses. It can be seen that, due to the lack of criterion to specify the spectral shape matching, the GM of the scaled ground motions overestimates

considerably the design spectrum in the plateau zone. However, it is observed that for the first two modes that dominate the response of the CSI structures (i.e., for short piers $T_1 = 1.81$ s and $T_2 = 1.8$ s, and for tall piers $T_1 = 2.32$ s and $T_2 = 2.28$ s) the response accelerations of the scaled ground motions are similar to those of the design spectrum.

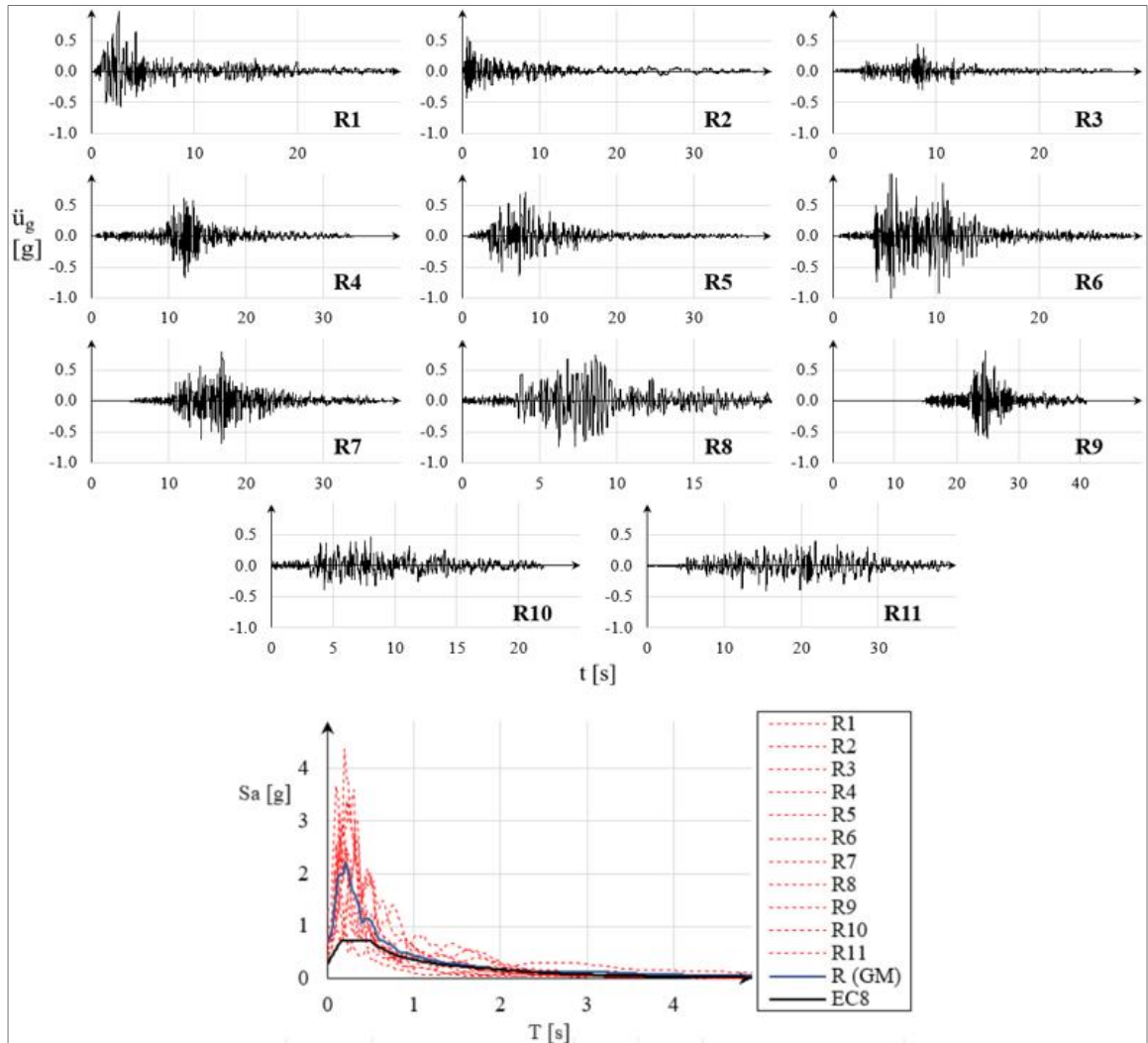


Fig. 6-5 Time-history of the individual scaled records R_i , and matching of their response acceleration spectra to the EC8 target spectrum with $PGA = 0.24$ g and site conditions B.

6.2.4 Analysis Process

The implicit Hilber-Hughes-Taylor (HHT) algorithm is selected to integrate the system of dynamic equilibrium equations. The numerical damping introduced by the HHT algorithm is controlled through the parameter α_{HHT} that is set equal to -0.333 in this work to provide the maximum numerical dissipation to the high-order frequency noise in the response (Hilber *et al.* 1977, Thomaidis *et al.* 2018). According to usual practice, an equivalent viscous damping of 5% was assumed for all the concrete sections through their material properties. An automatic incrementation is selected for the analysis that adapts the time-step to the requirements of the

problem nonlinearities (i.e., LRBs bilinear behaviour and rocking movement) arising during the ground motion, while the maximum and minimum time-steps of the analyses are set equal to 10^{-1} s and 10^{-6} s, respectively.

6.3 Analysis Parameters for the Bridges with Rocking Pier Isolation

6.3.1 Mesh Scheme for the Rocking Piers

The proposed mesh for the rocking piers of the RPI bridges (§6.2.2.2) results from the mesh-sensitivity analysis presented in this section, aiming at reducing the duration of the seismic analysis without affecting the accuracy of the results. The mesh-sensitivity analysis is expressed in terms of piers (see §6.2.2.2 and Fig. 6-4D); this procedure is implemented in the RPI bridge with short piers (§6.2.2.2) by applying the scaled ground motions along the two horizontal directions, separately (§6.2.3). Specifically, three different mesh schemes are considered for the rocking piers, namely (i) a fine mesh with x being equal to 0.1 m or 6% of the Contact Surface (CS), (ii) a medium-size mesh with $x = 0.15$ m (i.e., 10% of the CS) and (iii) a coarse mesh with $x = 0.3$ m (i.e., 20% of the CS). It is noted that the generated mesh for the members that are in contact with the rocking piers (i.e., footings and superstructure) are adjusted according to the smallest element of the rocking pier interfaces (see §6.2.2.2 and Fig. 6-4C). For the examined RPI bridges, a conservative value for the static CoF at the rocking interfaces is selected that is equal to $\mu_s = 0.45$ (§6.3.2).

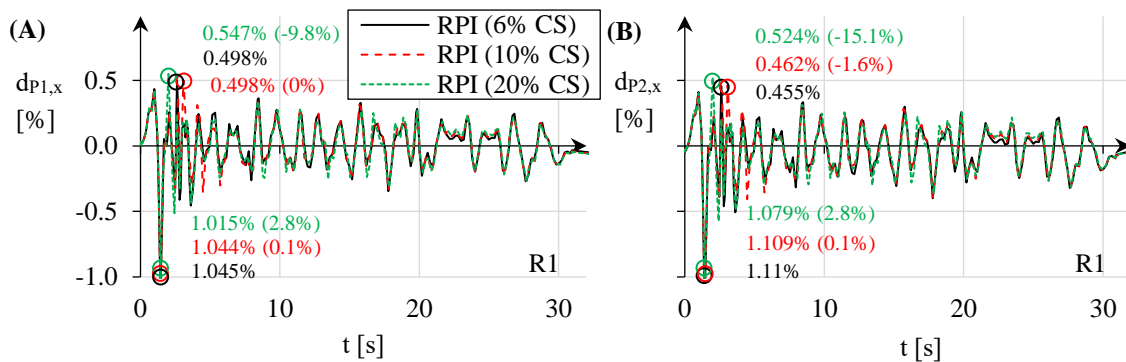


Fig. 6-6 Histories of the total longitudinal drifts of (A) pier P1 ($d_{P1,x}$) and (B) pier P2 ($d_{P2,x}$) for the RPI bridge with short piers. Results obtained when subject to the scaled R1, considering three alternatives for the mesh scheme of the rocking piers.

Fig. 6-6A, B present the histories of the longitudinal pier P1 drifts ($d_{P1,x}$) and pier P2 drifts ($d_{P2,x}$), respectively, when subjected to the scaled historic motion R1 applied in the longitudinal direction; it is noted that the results presented are equivalent in terms of the mesh sensitivity to those for the transverse direction and for the rest of the ground motions. The values in brackets for cases (ii-red) and (iii-green) denote the corresponding percent difference in peak pier drifts with the finest mesh scheme examined in this study (i.e., mesh i-black). It is observed that the RPI bridges with fine and intermediate-size meshes yield very similar response-histories throughout the whole rocking motion, with a maximum difference in peak values of 1.5%. However, compared to

the results obtained with the finest mesh, the model with the largest elements (*iii*) overestimates the peak drift up to 10% in the short pier P1 and up to 15% in the tall one P2. Considering the large computational time required with the finest mesh, the one with intermediate-size elements (*ii*) is selected for the seismic analysis of both RPI bridges with short and tall piers.

6.3.2 Coefficient of Friction at the Rocking Interfaces

A crucial issue for the free-standing rocking piers studied herein is their adequacy to provide sufficient recentring capacity after a strong seismic event. This can be undermined by the potential sliding at the rocking interfaces given that no specific measures were provided to prevent this type of displacements (e.g., additional devices as in §2.4.1.1, and/or grooves as adopted in §3.2, §4.2 and §5.2). The effect of CoF at the rocking interfaces (μ_s) on the recentring capability of the rocking piers is examined by exploring two alternatives, namely (*i*) a nominal value of the static CoF on concrete-to-concrete surfaces equal to $\mu_s = 0.9$ (Mohamad *et al.* 2015), and (*ii*) a conservative value of the static CoF that is obtained by applying a safety factor of two to the nominal value, thus resulting in $\mu_s = 0.45$ (Ou *et al.* 2007, ElGawady & Dawood 2012, Sideris 2015, Li *et al.* 2017). The effect of this parameter is examined in the RPI bridge with short piers (§6.2.2.2, §6.3.1) subject to the scaled ground motions (§6.2.3); it is noted that this type of analysis is conducted by exciting the structures simultaneously along the longitudinal and transverse directions in order to derive the total horizontal displacement of the piers, considering that the corresponding analyses by exciting the structures independently in the two horizontal directions after combining these values with the Square Root of the Sum of Squares (SRSS) slightly underestimates the horizontal displacements of the piers.

The recentring capability of the rocking piers is illustrated in Fig. 6-7 with the history of displacement at the four pivoting joints of the bottom interface (Fig. 6-7A) of each pier. Fig. 6-7B, C present the histories of the total horizontal displacements of these joints for pier P1 ($u_{P1,xy}$) when subjected to the scaled ground motions R5 and R11, respectively, for both values of μ_s . In general, the smaller the value of μ_s , the larger are the permanent displacements of the short pier at the end of the ground motion, as expected. Specifically, for the record R5 the conservative value of μ_s makes pier P1 shift from its initial position approximately 10 mm and twist about 0.2° counter-clockwise after the earthquake stops, whereas the nominal value of μ_s limits the permanent displacements to 3 mm and the twisting to 0.1° counter-clockwise. Similarly, considering the record R11, the lower value of μ_s leads to permanent displacements of 14 mm without twisting compared to the larger value of μ_s that leads to only 5 mm with negligible twisting (0.1° counter-clockwise).

Similarly, Fig. 6-7D, E present the histories of the total horizontal displacements of the four pivoting joints at the bottom interface of pier P2 ($u_{P2,xy}$) when subjected to motions R3 and R6, respectively. The value of μ_s does not affect the recentring capability of the tall pier when subjected to ground motion R3, showing the same permanent displacement at the end of the earthquake of around 6 mm in both cases. On the other hand, conservatism in the value of μ_s leads to larger

permanent displacements in the pier P2 for the R6 ground motion, increasing it from 2.5 mm when $\mu_s = 0.9$ to approximately 3.5 mm with $\mu_s = 0.45$.

Therefore, it is verified that the smaller the value of μ_s the larger the permanent displacements of the rocking piers due to sliding at the rocking interface, especially for the short/squat pier. In the following, this study adopts the conservative value for the static CoF at all the rocking interfaces ($\mu_s = 0.45$).

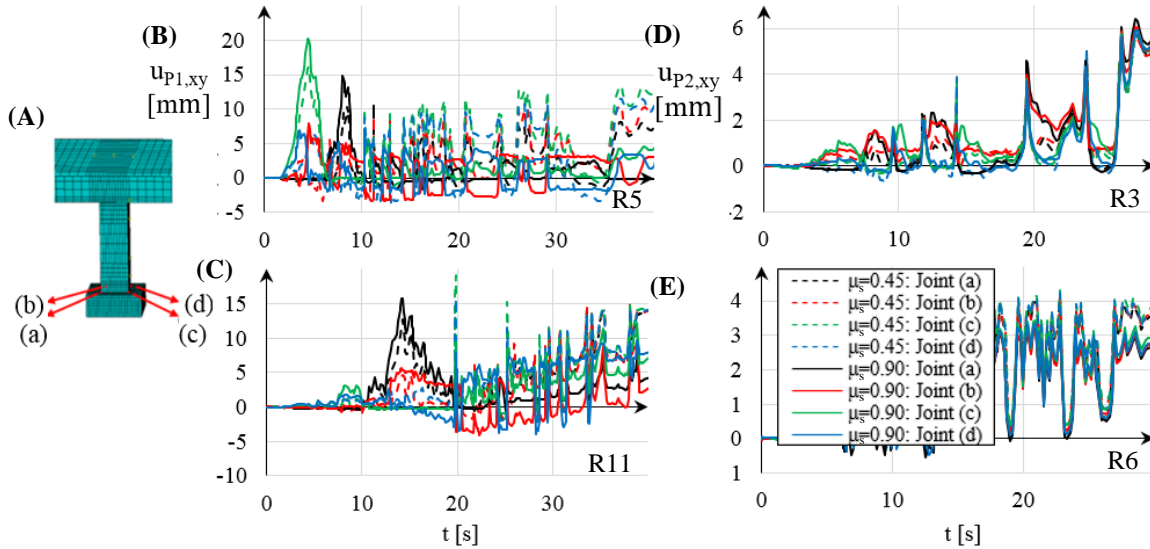


Fig. 6-7 (A) Layout of the corner joints at the bottom surface of the rocking piers, and histories of the total horizontal displacements of pier P1 ($u_{P1,xy}$) subject to the scaled (B) R5 and (C) R11, and of pier P2 ($u_{P2,xy}$) subject to (D) R3 and (E) R6 for the RPI bridge with short piers. Results obtained considering two alternatives for the static CoF value to describe sliding at the rocking interfaces.

6.4 Seismic Response of Bridges with Conventional Seismic and Rocking Pier Isolation

The comparison of the seismic responses of the bridges designed to the CSI and RPI concepts focuses on detecting the differences in terms of the stability of the structure (i.e., considering response parameters such as displacements, drifts and BMs), rather than focusing on the safety of each alternative design against the corresponding failure mode that has been examined in several studies in the past (i.a., Agalianos *et al.* 2017). In this respect, the CSI bridges of either pier configuration survive the design spectrum-compatible ground motions without exceeding the displacement capacity of the LRB. It is noted that the piers of the CSI bridges are assumed to be designed for elastic behaviour under the design seismic action (§6.2.2). Additionally, the RPI bridges resist the design ground motions without reaching the prevailing failure mode of the abutment-backfill system (§6.2.2.2). This is due to the fact that the displacement on the abutments does not exceed the yield displacement of this member (§6.2.1) that is approximately 16 mm according to Caltrans (2013); this is also the case in the CSI bridges. In this regard, the simplified modelling procedure that was adopted for the abutment-backfill system (i.e., linear spring and

dashpot elements as explained in §6.2.2.1 and §6.2.2.2) is valid, considering that this member remains in the elastic range for all the examined cases.

6.4.1 Bridge with Short Piers

This section includes the comparison between the CSI and RPI alternatives for the bridge configuration with short piers (i.e., the original height of the piers in the bridge overpass as explained in §6.2.2.1.1 and §6.2.2.2). The majority of the responses presented in the following result from the application of the scaled ground motions (§6.2.3) separately in the two horizontal directions (i.e., the analysis is conducted applying the same earthquake only in X direction and then in Y direction, but not applying both at the same time).

6.4.1.1 Superstructure Displacements

Fig. 6-8A summarises the peak deck relative displacements along the X-axis ($u_{deck,x}$) when the short CSI and RPI bridges are excited in this direction; it is noted that the results of this bar graph refer to the superstructure segment (P1-P2) because the deck moves longitudinally as a rigid body and the same peak longitudinal displacements were found at any point of the superstructure in both isolation techniques. Fig. 6-8B presents the corresponding displacements along the Y-axis ($u_{deck,y}$) when the structures are subjected to the ground motions transversely. Unlike the longitudinal response in Fig. 6-8A, the transverse displacements in Fig. 6-8B refer to the largest ones in the entire deck for both isolation alternatives.

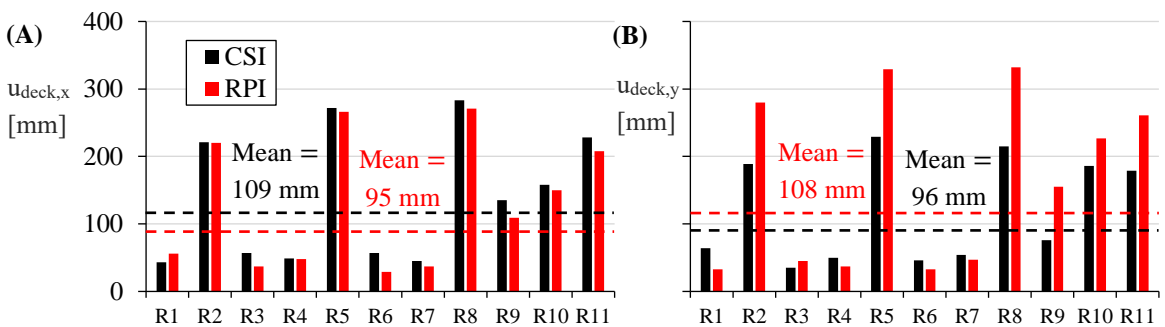


Fig. 6-8 Peak superstructure relative displacements of segment (P1-P2) in the (A) longitudinal ($u_{deck,x}$) and (B) transverse directions ($u_{deck,y}$) for the CSI and RPI bridges with short piers. Results obtained when subject to the scaled Ri.

Fig. 6-8A, B include with dashed lines the mean values of the peak deck displacements for both isolation techniques. This is done due to the significant record-to-record variability that was found in both directions and in both isolation techniques, and it is approximated to a Coefficient of Variation (CoV) value of 64% for the CSI alternative and 74% for the RPI one in both directions. The high CoV values are attributed to the large scatter in the spectra of the scaled records that have been selected without consideration of the spectral shape (see Fig. 6-5). The CSI bridge with short piers shows the largest mean peak superstructure displacement for all the examined cases presented in Fig. 6-8, which occurs longitudinally: $u_{deck,x} = 109$ mm. On the other hand, the RPI approach

shows larger mean peak superstructure displacement transversely than the bridge with CSI, and this value is equal to $u_{deck,y} = 108$ mm. Comparison between the horizontal deck displacements for the same isolation alternative shows that in seven out of the eleven examined cases the CSI bridge presents relatively larger longitudinal deck displacements ($u_{deck,x}$) than those in the transverse direction ($u_{deck,y}$), with an average increase of 37%. Nevertheless, the opposite is observed for the RPI bridge, which shows larger $u_{deck,y}$ values compared to $u_{deck,x}$ in nine cases, with a corresponding average increment of 28%.

Fig. 6-8A shows that the short CSI and RPI bridges present comparable peak values of $u_{deck,x}$ for all the examined cases, with maxima of 283 and 271 mm, respectively. In fact, the CSI alternative leads to slightly larger values of $u_{deck,x}$ than the RPI one in ten out of the eleven examined cases, with an average increase of 22%. However, this is not the case for the transverse displacements shown in Fig. 6-8B, where in most cases (seven out of eleven) the short RPI system presents larger transverse deck displacements than the corresponding bridge with CSI, and in some cases the differences are significant (i.e., the increase in the transverse displacement demand of the rocking bridge is up to 104% with respect to the bridge with conventional isolation). The largest $u_{deck,y}$ value is found for the RPI bridge and is equal to 332 mm, whereas the maximum value for the CSI deck is limited to 229 mm. Therefore, in the bridge with short piers the rocking pier isolation can reduce slightly the longitudinal response of the superstructure in comparison with the conventional isolation of the deck, but the RPI increases the deck displacements in the transverse direction, and in some cases considerably. Overall, both isolation designs in bridges with short piers result in very large displacements of the superstructure in both horizontal directions.

Fig. 6-9A, B summarise the peak permanent displacements for the deck segment (P1-P2) longitudinally ($u_{deck,x-(per.)}$) and transversely ($u_{deck,y-(per.)}$), respectively, for the CSI and RPI bridges with short piers; furthermore, two typical force-displacement ($F-u$) hysteresis rules of one LRB at the top of pier P1 are also included. In general, the short CSI structure develops larger permanent displacements of the superstructure than those observed in the RPI bridge in all the examined cases, and this is due to the low code-defined yield displacement of the LRBs (20.5 mm in both directions as shown in Fig. 6-2B and in the first response cycle in Fig. 6-9A, B). Specifically, the superstructure in the CSI system has a maximum permanent displacement of 105 mm longitudinally and transversely. On the other hand, the RPI deck recentres completely in most cases, with maximum permanent displacements of only $u_{deck,x-(per.)} = 17$ mm and $u_{deck,y-(per.)} = 12$ mm; this permanent movement of the deck in the RPI bridge is due to the horizontal slip at the rocking interfaces, which is insignificant even for the low CoF value that was determined in §6.3.2. As an example, consider the difference in terms of the recentring capability of the superstructure for the R8 record, for which the short CSI bridge has permanent longitudinal and transverse displacements that are 1325% and 4915% larger than those in the RPI structure, respectively. Therefore, using the rocking approach in the short bridge enhances the recentring capability of the superstructure compared to the conventional seismic isolation design through LRBs for all the examined cases, by showing negligible permanent deck displacements even for this case where no additional recentring devices were utilised (see §2.4.1.1).

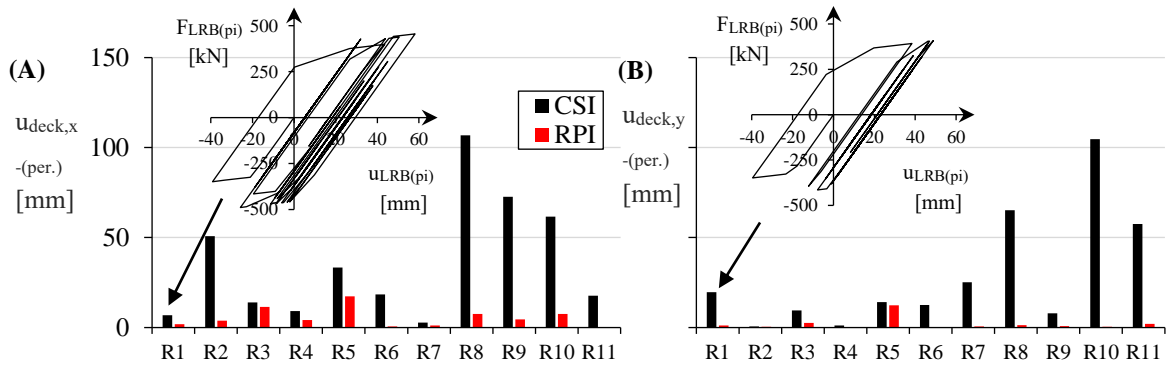


Fig. 6-9 Peak permanent superstructure displacements of segment (P1-P2) in the (A) longitudinal ($u_{deck,x-(per.)}$) and (B) transverse directions ($u_{deck,y-(per.)}$) for the CSI and RPI bridges with short piers. Results obtained when subject to the scaled R_i .

6.4.1.2 Superstructure Bending Moments

Fig. 6-10A, B, C present the maximum BMs in the longitudinal direction that are developed at the two end spans ($M_{deck,y-(A1-P1)}$, $M_{deck,y-(P2-A2)}$) as well as at the central span of the superstructure ($M_{deck,y-(P1-P2)}$), respectively. The figure compares the results obtained for the short CSI and RPI bridges for all the ground motions when applied in the longitudinal direction. The contribution of the gravity loads at the different spans to the flexural response of the deck is also included (dotted line), as well as the BM that initiates yielding in the deck considering the reinforcement of the actual overpass (dashed line) (Gkatzogias & Kappos 2016). As expected, the CSI alternative leads to a relatively small variability in the demand of flexure at the different deck spans, showing a CoV value of around 4% for both end spans and around 0.4% for the central span. However, this is not the case for the short RPI bridge, where the different excitations lead to significantly different deck uplifts at the pier locations (P1 and P2) that result in CoV values of 43%, 21% and 9% along the spans (A1-P1), (P2-A2) and (P1-P2), respectively.

Comparison between the peak BMs at the end spans for the short CSI and RPI bridges in Fig. 6-10A, B shows that the seismic demand for deck BMs, obtained after subtracting the static BM from the total value, is considerably amplified for the RPI case. Specifically, the RPI solution increases the seismic BMs for both end spans in every case examined compared to the CSI structure, and the average increases are equal to 160% and 80% for the end spans (A1-P1) and (P2-A2), respectively. The considerable amplification in the flexure of the RPI deck is attributed to the negligible uplift of the deck at the abutments (a maximum of 8 mm is found for all the examined cases) and the considerable vertical movement at the locations of the piers (at least three times larger than that at the abutment seats), as shown in Fig. 6-11. This is echoed in Agalianos *et al.* (2017), who observed similar increases in the BM demand at both end spans when comparing rocking pier isolation with the conventional one. However, a higher increase in the BM value occurs in this work for the end span that connects the abutment with the shortest pier ($M_{deck,y-(A1-P1)}$) compared to that in the opposite end span ($M_{deck,y-(P2-A2)}$). This is due to the fact that squatter piers like P1 ($\alpha_{P1} = 0.28$ rad) are forced to develop more uplift during the rocking motion than slenderer piers like P2 ($\alpha_{P2} = 0.21$ rad). Therefore, it can be concluded here that rocking pier isolation shows a detrimental effect on the flexural response of both end spans by increasing their BM demand

compared to the conventional isolation technique, and this becomes more significant at the end span that is next to the shortest pier. Nevertheless, both end spans of the RPI bridge with short piers show a considerable reserve capacity against yielding of the deck because the yield moment of the superstructure (governed by ‘non-seismic’ loads) is approximately 30 MN·m (Gkatzogias & Kappos 2016).

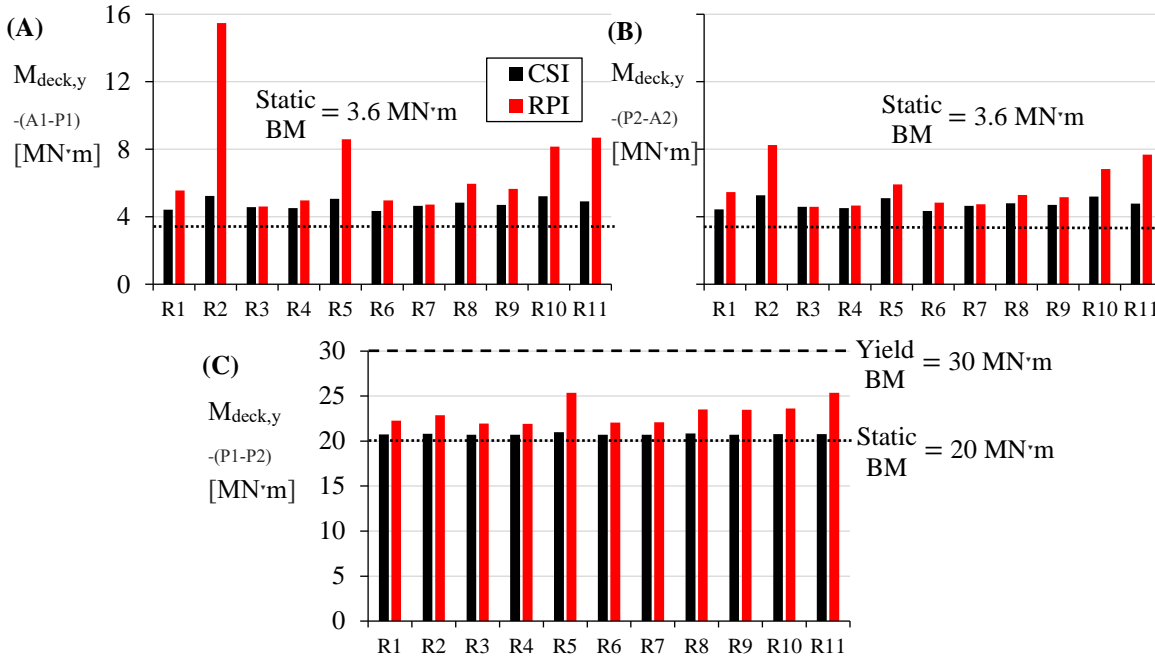


Fig. 6-10 Peak total BMs in the longitudinal direction at (A) the side span (A1-P1) ($M_{deck,y-(A1-P1)}$) and (B) the side span (P2-A2) ($M_{deck,y-(P2-A2)}$) as well as (C) the intermediate span (P1-P2) ($M_{deck,y-(P1-P2)}$) for the CSI and RPI bridges with short piers. Results obtained when subject to the scaled Ri.

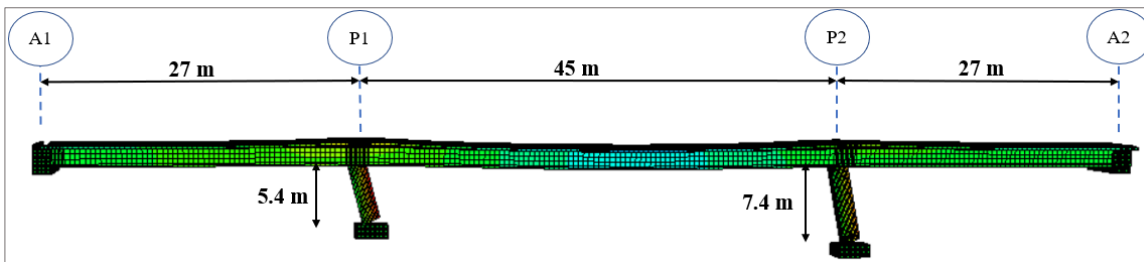


Fig. 6-11 FE model of the RPI bridge with short piers during rocking motion in the longitudinal direction, and differential uplifts of the superstructure at the different supports.

Fig. 6-10C shows an interesting result at the central span (P1-P2), not found in the literature; the RPI bridge with short piers increases the seismic flexural demand in the central span of the deck for all ground motions compared to the CSI structure. The average increase in the seismically induced BMs at the central span is 300%, showing that this increase is significantly high. This is attributed to the different uplift of the two rocking piers that subsequently force the superstructure to experience differential vertical movements as observed in Fig. 6-11. The result is that flexural demand in the intermediate span of the short RPI bridge is closer to its yield moment than in the

CSI bridge; e.g., when subjected to ground motions R5 and R11 the RPI deck reaches 85% of its flexural capacity, whilst this value is kept around 70% in the CSI bridge in all the examined cases. Therefore, special attention to the deck reinforcement is required when the rocking pier isolation is implemented in short irregular structures, while the flexural response of the different spans is not favoured compared to the same span arrangement in a conventionally isolated system, especially for the intermediate span.

6.4.1.3 Pier Drifts

Fig. 6-12A, B present the peak and mean (dashed line) total drifts of the short pier P1 in the longitudinal ($d_{P1,x}$) and transverse directions ($d_{P1,y}$), respectively, for the two isolation approaches subject to the scaled ground motions. In general, the rocking pier P1 shows higher variations in drift demands with mean and CoV values in both directions of around 1.8% and 74%, respectively, compared to the conventional member that limits the corresponding values to around 0.13% and 35%, respectively. In this regard, the rocking pier P1 increases the drift demands compared to the member with CSI on average 1310% longitudinally and 1815% transversely. Accordingly, Fig. 6-12C, D present the corresponding drifts of pier P2 ($d_{P2,x}$ and $d_{P2,y}$). With respect to the short pier P1 presented before, the tall rocking pier P2 shows smaller mean drift value that is approximated to around 1.3%, while the behaviour of conventional pier P2 is expected by increasing its drift demand to 0.2% (due to flexure that is directly related to its height); the CoV values are of the same magnitude with those presented before for pier P1 for both isolation alternatives. Comparison between the two solutions for pier P2 shows that the average increments of the total drift in the rocking member compared to that in the CSI bridge is 530% longitudinally and 865% transversely. Therefore, piers that are isolated through RPI increase considerably their drifts with respect to the corresponding conventional members, however this increase is less in the taller/slenderer piers.

Previous experimental and numerical works have also observed much larger drifts for rocking piers compared to conventional ones (i.e., Roh & Reinhorn 2008, ElGawady & Sha'Ian 2011, Agalianos *et al.* 2017). However, and despite the large drifts in the rocking piers, they do not reach the theoretical overturning threshold (i.e., the resultant of the piers does not fall outside their footprint). This overturning threshold is approximately $d_{P1(x,y)} = 13\%$ and $d_{P2(x,y)} = 10\%$, which corresponds to a horizontal displacement of 0.75 m for both piers. Therefore, both rocking piers reach a mean value of only 13% of their overturning capacity that indicates a substantial margin of safety against collapse of the vertical members, notwithstanding that the abutment failure mode is activated prior to overturning (see §6.2.2.2).

Fig. 6-12 gives an interesting outcome for the short RPI system. Specifically, the short rocking pier P1 always has larger peak drifts than the tall rocking pier P2, in both directions. The ratio of the peak drifts in pier P1 over those in pier P2 for each ground motion in each direction has very constant values that range between 1.3 and 1.4. This is basically the ratio between the height of the tall pier ($h_{P2} = 7.4$ m) to that of the short pier ($h_{P1} = 5.4$ m), which is 1.37. This is because both rocking piers have similar peak horizontal displacements for all the examined cases, despite their different drifts. This result is not only observed for the peak displacements, but also during the

whole response-history of the rocking piers. Therefore, this bridge configuration verifies the assumption that simplified the analytical formulation of free-standing asymmetric bridges in §4.2, in which both free-standing rocking piers were considered to have the same longitudinal displacement despite their different height.

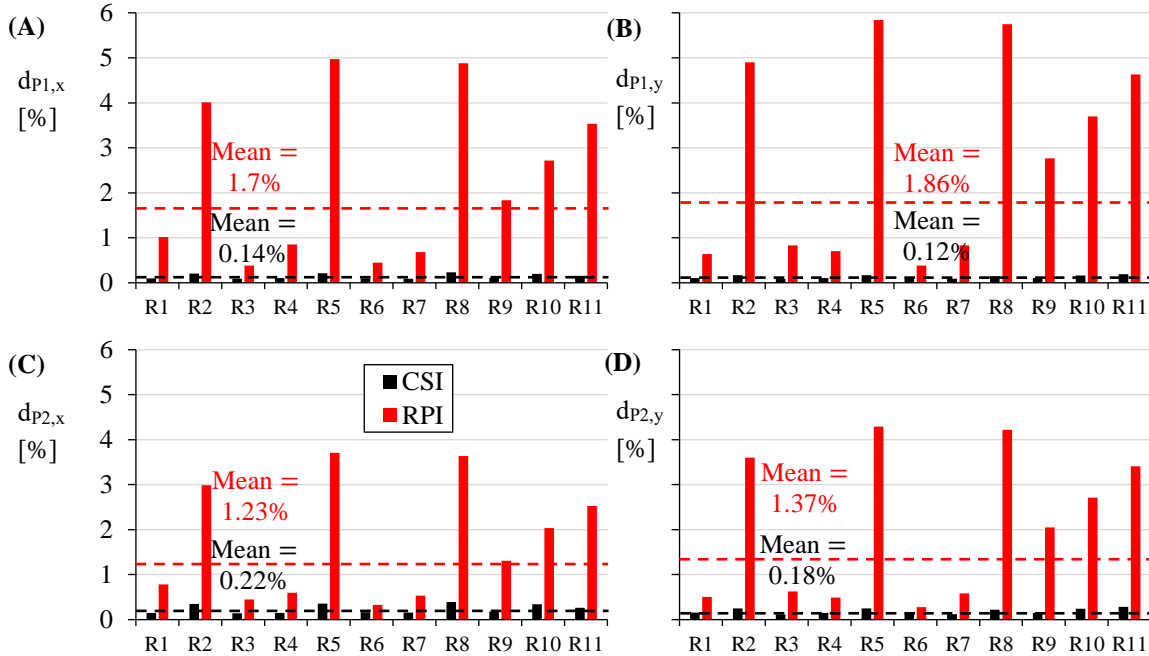


Fig. 6-12 Peak total drifts of pier P1 in the (A) longitudinal ($d_{P1,x}$) and (B) transverse directions ($d_{P1,y}$) and of pier P2 in the (C) longitudinal ($d_{P2,x}$) and (D) transverse directions ($d_{P2,y}$) for the CSI and RPI bridges with short piers. Results obtained when subject to the scaled R_i .

In order to explore the potential seismic demand for flexural deformation in the rocking piers of the short RPI bridge, the peak drift response presented in Fig. 6-12 is analysed into its rigid body and flexural components. To this end, Fig. 6-13A, B present the peak and mean (dashed line) drift components of rocking pier P1 longitudinally ($d_{P1,x}$) and transversely ($d_{P1,y}$), respectively, whereas Fig. 6-13C, D present the corresponding drifts of rocking pier P2 ($d_{P2,x}$ and $d_{P2,y}$). It is observed that the peak values for the rigid body drift component of both rocking piers are similar to the total drifts of the members presented in Fig. 6-12. This is particularly apparent for the mean values shown in each bar graph, where the rigid body component in the rocking piers accommodates around 90% of the total movement of the members, thus confirming the study of Agalianos *et al.* (2017) that the rigid body response dominates the rocking motion of free-standing piers. Nevertheless, there is some bending demand in the two rocking piers in both directions that, although it is significantly smaller than the contribution of the rigid body motion, it is not zero in any of the examined cases. Specifically, the flexural drift component in the short rocking pier P1 shows a mean value of 0.15% in both directions, while the corresponding value for the tall rocking pier P2 is reduced to 0.1%. Thus, flexural response is found in both rocking piers, and this becomes more important for the short/squat member. It is interesting to note that these mean values for the flexural drift component of pier P1 in the RPI bridge are slightly larger than those presented in Fig.

6-12A, B for the total drift of the corresponding conventional pier of the CSI bridge, while the opposite occurs for the rocking pier P2 and the conventional member of the CSI alternative as can be seen in Fig. 6-12C, D. In this regard, Fig. 6-13 suggests that there is notable bending in the rocking piers, identical to that of the conventional members, and, therefore, the flexural behaviour of the piers in the two isolation alternatives needs to be addressed in more detail.

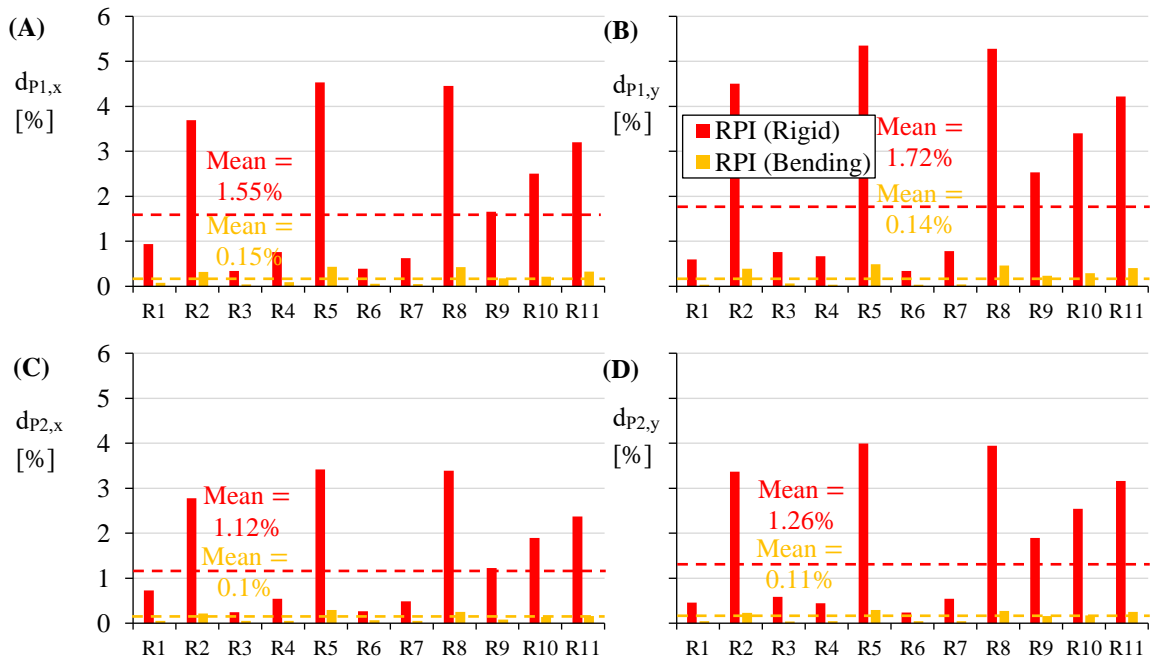


Fig. 6-13 Peak drift components separated into rigid body and bending drifts of pier P1 in the (A) longitudinal ($d_{P1,x}$) and (B) transverse directions ($d_{P1,y}$) and of pier P2 in the (A) longitudinal ($d_{P2,x}$) and (B) transverse directions ($d_{P2,y}$) for the RPI bridge with short piers. Results obtained when subject to the scaled Ri.

6.4.1.4 Pier Bending Moments

The focus here is on the flexural response of the short pier P1 for the two isolation alternatives. Fig. 6-14A presents the position of three different sections of pier P1 that are considered to examine the bending behaviour locally, namely section (1) at the bottom of the pier, section (2) at mid-height, and section (3) at the top. The peak BMs in the longitudinal direction along with the corresponding mean values in dashed lines are presented for the three different sections of pier P1 ($MP_{1,y-(1)}$, $MP_{1,y-(2)}$, $MP_{1,y-(3)}$) in Fig. 6-14B, C, D, respectively, for both the CSI and RPI alternatives when subjected to the ground motions longitudinally; it should be noted that these peak BM values for the rocking piers occur just before the member uplifts and enters rocking motion, as is the case in previous studies (i.a., Acikgoz & DeJong 2018). Moreover, equivalent trends to those presented below occur for the BMs in the transverse direction for pier P1. Comparing the BMs developed at the different sections for the same isolation alternative shows that pier P1 in the CSI bridge has the largest BMs at section (1) of the member, and these BMs progressively decrease for sections (2) and (3), with corresponding mean values of around 9.4 MN·m, 6.1 MN·m and 0.6 MN·m, respectively. However, this is not exactly the case for the rocking pier P1 of the short RPI bridge; although the rocking member shows the largest BMs at section (1) with mean value of 9.2 MN·m,

larger BMs are found at the top section (3) of the pier than at the middle section (2) in seven of the eleven ground motions, showing mean values for sections (3) and (2) of around 2.4 MN·m and 1.9 MN·m, respectively.

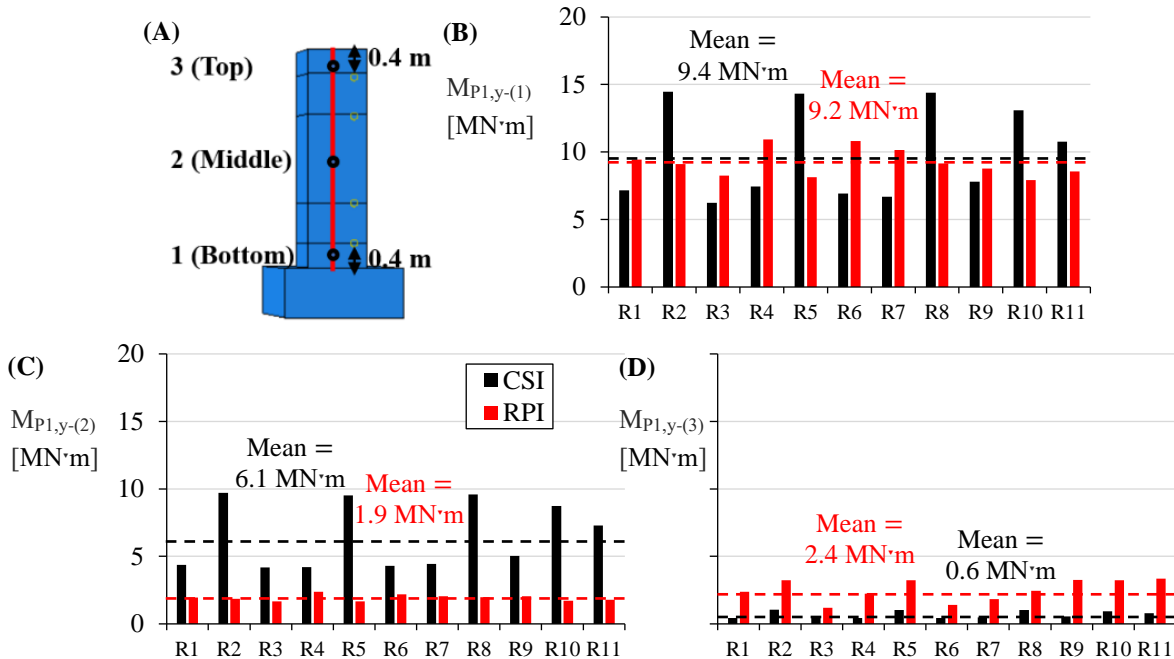


Fig. 6-14 (A) Position of the examined pier sections in the beam elements, as well as peak BMs in the longitudinal direction of pier P1 at (B) section 1 ($M_{P1,y-(1)}$), (C) section 2 ($M_{P1,y-(2)}$) and (D) section 3 ($M_{P1,y-(3)}$) for the CSI and RPI bridges with short piers. Results obtained when subject to the scaled Ri.

In an effort to elaborate more on the BM distribution of the piers, Fig. 6-15A, B show typical BM diagrams of pier P1 in the CSI and RPI bridges, respectively, that are constructed based on the mean BM values discussed before. It can be seen that the conventional member presents a predictable cantilever behaviour (i.e., almost zero BM at the partially free end, and high BM value at the bottom fixed section), but the rocking member reveals regions close to the rocking interfaces where bending is high, while this flexural response fades towards the midpoint of the section; this was also observed in Roh & Reinhorn 2009. This indicates that rocking motion at the mid-height of the pier is mainly accommodated by rigid body motion. However, and although same support conditions are adopted at the bottom and top rocking interfaces (i.e., the pier is simply resting on both surfaces), the flexural response at the bottom section (1) of the rocking pier is around four times larger than that at the top one (3). Therefore, a higher degree of fixity is achieved at the bottom section of the squat rocking pier compared to the top one (Roh & Reinhorn 2009). This can be attributed to the decreased effect of the weight at the top section of the rocking element compared to the bottom one, thus allowing rocking and sliding effects to occur more easily in this region and, therefore, relieve the top section from significant bending.

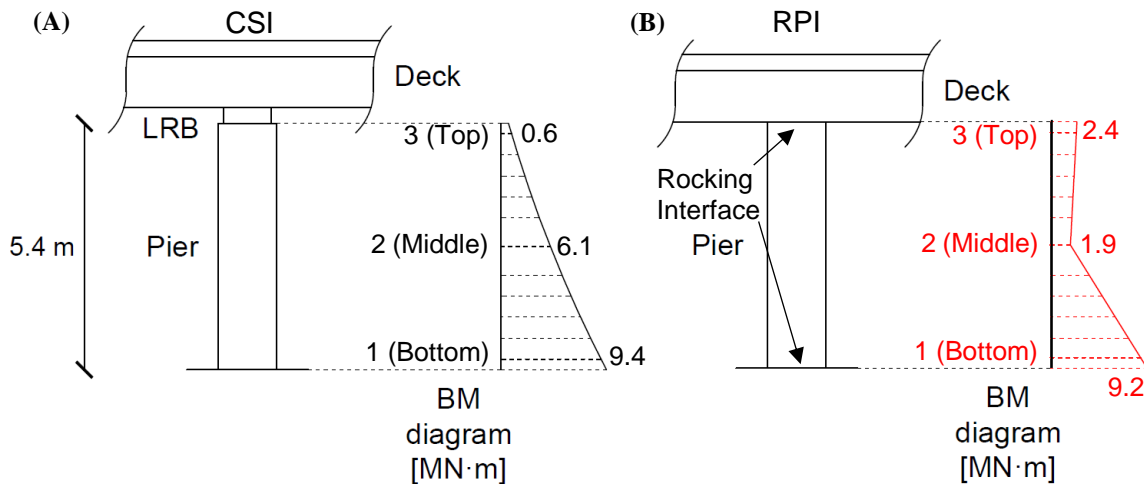


Fig. 6-15 Typical BM diagram of pier P1 in the (A) CSI and (B) RPI bridges with short piers, accounting for the mean BM values when subject to the scaled Ri.

Fig. 6-14 also allows to compare the flexural behaviour of pier P1 in the two different isolation techniques. Interestingly, Fig. 6-14B shows that the pier P1 in the RPI bridge has $M_{P1,y-(1)}$ values that are locally higher than those of the corresponding pier in the CSI alternative in six out of the eleven examined cases with an average increase of 38%, thus indicating that the level of fixity at the bottom section of the rocking pier exceeds that of the corresponding conventional pier. Therefore, reinforcement design should be considered for the rocking member in that respect. On the other hand, Fig. 6-14C shows that bending dominates at section (2) of the CSI pier compared to the rocking pier, and this is expected considering that the rocking member accommodates its movement in this section by rigid body motion; to this end, the conventional pier P1 increases the BM demand in section (2) compared to the corresponding rocking member in all the examined cases with an average increase of 245%. The opposite is observed at the top section (3); Fig. 6-14D indicates that the cantilever pier P1 of the CSI bridge shows negligible flexural response at section (3), and the RPI alternative increases the flexural demand on this pier on average 290%. Overall, and although free-standing rocking piers are expected to accommodate their movement through rigid body rotations under horizontal loads, bending should not be underestimated in short/squat elements that are found to have demand of BMs close to the rocking interfaces that can be larger than that in piers with the same geometry located in bridges with conventional isolation and, consequently, a reinforcement design procedure may need to be followed for them.

The same comparison is conducted for the tall pier P2 of the CSI and RPI bridges in Fig. 6-16A, B, C, which include the demand of BMs in the longitudinal direction in terms of peak and mean responses for the three different sections ($M_{P2,y-(1)}$, $M_{P2,y-(2)}$, $M_{P2,y-(3)}$); it is noted that the peak BMs for the rocking piers occur just before the member initiates rocking motion, while equivalent trends to those discussed below occur for the BMs in the transverse direction. Fig. 6-17A, B present typical BM diagrams of pier P2 for both isolation alternatives based on the mean BM values of all the ground motions. In general, pier P2 shows similar BM distribution to that in the short pier P1, for both isolation alternatives (see Fig. 6-15A, B). Specifically, the conventional pier P2 decreases the BM values from bottom and top and, accordingly, the rocking pier shows

larger BMs at regions close to the rocking interfaces compared to the midpoint of the pier. However, and although the tall conventional pier shown in Fig. 6-17A shows predictable behaviour by increasing the BMs with respect to the short one for sections (1) and (2) (section (3) remains practically unaffected) showing mean values of around 11.7 MN·m and 7.3 MN·m, respectively (see Fig. 6-15A), the tall rocking pier develops BMs that are always smaller for all the examined sections compared to the short rocking pier (see Fig. 6-15B). To this end, Fig. 6-17B shows that the tall rocking pier P2 reduces the mean $M_{P2,y-(1)}$, $M_{P2,y-(2)}$, $M_{P2,y-(3)}$ values to 5.3 MN·m, 0.4 MN·m and 0.6 MN·m, respectively. In this regard, slenderer rocking piers also suffer from bending, however they lead to decreased flexural demands compared to squatter configurations, and this is expected considering that the slender rocking piers are easier to enter rocking motion (i.e., uplift as explained by Eq. (3-8)) compared to the squat configurations that delay this initiation and develop increased flexural stresses. Last but not least, the effect of the weight seems to be the parameter that determines the level of fixity at the rocking interfaces of the piers, and the resulting difference in the BMs that are developed at the two rocking interfaces (bottom and top). Specifically, Fig. 6-17B shows that the slender rocking pier P2 reduces the mean BM at the top section (3) compared to the bottom section (1) around nine times, which opposes the results found for the short rocking pier P1 (i.e., the top section shows four times smaller BM than the bottom section as shown in Fig. 6-15B). Therefore, slender rocking piers are expected to show higher differences in the flexural response at bottom and top sections of the element compared to squatter configurations, and this is directly related to the increased weight that is applied at the bottom section of tall/heavy piers, thus achieving a higher degree of fixity.

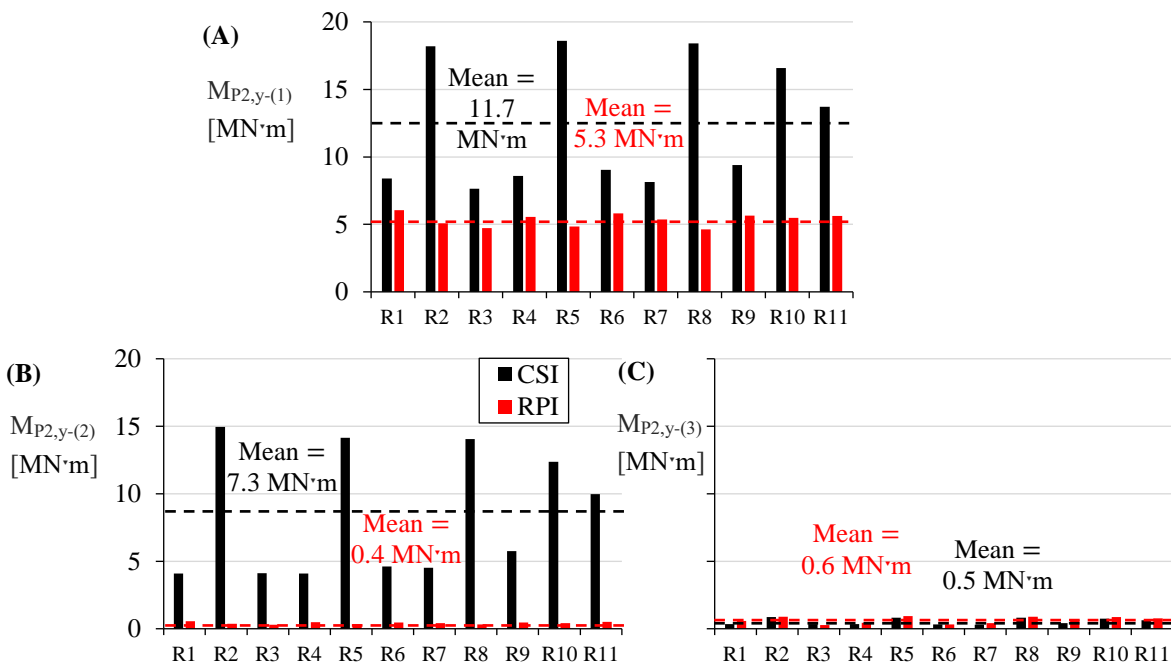


Fig. 6-16 Peak BMs in the longitudinal direction of pier P2 at (A) section 1 ($M_{P2,y-(1)}$), (B) section 2 ($M_{P2,y-(2)}$) and (C) section 3 ($M_{P2,y-(3)}$) for the CSI and RPI bridges with short piers. Results obtained when subject to the scaled Ri.

Comparison between the two isolation alternatives for pier P2 shows that the conventional pier has a BM demand at section (1) that is always higher than that of the rocking member with an average increase of 120% as shown in Fig. 6-16A. Accordingly, Fig. 6-16C shows that the differences in the $M_{P2,y-(3)}$ values are reduced with respect to the short pier (see Fig. 6-14D), and the BMs in the rocking pier are so small that become comparable to those observed in the conventional one. In this regard, the BMs at section (3) increase for the rocking pier P2 compared to that of the CSI system in nine out of the eleven examined cases, with an average increase of only 18%; however, these BM values are considered negligible in a design context. On the other hand, and similarly to the comparison that was conducted for the short pier P1 (see Fig. 6-14C), the conventional pier P2 shows higher BMs at the intermediate section (2) for all the examined cases compared to the corresponding rocking pier, as shown in Fig. 6-16B. Therefore, flexural response is more important in conventional than in rocking piers when taller/slenderer configurations are examined that opposes the result found for the short/squat member.

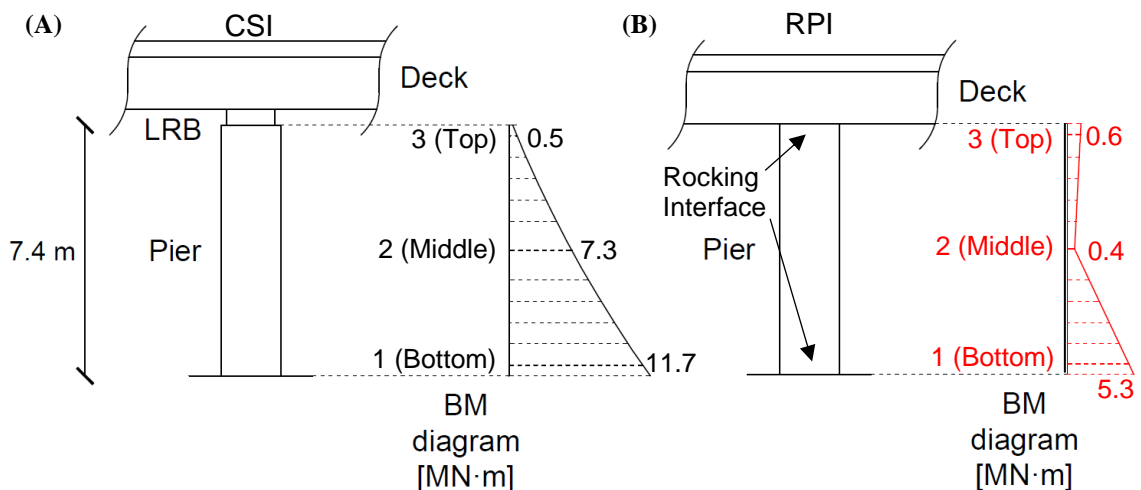


Fig. 6-17 Typical BM diagram of pier P2 in the (A) CSI and (B) RPI bridges with short piers, accounting for the mean BM values when subject to the scaled Ri.

6.4.1.5 Pier Recentring Capacity

The recentring capability of the free-standing rocking piers of the short RPI bridge is assessed by studying the histories of the total horizontal displacements at the four corner joints of the pier at the bottom rocking interface, shown in Fig. 6-18A; it is noted that this type of analysis is conducted by exciting the structures simultaneously along the longitudinal and transverse directions with the ground motions presented in §6.2.3.

Fig. 6-18B, C show the histories of the total horizontal displacements of these joints for pier P1 ($u_{P1,xy}$) when subjected to the scaled ground motions R1 and R2, while Fig. 6-18D, E show the corresponding displacement history for pier P2 ($u_{P2,xy}$) subject to the scaled ground motions R5 and R7, respectively. The results show that the four bottom joints of the short rocking pier P1 when subjected to the R1 record have identical response-histories throughout the whole rocking motion, resulting in a permanent movement of approximately 8 mm (without torsional rotation around the vertical axis of the pier), while the different response-histories for the four bottom P1 joints subject

to the R2 motion lead to a permanent displacement of around 10 mm with a simultaneous torsional rotation of 0.4° clockwise. However, lower permanent displacements occur for the tall pier P2. Specifically, for the first case (R5), pier P2 shows a permanent displacement of only 1 mm, while for the second case (R7) the rocking pier is displaced approximately 8 mm. Therefore, the tall/slender pier performs better with regard to recentring of the bridge than the short/squat pier. This is due to the fact that squat piers are more prone to sliding than slender ones (Pompei *et al.* 1998). Overall, and although sliding is allowed by considering a low value for the CoF at the rocking interfaces ($\mu_s = 0.45$), both rocking piers have negligible permanent displacements at the end of the earthquake, which indicates that the free-standing bridge with rocking pier isolation has sufficient recentring capacity in its vertical members, and this is mainly offered by the heavy superstructure. Additionally, these results show that the assumption of no sliding that was made in §3.2 in order to formulate analytically the longitudinal rocking motion of bridges is validated for the examined bridge configuration with short piers, while the sliding effects throughout rocking motion are marginal.

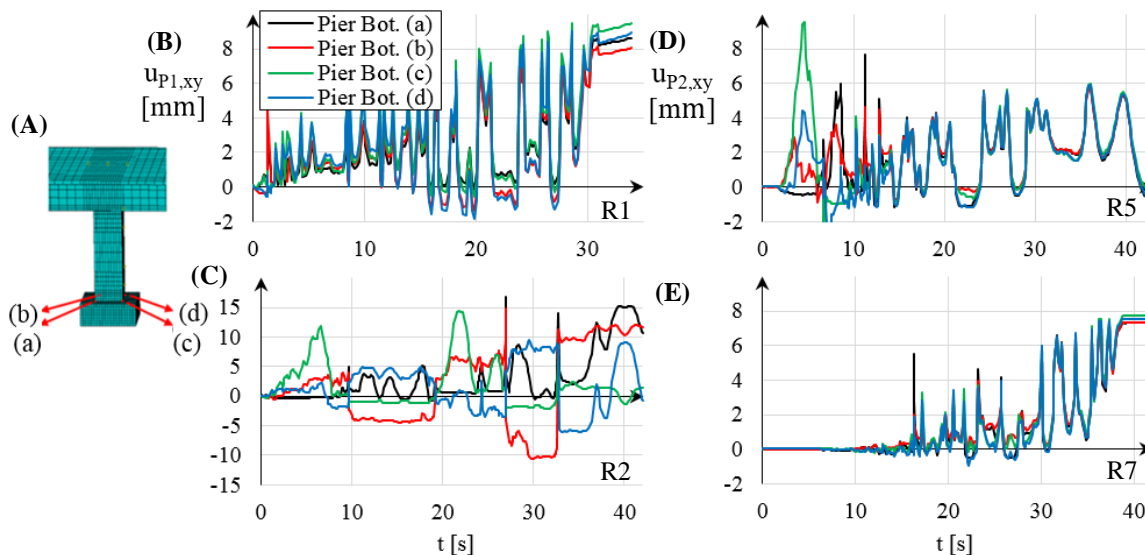


Fig. 6-18 (A) Layout of the corner joints at the bottom surface of the rocking piers, and histories of the total horizontal displacements of pier P1 ($u_{P1,xy}$) subject to the scaled (B) R1 and (C) R2 and of pier P2 ($u_{P2,xy}$) subject to (D) R5 and (E) R7 for the RPI bridge with short piers.

6.4.2 Bridge with Tall Piers

This section extends the comparison between the CSI and RPI isolation alternatives in a bridge configuration with tall piers (§6.2.2.1.2 and §6.2.2.2), with a view to identifying potential differences in the relative performance of each isolation technique, compared to that found for the short configuration in §6.4.1.

6.4.2.1 Superstructure Displacements

Fig. 6-19A, B summarise the peak displacements of the superstructure supported on tall piers in the longitudinal ($u_{deck,x}$) and the transverse directions ($u_{deck,y}$), respectively, along with the mean values for each case; the results refer to the deck segment (P1-P2) for the reasons explained in §6.4.1.1. Both graphs show that the record-to-record variability is still high with CoV values that are of the same order of magnitude as those in the short-pier bridges (§6.4.1.1); these values are 56% and 63% for the CSI and RPI alternatives, respectively. However, the tall CSI and RPI bridges develop larger relative displacements of the superstructure in both horizontal directions compared to the corresponding cases of the short bridge (see Fig. 6-8A, B), which are on average 23% higher for the tall CSI bridge and 57% for the tall RPI structure. Another difference from the short-pier bridges (§6.4.1.1) is that, contrary to the CSI deck that shows lower stiffness longitudinally than transversely regardless of the piers height, the tall RPI bridge develops larger deck displacements in the longitudinal direction in seven out of the eleven examined cases (4.5% increase in the mean value), which was not the case in the corresponding RPI bridge with short piers. In this regard, a general trend regarding the behaviour of the superstructure in the rocking approach in the two horizontal directions cannot be clearly observed.

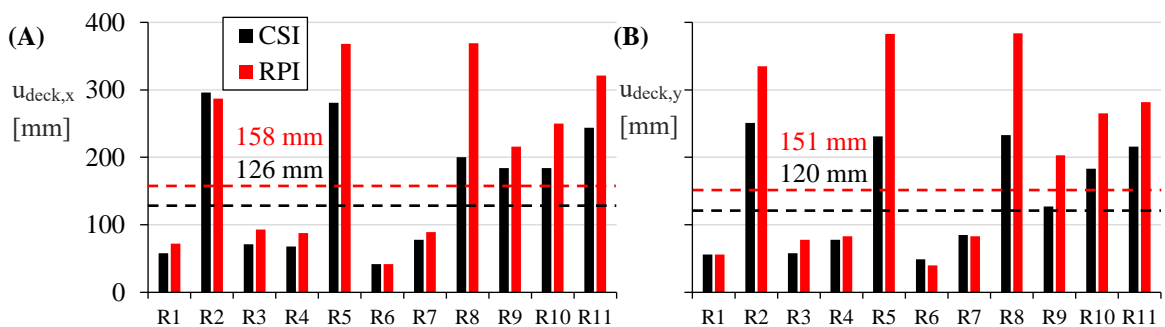


Fig. 6-19 Peak superstructure relative displacements of segment (P1-P2) in the (A) longitudinal ($u_{deck,x}$) and (B) transverse directions ($u_{deck,y}$) for the CSI and RPI bridges with tall piers. Results obtained when subject to the scaled R_i .

In general, Fig. 6-19A, B show that the tall RPI bridge develops larger deck displacements in both horizontal directions than the corresponding CSI bridge. Specifically, the RPI alternative has larger $u_{deck,x}$ and $u_{deck,y}$ demands than the CSI bridge in nine out of the eleven examined, with an average increase of 35% in both directions. The tall RPI bridge develops mean deck displacements in the two horizontal directions equal to $u_{deck,x} = 158$ mm and $u_{deck,y} = 151$ mm, while for the tall CSI bridge these values reduce to $u_{deck,x} = 126$ mm and $u_{deck,y} = 120$ mm. In this regard, the tall RPI bridge shows the largest deck displacements in either direction, in contrast to what was found for the short configuration where the RPI alternative outperformed the longitudinal behaviour of the CSI (§6.4.1.1). Overall, the rocking approach in bridges should be considered as an isolation technique associated with deck displacements slightly larger than in a system that uses CSI; however, this outcome cannot be countified easily considering that it refers to a specific case study.

Fig. 6-20A, B summarise the peak permanent displacements of the central deck span (P1-P2) in the longitudinal ($u_{deck,x-(per.)}$) and the transverse ($u_{deck,y-(per.)}$) directions, respectively, along with

two typical curves related to the hysteretic behaviour of the LRBs as determined from the FE analyses. The tall CSI bridge shows slightly lower permanent deck displacements in both horizontal directions compared to the corresponding short system (see Fig. 6-9A, B), with an average decrease for the tall configuration of 7% longitudinally and 39% transversely. However, it is notable that the permanent displacements of the superstructure in the rocking bridge with tall piers are much larger than in the structure with short rocking piers (see Fig. 6-9A, B); this increase for the tall RPI bridge is on average 210% in the horizontal direction and 480% in the transverse one. The increase in permanent displacements in the tall bridge with rocking pier isolation is attributed to its very large deck displacements in both horizontal directions (see Fig. 6-19). In this regard, there are cases shown in Fig. 6-20 for the tall bridge where the deck moves more in the RPI alternative than the CSI one, and in some cases considerably as shown for the R5 record. Nevertheless, the superstructure of the tall RPI bridge fully recentres in most of the examined cases, thus confirming this advantage of the rocking system that is crucial for the uninterrupted use of the bridge. Therefore, the RPI alternative in the tall bridge, on one hand increases the displacements of the superstructure compared to the corresponding CSI system, on the other hand it enhances the recentring of the superstructure compared to the conventional isolation (here through LRBs); due to the uncertainty in ground motion characteristics, there are exceptions to the previous findings for some specific ground motions in the tall bridge.

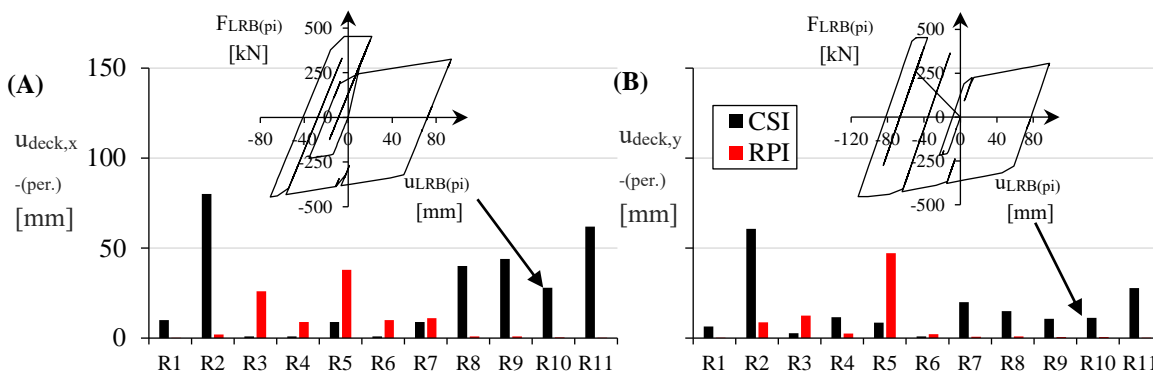


Fig. 6-20 Peak permanent superstructure displacements of segment (P1-P2) in the (A) longitudinal ($u_{deck,x(per.)}$) and (B) transverse directions ($u_{deck,y(per.)}$) for the CSI and RPI bridges with tall piers. Results obtained when subject to the scaled R_i .

6.4.2.2 Superstructure Bending Moments

Fig. 6-21A, B, C summarise the demand for flexural response in the two end spans as well as the intermediate span of the deck, respectively. This is done by presenting the peak total BMs in the longitudinal direction in these three regions of the deck ($M_{deck,y-(A1-P1)}$, $M_{deck,y-(P2-A2)}$ and $M_{deck,y-(P1-P2)}$). Comparison with the flexural response of the deck in the short bridges (see Fig. 6-10A, B, C) shows that the BMs in the different superstructure spans of the CSI bridge seem to be unaffected by the arrangement of the piers, resulting in similar BM values for each specific span. However, this is not the case for the RPI bridge, while the tall structure leads to lower flexural demand along the entire deck than the corresponding short one, for all the examined ground motions; this decrease is more evident in the end spans, and it is on average 18%, 13% and 5% for

the spans (A1-P1), (A2-P2) and (P1-P2), respectively. This effect is attributed to the fact that the rocking piers in the tall bridge are taller/slenderer ($\alpha_{P1} = 0.09$ rad and $\alpha_{P2} = 0.07$ rad) and, therefore, they have lower uplift demands than the shorter/squatter piers of the short bridge ($\alpha_{P1} = 0.28$ rad and $\alpha_{P2} = 0.21$ rad) (see Fig. 6-11). It is also interesting to note that the left end span (A1-P1) in the tall rocking bridge shown in Fig. 6-21A has similar flexural demand as the right end span (A2-P2) shown in Fig. 6-21B, thus opposing to the results found for the short RPI bridge (see Fig. 6-10A, B), and this is due to the fact that the difference in the slenderness of the two piers in the tall bridge is smaller than in the short one. Specifically, the tall RPI bridge increases the BM values at the end span next to pier P1 on average by only 7% compared to the end span next to pier P2, while the corresponding increase in the short RPI configuration is around 18%. Therefore, the flexural demand along the deck in bridges with rocking pier isolation and slender piers is distributed more uniformly, which is an advantage from the design point of view.

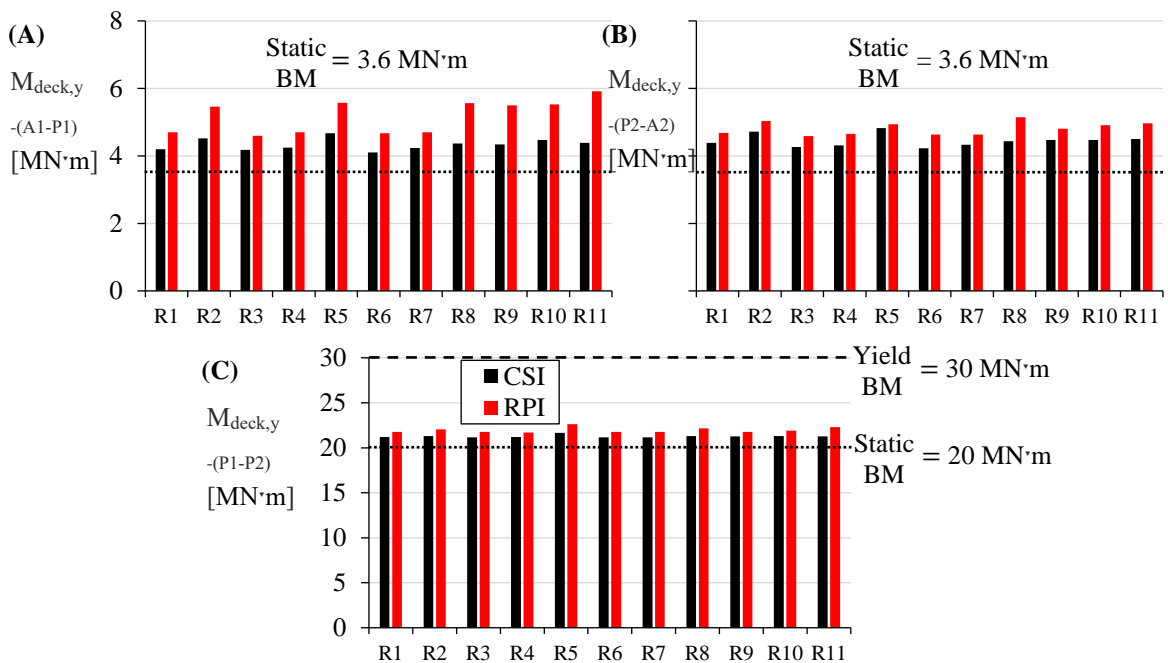


Fig. 6-21 Peak total BMs in the longitudinal direction at (A) the side span (A1-P1) ($M_{deck,y-(A1-P1)}$) and (B) the side span (P2-A2) ($M_{deck,y-(P2-A2)}$) as well as (C) the intermediate span (P1-P2) ($M_{deck,y-(P1-P2)}$) for the CSI and RPI bridges with tall piers. Results obtained when subject to the scaled Ri.

As noted for the bridge with short rocking piers (§6.4.1.2), Fig. 6-21A, B, C show that the BM distribution for all spans of the deck in the tall RPI bridge are also larger than those obtained in the corresponding CSI alternative, for all ground motions. This confirms that rocking pier isolation is detrimental in terms of the flexural demand of the deck compared to the conventional alternative. In this respect, the tall RPI system increases the seismically induced BMs for all spans compared to the corresponding CSI structure on average 110% for the end span (A1-P1), 45% for the end span (P2-A2), and 50% for the intermediate span (P1-P2). It is noted that the corresponding increases for the short configuration are much larger (§6.4.1.2), highlighting the importance of this phenomenon in bridges with low slenderness piers. From the seismic performance point of view,

both end spans of the tall pier bridge reach merely 20% of their yielding capacity regardless of the isolation technique that is adopted as shown in Fig. 6-21A, B, while this percentage increases up to 75% and 71% in the intermediate span for the RPI and CSI alternatives, respectively, as it is observed in Fig. 6-21C; it is noted that the rocking short-pier bridge has BM demands at the central span that are closer to their yielding capacity (85%) than in the corresponding tall-pier rocking bridge, while the BM demand in the CSI is largely unaffected by the slenderness of the piers (70% of the BM yielding capacity is reached in the tall and in the short CSI bridges). Therefore, the rocking approach shows a detrimental effect on the flexural behaviour of the superstructure compared to a conventional isolation technique, but this becomes less apparent for taller/slenderer piers.

6.4.2.3 Pier Drifts

Fig. 6-22A, B show the peak and mean total drifts of pier P1 in the longitudinal ($d_{P1,x}$) and in the transverse directions ($d_{P1,y}$), respectively, and accordingly Fig. 6-22C, D summarise the corresponding drifts of pier P2 ($d_{P2,x}$, $d_{P2,y}$) for the tall-pier bridge when designed with CSI or RPI. In general, the tall piers of the CSI bridge increase considerably the horizontal drifts compared to the corresponding short piers (see Fig. 6-12); this is on average 220% in both directions for pier P1 and, accordingly, 190% for pier P2. This was expected considering that taller piers that are fixed at the bottom section develop larger flexural deformations than shorter ones. However, exactly the opposite occurs in the RPI bridge. In fact, Fig. 6-22 shows that the rocking piers of the tall configuration reach merely 60% of the mean drift of the corresponding piers in the short RPI bridge in both directions (see Fig. 6-12). Therefore, the taller/slenderer the rocking pier, the lower is the demand for horizontal drift in this member. This is due to the large value of the pier height, which appears in the denominator when calculating the drift ratio and it increases more than the horizontal displacement demand (in the numerator). Elaborating further, it can be observed from Fig. 6-12 and Fig. 6-22 that the two piers of the tall RPI bridge reach larger peak displacements in both horizontal directions than the corresponding members of the short configuration, with an average increase of 65% for both piers. However, this increase cannot counteract the corresponding increase in the pier height that is 200% for both rocking piers P1 and P2, thus resulting in much lower horizontal drifts for the piers of the tall bridge.

Accordingly, the theoretical overturning threshold in terms of drift values decreases considerably for the taller rocking piers with respect to the shorter ones (§6.4.1.3), because the overturning threshold corresponds to a 0.75 m horizontal displacement of the pier regardless its height, while the denominator increases for the tall rocking piers, thus resulting in $d_{P1(x,y)} = 4.6\%$ and $d_{P2(x,y)} = 3.4\%$. In this respect, both rocking piers of the tall bridge decrease their safety margin against overturning compared to the corresponding members of the short configuration (§6.4.1.3), reaching for pier P1 a mean value of 20% of its overturning capacity, and of 21% for pier P2. Therefore, it is verified numerically that slender bridges with rocking pier isolation are more vulnerable against overturning of the vertical members than squatter ones, despite the ostensibly much lower pier drifts that occur in the former. It is also interesting to note that based on the same

reasoning presented in §6.4.1.3, the tall rocking bridge configuration increases the range for the ratio of the pier P1 drifts to those of pier P2 to a minimum of 1.1 and to a maximum of 1.5, thus indicating that the assumption in §4.2 is less valid in rocking bridges with tall/slender piers.

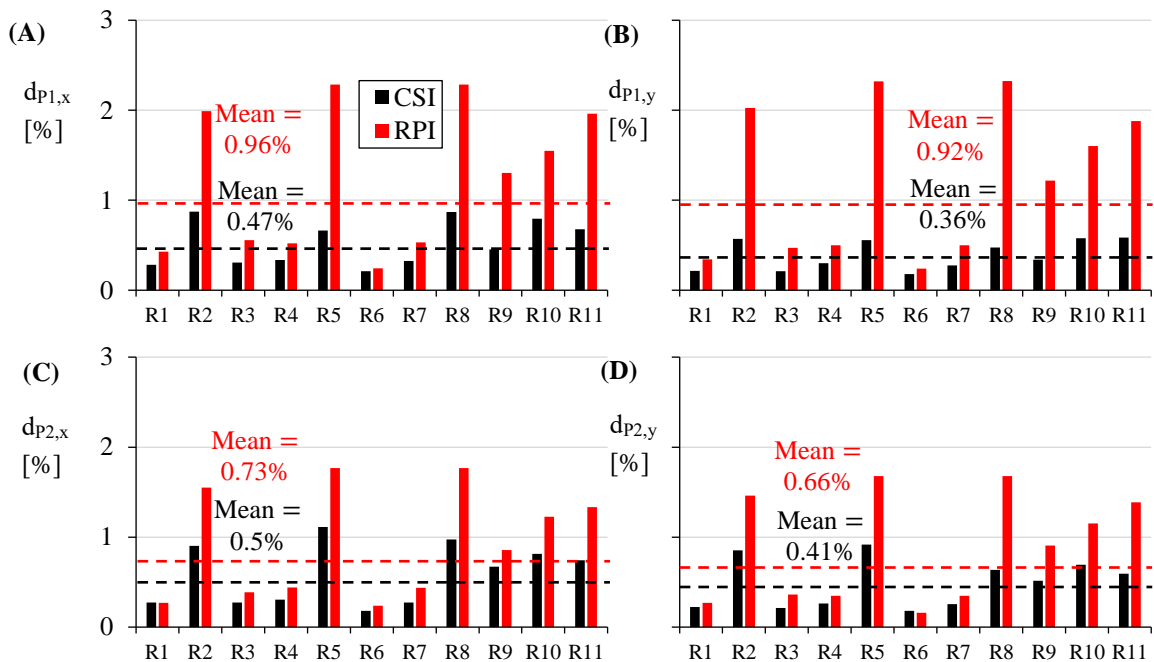


Fig. 6-22 Peak total drifts of pier P1 in the (A) longitudinal ($dp_{1,x}$) and (B) transverse directions ($dp_{1,y}$) and of pier P2 in the (A) longitudinal ($dp_{2,x}$) and (B) transverse directions ($dp_{2,y}$) for the CSI and RPI bridges with tall piers. Results obtained when subject to the scaled R_i .

Fig. 6-22 also shows that, in general, the rocking piers in the tall bridge increase the horizontal drifts compared to those with conventional isolation, and this is along the same line as in the short-pier bridges discussed in §6.4.1.3. The RPI alternative in the tall configuration increases the pier P1 drift compared to the CSI technique on average by 115% and 180% in the longitudinal and the transverse directions, respectively, and in pier P2, this increase is around 60% in both directions. However, these increments are much lower than those found in the short-pier bridges in §6.4.1.3. Additionally, there are two particular records (R1 longitudinally and R6 transversely) for which pier P2 has slightly larger drifts in the tall CSI bridge than in the RPI structure. Therefore, tall/slender piers can show larger drifts when designed conventionally compared to the corresponding rocking member.

6.4.2.4 Pier Bending Moments

The flexural demand in a pier of the tall CSI and RPI bridges is shown in Fig. 6-23, while Fig. 6-24A, B include the corresponding BM diagrams. The results refer only to pier P2 for brevity (i.e., the tallest pier examined herein), while the same trends were observed for pier P1. Similarly to §6.4.1.4, the rocking piers reveal their peak BM just before they enter rocking motion (Acikgoz & DeJong 2018). Fig. 6-24A shows that the BM demand at the bottom part of the pier P2 (section (I)) in the tall CSI bridge is always larger than that in the same member of the short configuration

(see Fig. 6-17A) with an average increase of 14%; this is expected considering that piers in the CSI bridge are fixed at their base and the taller they are, they develop a higher BM in this position. However, this is not the case for the intermediate and top parts of the pier P2 (sections (2) and (3), respectively) in the tall CSI bridge; compared to the CSI structure supported by short piers (see Fig. 6-17A), the BM demand in sections (2) and (3) of P2 is on average 45% and 60% lower, respectively, in the tall CSI bridge. Similarly, Fig. 6-24B shows that the tall bridge with rocking pier isolation decreases the BM demand in P2 compared to the short RPI structure (see Fig. 6-17B), with an average decrease of 31%, 27% and 5% for sections (1), (2) and (3), respectively. Therefore, the results confirm that flexural response is less important in a rocking pier, the lower is the slenderness of the member, and this is due to the fact that these members are more prone to enter rocking motion than stockier members. Additionally, the increased effect of the total weight applied at the bottom section of the rocking pier and the resulting level of fixity at the bottom section of the rocking pier is also apparent, revealing a mean BM at the bottom section (1) that is seven times larger than that at the top section (3).

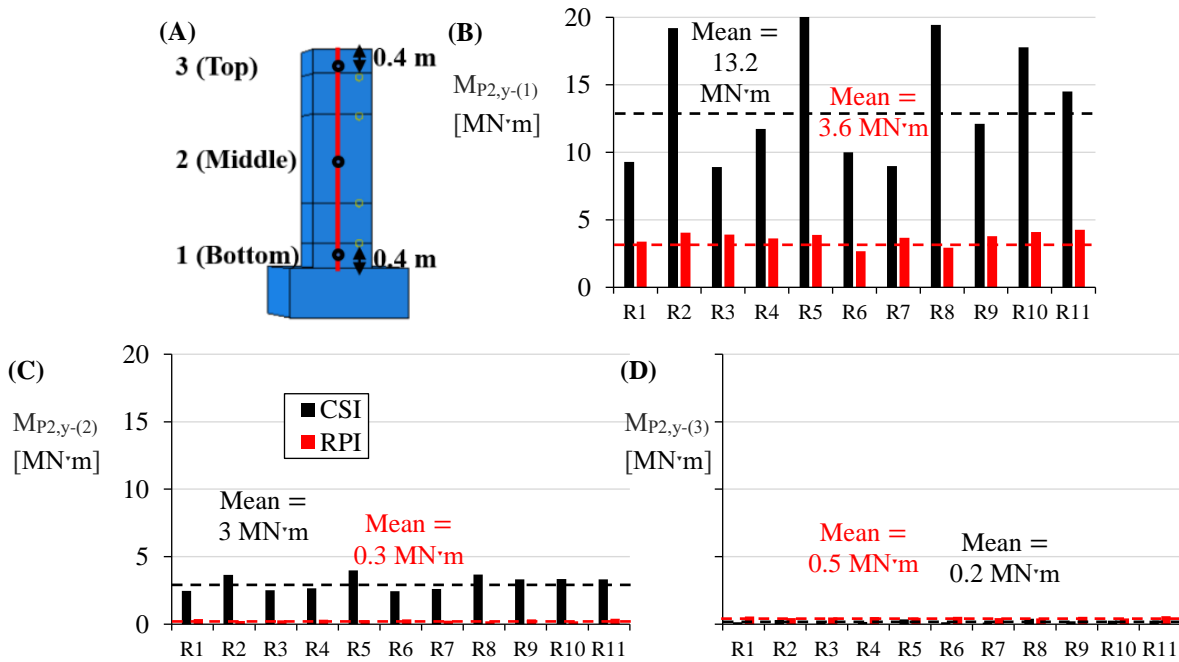


Fig. 6-23 (A) Position of the examined pier sections in the beam elements, as well as peak BMs in the longitudinal direction of pier P2 at (B) section 1 ($M_{P2,y-(1)}$), (C) section 2 ($M_{P2,y-(2)}$) and (D) section 3 ($M_{P2,y-(3)}$) for the CSI and RPI bridges with tall piers. Results obtained when subject to the scaled R_i .

In this respect, Fig. 6-23B, C, D allow to compare the two isolation alternatives for pier P2 of the tall-pier bridge, showing that, in general, the tall pier shows larger or equivalent BMs along its height in the CSI bridge compared to the rocking structure; this is also the case for the slenderer rocking pier in the corresponding short structure (see Fig. 6-16A, B, C), but it wasn't for the corresponding squatter rocking pier in the same structure (see Fig. 6-14B, C, D). Specifically, Fig. 6-23B shows that the conventional pier P2 develops considerably larger BMs at section (1) compared to the rocking pier P2 (the average increase is 280%), and, accordingly, Fig. 6-23C for

section (2) shows an average increase of 980%. Similar BM values occur for the top (3) section for the two isolation alternatives as shown in Fig. 6-23D, however the magnitudes for both cases are marginal. Therefore, the results confirm that flexural response prevails for all the examined sections in a conventional pier compared to the corresponding rocking member when tall/slender members are considered, while the latter accommodates its movement mainly by rigid body motion.

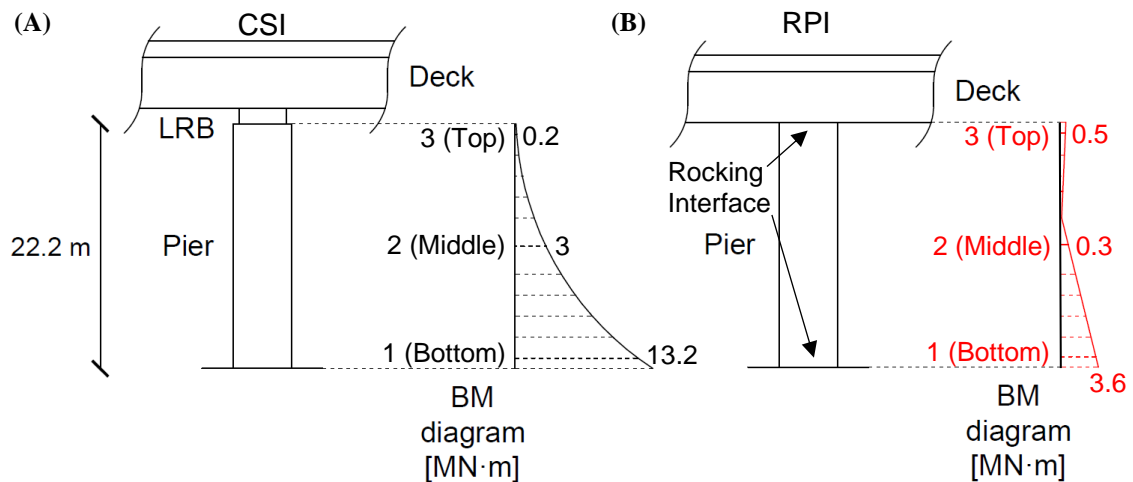


Fig. 6-24 Typical BM diagram of pier P2 in the (A) CSI and (B) RPI bridges with tall piers, accounting for the mean BM values when subject to the scaled Ri.

6.4.2.5 Pier Recentring Capacity

The recentring capability of the free-standing rocking piers in the tall RPI configuration is assessed through the movement of the bottom corner joints of each pier shown in Fig. 6-25A. It is noted that the tall RPI bridges are excited by the same ground motions that were utilised for the short-pier configuration (§6.4.1.5) with a view to detecting differences in the recentring capability of the short and tall rocking piers.

The results in Fig. 6-25B, C, D, E show that the slender rocking piers of the tall bridge have more recentring capacity than the stockier piers in the short configuration (see Fig. 6-18B, C, D, E), which is in agreement with Pompei *et al.* (1998). Specifically, the results for the tall RPI bridge show that rocking pier P1 is shifted by only 0.4 mm and has a permanent dislocation of approximately 2 mm with a simultaneous torsional rotation of 0.1° when subject to motions R1 and R2, respectively. On the other hand, the rocking pier P2 shows a permanent displacement of no more than 1 mm for both cases. It is noted that in the tall bridge the superstructure mass effect parameter is $\gamma = 9.8$ and is much lower than that for the short-pier bridge ($\gamma = 29.3$), however, this does not affect the high recentring capability of the free-standing rocking piers. On the contrary, the slenderer the rocking piers, the less are the sliding effects at the interfaces, which again validates the no-slip assumption adopted in the analytical formulation (§3.2).

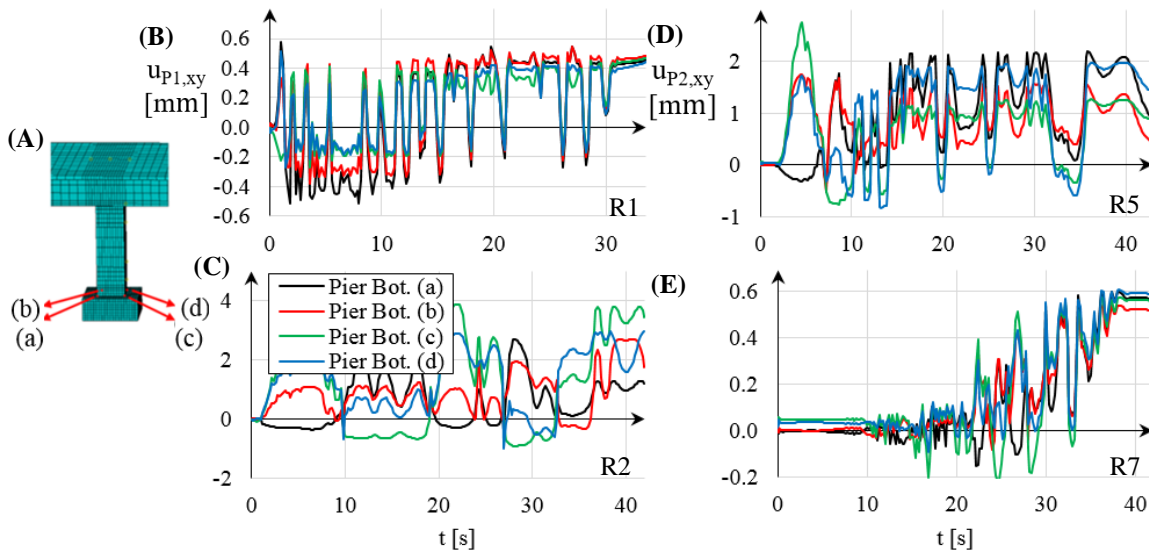


Fig. 6-25 (A) Layout of the corner joints at the bottom surface of the rocking piers, and histories of the total horizontal displacements of pier P1 ($u_{P1,xy}$) subject to the scaled (B) R1 and (C) R2 and of pier P2 ($u_{P2,xy}$) subject to (D) R5 and (E) R7 for the RPI bridge with tall piers.

6.5 Closing Remarks

Chapter 6 presented a numerical analysis of a bridge that was isolated either conventionally or through rocking pier isolation. The reference structure was an actual overpass that has two piers of unequal height, permitting to assess the effect of this asymmetry on the rocking response. A modified version of this bridge was also studied, with piers three times taller than in the original bridge to assess the effect of pier height/slenderness. A ‘purely’ free-standing rocking configuration was examined (i.e., without utilising supplemental or special elements) by allowing sliding at all the rocking interfaces, and it was compared with a conventional isolation technique through LRB devices designed according to EC8 (CEN 2005b). The seismic action was introduced in the form of eleven natural records scaled to the Code spectrum that were applied independently and simultaneously in the longitudinal and the transverse direction (dependent on the examined parameter), and analysis was carried out using the commercial FE software ABAQUS CAE. The following conclusions were drawn from the analyses presented in this chapter;

- RPI shows large horizontal deck displacements that in most cases exceed those of the bridge with CSI. Nevertheless, the restoring capability of the superstructure is enhanced when isolated through rocking by reducing significantly the residual displacements compared to the bridges with conventional isolation, even in this case where a ‘bare’ rocking configuration was adopted, thus revealing the high potentials of this ‘unconventional’ isolation technique. This important conclusion indicates that repair and downtime costs after large earthquake can be reduced or eliminated with rocking pier isolation.

- Rocking pier isolation increases the flexural demand at both end spans of the deck compared to the same span arrangement in the conventionally isolated system. This was attributed to the significant uplift of the deck at the position of the rocking piers, and to the negligible uplift at the position of the abutments due to the free support conditions that were selected for this position. In this regard, the larger the uplift of the pier, the higher the increase in the BM demand and, therefore, this effect becomes particularly significant at the end span between the abutment and the shortest pier. It should be noted though that the flexural demand in the end spans of the deck in the rocking approach can be reduced using bearings at the abutment seats (e.g., simple with uplift capacity or sliding) to allow the vertical motion of the deck at these locations.
- Based on the reasoning that was presented in the previous remark, the rocking pier isolation alternative increases the flexural strains at the intermediate span of the superstructure compared to the conventionally isolated system, as is shown for the first time herein. This is related to the irregularity in the height of the piers, which induces differential uplifts in the piers and the deck (see Fig. 4-13D, E and Fig. 6-11). Therefore, the central span in symmetric bridges with rocking pier isolation is not expected to reveal such behaviour. This observation becomes particularly important in a performance assessment context, considering the higher BMs that occur at the central span due to the gravity loads.
- The piers that are isolated through rocking have a significantly larger drift demand compared to those in bridges with conventional isolation (see Fig. 2-18), particularly the less slender the piers. Additionally, and with respect to rocking piers only, less slender configurations show much larger horizontal drifts compared to slender members. However, this should not be related to the collapse prevention limit state, considering that slenderer rocking piers show higher vulnerability to overturning compared to less slender members. In any case, overturning of the piers is practically impossible to occur in a design context, considering that the reserve capacity against pier overturning is around 75% regardless of the pier slenderness, thus confirming the analytically obtained results in §5.4. This is even more the case considering that the vertical component of ground motion, which was neglected in all chapters of this thesis, leads to upthrow and, therefore, further prevents overturning failure (see §2.3.1.4).
- Both rocking piers show similar horizontal displacements at the top, particularly in the structure with short piers, and this supports the assumption made in §4.2.
- Despite the fact that rigid body motion prevails in rocking piers, flexural strains do develop and correspond to a particular BM distribution (see Fig. 6-15B, Fig. 6-17B, Fig. 6-24B). In this respect, higher flexural strains are found close to the rocking interfaces of the member and, specifically, flexural response is more important at the bottom section of the rocking pier, and it is followed by the top section. The higher flexural response at the bottom section of the rocking pier seems to be attributed to the higher degree of fixity that is achieved in this region due to the increased effect of the weight compared to the top section that can reveal a slide-

rock movement more easily. Finally, the flexural response fades towards the middle section of the rocking element where movement is mainly accommodated by rigid body rotation.

- Flexural response is less important, the slenderer is the rocking pier, and this is due to the fact that slenderer rocking piers are more prone to enter rocking motion than squatter members that delay uplift (see Fig. 2-4) and, consequently, suffer from bending effects.
- Rocking pier isolation can lead to increased BMs at the critical bottom section of the pier compared to a conventional member, and this occurs for the stockiest pier examined in this chapter. Therefore, the reinforcement design of the rocking piers may need to follow the procedure followed for the conventional piers. In the same context, increased BMs appear at the top section of all the rocking piers examined herein compared to the conventional members, but with much lower values compared to the bottom section, and in that sense less important in a design context.
- The free-standing rocking piers, especially the slenderer members, show low sliding effects, high recentring capacity and negligible permanent displacements and rotations at the end of the design earthquake, even though a low value of CoF was considered at the rocking interfaces. This is attributed to the beneficial effect of the superstructure that seems to contribute to the restoring capability of the bridge by preventing sliding effects. This important conclusion highlights the importance of the superstructure in the overall rocking response of bridge piers and, therefore, simplified modelling techniques to model the superstructure effect (e.g., a high compressive force, see §2.5) are not recommended. In an effort to relate the effect of the deck mass in the recentring capability of the rocking mechanism, it is observed that structures with a superstructure mass effect $\gamma \geq 9$ show negligible sliding effects and provide sufficient recentring to the vertical members after ground motion finishes. In this regard, the assumption of no sliding during rocking motion that was made in §3.2 is validated. Nevertheless, it is noted that the vertical component of the ground motions, which can be proven detrimental in terms of recentring of rocking piers, is ignored in this study (see §2.3.1.4).
- From the foregoing discussions, RPI is more efficient than a CSI technique when implemented in bridges with tall piers (or with piers of low slenderness) compared to bridges with short/squat piers. In order to quantify the effect of pier slenderness in rocking, a bridge with short/squat rocking piers should be related to a pier slenderness of at least $\alpha = 0.2$ rad, while the corresponding slender configurations should be related to piers of maximum slenderness $\alpha = 0.1$ rad. However, the response of irregular bridges with rocking pier isolation is also associated with the difference in the slenderness of the supporting members that should not be neglected in the design.

To summarise, rocking pier isolation improves several aspects of the response obtained with conventional isolation in bridges, particularly the recentring capability of the superstructure, with benefits regarding the uninterrupted use of the bridge. However, several issues have to be addressed

in the design of the 'structural' rocking members, and special attention needs to be paid to the detailing of the reinforcement in the deck and in the piers, as well as potential non-linear effects in the rocking surfaces of the piers that can differentiate some of the outcomes determined herein (i.e., flexural response in the rocking piers).

Chapter 7

Conclusions and Recommendations for Future Research

This thesis examined the seismic behaviour of bridges with piers that are free to rock at both ends, and the interaction between the deck and the abutments. Motivation for this research comes from the fact that, although there is a large body of knowledge showing that free-standing rocking columns and relevant frames present a better seismic response than conventional structures, previous works on bridges with rocking piers are based on simplifications that are not applicable to realistic bridge configurations. Consequently, this research aimed at addressing the rocking response of bridges with realistic analytical and numerical models to explore whether isolation of bridges through rocking can be considered as a viable alternative for the next generation of earthquake-resistant bridges.

In this respect, an extensive review of the State-of-the-Art was presented in Chapter 2 to identify the relevant gaps in this research topic, in line with the three core research objectives presented in §1.2. Initially, studies addressing the seismic response and the analytical dynamics of rocking columns and relevant frames were presented, along with the main modelling techniques and assumptions that have been found essential in simplified analytical tools of this type, setting the basis for the corresponding analytical derivations presented in Chapters 3 and 4. Chapter 2 continues with current proposals on bridge pier configurations that aim at mitigating the inherent disadvantages of these members when isolated through ‘bare’ structural rocking, contrasting through the proposals made in Chapter 5 that aim at exploiting the inherent advantages of this isolation technique in bridge piers considering that prefabrication is selected. Finally, this review of the State-of-the-Art closes with studies related to bridges with rocking piers and identifies the simplifications that were adopted therein; these simplifications were taken into account in Chapter 6.

7.1 Conclusions

The conclusions gathered in the following sections of this chapter are aligned with the three core research objectives presented in §1.2, namely, (i) analytical modelling of bridges with rocking piers in §7.1.1, (ii) proposal of non-conventional pier configurations for bridges with rocking piers in §7.1.2, and (iii) comparative assessment of conventional seismic isolation and rocking pier isolation in bridges in §7.1.3. The key issues that had to be addressed for each research objective are presented in a bullet-point format, followed by the main findings in plain text and numbered-point format for each case; the reader is referred to §3.4, §4.4, §5.4 and §6.5 for a more detailed

discussion of the outcomes of each chapter. The recommendations for future research are provided in §7.2 following the same format for the sections.

7.1.1 Analytical Modelling of Bridges with Rocking Piers

Chapters 3 and 4 presented simplified models for predicting the longitudinal response of bridges with rectangular rocking piers of symmetric and asymmetric configurations, respectively. These models expand the literature on the corresponding frame models with rectangular rocking columns, by considering the effects of the abutment-backfill system on the overall bridge dynamics.

The key issues addressed with regard to the determination of the longitudinal rocking response of the bridges with rectangular rocking piers were the following;

- Consideration of the overall effect of the abutment-backfill system through (i) the end joint between the superstructure and the abutment, (ii) the impact of the superstructure on the abutment backwall, (iii) the vertical effect of the seats at the abutments, and (iv) the longitudinal effect of the abutment and the backfill at each end of the deck. Additionally, different span arrangements were also considered to represent a more realistic bridge configuration.
- Introduction of a failure mode not addressed in previous analytical studies on rocking, related to the ultimate capacity of the abutment-backfill system that complements the criterion of overturning of the rocking piers.

The formulation of the longitudinal rocking motion of the symmetric and asymmetric bridges was based on two core assumptions to facilitate the problem, while a third assumption was made for the asymmetric case to simplify the high complexity of the system. The common assumptions for both systems were (i) all the structural members are considered rigid, thus ignoring their deformability, and (ii) sliding effects are not expected to occur during initiation and throughout the entire motion. An additional assumption was made for the analysis of asymmetric bridges that is related to (iii) the identical longitudinal movement of the two free-standing rocking piers with different height. These three assumptions have been found to be consistent with the finite element results discussed in Chapter 6. Specifically, the numerical results presented in §6.4.1.4 and §6.4.2.4 validate assumption (i), proving its validity for bridges with rocking piers of low slenderness as those adopted for examining the seismic performance in §3.3.1 and in §4.3.1. On the other hand, assumption (ii) is considered valid, particularly for slender piers, according to §6.4.1.5 and §6.4.2.5, notwithstanding the grooves adopted in Chapters 3 and 4 to prevent the effect of sliding. In the same context, assumption (iii) for the asymmetric bridge is validated in §6.4.1.3 and §6.4.2.3.

The following novel contributions and conclusions apply with regard to the effect of the abutment and the backfill on the rocking response of bridges compared to equivalent frame models that neglect it, as well as the effect of asymmetry in the height of the piers on bridges with rocking piers;

1. The equation of motion of a bridge with rocking piers accounting for the effect of the abutment-backfill system is significantly different from that of the simple frame model

Specifically, equation of motion of a bridge with rocking piers is divided into two stages: (i) before the superstructure contacts the abutment backwall, and (ii) after closure of the gap at the bridge joints. In the first stage (i), the rocking motion of a bridge follows the equation of motion of the frame system described by Makris & Vassiliou 2013 and Dimitrakopoulos & Giouvanidis 2015 for symmetric and asymmetric configurations, respectively. This is because of the marginal longitudinal resistance of the sliding bearings at the abutment seats (see (i) in point 2). However, at the second stage (ii), after the gap is closed and the deck activates the abutment-backfill system longitudinally, an additional term that describes the influence of the stiffness as well as the material and radiation damping of the backfill is integrated in the equation of motion. This introduces a new factor (q) in the equation of motion that expresses the level of contribution of the abutment-backfill system in rocking response. Larger values of q result in more significant contributions of the abutment-backfill system to the rocking response, which corresponds to bridges with relatively low weight or with higher degree of asymmetry considering constant dimensions in one of the two supporting members.

2. The frictionless sliding bearings adopted at the abutment seats lead to same initiation of rocking motion and lower energy dissipation at each impact at the rocking interfaces compared to the simple frame model without end supports

Specifically, these support conditions at the abutment seats (i) allow the free motion of the superstructure longitudinally (so long as the gap is not closed), while (ii) they support the superstructure in the vertical direction, thus reducing the superstructure weight that goes to the piers compared to the corresponding frame model. Thanks to condition (i) the minimum base acceleration that triggers rocking is the same in a bridge with rocking piers and in the corresponding frame without end supports. On the other hand, condition (ii) leads to lower energy dissipation at each impact at the rocking interfaces for a bridge structure compared to an equivalent frame with same dimensions, and this effect becomes particularly important in highly asymmetric systems.

3. A new ‘failure spectrum’ using pulse-type motions called Failure Minimum Acceleration Spectrum was introduced to extend the ‘traditional’ overturning spectrum (OMAS) that was typically adopted for frames with rocking columns

The FMAS differs from the corresponding OMAS (i) in the failure modes considered, accounting for an additional failure mode associated with the ultimate capacity of the abutment-backfill system, and (ii) with regard to the determination of the so-called ‘self-similar’ response adopted so far for frame models (i.e., frames with rocking columns of same width, height and superstructure mass effect return identical failure curves independently of the mass of the structure that is not the case in bridges due to the presence of the abutment-backfill system). In the same context with (i), the failures due to pier overturning modes for bridges and frames have, generally, a similar failure shape (i.e., higher vulnerability to low-frequency pulses that

progressively decreases for medium- and high-frequency pulses), while the newly adopted failure mode for the bridge structure shows a different failure curve of ‘sickle’ shape (i.e., higher vulnerability to medium-frequency pulses depending on the value of q).

4. The new finding that the simple frame model is not capable of accurately predicting the rocking response of bridges with end supports

This is due to the fact that, first and foremost, the frame model cannot capture the potential failure of the abutment-backfill system. The results of the present thesis show that conventional bridges are more likely to fail due to excessive longitudinal displacement demand at the abutments than due to overturning of the piers. Additionally, the frame model overestimates considerably the seismic response of bridges in terms of (mainly) rocking amplitudes leading to configurations that are more prone to overturn compared to the model accounting for the abutment-backfill system; this can be attributed to the fact that the frame model ignores (i) the longitudinal suppression of free rocking motion that is offered by the stiffness of the abutments, and (ii) the increased energy dissipation that stems from soil damping at the abutments and the pounding effect. Moreover, the frame model can be unconservative and predict overturning for ground motions of higher amplitude than those that lead to the abutment-backfill failure in the proposed bridge model.

5. The newly developed model accounting for the effect of the abutment-backfill system shows that the joint length highly influences the seismic performance of bridges with rocking piers

Specifically, Fig. 3-13 shows that the smallest gap results in the bridge developing 66% of its capacity against activating the abutment failure mode, while these values are 54% and 84% for the medium and large joint lengths in the same structure, respectively. Therefore, a high variation is observed, but a general trend cannot be determined; further discussion on this aspect is given in §7.2.1.

6. The lack of regularity in the pier height does not affect the dominant failure mode and its activation, but the rocking response of the asymmetric bridges shows significant uplifts of the deck

Specifically, the kinematics of bridges with rocking piers of different height are significantly different and more complex than those of regular bridges due to the irregularity in the height of the piers. This leads the asymmetric bridges to show significant deck rotations that are not observed in the symmetric bridge, resulting in higher deck uplifts for the asymmetric system.

7. A ‘simplified’ model was proposed for minimising the high computational cost that was found for analysing asymmetric bridges

To do so, the complex expressions describing the derivatives of the dependent degrees of freedom of the system are substituted by simple linear and quadratic expressions. This reduces the computational cost by approximately 90% without affecting the accuracy of the results. It is noted that the proposed ‘simplified’ model also applies to asymmetric frames with rectangular rocking columns presented by Dimitrakopoulos & Giouvanidis 2015.

7.1.2 Proposal of Non-Conventional Pier Configurations for Bridges with Rocking Piers

Chapter 5 explored the possibility of utilising pier configurations that are non-conventional either in cross-section or in elevation, thus opposing the ‘traditional’ rectangular rocking piers adopted in Chapters 3 and 4. The proposed ‘non-rectangular’ pier configurations are based on the fact that rocking piers show negligible flexural strains during rocking motion, however this was found valid only for slender piers according to §6.4.1.4 and §6.4.2.4 that is in line with the rocking piers adopted in §5.3.1 (see further discussion in that respect in §7.2.2). In this regard, rocking piers with I shapes in cross-section (see Fig. 5-1B for the proposed dimensions) and barbell shapes in elevation (accordingly, see Fig. 5-1C) were proposed, and their seismic performance was studied utilising the analytical model presented in Chapter 3.

The key issue addressed with regard to the determination of the longitudinal rocking response of the bridges with non-conventional rocking piers was the following;

- Consideration of the reduced inherent restoring mechanisms (mass and mass moment of inertia) that stem from the lighter piers with ‘non-rectangular’ shape compared to the ‘traditional’ rectangular-in-elevation rocking piers.

The following novel contributions and conclusions apply with regard to the efficiency of the proposed non-conventional rocking pier configurations compared to the ‘traditional’ rectangular piers in bridges;

1. The proposed non-conventional pier configurations lead to non-negligible economic benefits in terms of use of concrete
Specifically, for a conventional ‘short’ bridge with deck length of 86 m (see §5.2.1 for dimensions and Fig. 5-3), using I piers in cross-section and I piers in elevation reduces 5% and 8% the total mass of the bridge compared to that in a structure with conventional rectangular piers, respectively, and these reductions increase up to 6% and 10% in a longer bridge with nine rocking piers and a deck of 600 m.
2. The most economic configuration for the piers (i.e., with barbell shape) shows the best seismic performance, and it is followed by the I-shaped in cross-section and rectangular piers
Specifically, under the design ground motion, the bridges with non-conventional rocking piers show slightly improved response with reduced rocking amplitudes compared to the same structures with rectangular rocking piers. Accordingly, in ‘extreme’ ground motions, the bridges with piers of non-conventional configuration protect more effectively from damage in the abutments and from overturning of the piers. The enhanced seismic behaviour of bridges with non-conventional rocking piers is directly related to the reduction of the total mass compared to the bridge with rectangular rocking piers (see point 1) that leads to (i) lower

seismic forces, (ii) increased stabilising effect of the deck, (iii) increased suppression provided by the abutment-backfill stiffness, (iv) increased energy dissipation through the material and the radiation damping of the backfill soil, and (v) unaffected energy dissipation through the impacts at the rocking interfaces.

3. Overturning of the piers is practically impossible to occur under longitudinal rocking regardless of their shape

In this respect, the reserve capacity against overturning is around 75% under horizontal earthquakes with peak ground acceleration as high as 0.72 g. These findings should be also related to the effect of the abutment-backfill system and the relevant comparison with the frame model without end supports presented in §7.1.1.

7.1.3 Comparative Assessment of Conventional Seismic Isolation and Rocking Pier Isolation in Bridges

Chapter 6 compares the seismic performance of bridges with a conventional seismic isolation technique and with rocking pier isolation by means of detailed numerical finite element models, to identify the inherent advantages and disadvantages of each isolation approach. Further attention was paid to the effect of pier height/slenderness on the seismic response of bridges with rocking piers, to detect the differences in the response quantities of this isolation approach when implemented in bridges with rocking piers of high (i.e., short piers) and low slenderness (i.e., tall piers).

The key issues addressed with regard to the comparative assessment of the two isolation alternatives in bridges were the following;

- Consideration of a bridge configuration wherein rocking pier isolation is expected to disbenefit its seismic response.
- Assess the validity of the main simplifications adopted in previous chapters and in the literature for examining bridges with rocking piers.
- Identify the differences in the seismic response of these bridges (i.e., displacements and bending moments for piers and deck) in terms of the stability of the structure.
- Establish the range of pier height and slenderness where rocking pier isolation is more effective.

In this regard, two asymmetric bridges were proposed for the comparison with short and tall piers, while the bridge with rocking pier isolation assumes realistic interface conditions, contact interaction between superstructure and abutments as well as deformable sections for all the members.

The following novel contributions and conclusions apply with regard to the comparison of bridges with a conventional seismic isolation technique through bearings and rocking pier isolation;

1. Rocking pier isolation of bridges can be considered as an isolation technique that entails high horizontal deck displacements, similar to those in bridges with conventional seismic isolation
This observation should be related to the high drift demands that were found for the rocking piers that significantly exceed those of conventionally isolated piers, especially in the case of short/squat piers. Therefore, the rocking piers examined herein show similar flexibility in both horizontal directions to that of the conventionally isolated bridge.
2. Rocking pier isolation of bridges shows negligible permanent deck displacements enhancing the seismic performance of this member when isolated conventionally
Specifically, the superstructure in the rocking approach recentres completely in most of the examined cases eliminating the high permanent displacements that were found for the corresponding member of the conventional isolation approach, resulting from the non-linear behaviour of the isolation devices.
3. The rocking pier bridge system increases the flexural demand at all the deck spans compared to the same span arrangement in the conventionally isolated system
This finding is explained (i) for the end spans due to the differential uplift of the deck at the locations of the abutment seats (negligible uplift) and the rocking piers (significant uplift), and (ii) for the intermediate spans due to the different height of the piers that are forced to uplift differentially. In this regard, the effect of (i) is more apparent for bridges with squat piers, while the effect of (ii) in bridges with piers of high difference in their slenderness, and these are directly related to the uplift demand in the rocking piers.
4. Rocking piers can show higher flexural demand at the critical bottom section compared to the conventionally isolated ones that are fixed at that section
This is the case in short/squat piers, but the opposite occurs for tall/slender ones due to the fact that these members when fixed at their bottom section show very high bending moment demand, while this demand reduces for tall rocking piers (see also point 4 below).

The following novel contributions and conclusions apply with regard to the effect of pier height/slenderness on the seismic response of bridges with rocking pier isolation;

1. The tall rocking pier bridge develops (i) increased horizontal deck displacements, and (ii) lower vertical deck displacements than the short one; condition (ii) leads to lower bending moments at the superstructure for the tall system
These observations are justified by the fact that the taller rocking piers (with heights of 16.2 m and 22.2 m) show (i) larger horizontal displacements, and (ii) lower vertical displacements than the corresponding short members (accordingly, pier heights are 5.4 m and 7.4 m); it is noted,

though, that overturning is practically impossible to occur in rocking piers, thus confirming numerically the analytical finding presented before (see point 3 in §7.1.2).

2. The two free-standing rocking piers of each bridge show similar horizontal displacements during the entire rocking motion, validating the relevant assumption that was made in §4.2 to facilitate the analytical formulation
3. The free-standing rocking piers develop higher flexural strains close to the rocking surfaces, especially at their bottom section, while this response attenuates towards the midpoint where pier movement mainly consists in rigid body rotation
4. The flexural response of a rocking pier decreases considerably for a taller/slenderer member compared to the corresponding shorter/squatter one with the same cross-section
This is explained considering that taller rocking piers are more prone to enter rocking motion. In this regard, slender free-standing rocking piers behave more as rigid rocking blocks capped with a massive beam, thus validating the assumption to ignore deformability for these piers in the analytical model presented in §3.2.
5. Rocking piers show negligible sliding effects during ground motion, and high recentring capability with negligible permanent displacements and rotations at the end of excitation
This observation is more apparent for slender rocking piers. In this regard, the assumption of ignoring all sliding effects in Chapters 3, 4, 5 to facilitate the analytical derivations is justified. This conclusion highlights the importance of the superstructure in the overall rocking response of bridge piers and, therefore, simplified modelling techniques to model the superstructure effect are not recommended.
6. Overall, pier rocking is preferable to be used in bridges with tall piers than short ones as it improves more features of conventionally isolated bridges

7.2 Recommendations for Future Research

This section begins with some proposals for further research on the topic of bridges with rocking piers that apply to all the research objectives presented before and are presented in the next paragraph, while specific recommendations for each research objective are listed in a bullet-point format in the next sub-sections. The sequence of the proposals represents research topics sorted in descending order of priority/importance in the author's opinion, with a view to enhancing the approaches presented in this thesis and, consequently, strengthening the main aims of this research as stated in §1.2. It should be noted that some of the specific proposals that are made for each research objective may also apply to other objectives due to the coherence of the topic examined in this thesis.

Implementation of rocking pier isolation in real-life bridge projects has been scarce and this is mainly due to the fact that more experimental work is required in this field to validate the accuracy of the analytical and numerical approaches that have been followed by several research teams. In this regard, these experimental studies should aim at further quantifying the uncertainties that govern the rocking motion of ‘bare’ bridge configurations (e.g., level of sliding, concrete spalling when a concrete-to-concrete surface is selected) and, therefore, leading to the development of code standards for bridges with rocking pier isolation. Moreover, all chapters of this thesis addressed rocking piers with a free-standing configuration, considering that this is the more efficient way to establish the inherent advantages and disadvantages of this isolation technique in bridges, a system that has not been thoroughly examined in previous studies or that has been addressed adopting several simplifications. However, it is recognised that bridge owners would be reluctant to adopt such a ‘bare’ and ‘unconventional’ isolation technique in real bridge projects due to the high uncertainty inherent (or, perhaps perceived) in structures of this type (e.g., level of sliding). From this perspective, the integration of supplemental devices, in particular unbonded tendons (see §2.4.1.1) in bridges with rocking pier isolation is important to minimise the possibility of having to recentre the deck and the piers after the earthquake, which is simply not feasible in most cases. In the same direction, using prefabricated piers in the context of accelerated bridge construction combined with the still not properly quantified effect of the vertical component of the seismic action (see §2.3.1.4) suggests the need for supplementing ‘bare’ rocking piers with additional recentring capacity. Regardless of the use of supplemental devices, further investigation is needed on the effect of vertical component of ground motion on the seismic response of bridges with rocking piers.

7.2.1 Analytical Modelling of Bridges with Rocking Piers

Future research on the longitudinal response of bridges with rocking piers should include the following;

- Validation of the analytical approaches through experimental and/or numerical results. This proposal aims to establish the accuracy of the analytical approaches in terms of capturing response parameters (e.g., deck displacements, activation of either failure mode etc). In this respect, several studies have tackled this critical issue in rocking columns and relevant frames (i.a., Agalianos *et al.* 2017, Thomaidis *et al.* 2018, Bachmann *et al.* 2018) and showed that these analytical derivations are capable of predicting quite satisfactorily several rocking response parameters measured experimentally or derived numerically, as well as predicting the safety of the structure from the seismic performance point of view. However, the validation of the analytical expression that accounts for the effect of the abutment-backfill system in the rocking response of realistic bridge configurations remains an open research issue. Additionally, the analytical models presented in Chapters 3 and 4 assume rigid sections for all the structural members, thus neglecting the vertical deflections at the end spans (i.e., when working as deformable cantilevers). This was found not to affect the seismic rocking response

of the structure when analysed analytically. However, further comparisons of the analytical solutions with experimental and/or numerical results are required with a view to further establishing the negligible effect of this assumption on the rocking response of a bridge, including the value of coefficient of restitution when an impact at the rocking interfaces takes place. In the same context, bridge configurations with short end spans, different span ratios and different number of spans/piers are also worth exploring in that respect.

- Consideration of a more sophisticated force-displacement behaviour for the abutment-backfill system. The simplified analytical models presented in Chapters 3, 4 and 5 adopt an equivalent linear spring to describe the stiffness of the abutment-backfill system (see §3.3.4.1). However, several studies addressed aspects of the nonlinear behaviour of the abutment-backfill system, highlighting its behaviour in the seismic response (i.a., Shamsabadi *et al.* 2010, Xie *et al.* 2017). To this end, the nonlinear force-displacement behaviour of the abutment-backfill system should be taken into account in the rocking response of the bridge structure, and this is particularly important considering the high vulnerability of this member in a performance assessment context (i.e., abutment failure mode is the predominant mode of the bridge with rocking piers). Accordingly, more sophisticated models should be considered for the impact of the superstructure on the abutment backwall accounting for the effect of the coefficient of friction of this impact (i.a., Shi & Dimitrakopoulos 2017), and the impact of the structure at the rocking interfaces accounting for the effect of a more realistic centre of rotation for the rocking piers (see §2.3.1.2 and Fig. 2-8).
- Further examination of the effect of the joint gap between the superstructure and the abutment backwall. The gap size was found to influence the effective stiffness of the deck in the closed-gap stage significantly, and a general trend with regard to this behaviour cannot be observed (see §3.3.4.3, and point 5 in §7.1.1). Therefore, it is foreseen fruitful to conduct an in-depth examination of this behaviour. This could lead to the recommendation of an optimum gap size that, combined with the in-service requirements of the bridge joints, may be related to the overall seismic response of the bridge and the resulting contribution of the abutment-backfill system (q).
- Exploration of practical techniques to minimise sliding effects in rocking piers. As explained before, neglecting sliding is a fairly valid assumption in the analytical model that was supported by the results obtained in §6.4.1.5 and §6.4.2.5, but it still remains an open and challenging issue. This thesis proposes grooves at both ends of the rocking piers (see Fig. 3-1, Fig. 4-1, Fig. 5-1) in order to prevent the detrimental consequences of sliding during the rocking motion. However, the optimal configuration of these grooves, including their length and depth, is an issue that warrants further examination, and this should be done based on two main criteria: (i) the rocking motion of the piers is not restrained, considering that impacts on these grooves could damage their integrity, and (ii) the gap between the pier and the groove edge should be small enough to prevent significant permanent displacements of the piers. A configuration for the grooves with rounded edges is worth exploring, considering that criterion (i) would be

satisfied to higher extent compared to grooves with sharp edges, while criterion (ii) is not expected to be affected from the proposed curvature. The configuration with rounded edges could also be extended to the rocking piers with a view to avoiding the undesirable effect of spalling in these members. Fig. 7-1B presents the proposed pier and groove configurations with rounded edges as opposed to the one adopted in this thesis (and in most of studies with rocking piers) with sharp edges shown in Fig. 7-1A. It is noted that the rocking pier with rounded edges is more prone to overturn due to its lower slenderness (α_i) and size (R_i) compared to the same member with sharp edges (see §2.3.1.3), however the high overturning stability of the rocking piers is not expected to be decreased considerably.

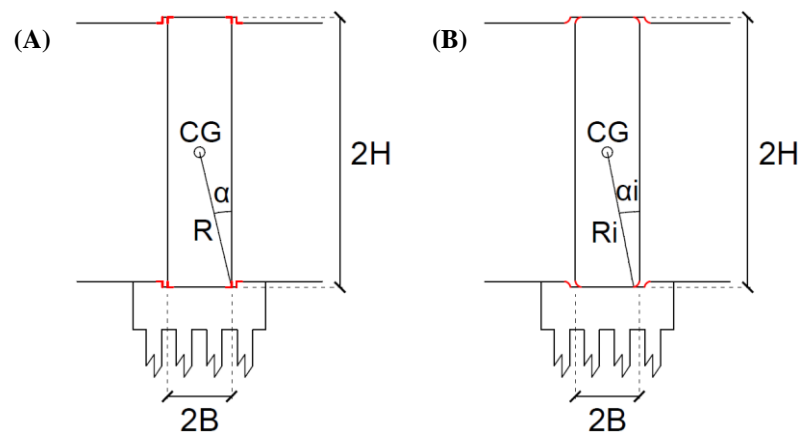


Fig. 7-1 Schematic of a rectangular pier with rocking surfaces and end grooves formed with (A) sharp edges, and (B) rounded edges (highlighted in red).

- Consideration of ‘hybrid’ approaches in bridges with rocking piers. Frames with rocking columns and flag-shaped hysteretic behaviour have been found to enhance the seismic response of ‘bare’ configurations (see §2.3.2.3 and Table 2-4). It is worth investigating if the same applies to bridge structures that have vertical supports and frictionless sliding bearings at the abutment seats that do not restrain the longitudinal motion of the superstructure. Aiming at further improving the seismic performance of the bridge, mainly in terms of reducing the longitudinal deck displacements and better protecting the integrity of the abutment-backfill system, a new configuration is proposed involving restraining the superstructure at the abutment seats through bearings with longitudinal resistance (and uplift capacity, see §7.2.3) and flag-shaped hysteretic behaviour for the rocking piers. This improved configuration is expected to enhance the seismic performance of the structure.
- Formulating the rocking response of a bridge with rocking piers in the transverse direction. The analytical models developed in Chapters 3 and 4 examine only longitudinal rocking, neglecting the appearance of transverse response. Rocking motion in the transverse direction can be expressed by the corresponding frame models (i.e., one or more rocking columns capped with a massive beam) and free ends. However, the rigidity of the superstructure, usually adopted in analytical solutions of this type, cannot be considered in this direction, while different transverse displacements occur at different locations of the superstructure as explained in

§6.4.1.1 and §6.4.2.1. Therefore, the flexibility of the superstructure in the transverse direction along with the transverse gaps at the ends of the superstructure should be considered in the formulation.

7.2.2 Proposal of Non-Conventional Pier Configurations for Bridges with Rocking Piers

Future research with regard to proposing alternative pier configurations in bridges with rocking piers entails the following;

- Study of the flexural response of rocking piers with non-conventional configuration. The pier configuration with I shape in elevation has been found to enhance the seismic performance of bridges with relatively heavy piers (including the ‘traditional’ rectangular one), and at the same time it reduces the cost and environmental impact of the structure by reducing the use of concrete. However, this was studied under the assumption that the piers are completely rigid, and this is observed not to be the case in the numerical analysis presented in §6.4.1.4 and §6.4.2.4 with conventional piers, especially for short/squat rectangular members. Considering that the flexural strains at the mid-height of the rocking piers were found to be relatively small regardless of the pier slenderness, the proposed web section (see Fig. 5-1C for details) is expected to resist this bending moment demand. However, the relatively large flexural demand in the piers close to the rocking interfaces indicates the need to examine the seismic response of bridges with non-conventional rocking piers using rigorous finite element models, and to explore the effects of increasing the flange height by means of extensive parametric analyses. In addition, wrapping the critical segments of the non-conventional rocking columns with fibre-reinforced polymers to increase their strength locally is also worth exploring.
- Further development of the proposed non-conventional rocking piers to improve their seismic performance. As explained in Chapter 5 and §7.1, the proposed non-conventional pier configurations exploit the inherent advantages of rocking pier isolation and accelerated bridge construction. However, the disadvantages of this isolation approach to rocking piers related to the recentring capacity, the energy dissipation, and the behaviour of the interface material in these members, are not addressed. Specific recommendations for improving these drawbacks were made in §2.4.1.1, §2.4.1.2, §2.4.1.3, respectively, based on relevant studies that implemented enhanced techniques in rectangular rocking piers. Therefore, the focus of future research should be the examination of the same techniques in piers with ‘non-rectangular’ shapes. In the same direction, the use of rubbers at the rocking surfaces of the piers has already been established as a satisfactory technique in rectangular members providing (i) higher energy dissipation than the stiffer concrete interface (see §2.4.1.2), and (ii) avoidance of the undesirable effect of spalling at the concrete edges (see §2.4.1.3); these should be extended to piers with non-conventional configuration.

- Study the effect of pier slenderness in bridges with rocking piers of given height and rectangular section. Chapter 5 examined the effect of pier shape in members with given slenderness, proposing non-conventional pier configurations that lead to reduced overall cost and enhanced seismic performance, despite their reduced restoring mechanisms compared to rectangular rocking piers with the same slenderness. Similarly to the non-conventional pier configurations, reduction of pier slenderness for a given pier height leads to economic benefits (i.e., lighter structures), but at the same time reduces the inherent restoring mechanisms of the system (see also §2.3.1.3 for the effect of reduced α and reduced R in free-standing rocking columns). Therefore, the reduction of pier slenderness for a given height in bridges with rocking piers can lead to the same four beneficial for rocking performance conditions mentioned in point 2 of §7.1.2. However, it should be noted that the dissipated energy at each impact at the rocking interfaces is expected to decrease in bridges with rocking piers of reduced slenderness (i.e., the smaller the contact surface, the lower is the energy dissipation at each impact at the rocking interfaces) that is not the case in the proposed non-conventional pier configurations. Therefore, the effect of pier slenderness in bridges with rocking piers needs to be carefully examined.

7.2.3 Comparative Assessment of Conventional Seismic Isolation and Rocking Pier Isolation in Bridges

Future research on enhancing the seismic performance of bridges with rocking piers from the numerical point of view should address the following;

- Examination of the flexural strains developed in rocking piers. In Chapter 6, an important finding emerged: rocking piers can have significant flexural demand. This is traditionally ignored in analytical studies of rocking structures and, therefore, it should be further examined through finite element models that account for nonlinearities in concrete response, and experimental testing to verify the existence of this flexural demand in the piers. With regard to the bending moment demand at the different sections of the rocking pier, a significant flexural response was found at the bottom critical section of the rocking piers that for short/squat members was found more important than that in conventional piers that are fixed at the bottom. In this regard, proper design of the reinforcement for this region is important. Additionally, the lower bending moments at the top section of the rocking pier compared to those at the bottom one should be further studied accounting for the slide-rock movement at this section, which seems to relieve it from flexural strains.
- Consideration of ‘hybrid’ rocking solutions to isolate the movement of the superstructure from that of the substructure. This proposal is based on the fact that rocking motion increases the flexural response in the superstructure in both bridge configurations examined in Chapter 6 compared to the conventional isolation technique, and this is directly related to the uplift demand of the rocking piers. In this respect, the soffit of the rocking deck at the abutment seats

should be attached to isolation devices (bearings) with uplift capacity that would relieve the end spans from the significant flexural response that was found in Chapter 6 due to the differential uplifts at the abutment seats and the rocking piers. Moreover, the isolation devices should provide sufficient horizontal resistance to decrease the large horizontal deck displacements that were found for the bridge with rocking piers. In the same context, and for the intermediate spans, the difference in the slenderness of the supporting members is important for the bending moment demand at this section of the superstructure, and the designer should try to reduce this difference. If this is not feasible, it is proposed to explore a ‘hybrid’ rocking approach by allowing the tall piers to rock freely while the short ones should be connected to the deck with base isolation devices in order to relieve the superstructure from significant vertical movement of the short/squat piers.

- Consideration of spatial variability of the ground motions in bridges with rocking pier isolation. To best of the author’s knowledge, all previous studies on the seismic behaviour of bridges with rocking piers consider the seismic motion as synchronous and identical for all supports, therefore ignoring the spatial variability of the ground motions. However, it has already been established that the earthquake ground motion may significantly differ among the support points, especially for long bridges, in terms of amplitude, frequency content and arrival time (Hao 1989, Der Kiureghian & Keshishian 1997). The effect of spatial variability of the ground motions has been implemented in conventionally designed earthquake-resistant bridges, showing detrimental effects in some cases, and favourable in others (i.a., Sextos *et al.* 2003, Sextos & Kappos 2009). In bridges with rocking piers, this effect is expected to have a significant impact, either positive or negative, considering the uplift demand of the rocking piers and the resulting significant influence on the flexural response of the superstructure. Therefore, this effect needs to be quantified. In this regard, the ‘hybrid’ rocking approach presented in the previous recommendation with the utilisation of base isolation devices on top of short rocking piers could be important in bridges with rocking pier isolation under these ground motion conditions.

Appendix A

Supplement to Chapter 3

A.1 Analytical Model of the Rocking Response [§3.2]

A.1.1 Impact at the Rocking Interfaces [§3.2.5]

With reference to Fig. A-1A, B, C consider that all piers initially rock about CR A and C in the clockwise (positive) direction with a magnitude of the angular velocity $\dot{\theta}_I$, and reverse the rocking rotation smoothly to the counter-clockwise (negative) direction with angular velocity $\dot{\theta}_{II}$, now rotating around CR A' and C'. At the intermediate condition, where the bridge is at the at-rest position, the abutments serve as vertical supports (E and E') and carry part of the deck weight when impact is imminent. Hence, additional impulses ($\Lambda_{E,z}$ and $\Lambda_{E',z}$) originate at the abutment seats as can be seen in Fig. A-1B, which do not occur in the frame with rocking columns. As a result, in this study there are seven unknowns that need to be determined, namely the impulses at the CR A' of the two-side rocking piers in the longitudinal and vertical directions ($\Lambda_{A',x}$ and $\Lambda_{A',z}$), the impulses at the CR C' of the $[N - 2]$ intermediate rocking piers in both directions ($\Lambda_{C',x}$ and $\Lambda_{C',z}$), and those at the two abutment seats ($\Lambda_{E,z}$ and $\Lambda_{E',z}$) as well as the angular velocity after impact ($\dot{\theta}_{II}$). Without lack of accuracy, and when the bridge with rocking piers returns to the original at-rest position (when $\theta = 0$) after rocking is initiated, the following analogies based on tributary zones are adopted instantaneously among the impulses (or reaction forces as shown in Eq. (3-23)) that are developed at the different impact points, considering the assumptions of rigid deck and prevention of sliding at all impact faces (§3.2)

$$\Lambda_{E,z} = \Lambda_{E',z} = \frac{L_1}{L_1 + L_2} \Lambda_{B',z}, \quad (\text{A-1})$$

$$\Lambda_{B',x} = \frac{L_1 + L_2}{2L_2} \Lambda_{D',x} \quad \text{and} \quad \Lambda_{B',z} = \frac{L_1 + L_2}{2L_2} \Lambda_{D',z}. \quad (\text{A-2})$$

Eqs. (A-1) and (A-2) are used separately in order to reduce the number of unknowns in the impact problem. Specifically, the utilisation of Eq. (A-1) and the conservation of linear momentum just before and after the impact along the Z axis for the side piers establishes the relationships between the impulses at the points E and E' with those at CR A'

$$\Lambda_{E,z} = \Lambda_{E',z} = \frac{L_1}{L_1 + L_2} \left[\Lambda_{A',z} - m_{pier} B (\dot{\theta}_I + \dot{\theta}_{II}) \right], \quad (\text{A-3})$$

whilst Eq. (A-2) combined with the conservation of linear momentum in both directions for the side and for the intermediate piers relates the impulses at the CR C' and A'

$$\Lambda_{C',x} = \frac{2L_2}{L_1 + L_2} \Lambda_{A',x} + \frac{L_2 - L_1}{L_1 + L_2} m_{pier} H (\dot{\theta}_I - \dot{\theta}_{II}) \quad \text{and}$$

$$\Lambda_{C',z} = \frac{2L_2}{L_1 + L_2} \Lambda_{A',z} - \frac{L_2 - L_1}{L_1 + L_2} m_{pier} B (\dot{\theta}_I + \dot{\theta}_{II}). \quad (\text{A-4})$$

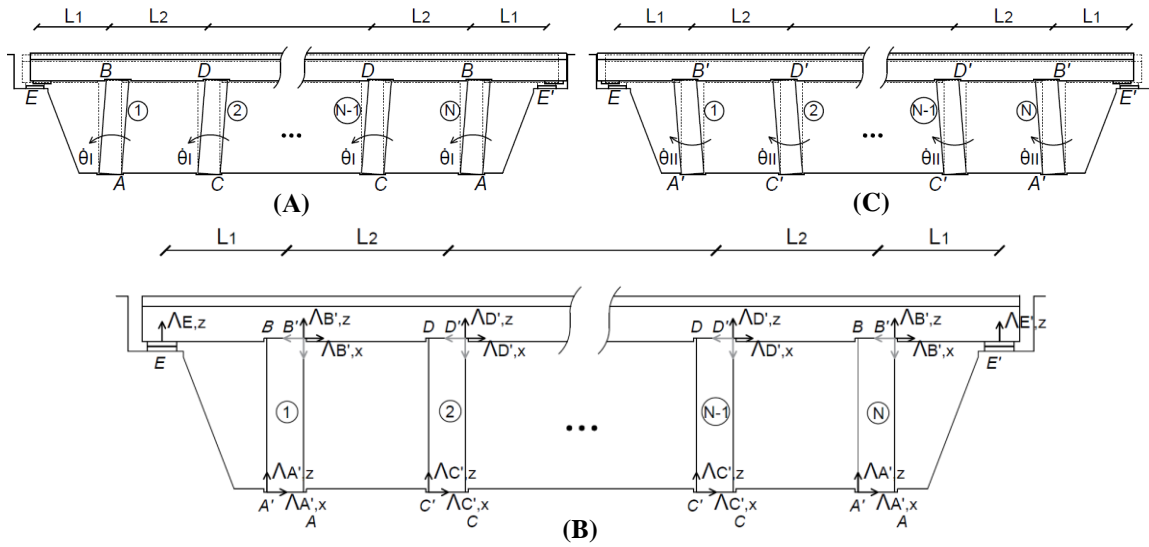


Fig. A-1 Schematic of the impact problem considered in the rocking motion of a symmetric bridge that (A) undergoes clockwise (positive) rotation with an angular velocity of the piers $\dot{\theta}_I$, (B) impacts at the corresponding pivot points and then reverses to (C) counter-clockwise (negative) rotation with an angular velocity of the piers $\dot{\theta}_{II}$.

Eqs. (A-3) and (A-4) reduce the unknowns of the impact problem from seven to only three ($\Lambda_{A',x}$, $\Lambda_{A',z}$ and $\dot{\theta}_{II}$). Hence, the following equations are considered in the determination of these unknowns;

1. Linear momentum along X axis for the entire bridge

$$2\Lambda_{A',x} + [N - 2]\Lambda_{C',x} = -[Nm_{pier} + 2m_{deck}] H (\dot{\theta}_I - \dot{\theta}_{II}). \quad (\text{A-5})$$

2. Linear momentum along Z axis for the entire bridge

$$\Lambda_{E,z} + 2\Lambda_{A',z} + [N - 2]\Lambda_{C',z} + \Lambda_{E',z} = [Nm_{pier} + 2m_{deck}] B (\dot{\theta}_I + \dot{\theta}_{II}). \quad (\text{A-6})$$

3. Angular momentum at point B' for a side pier

$$2H\Lambda_{A',x} + 2B\Lambda_{A',z} = \left[-m_{pier}H^2 + I_{pier}^{CG} \right] (\dot{\theta}_I - \dot{\theta}_{II}) + m_{pier}B^2 (\dot{\theta}_I + \dot{\theta}_{II}). \quad (A-7)$$

Eqs. (A-5) to (A-7) describe the impact problem when the rotation changes from positive to negative. The CoR at the rocking interfaces (η) in the rocking motion of the bridge is obtained by solving the system of Eqs. (A-5) to (A-7) and is given in Eq. (3-31).

A.2 Analysis Framework [§3.3]

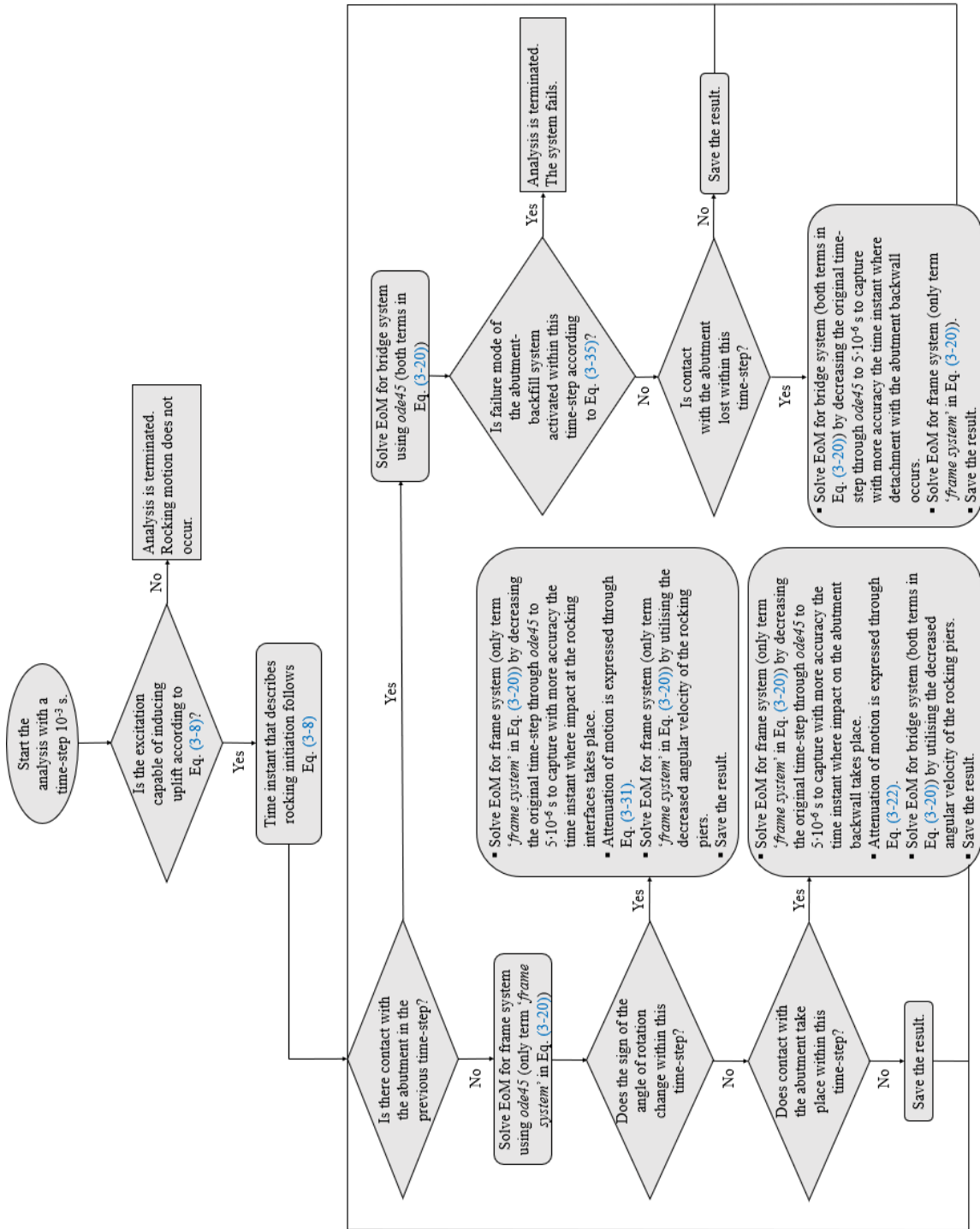


Fig. A-2 Flowchart of the MATLAB code to formulate the rocking motion of a symmetric bridge with rocking piers.

Appendix B

Supplement to Chapter 4

B.1 Analytical Model of the Rocking Response [§4.2]

B.1.1 Impact at the Rocking Interfaces [§4.2.5]

To solve the impact problem, let the displaced position of the bridge change from clockwise (negative) to counter-clockwise (positive) as shown in Fig. B-1A, B, C. Considering that additional reaction forces (or impulses) are developed in the abutment seats compared to the corresponding frame without abutments, there are seven unknowns that need to be determined, namely, the impulses $\Lambda_{A',x}$ and $\Lambda_{A',z}$ at CR A' of the tall pier, $\Lambda_{C',x}$ and $\Lambda_{C',z}$ at CR C' of the short pier, $\Lambda_{E,z}$ as well as $\Lambda_{E',z}$ at the two abutment seats E and E', respectively, and the angular velocity of the tall pier after the impact at the rocking interfaces $\dot{\phi}_{II}$. However, only five equations can be used to describe the impact problem. For this reason, two additional relationships between the impulses at the abutment seats and those at the pier-deck interfaces are introduced according to the rationale presented in §3.2.5

$$\Lambda_{E,z} = \frac{L_1}{L_1 + L_2} \Lambda_{B',z}, \quad (\text{B-1})$$

$$\Lambda_{E',z} = \frac{L_1}{L_1 + L_2} \Lambda_{D',z}. \quad (\text{B-2})$$

Introducing the conservation of linear momentum just before and after the impact at the rocking interfaces along the Z axis for the tall pier into Eq. (B-1) relates the impulses at point E with those at CR A'

$$\Lambda_{E,z} = \frac{L_1}{L_1 + L_2} \left[\Lambda_{A',z} - m_{pier,1} B (\dot{\phi}_I + \dot{\phi}_{II}) \right]. \quad (\text{B-3})$$

Similarly, Eq. (B-2) combined with the conservation of linear momentum for the short pier establishes the relationships between the impulses at point E' and those at CR C'

$$\Lambda_{E',z} = \frac{L_1}{L_1 + L_2} \left[\Lambda_{C',z} - m_{pier,2} B \bar{h} (\dot{\phi}_I + \dot{\phi}_{II}) \right]. \quad (\text{B-4})$$

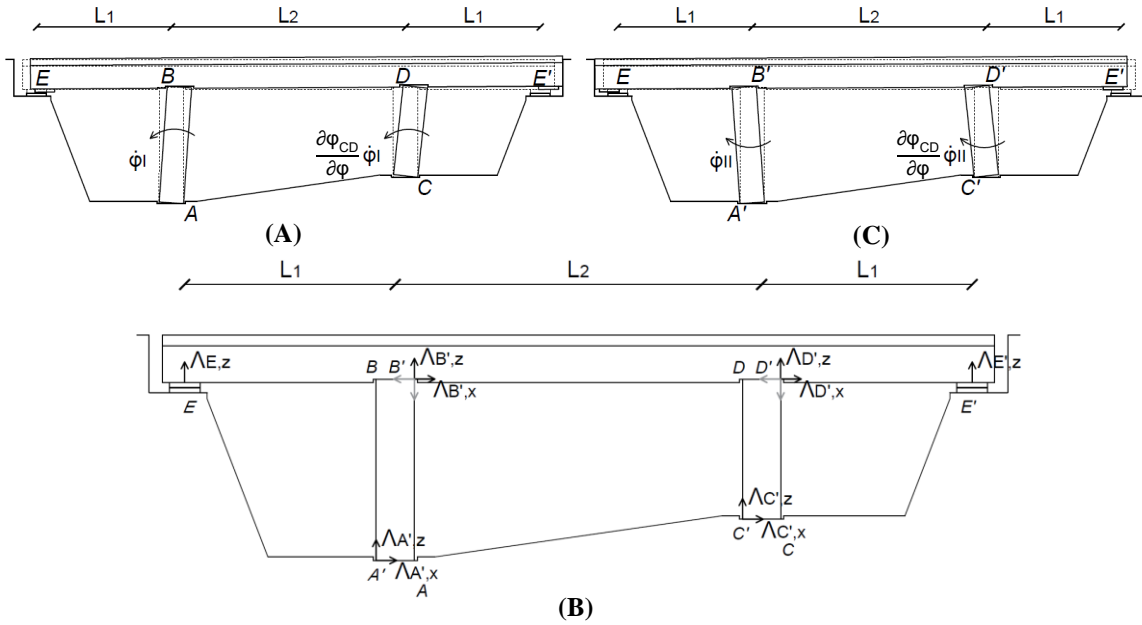


Fig. B-1 Schematic of the impact problem considered in the rocking motion of an asymmetric bridge that (A) undergoes clockwise (negative) rotation with an angular velocity of the tall pier $\dot{\phi}_I$, (B) impacts at the corresponding pivot points and then reverses to (C) counter-clockwise (positive) rotation with an angular velocity of the tall pier $\dot{\phi}_{II}$.

Eqs. (B-3) and (B-4) reduce the unknowns of the impact problem from seven to five ($\Lambda_{A',x}$, $\Lambda_{A',z}$, $\Lambda_{C',x}$, $\Lambda_{C',z}$ and $\dot{\phi}_{II}$), and the following equations are considered in the determination of these unknowns;

1. Linear momentum along the X axis for the entire bridge

$$\Lambda_{A',x} + \Lambda_{C',x} = \left[m_{pier,1} + m_{pier,2} + 2m_{deck} \right] H_1 (\dot{\phi}_I - \dot{\phi}_{II}) - 2m_{deck} \bar{b} \bar{h} [\bar{h} - 1] (\dot{\phi}_I + \dot{\phi}_{II}). \quad (\text{B-5})$$

2. Linear momentum along the Z axis for the entire bridge

$$\Lambda_{E,z} + \Lambda_{A',z} + \Lambda_{C',z} + \Lambda_{E',z} = 2m_{deck} B \bar{b} [\bar{h} - 1] (\dot{\phi}_I - \dot{\phi}_{II}) + \left[m_{pier,1} B + m_{pier,2} B \bar{h} + m_{deck} B (\bar{h} + 1) \right] (\dot{\phi}_I + \dot{\phi}_{II}). \quad (\text{B-6})$$

3. Angular momentum about B' for the tall pier

$$2H_1 \Lambda_{A',x} - 2B \Lambda_{A',z} = \left[m_{pier,1} H_1^2 - I_{pier,1}^{CG} \right] (\dot{\phi}_I - \dot{\phi}_{II}) - m_{pier,1} B^2 (\dot{\phi}_I + \dot{\phi}_{II}). \quad (\text{B-7})$$

4. Angular momentum about D' for the short pier

$$2H_2\Lambda_{C',x} - 2B\Lambda_{C',z} = \left[m_{pier,2}H_1H_2 - I_{pier,2}^{CG}\bar{h} \right] (\dot{\phi}_I - \dot{\phi}_{II}) - m_{pier,2}B^2\bar{h} (\dot{\phi}_I + \dot{\phi}_{II}). \quad (\text{B-8})$$

5. Angular momentum about A' for the entire bridge

$$\begin{aligned} & -[L_1 - B]\Lambda_{E,z} - [2H_1 - 2H_2]\Lambda_{C',x} \\ & + L_2\Lambda_{C',z} + [L_1 + L_2 + B]\Lambda_{E',z} = \\ & \left[\begin{array}{l} -m_{pier,1}H_1^2 - I_{pier,1}^{CG} - m_{pier,2}H_1(2H_1 - H_2) - I_{pier,2}^{CG}\bar{h} \\ -2m_{deck}H_1(2H_1 + h) + 2m_{deck}\left(\frac{L_2}{2} + B\right)B\bar{b}(\bar{h} - 1) \end{array} \right] (\dot{\phi}_I - \dot{\phi}_{II}) \\ & + \left[\begin{array}{l} m_{pier,1}B^2 + m_{pier,2}B\bar{h}(L_2 + B) + 2m_{deck}(2H_1 + h)\bar{b}h(\bar{h} - 1) \\ + m_{deck}\left(\frac{L_2}{2} + B\right)B(\bar{h} + 1) + I_{deck}^{CG}2\bar{b}(\bar{h} - 1) \end{array} \right] (\dot{\phi}_I + \dot{\phi}_{II}) \end{aligned} \quad (\text{B-9})$$

Eqs. (B-3) and (B-4) are substituted in the system formed by Eqs. (B-5) to (B-9), and its solution returns the four impulses ($\Lambda_{A',x}$, $\Lambda_{A',z}$, $\Lambda_{C',x}$, $\Lambda_{C',z}$) and the post-impact angular velocity of the tall pier ($\dot{\phi}_{II}$). The CoR at the rocking interfaces $\eta = |\dot{\phi}_{II}/\dot{\phi}_I|$ describes the attenuation of rocking motion when the relative rotation of the piers changes from negative to positive and is given by the bottom sign in Eq. (4-33).

Appendix C

Supplement to Chapter 6

C.1 Description of the Bridge Model and Analysis Outline [§6.2]

C.1.1 Original Bridge Overpass [§6.2.1]

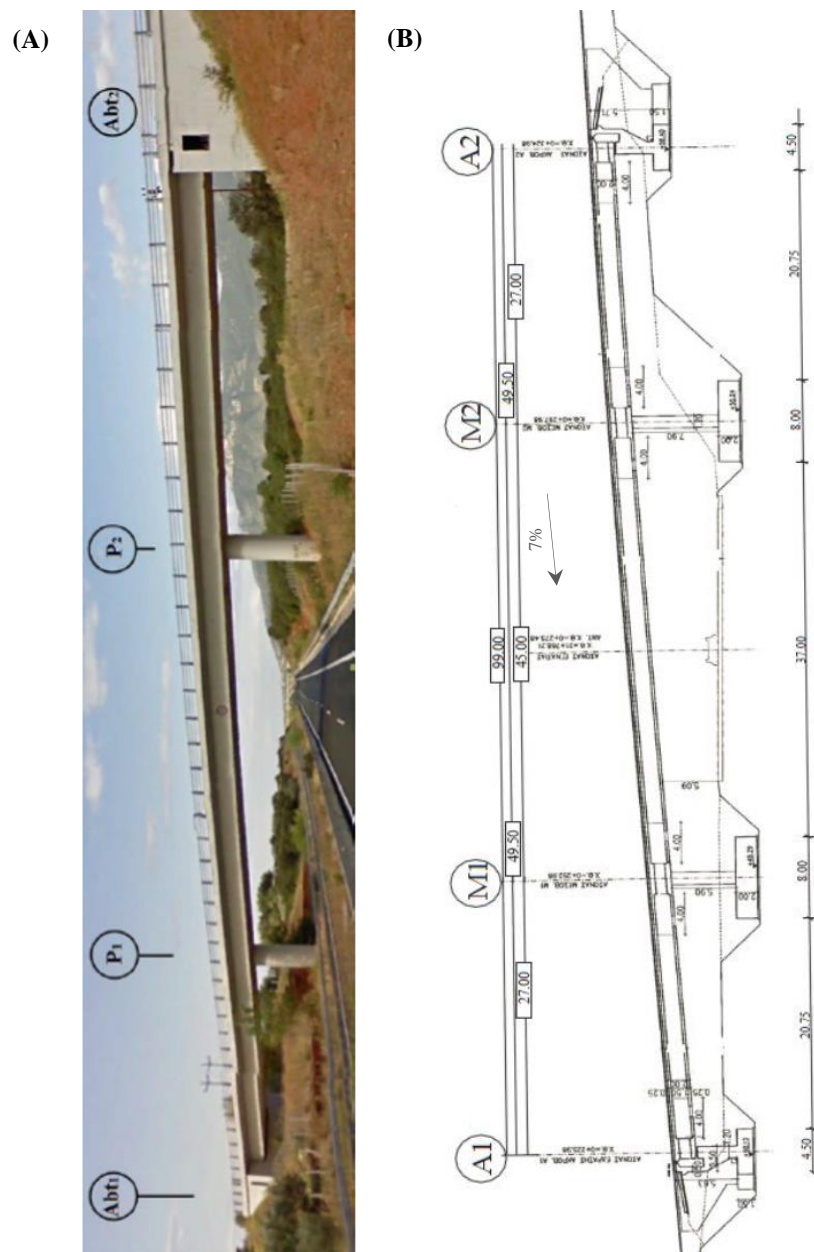


Fig. C-1 Overpass T7, Egnatia Motorway, N. Greece: (A) captured in Google Earth (2011) view (Gkatzogias 2017) and (B) schematic in the longitudinal direction (Egnatia Motorway 2002, Gkatzogias 2017).

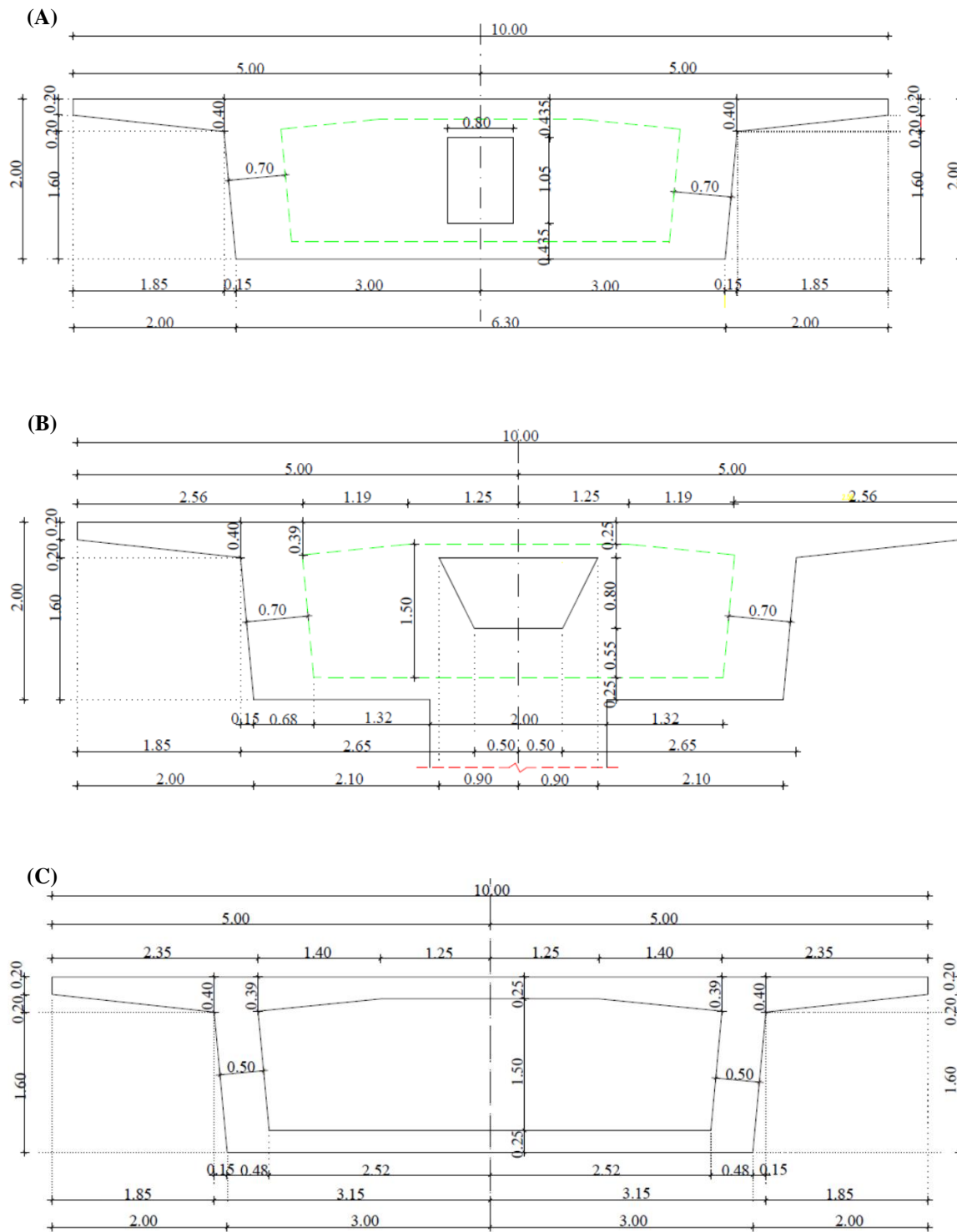


Fig. C-2 Schematic of the box girder section of Overpass T7 (Egnatia Motorway 2002, Paraskeva 2013) at the positions of (A) abutments, (B) piers and (C) spans.

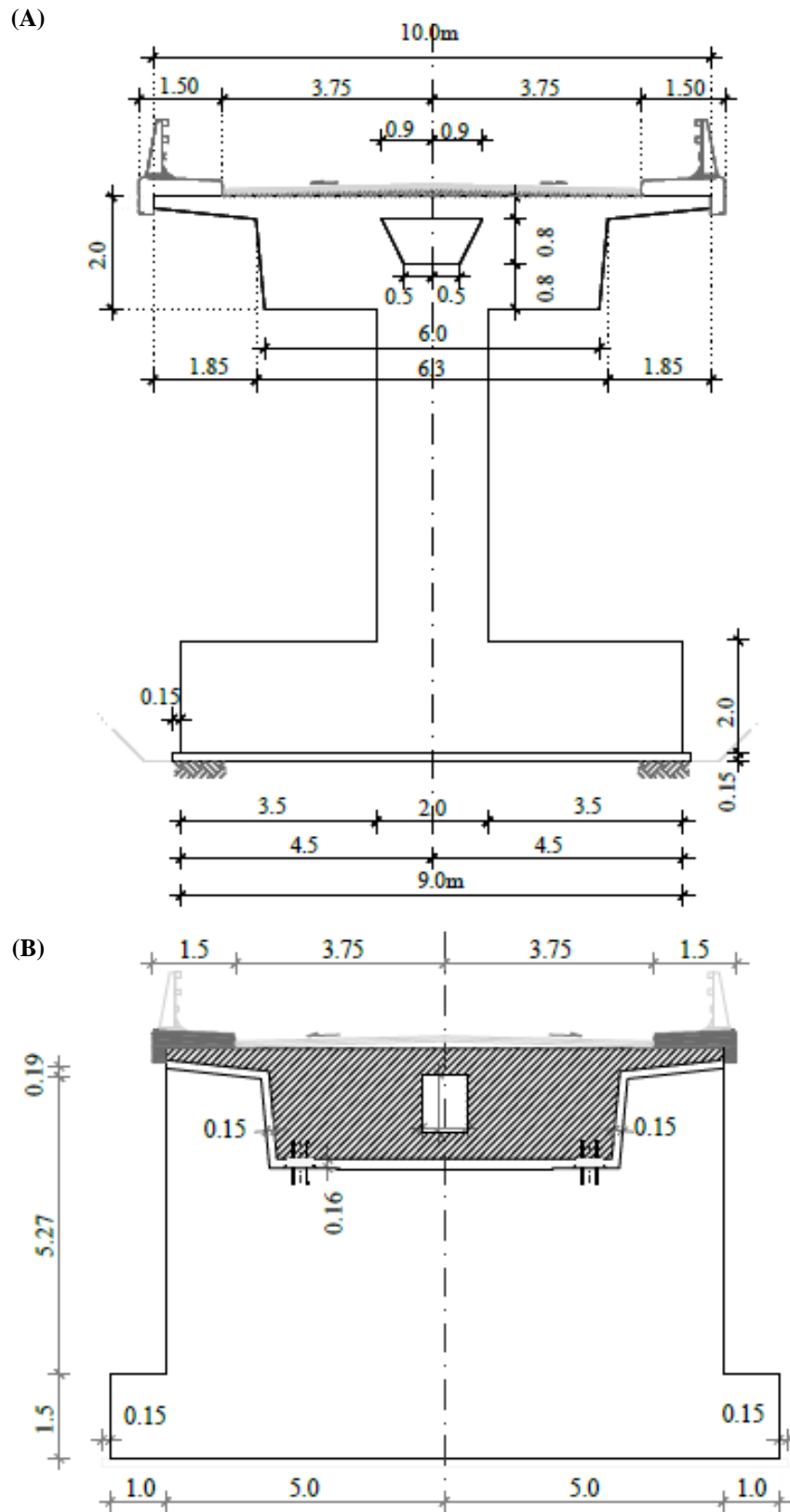


Fig. C-3 Schematic of lateral cross-section of Overpass T7 (Egnatia Motorway 2002, Gkatzogias 2017) in the locations of (A) Pier 1 and (B) Abutment 1.

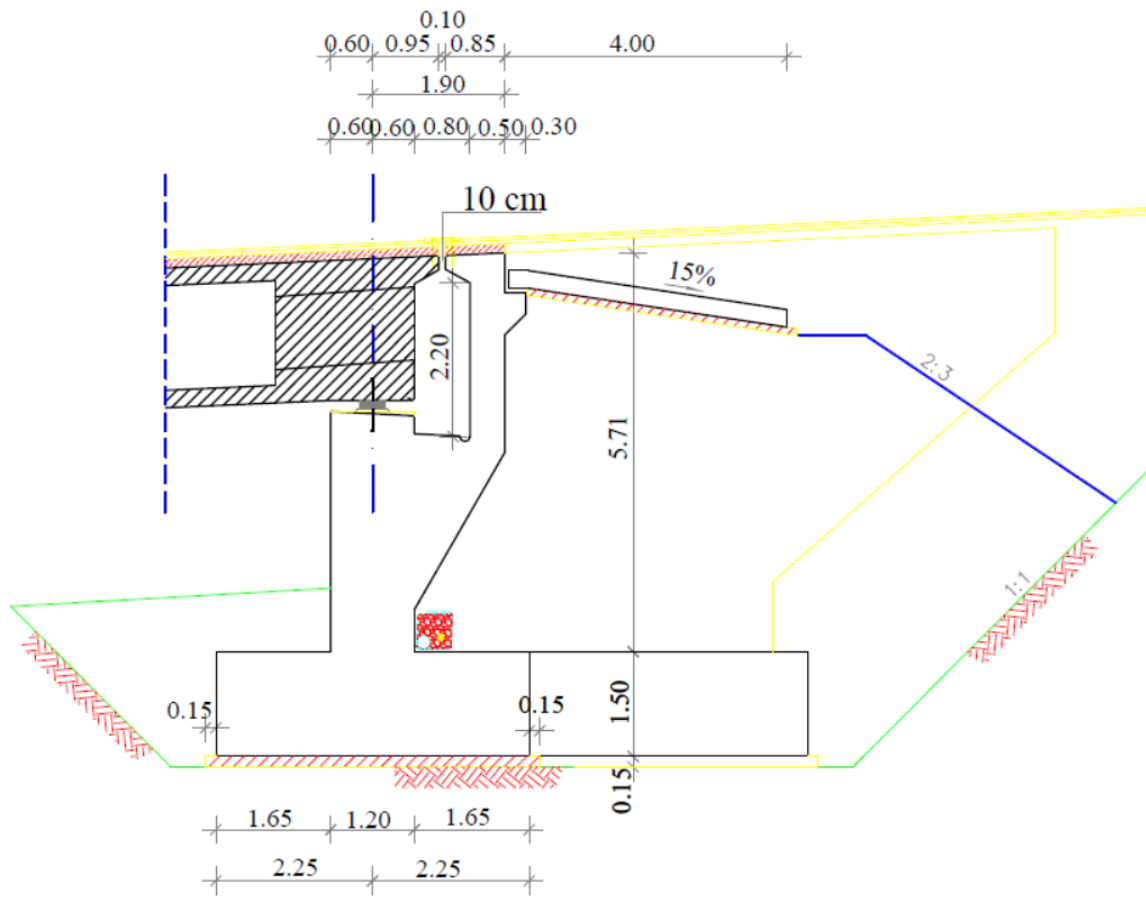


Fig. C-4 Schematic in the longitudinal direction of Abutment 2 of Overpass T7 (Egnatia Motorway 2002, Paraskeva 2013).

Appendix D

References

- AASHTO, 2010. Guide Specifications for Seismic Isolation Design. *American Association of State Highway and Transportation Officials*, Washington, USA.
- AASHTO, 2011. Guide Specifications for LRFD Seismic Bridge Design, 2nd Edition. *American Association of State Highway and Transportation Officials*, Washington, USA.
- ABAQUS CAE, 2018. Standard user's manual. *RI: Dassault Systèmes Simulia Corporation, ETH Zürich, Zürich, Switzerland.*
- Acikgoz, S., & DeJong, M.J., 2012. The interaction of elasticity and rocking in flexible structures allowed to uplift. *Earthquake Engineering and Structural Dynamics*, 41, 2177-2194.
- Acikgoz, S., & DeJong, M.J., 2014. The rocking response of large flexible structures to earthquakes. *Bulletin of Earthquake Engineering*, 12, 875-908.
- Acikgoz, S., & DeJong, M.J., 2018. A simple model to quantify rocking isolation. *Bulletin of the New Zealand Society of Earthquake Engineering*, 51 (1), 12-22.
- Agalianos, A., Psychari, A., Vassiliou, M.F., Stojadinovic, B., & Anastasopoulos, I., 2017. Comparative assessment of two rocking isolation techniques for a motorway overpass bridge. *Frontiers in Built Environment*, 3 (47), 1-19.
- Allen, R.H., Oppenheim, I.J., Parker, A.R., & Bielak, J., 1986. On the dynamic response of rigid body assemblies. *Earthquake Engineering and Structural Dynamics*, 14 (6), 861-876.
- Anagnostopoulos, S.A., 2004. Equivalent viscous damping for modelling inelastic impacts in earthquake pounding problems. *Earthquake Engineering and Structural Dynamics*, 33, 897-902.
- Anastasopoulos, I., Gazetas, G., Loli, M., Apostolou, M., & Gerolymos, N., 2010. Soil failure can be used for seismic protection of structures. *Bulletin of Earthquake Engineering*, 8, 309-326.
- Anastasopoulos, I., Kourkoulis, R., Gelagoti, F., & Papadopoulos, E., 2012. Rocking response of SDOF systems on shallow improved sand: An experimental study. *Soil Dynamics and Earthquake Engineering*, 40, 15-33.

Ancheta, D.T., Darragh, R.B., Stewart, J.P., Seyhan, E., Silva, W.J., Chiou, B.S.J., Wooddell, K.E., Graves, R.W., Kottke, A.R., Boore, D.M., Kishida, T., & Donahue, J.L., 2013. PEER NGA-West 2 Database. *Pacific Earthquake Engineering Research Center*, CA, USA. (<http://ngawest2.berkeley.edu/>)

Andisheh, K., Liu, R., Palermo, A., & Scott, A., 2018. Cyclic behavior of corroded fuse-type dissipaters for posttensioned rocking bridges. *Journal of Bridge Engineering*, 23 (4), 04018008.

ASCE, 2016. Minimum design loads and associated criteria for buildings and other structures. *American Society of Civil Engineers*, Virginia, USA.

Aslam, M., Scalise, D.T., & Godden, W.G., 1980. Earthquake rocking response of rigid blocks. *Journal of Structural Engineering Division*, 106, 377-392.

Athanassiadou, C.J., Penelis, G.G., & Kappos, A.J., 1994. Seismic response of adjacent buildings with similar or different dynamic characteristics. *Earthquake Spectra*, 10, 293–317.

Avgenakis, E., & Psycharis, I.N., 2020. An integrated microelement formulation for the dynamic response of inelastic deformable rocking bodies. *Earthquake Engineering and Structural Dynamics*, 49, 1072-1094.

Aviram, A., Mackie, K.R., & Stojadinovic, B., 2008. Effect of abutment modelling on the seismic response of bridge structures. *Earthquake Engineering and Engineering Vibration*, 7, 395-402.

Bachmann, J.A., Strand, M., Vassiliou, M.F., Broccardo, M., & Stojadinovic, B., 2018. Is rocking motion predictable?. *Earthquake Engineering and Structural Dynamics*, 47, 535-552.

Baker, M., 2018. How to get meaningful and correct results from your finite element model. *Technical Report, Technical University of Braunschweig*, Braunschweig, Germany.

Beck, J.L., & Skinner, R.I., 1974. The seismic response of a reinforced concrete bridge pier designed to step. *Earthquake Engineering and Structural Dynamics*, 2, 348-358.

Caltrans, 2013. Seismic design criteria version 1.7. *State of California Department of Transportation*, Sacramento, USA.

Caltrans, 2019. Seismic design criteria version 2.0. *State of California Department of Transportation*, Sacramento, USA.

Ceh, N., Jelenic, G., & Bicanic, N., 2018. Analysis of restitution in rocking of single rigid blocks. *Acta Mechanica*, 229, 4623-4642.

- CEN, 2002. Eurocode: Basis of structural design (EN1990). *Comité Européen de Normalisation*, Brussels, Belgium.
- CEN, 2004a. Eurocode 2: Design of concrete structures – Part 1-1: General rules and rules for buildings (EN1992-1-1). *Comité Européen de Normalisation*, Brussels, Belgium.
- CEN, 2004b. Eurocode 8: Design of structures for earthquake resistance – Part 1: General rules, seismic actions and rules for buildings (EN1998-1). *Comité Européen de Normalisation*, Brussels, Belgium.
- CEN, 2005a. Eurocode 8: Design of structures for earthquake resistance – Part 2: Bridges (EN1998-2). *Comité Européen de Normalisation*, Brussels, Belgium.
- CEN, 2005b. Structural bearings – Part 3: Elastomeric bearings (EN1337-3). *Comité Européen de Normalisation*, Brussels, Belgium.
- Ceravolo, R., Pecorelli, M.L., & Fragonara, L.Z., 2017. Comparison of semi-active control strategies for rocking objects under pulse and harmonic excitations. *Mechanical Systems and Signal Processing*, 90, 175-188.
- Chatzis, M.N., & Smyth, A.W., 2012. Modeling of the 3D rocking problem. *International Journal of Non-linear Mechanics*, 47, 85–98.
- Chatzis, M.N., Espinosa, M.G., & Smyth, A.W., 2017. Examining the energy loss in the inverted pendulum model for rocking bodies. *Journal of Engineering Mechanics*, 143 (5), 04017013.
- Chen, Y-H., Liao, W-H., Lee, C-L., & Wang, Y-P., 2006. Seismic isolation of viaduct piers by means of a rocking mechanism. *Earthquake Engineering and Structural Dynamics*, 35, 713-736.
- Cheng, C-T., 2007. Energy dissipation in rocking bridge piers under free vibration tests. *Earthquake Engineering and Structural Dynamics*, 36, 503-518.
- Cheng, C-T., 2008. Shaking table tests of a self-centering designed bridge substructure. *Engineering Structures*, 30, 3426-3433.
- Cheng, C-T., & Chen, F-l., 2013. Seismic performance of a rocking bridge pier substructure with frictional hinge dampers. *Smart Structures and Systems*, 14 (4), 501-516.
- Chow, N., 2017. Low-damage design philosophy for future earthquake-resistant structures. *Conference: ASME Pressure Vessels and Piping*, Waikoloa, Hawaii, USA.

- Constantinou, M.C., Kalpakidis, I., Filiatrault, A., & Ecker Lay, R.A., 2011. LRFD-based analysis and design procedures for bridge bearings and seismic isolators. *Technical Report MCEER*, New York, USA.
- DeJong, M.J., 2012. Amplification of rocking due to horizontal ground motion. *Earthquake Spectra*, 28 (4), 1405-1421.
- DeJong, M.J., & Dimitrakopoulos, E.G., 2014. Dynamically equivalent rocking structures. *Earthquake Engineering and Structural Dynamics*, 43, 1543-1563.
- Der Kiureghian, A., & Keshishian, P., 1997. Effects of incoherence, wave passage and spatially varying site conditions on bridge response. *Workshop: National Representation of Seismic Motion, Technical Report 97-0010. National Centre for Earthquake Engineering Research*.
- Di Egidio, A., & Contento, A., 2009. Base isolation of slide-rocking non-symmetric rigid blocks under impulsive and seismic excitations. *Engineering Structures*, 31, 2723-2734.
- Di Egidio, A., Zulli, D., & Contento, A., 2014. Comparison between the seismic response of 2D and 3D models of rigid blocks. *Earthquake Engineering and Engineering Vibration*, 13 (1), 1-12.
- Dimitrakopoulos, E.G., & DeJong, M.J., 2012a. Overturning of retrofitted rocking structures under pulse-type excitations. *Journal of Engineering Mechanics*, 138, 2294-2318.
- Dimitrakopoulos, E.G., & DeJong, M.J., 2012b. Revisiting the rocking block: closed-form solution and similarity laws. *Proceedings of the Royal Society A*, 468, 963-972.
- Dimitrakopoulos, E.G., & Fung, E.D.W., 2016. Closed-form rocking overturning conditions for a family of pulse ground notions. *Proceedings of the Royal Society A*, 472, 20160662.
- Dimitrakopoulos, E.G., & Giouvanidis, A.I., 2015. Seismic response analysis of the planar rocking frame. *Journal of Engineering Mechanics*, 141 (7), 04015003.
- Doolen, T.L., Tang, B., Saeedi, A., & Emani, S., 2011. To ABC or NOT?. *Public Roads*, 75 (3).
- Drosos, V.A., & Anastasopoulos, I., 2014. Shaking table testing of multi-drum columns and portals. *Earthquake Engineering and Structural Dynamics*, 43, 1703-1723.
- Drosos, V.A., & Anastasopoulos, I., 2015. Experimental investigation of the seismic response of classical temple columns. *Bulletin of Earthquake Engineering*, 13, 299-310.
- Du, X-L., Zhou, Y-L, Han, Q., & Jia, Z-L., 2019. Shaking table tests of a single-span freestanding rocking bridge for seismic resilience and isolation. *Advances in Structural Engineering*, 1-12.

- EAK2003, 2003. Greek seismic code. Athens, Greece.
- Egnatia Motorway, 2002. Overpass T7: Final design report. *Egnatia Motorway SA*, Greece.
- ElGawady, M.A., & Dawood, H.M., 2012. Analysis of segmental piers consisted of concrete filled FRP tubes. *Engineering Structures*, 38, 142-152.
- ElGawady, M.A., & Sha'Ian, A., 2011. Seismic behavior of self-centering precast segmental bridge bents. *Journal of Bridge Engineering*, 16 (3), 328-339.
- ElGawady, M.A., Booker, A.J., & Dawood, H.M., 2010. Seismic behavior of posttensioned concrete-filled fiber tubes. *Journal of Composites for Construction*.
- ElGawady, M.A., Ma, Q., Butterworth, J.W., & Ingham, J., 2011. Effects of interface material on the performance of free rocking blocks. *Earthquake Engineering and Structural Dynamics*, 40, 375-392.
- FEMA 356, 2000. Prestandard and commentary for the seismic rehabilitation of buildings. *American Society of Civil Engineers*, Washington, USA.
- Fielder, W.T., Virgin, L.N., & Plaut, R.H., 1997. Experiments and simulation of overturning of an asymmetric rocking block on an oscillating foundation. *European Journal of Engineering Mechanics Solids*, 16 (5), 905-923.
- Fiorentino, G., Forte, A., Pagano, E., Sabetta, F., Baggio, C., Lavorato, D., Nuti, C., & Santini, S., 2017. Damage patterns in the town of Amatrice after August 24th 2016 Central Italy earthquakes. *Bulletin of Earthquake Engineering*, 1-25.
- Frost, G., & Tilby, C., 2014. South Rangitikei railway bridge – Construction engineering. *Conference: The New Zealand Concrete Industry*, Taupo, New Zealand.
- Gasparini, D.A., & Vanmarcke, E.H., 1976. Simulated earthquake motions compatible with prescribed response spectra. *Massachusetts Institute of Technology*, MA, USA.
- Giouvanidis, A.I., & Dimitrakopoulos, E.G., 2016. The role of the prestressed tendons on the seismic performance of hybrid rocking bridge bents. *Conference: 7th ECCOMAS Thematic Conference on Computational Methods in Applied Sciences and Engineering* Crete, Greece.
- Giouvanidis, A.I., & Dimitrakopoulos, E.G., 2017a. Seismic performance of rocking frames with flag-shaped hysteretic behavior. *Journal of Engineering Mechanics*, 143 (5), 04017008.
- Giouvanidis, A.I., & Dimitrakopoulos, E.G., 2017b. Nonsmooth dynamic analysis of sticking impacts in rocking structures. *Bulleting of Earthquake Engineering*, 15, 2273-2304.

- Giouvanidis, A.I., & Dong, Y., 2020. Seismic loss and resilience assessment of single-column rocking bridges. *Bulleting of Earthquake Engineering*, 18, 4481-4513.
- Giouvanidis, A.I., Dimitrakopoulos, E.G., & DeJong, M.J., 2015. Seismic response of rocking bridge bents with parameterized flag-shaped hysteretic behaviour. *Conference: 10th Pacific Conference on Earthquake Engineering*, Sydney, Australia.
- Giouvanidis, A.I., Fragiadakis, M., & Dimitrakopoulos, E.G., 2017. Vulnerability assessment of flag-shaped hysteretic rocking bridge bents. *Conference: 6th ECCOMAS Thematic Conference on Computational Methods in Structural Dynamics and Earthquake Engineering*, Rhodes, Greece.
- Gkatzogias, K.I., 2017. Performance-based seismic design of concrete bridges for deformation control through advanced analysis tools and control devices. *Thesis (PhD)*, City, University of London, London, UK.
- Gkatzogias, K.I., & Kappos, A.J., 2016. Seismic design of concrete bridges: Some key issues to be addressed during the evolution of Eurocode 8 - Part 2. Concrete Structures *Conference: Hellenic Society of Concrete Research and Technical Chamber of Greece*, Thessaloniki, Greece.
- Hao, H., 1989. Effects of spatial variation of ground motions on large multiply-supported structures. *Technical Report*, University of California, Berkeley, California, USA.
- Hao, H., & Zhou, Y., 2011. Rigid structure response analysis to seismic and blast induced ground motions. *Procedia Engineering*, 14, 946-955.
- Harvey Jr., P.S., 2017. Behavior of a rocking block resting on a rolling isolation system. *Journal of Engineering Mechanics*, 143 (8), 04017045
- Haselton, C.B., Baker, J.W., Stewart, J.P., Whittaker, A.S., Luco, N., Fry, A., Hamburger, R.O., Zimmerman, R.B., Hooper, J.D., Charney, F.A., & Pekelnicky, R.G., 2017. Response history analysis for the design of new buildings in the NEHRP provisions and ASCE/SEI 7 standard: Part I: Overview and specification of ground motions. *Earthquake Spectra*, 33 (2), 373-395.
- Hilber, H.M., Hughes, T.J., & Taylor, R.L., 1977. Improved numerical dissipation for the time integration algorithms in structural dynamics. *Earthquake Engineering and Structural Dynamics*, 5, 283-292.
- Housner, G.W., 1963. The behavior of inverted pendulum structures during earthquakes. *Bulletin of the Seismological Society of America*, 53 (2), 403-417.

- Housner, G.W., Bergman, L.A., Caughey, T.K., Chassiakos, A.G., Claus, R.O., Masri, S.F., Skeltom, R.E., Soong, T.T., Spencer, B.F., & Yao, J.T.P., 1997. Structural control: Past, present, and future. *Journal of Engineering Mechanics*, 123 (9), 897-971.
- Hung, H-H., Liu, K-Y., Ho, T-H., & Chang, K-C., 2011. An experimental study on the rocking response of bridge piers with spread footing foundations. *Earthquake Engineering and Structural Dynamics*, 40, 749-769.
- Ikegami, R., & Kishinouye, F., 1947. A study on the overturning of rectangular columns in the case of the Nankai earthquake on December 21, 1946. *Bulletin of the Earthquake Research Institute, University of Tokyo*, 25, 49-55.
- Ikegami, R., & Kishinouye, F., 1950. The acceleration of earthquake motion deduced from overturning of the gravestones in case of the Imaichi Earthquake on December 26, 1949. *Bulletin of the Earthquake Research Institute, University of Tokyo*, 28, 121-128.
- Ishiyama, Y., 1982. Motions of rigid bodies and criteria for overturning by earthquake excitations. *Earthquake Engineering and Structural Dynamics*, 10, 635-650.
- Jankowski, R., 2007. Theoretical and experimental assessment of parameters for the non-linear viscoelastic model of structural pounding. *Journal of Theoretical and Applied Mechanics*, 45 (4), 931-942.
- Jeong, M.J., Suzuki, K., & Yim C-S., 2003. Chaotic rocking behaviour of freestanding objects with sliding motion. *Journal of Sound and Vibration*, 262, 1091–1112.
- Kajitani, T., Chang, S.E., & Tatano, H., 2013. Economic impacts of the 2011 Tohoku-Oki earthquake and tsunami. *Earthquake Spectra*, 29, 457-478.
- Kalliontzis, D., & Sritharan, S., 2018. Characterizing dynamic decay of motion of free-standing rocking members. *Earthquake Spectra*, 34 (2), 843-866.
- Kalliontzis, D., Sritharan, S., & Schultz, A., 2016. Improved coefficient of restitution estimation for free rocking members. *Journal of Structural Engineering*, 142 (12).
- Kam, W.Y., Pampanin, S., Palermo, A., & Carr, A.J., 2010. Self-centering structural systems with combination of hysteretic and viscous energy dissipations. *Earthquake Engineering and Structural Dynamics*, 39, 1083-1108.
- Kappos, A.J., Potikas, P., & Sextos, A.G., 2007. Seismic assessment of an overpass bridge accounting for non-linear material and soil response and varying boundary conditions.

Conference: ECCOMAS Thematic Conference on Computational Methods in Structural Dynamics and Earthquake Engineering, Rethymno, Greece.

Karavasilis, T.L., Blakeborough, T., & Williams, M.S., 2011. Development of nonlinear analytical model and seismic analyses of a steel frame with self-centering devices and viscoelastic dampers. *Computers and Structures*, 89, 1232-1240.

Kawashima, K., Unjoh, S., Hoshikuma, J.L., & Kosa, K., 2011. Damage of bridges due to the 2010 Maule, Chile, earthquake. *Journal of Earthquake Engineering*, 15 (7), 1036-1068.

Kirkpatrick, P., 1927. Seismic measurements by the overthrow of columns. *Bulletin of the Seismological Society of America*, 17, 95-109.

Konstantinidis, D., & Makris, N., 2005. Seismic response analysis of multidrum classical columns. *Earthquake Engineering and Structural Dynamics*, 34, 1243-1270.

Kounadis, A.N., & Papadopoulos, G.J., 2016. On the rocking instability of a three-rigid block system under ground motion. *Archive of Applied Mechanics*, 86, 957-977.

Kwon, O-S., & Elnashai, A.S., 2010. Fragility analysis of a highway over-crossing bridge with consideration of soil-structure interactions. *Structure and Infrastructure Engineering*, 6 (1-2), 159-178.

Leitner, E.J., & Hao, H., 2016. Three-dimensional finite element modelling of rocking bridge piers under cyclic loading and exploration of options for increased energy dissipation. *Engineering Structures*, 118, 74-88.

Li, C., Hao, H., & Bi, K., 2017. Numerical study on the seismic performance of precast segmental concrete columns under cyclic loading. *Engineering Structures*, 148, 373-386.

Lipscombe, P.R., & Pellegrino, S., 1993. Free rocking of prismatic blocks. *Journal of Engineering Mechanics*, 119 (7), 1387-1410.

Ma, Q.T., & Khan, M.H., 2008. Free vibration tests of a scale model of the South Rangitikei railway bridge. *Conference: New Zealand National Society for Earthquake Engineering*, New Zealand.

Marian, L., & Giaralis, A., 2014. Optimal design of a novel tuned mass-damper-inerter (TMDI) passive vibration control configuration for stochastically support-excited structural system. *Probabilistic Engineering Mechanics*, 38, 156-164.

Makris, N., 2014. A half-century of rocking isolation. *Earthquakes and Structures*, 7 (6), 1187-1221.

- Makris, N., 2018. Seismic Isolation: Early history. *Earthquake Engineering and Structural Dynamics*, 1-16.
- Makris, N., & Aghagholizadeh, M., 2019. Effect of supplemental hysteretic and viscous damping on rocking response of free-standing columns. *Journal of Engineering Mechanics*, 145 (5), 04019028.
- Makris, N., & Black, C.J., 2002. Uplifting and overturning of equipment anchored to a base foundation. *Earthquake Spectra*, 18 (4), 631-661.
- Makris, N., & Kampas, G., 2016a. Seismic protection of structures with supplemental rotational inertia. *Journal of Engineering Mechanics*, 04016089.
- Makris, N., & Kampas, G., 2016b. Size versus slenderness: Two competing parameters in the seismic stability of free-standing rocking columns. *Bulletin of the Seismological Society of America*, 106 (1).
- Makris, N., & Konstantinidis, D., 2003. The rocking spectrum and the limitations of practical design methodologies. *Earthquake Engineering and Structural Dynamics*, 32, 265-289.
- Makris, N., & Roussos, Y., 2000. Rocking response of rigid blocks under near-source ground motions. *Geotechnique*, 50 (3), 243-262.
- Makris, N., & Vassiliou, M.F., 2012. Sizing the slenderness of free-standing rocking columns to withstand earthquake shaking. *Archive of Applied Mechanics*, 82, 1497-1511.
- Makris, N., & Vassiliou, M.F., 2013. Planar rocking response and stability analysis of an array of free-standing columns capped with a freely supported rigid beam. *Earthquake Engineering and Structural Dynamics*, 42, 431-449.
- Makris, N., & Vassiliou, M.F., 2014a. Dynamics of the rocking frame with vertical restrainers. *Journal of Structural Engineering*, 141 (10), 04014245.
- Makris, N., & Vassiliou, M.F., 2014b. Are some top-heavy structures more stable?. *Journal of Structural Engineering*, 140 (5), 06014001.
- Makris, N., & Vassiliou, M.F., 2014c. The dynamics of a vertically restrained rocking bridge. *International Journal of Bridge Engineering*, 2 (3), 67-75.
- Makris, N., & Zhang, J., 2001. Rocking response of anchored blocks under pulse-type motions. *Journal of Engineering Mechanics*, 127 (5), 484-493.

- Mander, J.B., & Cheng C-T., 1997. Seismic resistance of bridge piers based on damage avoidance design. *Technical Report, NCEER-97-0014*, New York, USA.
- Mantawy, I.M., Thonstad, T., Sanders, D.H., Stanton, J.F., & Eberhard, M.O., 2016. Seismic performance of precast, pretensioned, and cast-in-place: Shake test comparison. *Journal of Bridge Engineering*, 21 (10), 04016071.
- Marriott, D., Pampanin, S., & Palermo, A., 2009. Quasi-static and pseudo-dynamic testing of unbonded post-tensioned rocking bridge piers with external replaceable dissipaters. *Earthquake Engineering and Structural Dynamics*, 38, 331-354.
- Mathey, C., Feau, C., Politopoulos, I., Clair, D., Baillet, L., & Fogli, M., 2016. Behavior of rigid blocks with geometrical defects under seismic motion: An experimental and numerical study. *Earthquake Engineering and Structural Dynamics*, 45, 2455-2474.
- MATLAB, 2016. Version 9.1.0.441655 (R2016). Natick, Massachusetts: The MathWorks Incorporation.
- Mavroeidis, G.P., Dong, G., & Papageorgiou, A.S., 2004. Near-fault ground motions, and the response of elastic and inelastic Single-Degree-of-Freedom (SDOF) systems. *Earthquake Engineering and Structural Dynamics*, 33, 1023-1049.
- Milne, J., 1885. Seismic experiments. *Transactions of the Seismological Society of Japan*, 8, 1-82.
- Mohamad, M.E., Ibrahim, I.S., Abdullah, R., Rahman, A.B., Kueh, A.B.H., & Usman, J., 2015. Friction and cohesion coefficients of composite concrete-to-concrete bond. *Cement & Concrete Composites*, 56, 1-14.
- Muthukumar, S., & DesRoches, R., 2006. A Hertz contact model with non-linear damping for pounding simulation. *Earthquake Engineering and Structural Dynamics*, 35, 811-828.
- Muto, K., Umemura, H., & Sonobe, Y., 1960. Study of the overturning vibration of slender structures. *Conference: 2nd World Conference on Earthquake Engineering*, Tokyo, Japan.
- Mylonakis, G., Nikolaou, S., & Gazetas, G., 2006. Footings under seismic loading: Analysis and design issues with emphasis on bridge foundations. *Soil Dynamics and Earthquake Engineering*, 26, 824-853.
- Naeim, F., & Kelly, J.M., 1999. Design of seismic isolated structures: From theory to practice. *Wiley*, New York, USA.

- Ogawa, N., 1977. A study on rocking and overturning of rectangular column. *National Research Centre for Disaster Prevention*, Tokyo, Japan.
- Ou, Y., Chiewanichakorn, M., Aref, A.J., & Lee, G.C., 2007. Seismic performance of segmental precast unbonded posttensioned concrete bridge columns. *Journal of Structural Engineering*, 133 (11), 1636-1647.
- Palermo, A., & Pampanin, S., 2008. Enhanced seismic performance of hybrid bridge systems: Comparison with traditional monolithic solutions. *Journal of Earthquake Engineering*, 12, 1267-1295.
- Palermo, A., Pampanin, S., & Calvi, G.M., 2004. Use of “controlled rocking” in the seismic design of bridges. *Conference: 13th World Conference on Earthquake Engineering*, Vancouver, Canada.
- Palermo, A., Pampanin, S., & Calvi, G.M., 2005. Concept and development of hybrid solutions for seismic resistant bridge systems. *Journal of Earthquake Engineering*, 9 (6), 899-921.
- Palermo, A., Pampanin, S., & Marriott, D., 2007. Design, modeling, and experimental response of seismic resistant bridge piers with post-tensioned dissipating connections. *Journal of Structural Engineering*, 133 (11), 1648-1661.
- Palermo, A., Liu, R., Rais, A., McHaffie, B., Andisheh, K., Pampanin, S., Gentile, R., Nuzzo, I., Granerio, M., & Loporcaro, G., 2017. Performance of road bridges during the 14 November 2016 Kaikoura earthquake. *Bulletin of the New Zealand Society for Earthquake Engineering*, 50, 253-270.
- Pampanin, S., 2012. Reality-check and renewed challenges in earthquake engineering: Implementing low-damage structural systems-from theory to practice. *Bulletin of the New Zealand Society for Earthquake Engineering*, 137-160.
- Papantonopoulos, C., Psycharis, I.N., Papastamatiou, D.Y., Lemos, J.V., & Mouzakis, H.P., 2002. Numerical prediction of the earthquake response of classical columns using the distinct element method. *Earthquake Engineering and Structural Dynamics*, 31, 1699-1717.
- Paraskeva, T.S., 2013. Inelastic analysis of the dynamic behaviour of concrete bridges. *Thesis (PhD)*, Aristotle University of Thessaloniki, Thessaloniki, Greece.
- Paraskeva, T.S., & Kappos, A.J., 2010. Further development of a multimodal pushover analysis procedure for seismic assessment of bridges. *Earthquake Engineering and Structural Dynamics*, 39 (2), 211-222.

- Pecorelli, M.L., & Ceravolo, R., 2017. Semiactive control of rigid blocks under earthquake excitation. *Earthquake Engineering and Structural Dynamics*, 47, 738-756.
- Pelekis, I., Madabhushi, G.S.P., & DeJong, M.J., 2019. Soil behaviour beneath buildings with structural and foundation rocking. *Soil Dynamics and Earthquake Engineering*, 123, 48-63.
- Pena, F., Prieto, F., Lourenco, P.B., Campos Costa, A., & Lemos, J.V., 2007. On the dynamics of rocking motion of single rigid-block structures. *Earthquake Engineering and Structural Dynamics*, 36, 2383-2399.
- Pompei, A., Scalia, A., & Sumbatyan M.A., 1998. Dynamics of rigid block due to horizontal ground motion. *Journal of Engineering Mechanics*, 124, 713-717.
- Priestley, M.J.N., & Grant, D.N., 2005. Viscous damping in seismic design and analysis. *Journal of Earthquake Engineering*, 9 (2), 229-255.
- Priestley, M.J.N., Evison, R.J., & Carr, A.J., 1978. Seismic response of structures free to rock on their foundations. *Bulletin of the New Zealand Society for Earthquake Engineering*, 11 (3), 141–150.
- Prieto, F., Lourenco, P.B., & Oliveira, C.S., 2004. Impulsive dirac-delta forces in the rocking motion. *Earthquake Engineering and Structural Dynamics*, 33, 839-857.
- Psychari, A., Agalianos, A., Vassiliou, M., Stojadinovic, B., & Anastasopoulos, I., 2017. Seismic performance of rocking isolated overpass bridge. *Conference: Earthquake Geotechnical Engineering*, Vancouver, Canada.
- Psycharis, I.N., & Jennings, P.C., 1983. Rocking of slender rigid bodies allowed to uplift. *Earthquake Engineering and Structural Dynamics*, 11, 57-76.
- Psycharis, I., Papastamatiou, D., & Alexandris, A., 2000. Parametric investigation of the stability of classical columns under harmonic and earthquake excitations. *Earthquake Engineering & Structural Dynamics*, 1093-1110.
- Rodgers, G.W., Mander, J.B., Chase, J.G., & Dhakal, R.P., 2016. Beyond ductility: Parametric testing of a jointed rocking beam-column connection designed for damage avoidance. *Journal of Structural Engineering*, 142 (8), C4015006.
- Roh, H.S., & Reinhorn, A.M., 2008. Dynamic response of weakened structures using rocking columns. *Conference: 14th World Conference on Earthquake Engineering*, Beijing, China.

- Roh, H., & Reinhorn, A.M., 2009. Analytical modeling of rocking elements. *Engineering Structures*, 31, 1179-1189
- Roh, H.S., & Reinhorn, A.M., 2010a. Nonlinear static analysis of structures with rocking columns. *Journal of Structural Engineering*, 135 (5), 532-542.
- Roh, H.S., & Reinhorn, A.M., 2010b. Modelling and seismic response of structures with concrete rocking columns and viscous dampers. *Engineering Structures*, 32, 2096-2107.
- Roussis, P.C., & Odysseos, S., 2017. Rocking response of seismically-isolated rigid blocks under simple acceleration pulses and earthquake excitations. *The Open Construction and Building Technology Journal*, 11, 217-236.
- Routledge, P.J., Cowan, M.J., & Palermo, A., 2016. Low-damage detailing for bridges – A case study of Wigram-Magdala bridge. *Conference: The New Zealand National Society for Earthquake Engineering*, New Zealand.
- Ryan, K.L., Kelly, J.M., & Chopra, A.K., 2005. Nonlinear model for lead-rubber bearings including axial-load effects. *Journal of Engineering Mechanics*, 131 (2), 1270–1278.
- Sakai, J., & Mahin, S.A., 2004. Mitigation of residual displacements of circular reinforced concrete bridge columns. *Conference: 13th World Conference on Earthquake Engineering*, Vancouver, Canada.
- Salehi, M., Sideris, P., & Liel, A.B., 2017. Numerical simulation of hybrid sliding-rocking columns subjected to earthquake excitation. *Journal of Structural Engineering*, 143 (11), 04017149.
- Saragoni, G.R., & Hart, G.C., 1974. Simulation of artificial earthquakes. *Earthquake Engineering and Structural Dynamics*, 2 (3), 249-267.
- Scalia, A., & Sumbatyan, M.A., 1996. Slide rotation of rigid bodies subjected to a horizontal ground motion. *Earthquake Engineering and Structural Dynamics*, 25, 1139-1149.
- Sextos, A.G., & Kappos, A.J., 2009. Evaluation of seismic response of bridges under asynchronous excitation and comparisons with Eurocode 8-2 provisions. *Bulletin of Earthquake Engineering*, 7, 519-545.
- Sextos, A.G., Kappos, A.J., & Ptilakis, K.D., 2003. Inelastic dynamic analysis of RC bridges accounting for spatial variability of ground motion, site effects and soil-structure interaction phenomena. Part 2: Parametric study. *Earthquake Engineering and Structural Dynamics*, 32, 629-652.

- Shamsabadi, A., Khalili-Tehrani, P., Stewart, J.P., & Taciroglou, E., 2010. Validated simulation models for lateral response of bridge abutments with typical backfills. *Journal of Bridge Engineering*, 15 (3), 302-311.
- Shenton, H.W., 1996. Criteria for initiation of slide, rock, and slide-rock rigid-body modes. *Journal of Engineering Mechanics*, 122, 690-693.
- Shi, Z., & Dimitrakopoulos, E.G. 2017. Comparative evaluation of two simulation approaches of deck-abutment pounding in bridges. *Engineering Structures*, 148, 541-551.
- Shi, B., Anooshehpour, A., Zeng, Y., & Brune, J.N., 1996. Rocking and overturning of precariously balanced rocks by earthquakes. *Bulletin of the Seismological Society of America*, 86 (5), 1364-1371.
- Sideris, P., 2012. Seismic analysis and design of precast concrete segmental bridges. *Thesis (PhD)*, State University of New York at Buffalo, New York, USA.
- Sideris, P., 2015. Nonlinear quasi-static analysis of hybrid sliding-rocking bridge columns subjected to lateral loading. *Engineering Structures*, 101, 125-137.
- Sideris, P., Aref, A.J., & Filiatraut, A., 2014a. Large-scale seismic testing of a hybrid sliding-rocking posttensioned segmental bridge system. *Journal of Structural Engineering*, 140 (6), 04014025.
- Sideris, P., Aref, A.J., & Filiatraut, A., 2014b. Quasi-static cyclic testing of a large-scale hybrid sliding-rocking segmental column with slip-dominant joints. *Journal of Bridge Engineering*, 19 (10), 04014036.
- Sideris, P., Aref, A.J., & Filiatraut, A., 2015. Experimental seismic performance of a hybrid sliding-rocking bridge for various specimen configurations and seismic loading conditions. *Journal of Bridge Engineering*, 20, 328-339.
- Sinopoli, A., 1989. Kinematic approach in the impact problem of rigid bodies. *Applied Mechanics Reviews (ASME)*, 42, S233-S244.
- Smith, M.C., 2002. Synthesis of mechanical networks: The inerter. *Institute of Electrical and Electronics Engineers Transaction on automatic control*, 47 (10), 1648-1662.
- Spanos, P.D., & Koh, A.S., 1984. Rocking of rigid blocks due to harmonic shaking. *Journal of Engineering Mechanics*, 110, 1627-1642.

- Stanton, J.F., Stone, W.C., & Cheok, G.S., 1997. A hybrid reinforced precast frame for seismic regions. *Precast/Prestressed Concrete Institute Journal*, 42 (2), 20-32.
- Symans, M.D., & Constantinou, M.C., 1999. Semi-active control systems for seismic protection of structures: A state-of-the-art review. *Engineering Structures*. 21 (6), 469–487
- Taniguchi, T., 2002. Non-linear response analyses of rectangular rigid bodies subjected to horizontal and vertical ground motion. *Earthquake Engineering and Structural Dynamics*, 31, 1481-1500.
- Taskari, O., & Sextos A., 2015. Multi-angle, multi-damage fragility curves for seismic assessment of bridges. *Earthquake Engineering and Structural Dynamics*, 44, 2281-2301.
- Ther, T., & Kollár, L.P., 2017. Refinement of the Housner's model and its application for the overturning acceleration spectra. *Conference: 16th World Conference on Earthquake Engineering*, Santiago, Chile.
- Ther, T., & Kollár, L.P., 2018. Overturning of rigid blocks for earthquake excitation. *Bulletin of Earthquake Engineering*, 16, 1607-1631.
- Thiers-Moggia, R., & Málaga-Chuquitaype, C., 2018. Seismic protection of rocking structures with inerters. *Earthquake Engineering and Structural Dynamics*, 48, 528-547.
- Thiers-Moggia, R., & Málaga-Chuquitaype, C., 2020a. Dynamic response of post-tensioned rocking structures with inerters. *International Journal of Mechanical Sciences*, 187, 105927.
- Thiers-Moggia, R., & Málaga-Chuquitaype, C., 2020b. Seismic control of flexible rocking structures using inerters. *Earthquake Engineering and Structural Dynamics*, 1-20.
- Thomaidis, I.M., Camara, A., & Kappos, A.J., 2018. Simulating the rocking response of rigid bodies using general-purpose finite element software. *Conference: 16th European Conference on Earthquake Engineering*, Thessaloniki, Greece.
- Thonstad, T., Mantawy, I.M., Stanton, J.F., Eberhard, M.O., & Sanders, D.H., 2016. Shaking table performance of a new bridge system with pretensioned rocking columns. *Journal of Bridge Engineering*, 21 (4), 04015079.
- Titirla, M., Zarkadoulas, N., Mitoulis, S., & Mylonakis, G., 2017. Rocking isolation of bridge piers using elastomeric pads. *Conference; 16th World Conference on Earthquake Engineering*, Santiago, Chile.

- Trono, W., Jen, G., Panagiotou, M., Schoettler, M., & Ostertag, C.P., 2015. Seismic response of a damage-resistant recentering posttensioned-HYFRC bridge column. *Journal of Bridge Engineering*, 20 (7), 04014096.
- Tso, W.K., & Wong, C.M., 1989a. Steady state rocking response of rigid blocks part 1: Analysis. *Earthquake Engineering and Structural Dynamics*, 18, 89-106.
- Tso, W.K., & Wong C.M., 1989b. Steady state rocking response of rigid blocks part 2: Experiment. *Earthquake Engineering and Structural Dynamics*, 18, 107-120.
- Tucker, C., & Ibarra, L., 2016. Effects of partial-design-strength concrete on the seismic performance of concrete-filled tube columns in accelerated bridge construction. *Journal of Bridge Engineering*, 21 (6), 04016023.
- Van Engelen, N.C., & Kelly, J.M., 2015. Correcting for the influence of bulk compressibility on the design properties of elastomeric bearings. *Journal of Engineering Mechanics*, 141 (6).
- Vassiliou, M.F., 2017. Seismic response of a wobbling 3D frame. *Earthquake Engineering and Structural Dynamics*, 1-17.
- Vassiliou, M.F., & Makris, N., 2011. Estimating time scales and length scales in pulse-like earthquake acceleration records with wavelet analysis. *Bulletin of the Seismological Society of America*, 101, 596-618.
- Vassiliou, M.F., & Makris, N., 2012. Analysis of the rocking response of rigid blocks standing free on a seismically isolated base. *Earthquake Engineering and Structural Dynamics*, 21, 177-196
- Vassiliou, M.F., & Makris, N., 2015. Dynamics of the vertically restrained rocking column. *Journal of Engineering Mechanics*, 2015, 141 (12), 04015049.
- Vassiliou, M.F., Mackie, K.R., & Stojadinovic, B., 2014. Dynamic response of solitary flexible rocking bodies: Modeling and behavior under pulse-like ground excitation. *Earthquake Engineering and Structural Dynamics*, 43, 1463-1481.
- Vassiliou, M.F., Truniger, R., & Stojadinovic, B., 2015. An analytical model of a deformable cantilever structure rocking on a rigid surface: Experimental validation. *Earthquake Engineering and Structural Dynamics*, 44, 2795-2815.
- Vassiliou, M.F., Mackie, K.R., & Stojadinovic, B., 2016. A finite element model for seismic response analysis of deformable rocking frames. *Earthquake Engineering and Structural Dynamics*, 42, 431-449.

- Vassiliou, M.F., Burger, S., Egger, M., Bachmann, J.A., Broccardo, M., & Stojadinovic, B., 2017. The three-dimensional behavior of inverted pendulum cylindrical structures during earthquakes. *Earthquake Engineering and Structural Dynamics*, 46 (14), 2261-2280
- Voyagaki, E., Psycharis, I.N., & Mylonakis G.E., 2012. Rocking response and overturning criteria for free standing blocks to single-lobe pulses. *Conference: 15th World Conference on Earthquake Engineering*, Lisboa, Portugal.
- Wacker, J.M., Hieber, D.G., Stanton, J.F., & Eberhard, M.O., 2005. Design of precast concrete piers for rapid bridge construction in seismic regions. *Washington State Department of Transportation*, Washington, USA.
- Wang, Z., Wang, J-Q., Liu, T-X., & Zhang, J., 2018. An explicit analytical model for seismic performance of an unbonded post-tensioned precast segmental rocking hollow pier. *Engineering Structures*, 161, 176-191.
- Wiebe, L., & Christopoulos, C., 2009. Mitigation of higher mode effects in base-rocking systems by using multiple rocking sections. *Journal of Earthquake Engineering*, 13, 83-108.
- Wilson, P., & Elgamal, A., 2010. Full-scale bridge abutment passive earth pressure experiment and simulation. *Journal of Geotechnical and Geoenvironmental Engineering*, 136 (12), 1634–1643.
- Xie, Y., Huo, Y., & Zhang, J., 2017. Development and validation of p-y modeling approach for seismic response predictions of highway bridges. *Earthquake Engineering and Structural Dynamics*, 46, 585-604.
- Xie, Y., Zhang, J., DesRoches, R. & Padgett, J.E., 2019. Seismic fragilities of single-columns highway bridges with rocking column-footing. *Earthquake Engineering and Structural Dynamics*, 1-22.
- Yim, C-S., & Chopra, A.K., 1984. Earthquake response of structures with partial uplift on Winkler foundation. *Earthquake Engineering and Structural Dynamics*, 12, 263-281.
- Yim, C-S., Chopra, A.K., & Penzien, J., 1980. Rocking response of rigid blocks to earthquakes. *Earthquake Engineering and Structural Dynamics*, 8, 565-587.
- Zhang, J., & Makris, N., 2001. Rocking response of free-standing blocks under cycloidal pulses. *Journal of Engineering Mechanics*, 127 (5), 473-483.
- Zhang, J., & Makris, N., 2002. Kinematic response functions and dynamic stiffnesses of bridge embankments. *Earthquake Engineering and Structural Dynamics*, 31, 1933-1966.

Zhang, J., Guan, Z., Liang, L., & Ling, X., 2018. Experimental study on longitudinal joints with accelerated construction features in precast multibox girder bridges. *Journal of Bridge Engineering*, 23 (1), 04017116.

Appendix E

Relevant Publications

- Thomaidis, I.M., Camara, A., & Kappos, A.J., 2017. Simulating the response of free-standing rocking rigid blocks using Abaqus/Standard. *Conference: SIMULIA UK Regional User Meeting*, Warrington, UK. (Based on the Transfer report of the present thesis)
- Thomaidis, I.M., Kappos, A.J., & Camara, A., 2019. Dynamics and seismic stability of planar symmetric rocking bridges. *Conference: 2nd International Conference on Natural Hazards & Infrastructure*, Crete, Greece. (Based on Chapter 3 of the present thesis)
- Thomaidis, I.M., Kappos, A.J., & Camara, A., 2019. Dynamics of planar asymmetric rocking bridges including the abutment contribution. *Conference: SECED 2019: Earthquake Risk and Engineering towards a Resilient World*, Greenwich, UK. (Based on Chapter 4 of the present thesis)
- Thomaidis, I.M., Kappos, A.J., & Camara, A., 2020. Dynamics and seismic performance of rocking bridges accounting for the abutment-backfill contribution. *Earthquake Engineering and Structural Dynamics*, 1-19. (Based on Chapter 3 of the present thesis)
- Thomaidis, I.M., Kappos, A.J., & Camara, A., 2021. Rocking vs conventional seismic isolation: Comparative assessment of asymmetric bridges in a design context. *Conference: 17th World Conference on Earthquake Engineering*, Sendai, Japan. (Based on Chapter 6 of the present thesis)